

REPORT DOCUMENTATION PAGE				Form Approved OMB No. 0704-0188	
<small>maintaining the data needed, and completing and reviewing the collection of information. Send comments regarding this burden estimate or any other aspect of this collection of information, including suggestions for reducing the burden, to Department of Defense, Washington Headquarters Services, Directorate for Information Operations and Reports (0704-0188), 1215 Jefferson Davis Highway, Suite 1204, Arlington, VA 22202-4302. Respondents should be aware that notwithstanding any other provision of law, no person shall be subject to any penalty for failing to comply with a collection of information if it does not display a currently valid OMB control number. PLEASE DO NOT RETURN YOUR FORM TO THE ABOVE ADDRESS.</small>					
1. REPORT DATE (DD-MM-YYYY) 24-04-2003		2. REPORT TYPE Final Report		3. DATES COVERED (From - To) 01-Apr-02 - 12-Aug-03	
4. TITLE AND SUBTITLE Study Of Plasma Parameter Distributions In Low Power Hall Effect And Ablative Pulsed Plasma Thrusters				5a. CONTRACT NUMBER ISTC Registration No: 2317	
				5b. GRANT NUMBER	
				5c. PROGRAM ELEMENT NUMBER	
				5d. PROJECT NUMBER	
6. AUTHOR(S) Dr. Alexandre Vesselovzorov				5d. TASK NUMBER	
				5e. WORK UNIT NUMBER	
7. PERFORMING ORGANIZATION NAME(S) AND ADDRESS(ES) Kurchatov Institute Kurchatov Sq. 1 Moscow 123182 Russia				8. PERFORMING ORGANIZATION REPORT NUMBER N/A	
9. SPONSORING/MONITORING AGENCY NAME(S) AND ADDRESS(ES) EOARD PSC 802 BOX 14 FPO 09499-0014				10. SPONSOR/MONITOR'S ACRONYM(S)	
				11. SPONSOR/MONITOR'S REPORT NUMBER(S) ISTC 01-7012	
12. DISTRIBUTION/AVAILABILITY STATEMENT Approved for public release; distribution is unlimited. /					
13. SUPPLEMENTARY NOTES <div style="float: right; font-size: 2em; font-weight: bold; margin-top: 10px;">20040625 081</div>					
14. ABSTRACT This report results from a contract tasking Kurchatov Institute for the results of studying a stationary plasma-low power-thruster (SPT) and an ablative pulsed plasma one (APPT). In the first part of the Report the results of studying the module characteristic for a small SPT and for the thruster plume. In particular there are represented the description of test facility and system of thruster performance and plume parameter measurements as well as the results of these measurements. In the second part of the Report, the results of studying some features of the physical processes in APPT, as well as an analysis of the produced results based on the numerical simulation for increasing their efficiency, are represented. A two-dimensional model of APPT has been developed. Interferometric investigations inside APPT discharge channel, piezoprobe measurements of dynamic pressure distributions and ultra high-speed photography with visualization of plasma flows have been carried out.					
15. SUBJECT TERMS EOARD, Propulsion, Engines and Fuels, Electric & Ion Propulsion					
16. SECURITY CLASSIFICATION OF:			17. LIMITATION OF ABSTRACT UL	18. NUMBER OF PAGES 264	19a. NAME OF RESPONSIBLE PERSON Ingrid J. Wysong
a. REPORT UNCLAS	b. ABSTRACT UNCLAS	c. THIS PAGE UNCLAS			19b. TELEPHONE NUMBER (Include area code) +44 (0)20 7514 4285



Russian Research Centre 'Kurchatov Institute'
Institute of Nuclear Fusion

« CONFIRM »

Director, RRC 'Kurchatov Institute'

Polyakov I.N.

FINAL TECHNICAL REPORT

On ISTC-Project No. 2317p

Duration: from April, 1, 2002 to March, 31, 2003 (12 Months).

***Study of plasma parameter distributions in low power
Hall Effect and Ablative Pulsed Plasma Thrusters.***

Project Manager

Vesselovzorov A.N.

Moscow 2003

ISTC-Project No. 2317p

Project Title:

**Study of plasma parameter distributions in low power Hall Effect
and Ablative Pulsed Plasma Thrusters**

Duration:

from April,1, 2002 to March , 31, 2003 (12 Months).

Project Manager

Name: **Vesselovzorov Alexandre Nikolaevich**
Title: Senior scientist, INF RRC "Kurchatov Institute"
Contact information:

Address: 1, Kurchatov Square, Moscow, 123182, Russia		
Tel: +7(095) 1967040	Fax: +7(095) 9430073	E-mail: vesel@nfi.kiae.ru

Participating Institutions

Leading Institution

Name: **Institute of Nuclear Fusion, Russian Research Centre "Kurchatov Institute"**

Address: 1, Kurchatov Square, Moscow, 123182, Russia		
Tel: +7(095) 1967136	Fax: +7(095) 7425868	E-mail: vesel@nfi.kiae.ru

PartnersName: **European Office of Aerospace Research and Development**

Contact information:

Address: 223/231 Old Marylebone Road, London, NW1 5 TH , UK		
Name of Contact Person: Dr. Ingrid Wysong		
Tel: +44 (0) 207 514 4285	Fax: +44 (0) 207 514 4960	E-mail: ingrid.wysong@london.af.mil

Abstract

A given report is based on the results of studying a stationary plasma-low power-thruster (SPT) and an ablative pulsed plasma one (APPT) made in accordance with the calendary plan of the studies on the ISTC-Project No.2317p for the period from April,1, 2002, to March, 31, 2003.

In the first part of the Report the results of studying the module characteristic for a small SPT and for a thruster plume. In particular there are represented the description of test facility and system of thruster performance and plume parameter measurements as well as the results of these measurements. Performance characterization was made for SPT-25 laboratory model having exit parts of the discharge chamber walls made of the Russian - borosil type - ceramics and French one, AINBN-type, and of the USA - ceramics, AX05-type.

Plume measurements were made for the optimized operation modes with discharge power $N \sim 100W$ and $N \sim 200W$. These measurements include determination of the accelerated ion distribution in off-axis angle allowing estimation of the accelerated ion flow divergence, measurements of the accelerated ions distributions in energy, plasma potential, electron temperature and plasma density number distributions in off-axis angle. In the process of the experiments, the study of the ion charge structure in the SPT-25-jet was also realized. The presence of one-, two-, three-, charged Xe- ions, as well as that of neutral atoms, was detected.

But as a whole the complex of the obtained data could be definitely used for checking of some theoretical interpretations of the discharge chamber material influence on thruster operation and its characteristics.

In the second part of the Report, the results of studying some features of the physical processes in APPT, as well as an analysis of the produced results based on the numerical simulation for increasing their efficiency, are represented. Two-dimensional model of APPT have been developed. Modeling shows that the model adequately describes formation and acceleration of a plasma flow in coaxial accelerating channel. The model gives a correct qualitative picture of separate stages of discharge in APPT. The features of propellant flow rate determine monotonous character of distribution of density, axial velocity of plasma, and magnetic field in the accelerating channel. The developed numerical model of APPT is a tool to improve thruster parameters.

Energy flux onto propellant, Teflon mass loss, current and voltage, near propellant bar electron density have been measured in APPT stand. The energy fraction released from the discharge region upon the propellant surface in the APPT is near 10^{-2} of the energy stored in the power supply source. Main part of measured flux is transferred by particles.

Interferometric investigations inside APPT discharge channel, piezoprobe measurements of dynamic pressure distributions and ultra high-speed photography with visualization of plasma flows have been carried out. Studies of spatial and temporal distributions of the electron density in the discharge channel make possible to reveal main distinctions of physical processes in the high efficiency APPT's defining the improved thruster characteristics.

Two APPT models having the level of bank energies 20 J and 40 J, are developed and tested. The improved APPT characteristics are obtained with completion of an optimization between parameters of an electric circuit and the sizes of an accelerating channel of the thruster, when the discharge is close to aperiodic.

Keywords: stationary plasma thruster, ablative pulsed plasma thruster, low power, theory, experiment, plasma parameters, plume, discharge chamber, material.

Authors of report:

1. Vesselovzorov A.N. - Project Manager
2. Alexeev Yu.A. - PHD
3. Antropov N.N. - Candidate of Technical Sciences
4. Grdlichko D.P. - senior engineer
5. Diakonov G.A. - Candidate of Technical Sciences
6. Kazeev M.N. - PHD
7. Kim V. - Professor
8. Kozlov V.I. - Candidate of Technical Sciences
9. Kozlov V.F. - Research scientist
10. Lazourenko A.V. - Candidate of Technical Sciences
11. Orlov M.M. - PHD
12. Pogorelov A.A. - Research scientist
13. Popov G.A. - Professor
14. Svirsky E.B. - Research scientist
15. Skrylnikov A.I. - Candidate of Technical Sciences
16. Smirnov V.A. - PHD
17. Tolstov Yu.C. - Research scientist
18. Umnitsyn L.N. - senior engineer
19. Yakovlev V.N. - senior engineer

Contents

	Page
I. Introduction	8
II. Study of stationary plasma-low power-thruster	8
II.1. Introduction	8
II.2. Methodology of the SPT-25 performance and plume characterization	9
II.3. Results of the SPT-25 performance characterization	10
II.3.1. SPT-25 characteristics with the output rings made of the borosil and AlNBN-ceramics	10
II.3.2. SPT-25 characteristics with the output rings made of the borosil and AX05-ceramics	12
II.3.3. Discussion over the produced results in the studies of an effect of various ceramics on the SPT-characteristics	13
II.4. Results of the SPT-25 plume plasma parameter measurements	14
II.4.1. Electron temperature, density and plasma potential distributions in SPT-25 jet	14
II.4.2. Plasma charge structure in the SPT-25 jet.	15
II.5. Conclusion	16
II.6. References for Section II	18
II.7. Appendix 1. Figures for Section II	19
III. Task 2. Ablative Pulsed Plasma Thruster Study	185
III.1. Introduction	185
III.2. Semi-Phenomenological Numerical Model of Plasma Acceleration in the APPT Thruster.	186
III.2.1. Problem statement	186
III.2.2. Two-dimensional non-steady model	187
III.2.3. Equations	187
III.2.4. Dimensionless equations	188
III.2.5. Boundary and initial conditions	188
III.2.5.1. Inlet plasma density	188
III.2.6. Results of Simulation	191
III.3. Heat Flux Transfer to the Propellant and Ablation Losses.	195
III.3.1. Experimental Stand for the Propellant Study	195
III.3.1.1. Diagnostics	196
III.3.2. Results of Experiments	197
III.3.2.1. Measurements of Energy Dissipated in a Thermal Skin-Layer.	201
III.3.2.2. Measurements of Radiative Part in the Energy Flux.	201

III.3.3.	Discussion of Results	202
III.4.	Study of plasma parameters and discharge optimization	207
III.4.1.	Study of the charged plasma component concentration in discharge channel	207
III.4.2.	Measurement procedure	207
III.4.3.	Test results and their discussion	214
III.4.4.	Piezoprobe Measurements of Impact Pressure in APPT Plasma Flow	219
III.4.5.	Ultra high speed photography with visualization of plasma flow	235
III.5.	Development and tests of the APPT model	250
III.6.	Conclusion	253
III.7.	Annex 2. Propellant Flow Rate Modeling	255
III.7.1.	Introduction	255
III.7.2.	Kinetics of Teflon Thermal Degradation	255
III.7.3.	Equation of Energy Transfer in the Propellant	257
III.7.4.	High Temperature Branches of Degradation	259
III.8.	References for Section III	261
IV.	List of presentations at conferences and meetings with abstracts	263

I. Introduction

Some results of studying two promising diagrams of electrorocket thrusters: stationary plasma – low power – thruster (SPT) (Task 1) and an ablative pulsed plasma one (APPT) (Task 2) are given in this Report. The studies were done in accordance with the technical calendary plan of the studies on the ISTC-Project No. 2317p for the period from April, 1, 2002 to March, 31, 2003.

II. Task 1. Study of stationary plasma-low power-thruster

II.1. Introduction

As it is known /1/ the secondary electron emission plays significant role in the physical processes inside the SPT accelerating channel. But there was not made systematical studies of this factor impact on SPT operation and performance in the former times. Only last years an increase of interest to SPT in the west countries stimulated some studies but they were mainly theoretical ones /2-4/. It is necessary to add that nowadays there are some plans to develop the so-called small SPT's for small spacecrafts. Because the less thruster size the more difficult to ensure high its thrust efficiency it seems more important to study impact of discharge chamber material for small SPT. Therefore it was decided to study within the work program of the ISTC project #2317p integral and plume characteristics of the SPT-25 laboratory model with the discharge chamber made of ceramics with different secondary electron emission.

Particularly it was necessary to determine:

- thruster performance, density and energy distributions of the accelerated ions at surface under control with the radius $R=(0,5-0,7)m$ with center at the point of crossing the thruster axis with output plane of the thruster and these measurements were to be made under powers $\sim 100W$ and $\sim 200W$ for small SPT with 2-3 discharge chamber materials;
- distributions of plasma density, plasma potential, electron temperature in the small SPT plume at the distances $(0,5-0,7)m$ and these measurements were to be made for small SPT with basic ceramics under power $\sim 100W$;
- charge structure of plasma flux flowing out from the thruster in various directions, neutral fraction included.

According to the work program one of the main tasks of studies within the ISTC #2317 project was determination of the SPT-25 characteristics for 2-3 discharge chamber materials having different secondary electron emission yield. This task was solved during fulfillment of works and in the 1st report /6/ issued on the mentioned project there were represented results of the SPT-25 characterization in the cases of its discharge chamber made of AlN-BN ceramics made in French and BN-SiO₂ called borosil or BGP ceramics produced in Russia.

In the mean time at CERN there were received data on these materials secondary electron emission yield (SEY).

In the second half-a-year (second stage of the studies) the data on the SPT-25 activity characteristics with the discharge chamber walls made of borosil and of the ceramics, AX05-type, based on the BN produced in the USA were obtained. Unfortunately during this phase of tests there was broken the heaterless cathode used in the 1st series of tests. Therefore there was realized the comparative study of characteristics with both materials and new cathode. Nowadays there are also available preliminary CERN data on the AX05 SEY. So, as a result of joint efforts connected with the mentioned project fulfillment there was obtained the 1st data pack for analysis of three discharge chamber wall material and their SEY influence on the SPT operation and characteristics. Thus, the task mentioned above was solved.

II.2. Methodology of the SPT-25 performance and plume characterization

Since early studies of the Stationary Plasma Thrusters (SPT) there was supposed that one of the key factors determining the discharge chamber material (ceramics) impact on thruster operation is the secondary electron emission of ceramics /1/. But as it was mentioned there was no direct experimental confirmation of this point as well as there was no systematic study of the mentioned impact. Nowadays due to the wide involvement of western scientists into SPT studies there is appeared great interest to the possible influence of ceramics properties on plasma dynamics inside the SPT accelerating channel and thruster performance. In this connection as one of the main tasks of study within the frames of given project there was specified in a work program the study of integral characteristics of thrusters having discharge chamber walls made of materials with definitely different secondary electron emission. These materials are as follows:

1. Russian borosil type ceramics consisting of the SiO_2 and BN as the main components.
2. AlNBN (ABN) type ceramics consisting of BN and AlN as the main components.
3. The ceramics, AX05-type, based on BN, is the USA-produced one.

The studies were done at two stages. At the first stage, SPT-characteristics, using the ceramics, borosil-type and AlN-BN-one, were compared. At the second stage, the comparisons were done for the ceramics borosil-type and for that of AX05-type. According to data obtained at CERN both these materials have significantly higher cross over energy ε' (corresponding to the secondary electron emission yield (SEY) $\sigma \approx 1$) than that one for the AlN-BN ceramics (Table 1).

Table 1. Cross over energy ε' values for different materials.

AlN-BN	20-40 eV
BN-SiO ₂	~ 80 eV
BN	~ 110 eV

For study there was used the SPT-25 type thruster model (Fig.1.1.) /5/ having magnetic system with one magnetization coil. Advantage of such model is small variation of the magnetic field topology under variation of magnetic field induction to optimize operation mode. This should simplify analysis of obtained data presented in a report. Discharge chamber wall exit parts (Fig.1.2.) were made as circular rings kept to magnetic system elements. So, it was possible to manufacture these rings of different materials. As it was mentioned above in the basic option there was used borosil type ceramics delivered by Russian manufacturer. The ABN samples were delivered by western supplier according to AFRL order and the second discharge chamber wall option was manufactured using this material. Thruster geometry and sizes of parts were identical within the manufacturing accuracy.

SPT-25 model was tested at test facility with vacuum chamber of 2m in diameter and 6m in length (Fig.1.3.). This chamber was equipped by thrustmeter having accuracy of measurements $\pm 3\%$ within the range of the thrust values 5-10 mN. Test facility has also system supplying gas (Xe) into the accelerating channel through anode and into cathode as well as power supply sources for all thruster circuits and measuring system (Fig.1.4.). The mass flow rate through anode was controlled and measured with accuracy $\pm 2\%$ within the range of (0,5-1)mg/s and cathode mass flow rate - with accuracy of $\pm 5\%$ under its value 0,1mg/s.

Test facility was equipped also by the system of the accelerated ion flow parameters measurement allowing determination of the accelerated ion current distribution along the semicircle with the center positioned at the thruster exit plane and with circle plane consisting of thruster axis. To realize these measurements there was used the RPA probe mounted on the boom rotating along

the mentioned plane within $\pm 90^\circ$ relative to the thruster axis (see Fig.1.3.). This system allows estimation of the thruster plume divergence and angular distribution of accelerated ions in energy.

Besides the mentioned main task there was specified also the necessity to characterize plasma parameter distributions in a small SPT plume under its operation with discharge power $N_d \approx 100W$ and basic type of ceramics (borosil). Such characterization was also made and obtained results are represented below.

To characterize the thruster model performance there were measured discharge current and thrust under different currents in magnetization coil for several fixed mass flow rates through anode and several fixed discharge voltage values. The range of mass flow rates through anode was varied within (0,5-1,0)mg/s. The range of discharge voltages was (125-250)V and their values were varied with step $\Delta U \approx 25V$. Thus, it was possible to determine possible discharge chamber material impact on the voltage-current characteristics, dependence of discharge current on magnetic field intensity as well as to determine thrust and thrust efficiency under different discharge conditions.

For operation modes with high enough thrust efficiency and powers $N_d=100W$ and $N_d=200W$ there was measured angular distributions of the accelerated ion current density and distributions of ions in energy for several of-axis directions.

The angular accelerated ion current distributions were determined under retarding potential $U_r=50V$ relative to cathode potential. Because plasma potential in a plume is (20-30)V usage of such retarding potential allows measurement of current created by ions with energies higher than (20-30)eV. It is necessary to note that nowadays there is no verified methodology for the accurate measurement of total ion current exhausting thruster. Usage of the mentioned retarding potential allows characterization of the angular distribution of ions in a plume able to have notable mechanical, thermal and erosion impacts on surfaces crossed by plume.

To measure the plasma parameter distributions in a plume in addition to RPA there was used cylindrical Langmuir probe with axis oriented to thruster exit. Due to existence of the accelerated ions in a plasma it is difficult to have satisfactory interpretation of probe characteristics. Experience coupled by authors of this report shows that probe characteristics close to classical one could be obtained only with cylindrical probe oriented as it was mentioned above. To verify this conclusion there were made special measurements with usage of cylindrical probe and emissive probe. These measurements gave satisfactory agreement of the plasma potential values measured by emissive probe and derived from probe characteristics obtained by cylindrical probe.

To estimate the ion back flows there were used system of flat probes positioned in a thruster exit plane (see Fig.1.3.).

Plasma parameters in a SPT-25 plume were determined for three distances of probes from the thruster exit, namely: along the semicircles with radiuses $R=0,3m$, $R=0,4m$ and $R=0,5m$. Sensitivity of measuring system did not allow obtaining of reliable data at larger distances.

II.3. Results of the SPT-25 performance characterization

II.3.1. SPT-25 characteristics with the output rings made of the borosil and AlNBN-ceramics.

Results of the SPT-25 option #1 (with borosil ceramics exit rings) performance characterization (Fig.1.5...1.28.) show that:

1. Model has typical for SPT voltage-current characteristics under great enough magnetic induction and there is saturation of thruster performance under high enough magnetization currents. It is possible to conclude also that under magnetization currents $I_m \geq (2,5-3)A$ there is no further increase of the thrust efficiency with increase of the magnetization current. So, the mentioned values could be considered as optimal ones. It is necessary to add that the mentioned characteristics were determined while magnetization current was reduced from

high values till low ones to reduce impact of the thruster model overheating taking place under low magnetization currents while discharge current is great.

There is confirmed the possibility to obtain acceptable total thrust efficiency of the SPT-25 model with discharge chamber walls made of borosil under its operation with discharge power $N_d \approx 100W$ and good enough performance level under discharge power $N_d \approx 200W$. It is necessary to note that the thrust efficiency η_{ta} values represented in Figures were calculated taking into account power losses for magnetization but not accounting for cathode mass flow rate. The performance data for the above mentioned operation modes parameters are represented below:

	Mode 1	Mode 2
Mass flow rate through anode, mg/s	0.6	0.7
Mass flow rate through cathode, mg/s	0.1	0.1
Discharge voltage, V	151	224
Discharge current, A	0.64	0.86
Discharge power, W	96.7	192.9
Thrust, mN	6.0	10.2
Magnetization current, A	2.82	2.93
Voltage at magnetization coil, V	2.49	2.65
Power losses for magnetization, W	7.02	7.76
Total power consumption, W	103.72	200.66
Specific impulse (taking into account the cathode mass flow rate)	885	1299
Total thrust efficiency, % (taking into account the cathode mass flow rate and power losses for magnetization)	0.253	0.324
Plume half angle for 95% of the accelerated ions determined by RPA probe measurements at $R=0,5m$	78.8	66.1

Integral characteristics of SPT-25 model option #3 with discharge chamber walls made of AlNBN are similar to that ones obtained for borosil case (Fig.1.29...1.49.) but under similar conditions discharge current is typically higher (see Fig.1.29., 1.36., 1.43.) and thrust is typically lower. That is why thrust efficiency in the case of AlNBN ceramics is lower (see Fig.1.35., 1.42., 1.49.). Moreover the range of the stable operation modes is more narrow, probably, due to reduction of the thrust efficiency.

Comparing the voltage-current characteristics of thruster under the same mass flow rate one can conclude that under low magnitudes of the magnetization current the discharge current in the AlNBN case is notably higher and only under high magnetization currents the discharge currents are comparable for both cases. So, there was found definite difference of integral characteristics for different materials. It is necessary to add that under discharge voltages $U_d \sim 200V$ or higher there is appeared breakdowns between anode and internal magnetic pole of the magnetic system creating hole in a internal discharge chamber exit ring and with this hole thruster model could not operate satisfactory. After the 1st such breakdown thruster model was repaired but after the 2nd breakdown it was decided that this concrete AlNBN ceramics is not acceptable for the SPT discharge chamber manufacturing. Therefore the plume measurements for this thruster model option was not made.

II.3.2. SPT-25 characteristics with the output rings made of the borosil and AX05-ceramics.

The main task of the given stage of works was the characterization of the SPT-25 under its operation with BN based ceramics of the AX05 type. Unfortunately during new stage of tests there was broken the heaterless cathode (cathode #1) used in the 1st series of tests and there was no

possibility to repair it quickly enough. Therefore it was decided to realize new series of tests with the cathode (cathode #2) for the SPT-100 type thruster. Surely this cathode is oversized for the SPT-25 and it is difficult to operate it under mass flow rates through the cathode $\dot{m}_c \approx 0,1$ mg/s. Therefore there was used an additional heating of this cathode by power ~ 25 W. Due to the mentioned changes the thruster characteristics were changed. That is why to compare these characteristics for new pair of materials there was made their determination with both materials under operation with new cathode.

As it was mentioned above replacing of cathode had changed the thruster characteristics significantly, namely: with new cathode the discharge current and thrust are lower than that ones with the heaterless cathode (Fig. 1.50.-1.57.) and finally the thrust efficiency is also lower (Fig.1.58.-1.61.). This is an indication that the SPT-25 with new cathode even with additional heating can not operate effectively enough. Nevertheless thruster characteristics are repeatable what was checked with borosil ceramics. Therefore it was decided to realize new phase of the comparative study of material impact on thruster characteristics with new cathode (cathode #2).

The tests were made in the same vacuum chamber of 2m in diameter and 6 m in length, with the same instruments and devices for the measurement of electric parameters, thrust, mass flow rates and plume parameters as it was described in /6/. Additionally there were measured the discharge voltage and current oscillations intensity by registering of their (5-10) occasional traces by digital oscilloscope, realizing their Fourier-analysis within the range of frequencies 0-250 kHz and calculating the mean RMS amplitudes of the discharge voltage and current oscillations for 50 harmonics. There was made also determination of the dominating oscillation frequency. Obtained oscillation characteristics for the borosil case confirm that operation modes with different cathodes are different (Fig.1.62.-1.73.). This is an indication of fact that the discharge chamber material is only one among many of factors determining the SPT operation and characteristics.

There were made also the calculation of the magnetic field topology (Fig. 1.74.) using standard codes and measurement of the magnetic field radial component along the accelerating channel mid surface (Fig.1.75.). Obtained results show that:

- magnetic field is mainly radial inside the SPT-25 accelerating channel (see Fig.1.74.);
- there is an indication of some magnetics saturation under magnetization currents exceeding ~ 3 A (Fig.1.75.) what is to be taken into account under analysis of the obtained data.

Results of the comparative SPT-25 characteristics determination with two different ceramics (Fig. 1.76...1.154.) show the following:

- as in the case of AlN-BN/BGP pair there are some differences in voltage-current characteristics under low magnetic fields in the case of borosil/AX05 pair and with increase of magnetic field these differences become negligible (Fig.1.76.,1.82., 1.88.);
- in the case of AX05 the discharge current under low magnetic fields is typically a little bit higher (see Fig.1.76., 1.82., 1.88.) and thrust is a little bit lower than in borosil case, therefore the thrust efficiency under low magnetic fields is a little bit lower in the AX05 case (see Fig. 1.81., 1.87., 1.92.);
- dependences of integral parameters on magnetization current are qualitatively the same as for the AlN-BN/borosil pair (see Fig.1.93...1.108.);
- the oscillation characteristics (see Fig.1.109...1.142.) are significantly different for significant part of the operation modes (see Fig. 1.113...1.115., 1.124...1.126.) and have no direct link with the discharge current behaviour (see Fig.1.86. and Fig.1.115., 1.116);
- dependences of the oscillation intensity on the magnetization current are more or less similar for BGP and AX05 cases (see Fig.1.127...1.134.), but character of the dominating oscillation mode frequency dependences on this current are different at least under low voltages(see Fig.1.135...1.142.);

– the plume divergence general behaviour is similar for both materials (see Fig.1.143...1.154.).

II.3.3. Discussion over the produced results in the studies of an effect of various ceramics on the SPT-characteristics.

Considering obtained results it is possible to note that it is difficult to explain all of them using one or another model due to complexity of processes in the SPT discharge. Therefore these results could be considered as data base for the further analysis. Taking this into account there is represented in a report the maximum of primary results because only complex analysis of these results can give satisfactory their theoretical interpretation. An another point is that even represented data in spite of their great volume are not full enough. In particular there are no data on the local plasma parameter distributions inside the accelerating channel. These data, especially information on the electron energy distribution along the accelerating channel, would be exclusively beneficial for the analysis of the discharge chamber material and its secondary electron emission influence on thruster operation and performance. So, it seems prospective to continue study in order to get the mentioned data. In the mean time it seems possible to make some conclusions, namely:

1. The discharge chamber material has definite impact on the thruster operation and performance (this fact is well known) and this impact, probably, is connected with the redistribution of all local parameters (to be checked by the direct measurements) causing notable change of thrust and thrust efficiency even under great enough magnetic fields while voltage-current characteristics and dependences of discharge current on the magnetization current are very close for different materials.

The mentioned changes could be connected with difference of the secondary electron emission yield but as it was mentioned above such conclusion is to be checked by additional measurements. The main concern is that even under great enough magnetic fields ($I_m \geq 2.5$ A for SPT-25 with borosil and AlN-BN cases) there is no notable difference of the discharge current expected for material with higher SEY (AlN-BN) due to increase of the near wall conductivity but thrust value in this case is evidently less. The first fact indicate that, probably, the ion and electron currents at the thruster exit under comparable operation modes are close for both cases (to be checked by measurements), but the acceleration efficiency is different due to difference of the all local parameter distributions resulting in different wall losses, mean ions energy etc(to be checked by measurements).

It is necessary to add that for material with great secondary emission ($\sigma > 1$) under operational conditions there is another possibility to get higher discharge current than that one connected with increase of the near wall conductivity, namely: there is the possibility to obtain an additional current through bulk of insulator as through conducting material. This possibility is confirmed by two breakdowns registered during the SPT-25 operation with the AlN-BN insulator. These breakdowns appeared during operation under high voltages (~200V) and high discharge currents (low magnetic fields) and were providing the axially directed channel with almost circular cross-section and diameter of ~0,5 mm, going in the internal replacable ring bulk from the anode side to the cathode side.

Increase of the discharge current due to evaporation of the ceramics material could be significant enough because this evaporation significantly increase gas medium density inside the accelerating channel during short time. But in the prebreakdown phase it is to be also notable to start significant heating of the future breakdown channel. So, probably, an increase of the discharge current under low magnetic fields for AlN-BN case noted in /6/ was caused by this parasite prebreakdown current through insulator bulk. This current has occasional character and was able to disturb somewhere the voltage-current characteristics for the considered case. This idea appears, if one takes into account that for many different comparable operation modes the discharge currents are very close.

2. If the discharge current values for comparable operation modes and materials with different SEY could be considered as close one, this does not mean that the secondary emission and near wall conductivity does not play any role. Indeed, there were studied within this project the operation modes with relatively low discharge voltages and consequently with not too high electron energies. For these conditions the mean electron temperatures could be within the range of 10-20 eV and plasma densities near the walls $\sim (2 - 5) \cdot 10^{11} \text{ 1/cm}^3$. The corresponding Debye length could be within the range of 0.015-0.05 mm that is comparable with the scale of the surface roughness after mechanical treatment. The nonsmoothness of the equipotential surfaces within the Debye layer can cause an additional electron drift momentum dissipation [7]. This means that significant part of electrons interacting with the Debye layer can change their drift momentum and give their input into the near wall current in spite of the fact that only small part of electrons was able to impinge the wall surface. So, probably, the part of electrons interacting with wall with appearance of the secondary emission was small in the studied conditions in comparison with that one changing their drift momentum and giving impact into the near wall current.
3. Relatively low discharge voltages and electron temperatures can explain not so significant difference in the characteristics obtained for the second studied pair of materials (borosil/AX05). Indeed, due to low electron energies there was not so much electrons able to reach the level of energies close to cross over energy for the secondary electron emission. Probably, due to this there was not appeared significant changes of thruster characteristics in spite of notable difference in SEY. But considering the oscillation characteristics one can tell that there was observed definite changes of thruster operation.

To clarify the discussed points as it was mentioned above it is necessary to fulfil more measurements. The most useful are to be the local plasma parameter measurements inside the discharge chambers with walls made of different materials.

II.4. Results of the SPT-25 plume plasma parameter measurements

II.4.1. Electron temperature, density and plasma potential distributions in SPT-25 jet.

As it was mentioned above these measurements were made with usage of RPA and cylindrical probes. Data obtained by RPA probe at $R=0,5\text{m}$ (Fig.1.155.) gave the plume half angle values represented above. Measurements made by RPA and measurements of plasma parameters by cylindrical probe (Fig.1.156...1.163.) at different distances gave results allowing to conclude that:

- mean energy of ions is reduced significantly under off-axis angles higher than 45° (see Fig. 1.156., 1.160.) and it is interesting that difference between discharge voltage and mean ion energy maximum is almost the same under $U_d=150\text{V}$ and $U_d=225\text{V}$;
- plasma potential distributions (Fig.1.157., 1.161.) has maximum in vicinity of thruster axis and level of potential (20-22V) in this zone is close to that one obtained for other thrusters;
- there was obtained great enough difference of the plasma potential values determined at different distances and under large off-axis angles (see Fig.1.161.) but this result should be checked in a future;
- maximum of electron temperature is at level of $\sim 1\text{eV}$ (see Fig.1.158., 1.162.) and also slightly increased in direction to the thruster axis;
- near axis plasma potential and electron temperature values are not changed significantly with increase of distance from the thruster exit;
- there is still great difference (by 3-5 times) in plasma density numbers derived from the probe electron current value at plasma potential and from probe ion current (Fig.1.159., 1.163.) what could be explained by significant impact of the accelerated ions on probe ion current because even

cylindrical probe collects significant number of these ions (because thruster is extended source of the accelerated ions moving along different directions) and for estimation of the real plasma density number it seems better to use values derived from the magnitude of the electron current at plasma potential);

- increase of discharge voltage and power causes increase of the ion current density in a near axis zone of plume (see Fig. 1.155.) and plasma density number in this zone (see Fig.1.159. and Fig.1.163.) while distributions of other parameters seem similar at least on character and level of magnitudes.

II.4.2. Plasma charge structure in the SPT-25 jet.

A MX-7304 mass-spectrometer was used for measuring the plasma charge structure in the SPT-25 jet in a given study.

The equipment disposition in the measurements is shown in Fig.1.164. The SPT-25 was placed upon a rotating platform inside the vacuum chamber which was evacuated by a high vacuum pump, H-200, and the mass-spectrometer, MX-7304, was fixed immobile upon a vacuum chamber flange. The SS-shield protected the details of a vacuum lock against the SPT-25 ion beam effect. The shield with a mesh was necessary for cutting electrons off and for limiting the ion beam (1,5mm in diameter). A potential sufficient for repulsion of all the jet electrons was applied to the screen grid. The lens with a mesh and the ionizer form the focusing system which allows one to adjust - in a short range - the ion beam direction and, thus, to use a maximally-possible amount of the beam ions for an analysis with the mass-spectrometer. Moreover, a lens with a grid could perform the role of an electrostatic ion energy analyzer and, when necessary, could completely cut the ions off, allowing to pass the neutral beam component only. The ionizer was used for an analysis of the neutral beam component and for the ionization of a calibrating gas under the mass-spectrometer calibration respective to the mass (mass filter transmission coefficient determination). MX-7304 is a mass-spectrometer of a dynamic type [8], its principle of action is based on the fact that the ions of a definite mass (ions of a substance under analysis), passing through a hyperbolic high frequency electric field, have a limited amplitude of oscillations, meanwhile the amplitudes of other ion oscillations rise in time without any limits. These ions enter the surfaces of electrodes, being neutralized there. The ions with the limited oscillation amplitude are collected with the collection and their intensity is registered - via an amplifier - with a tape recorder.

In the process of the experiments, the study of the ion structure in the SPT-25 jet was done under operation of the thruster in the power range, $N=(100-200)W$ at the Xe-consumption, $m=(0.6-0.7)$ mg/s, under pressure of $p_c=(3-4) \cdot 10^{-5}$ mm Hg in the vacuum chamber.

Some fragments of a typical - plasma-jet - mass-spectrogram for SPT-20 are shown in Fig.1.165. A considerable width of the element isotope lines is provided by a great spread in the ion energies. In the treatment of mass spectrograms the ion current value with this or that charge was determined as an integral over all the isotopes, i.e. as an area, S , under the intensity distribution curve, $j(M)$, with the corresponding coefficients, k_1 and k_2 .

$$I = k_1 k_2 \int_{M_{\min}}^{M_{\max}} j(M) dM = k_1 k_2 S$$

Here, the coefficient k_1 takes account of a change in the display scale with respect to masses (for Xe^+ $k_1 = 1$, for Xe^{++} $k_1 = 2$); k_2 is the transmission coefficient for the mass-spectrometer probe with respect to masses. The coefficient k_2 depends on the mass-spectrometer adjustment conditions, and the precise determination of this coefficient requires the mass-spectrometer calibration with respect to masses.

However, in our experiments, under mass-spectrometer operation conditions with a low resolving power, this coefficient could be accepted to be equal $k_2 \approx 1$ for Xe^+ and Xe^{++} /8/.

Here are some data on the plasma charge structure in the near-axial jet section, at the distance of 700mm from an SPT-25 operating under conditions, when $N = 200W$ (discharge voltage, $U=225V$), as an example. The presence of one-, two-, three-charged xenon ions was detected, as well as neutral atoms, in the following proportions: $Xe^+ - 63\%$; $Xe^{++} - 13\%$; $Xe^{+++} - 3\%$ and $Xe^0 - 21\%$.

The nature of some changes in the plasma charge structure, dependent on the SPT-25 jet angle, is shown in Fig.1.166.

The given dependencies have mainly a qualitative nature, since the mass-spectrometric useful signal, with a departure from the near-axial jet section, becomes to be comparable with a noise level, accompanying the SPT-25 operation.

II.5. Conclusion

On base of the represented in a report data it is possible to conclude that the discharge chamber material has definite impact on the SPT performance. This impact could be reduced to the following:

1. Discharge chamber material determines the possible range of the operation modes. In particular it was obtained that concrete samples of the US made AlNBN ceramics have significantly lower breakdown resistivity than borosil type ceramics.
2. Discharge chamber material has definite impact on thruster characteristics and performance. In particular:
 - thruster model with tested AlNBN type ceramics generally ensures larger discharge current and lower thrust under comparable conditions and this difference is more significant under operation modes with low magnetic induction inside the accelerating channel;
 - there was confirmed the acceptable performance level of the SPT-25 model with the borosil type ceramics (total thrust efficiency $\sim 0,25$ under specific impulse $I_{sp} \sim 885s$, total power consumption $N \sim 104W$ and total thrust efficiency $\sim 0,32$ under specific impulse $I_{sp} \sim 1300s$, total power consumption $N \sim 201W$).

The results of measuring the SPT-25 plasma jet parameters have shown that:

1. The SPT-25 plume divergence is higher than for optimized SPT's of increased sizes what is explained by usage of one magnetization coil in the magnetic system.
2. Plasma parameter distributions in a SPT-25 plume are qualitatively similar to the corresponding distributions for larger optimized SPT's (plasma potential values are at level of $\sim 20V$, electron temperature $\sim 1eV$). Mean energy of the accelerated ions near the axis are also close to that ones for the larger SPT's.
3. In the SPT-25-jet, as well as in the SPT of a greater size, the presence of single-, double-, triple-charged xenon ions, as well as that of neutral atoms, has been detected.

As a result of works according to the work program there was obtained the data pack allowing together with results of the secondary electron emission determination to realize some analysis of this emission impact on the SPT operation and characteristics. It is shown also the necessity of the further studies and one of the prospective ways to clarify the appeared questions is to realize the local plasma parameter measurements inside discharge chambers with wall made of materials with different SEY. Thus, results of the fulfilled works give new data on the discharge chamber material impact on the SPT operation and performance.

II.6. References for Section II.

1. A.I.Morozov and V.V.Savelyev. Fundamentals of stationary plasma thruster theory-Review of Plasma Physics, 25-Kluwer academic/plenum publisher, 233 Spring Street, New York 10013-1578.
2. J.M.Fife, M.Martinez-Sanches, J.Scabo. A numerical study of Low-Frequency Discharge Oscillations in Hall Thrusters-paper AIAA-97-3052 at 33rd JPC, July 6-9, 1997, Seattle, WA.
3. S.Locke and U.Shumlak. A Numerical Study of the Effect of Channel Insulator Discontinuity on Hall Thruster Discharge –paper IEPC-01-23 at 27th IEPC, October 15-19, 2001, Pasadena, California.
4. E.Ahedo and F.I.Parra. Model of radial plasma-wall interactions in a Hall thruster discharge-paper AIAA-4106 at 38th JPC, 7-10 July, 2002, Indianapolis, IN.
5. B.A.Arhipov et al. Small SPT Unit Development and Tests – Proceedings of the 3rd International Conference on Spacecraft Propulsion, 10-13 October, Cannes, France.
6. A.Veselovzorov et al. Report on ISTC-Project #2317p for the period from April, 1, to September, 30, 2002. Moscow, RSC “Kurchatov Institute”, 2002.
7. V.Egorov, V.Kim, A.Semenov, I.Shkarban. Nearwall processes and their influence on the operation of accelerators with closed drift of electrons-paper in the book “Ion Injectors and plasma accelerators”, Moscow, Energoatomizdat, 1990, pp.56-68 (in Russian).
8. G.I. Slobodenuk. Quadrupolar mass-spectrometers. Moscow, Atomizdat, 1974.

II.7. Appendix 1.

•

Figures for Section II.

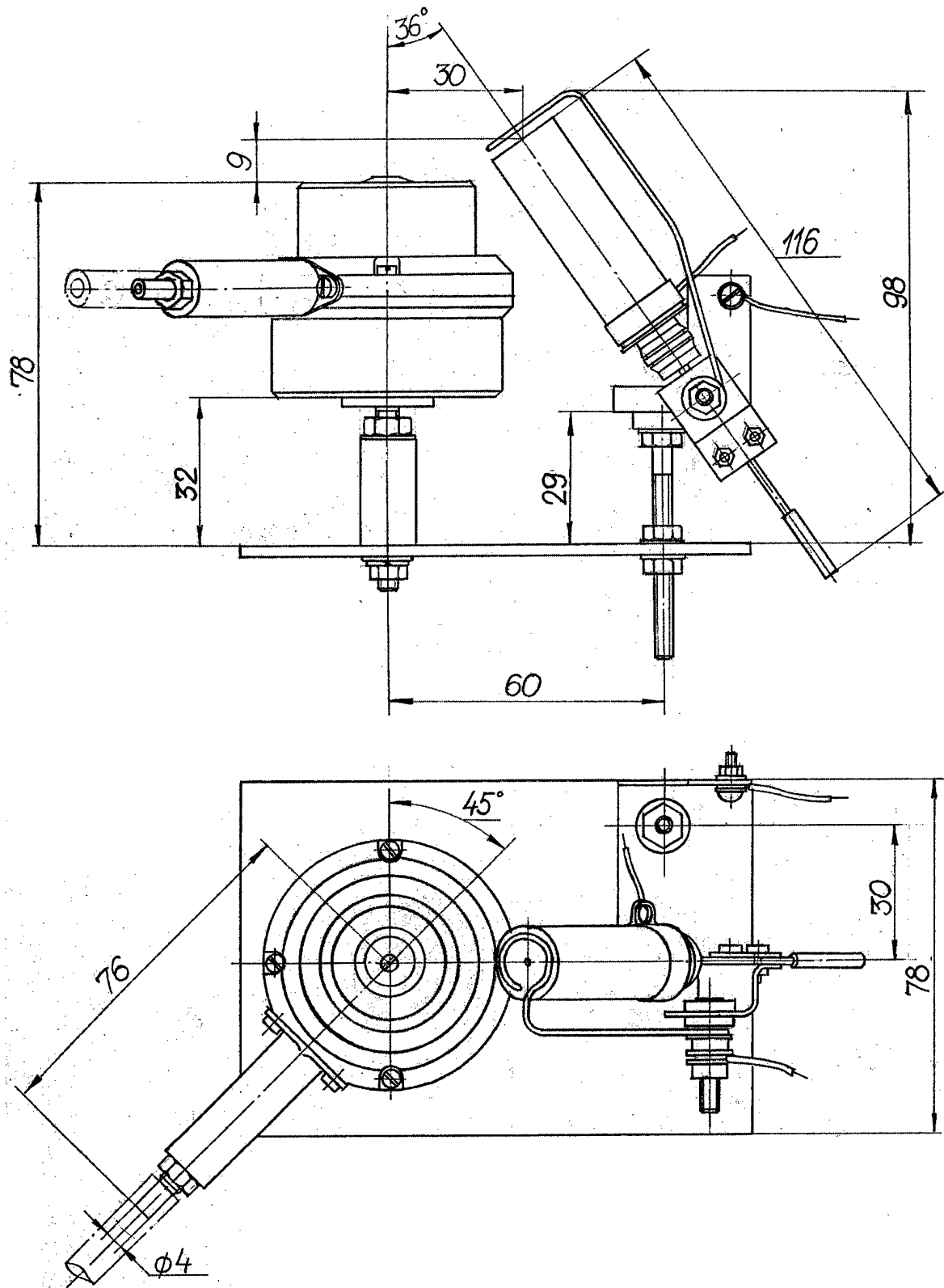


Fig.1.1. SPT-25 experimental unit

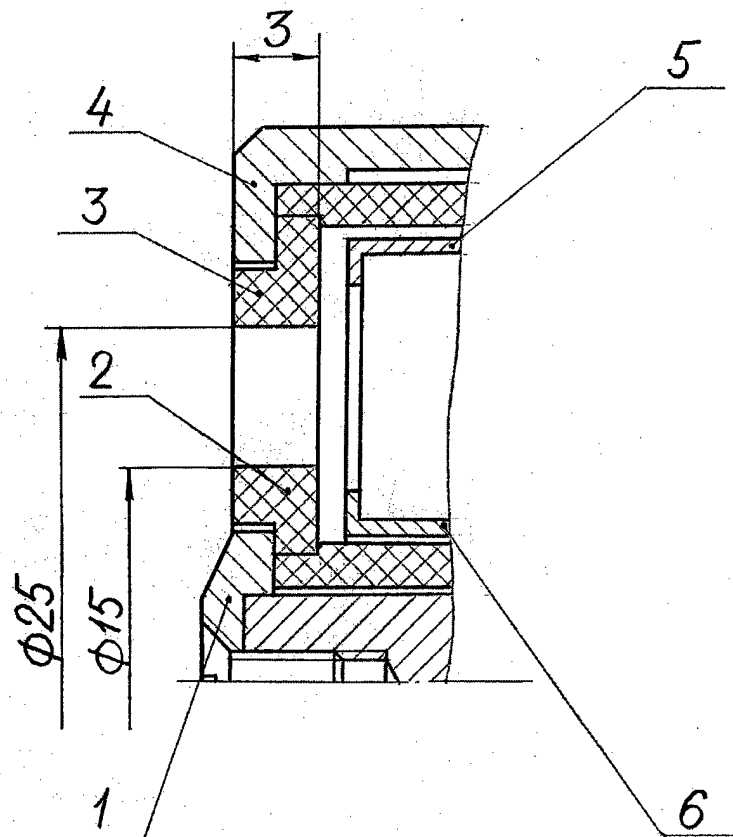


Fig.1.2. SPT-25 exit part diagram

- 1 – internal magnetic pole
- 2 – internal ceramic ring
- 3 – external ceramic ring
- 4 – external magnetic pole
- 5 – external anode ring
- 6 – internal anode ring

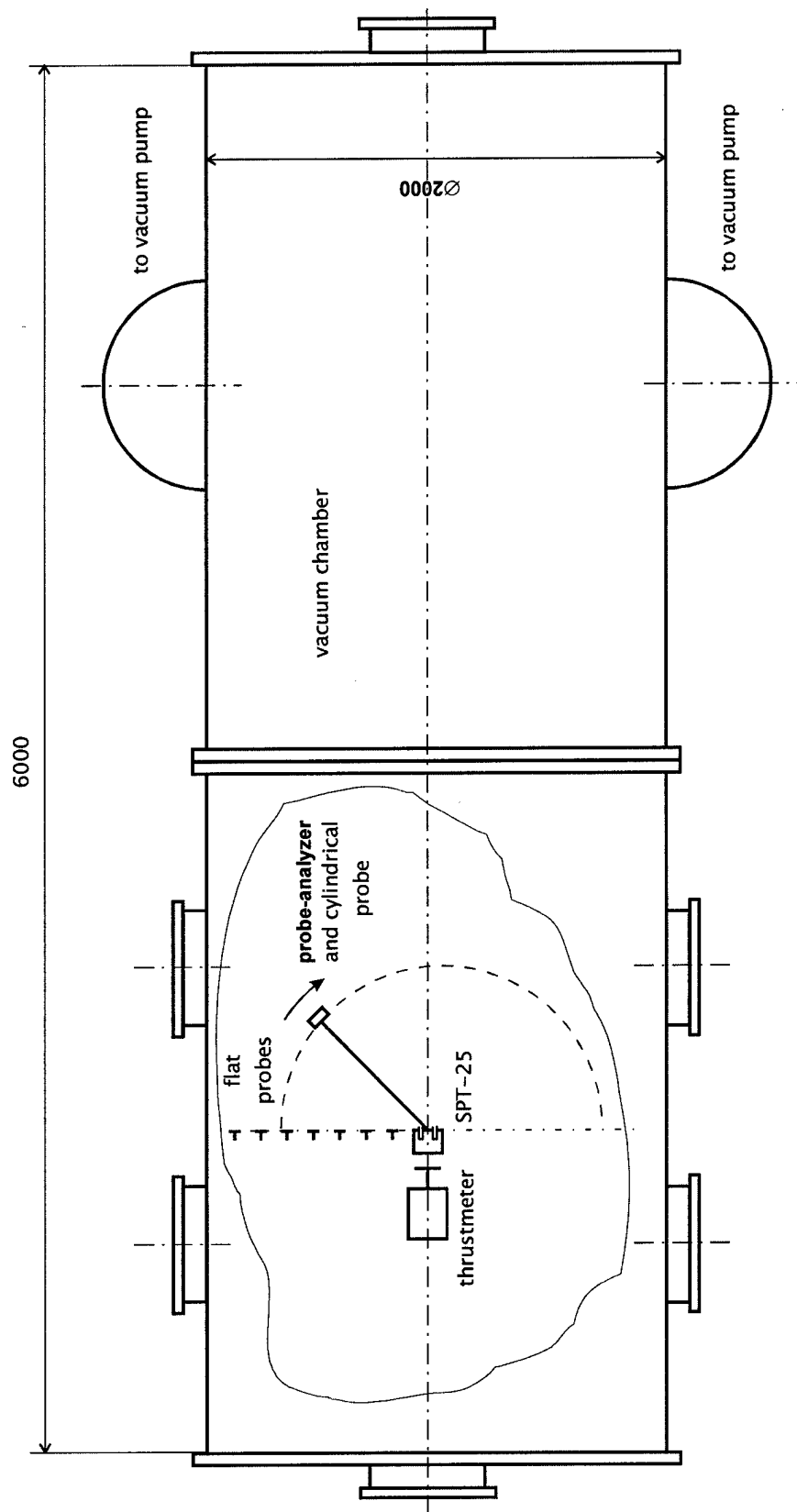


Fig.1.3. Schematic of the vacuum chamber.

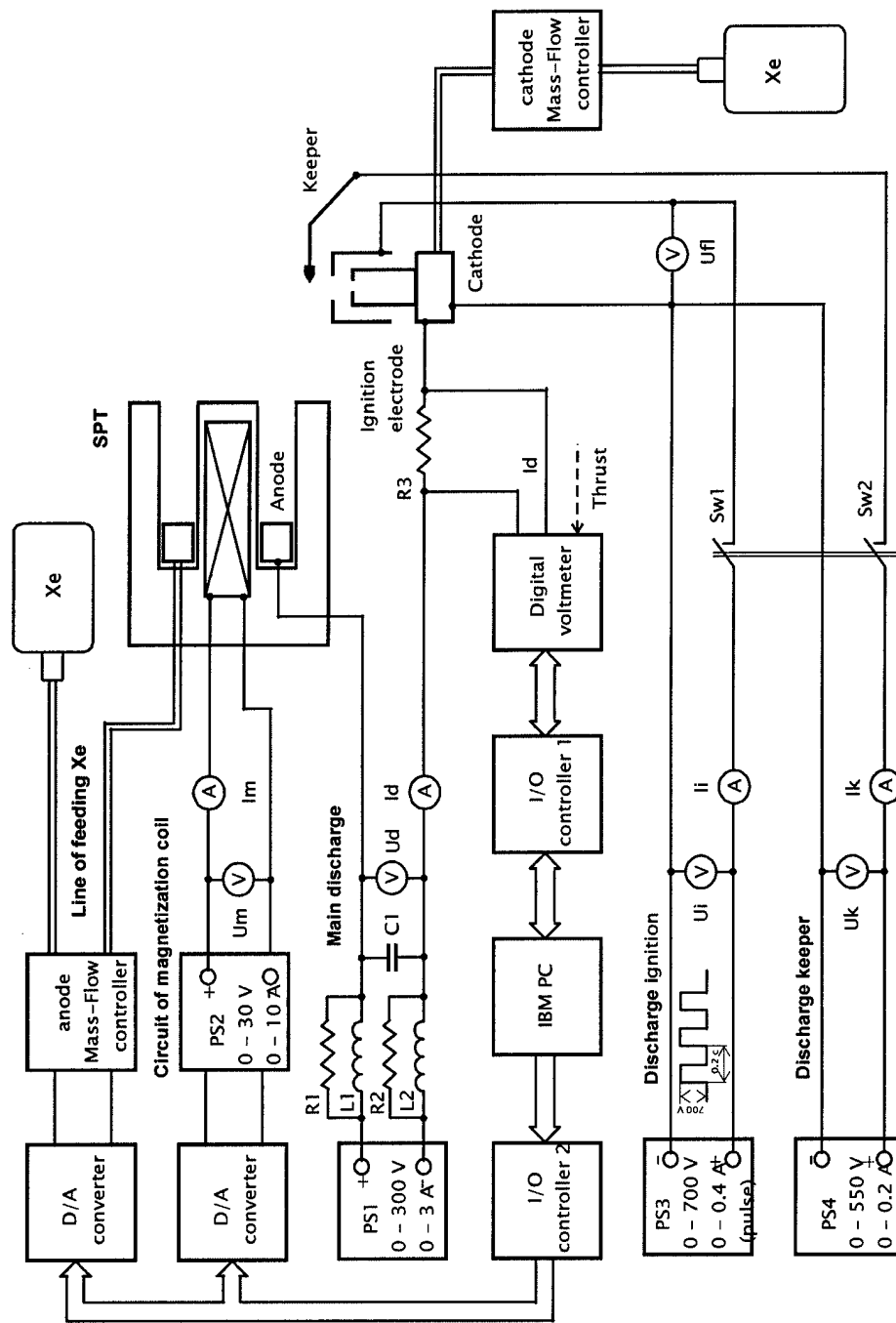


Fig.1.4. The scheme of the power supplies and of automatic system.

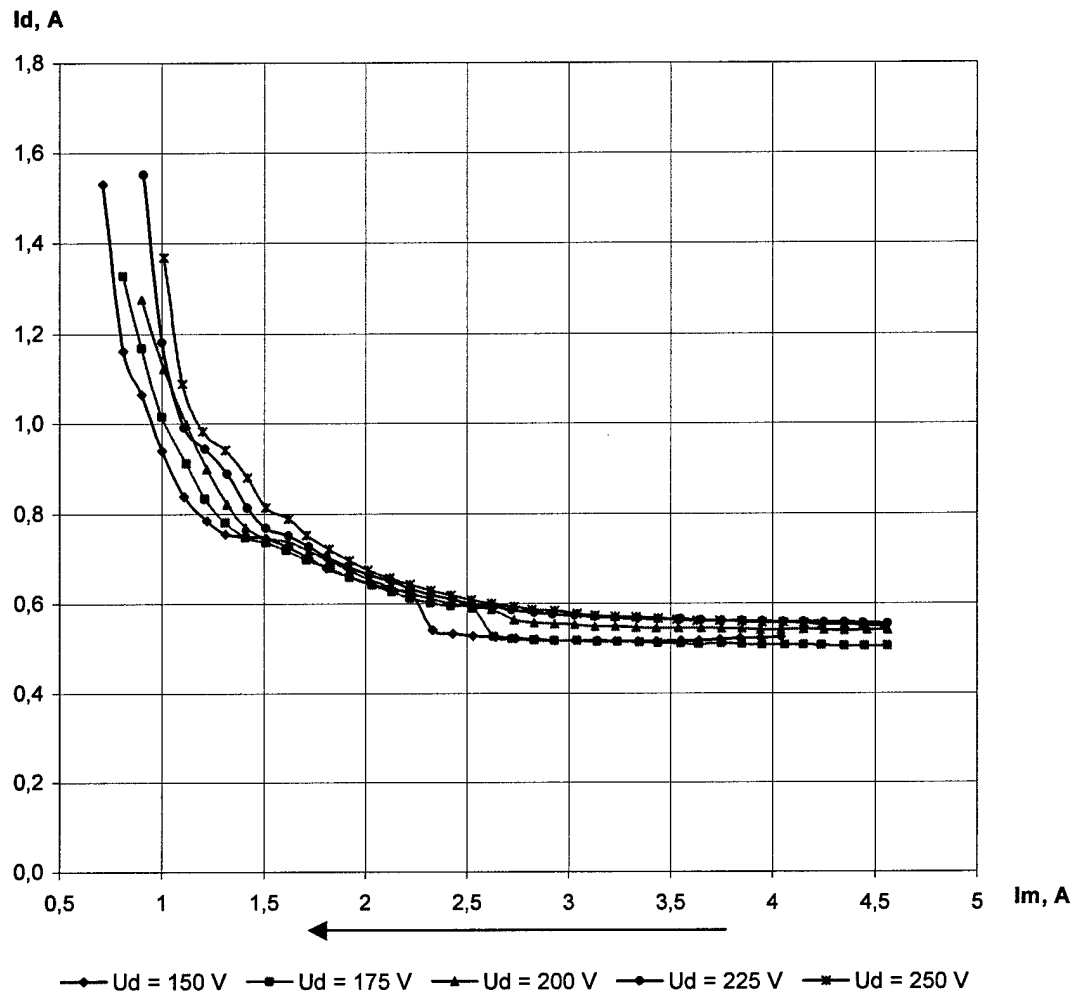
SPT-25 #1, $m_a=0.5$ mg/s

Fig.1.5. Discharge current versus the magnetization current

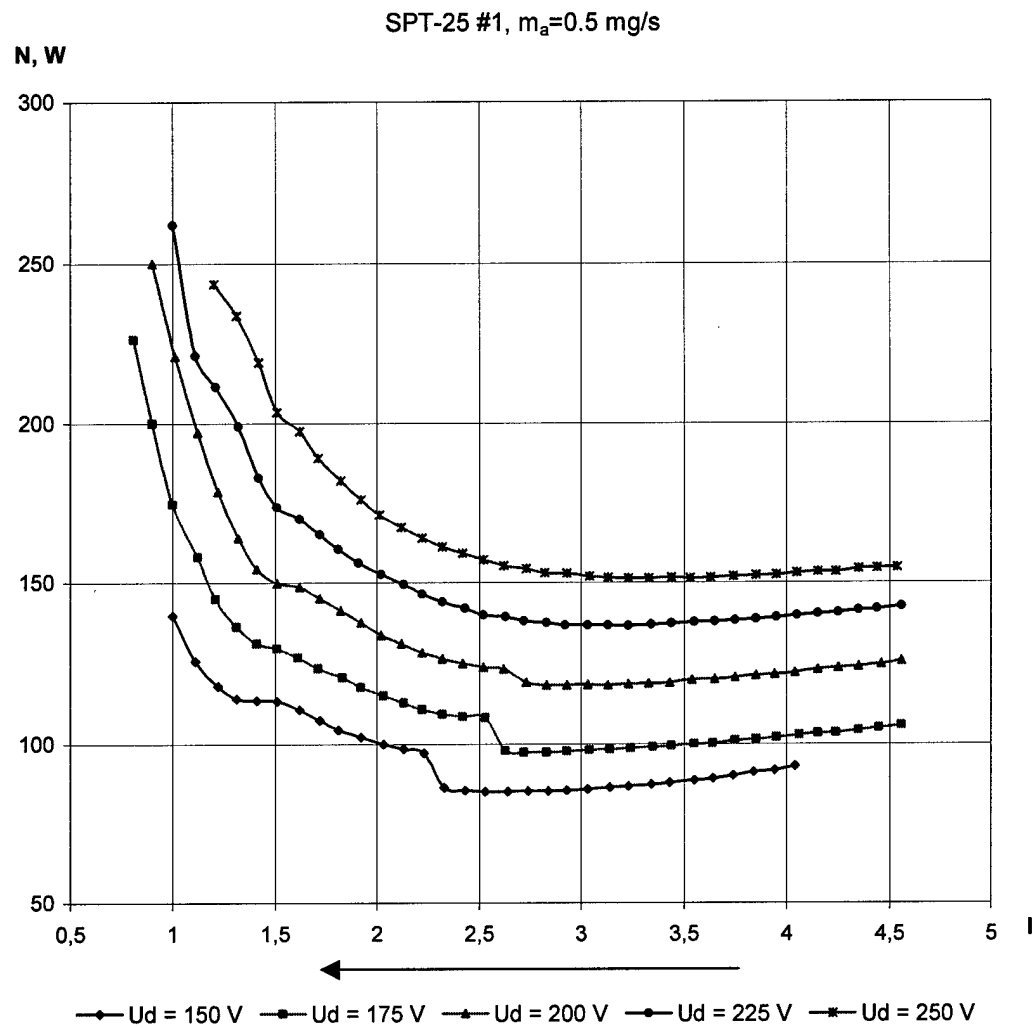


Fig.1.6. Discharge power versus the magnetization current

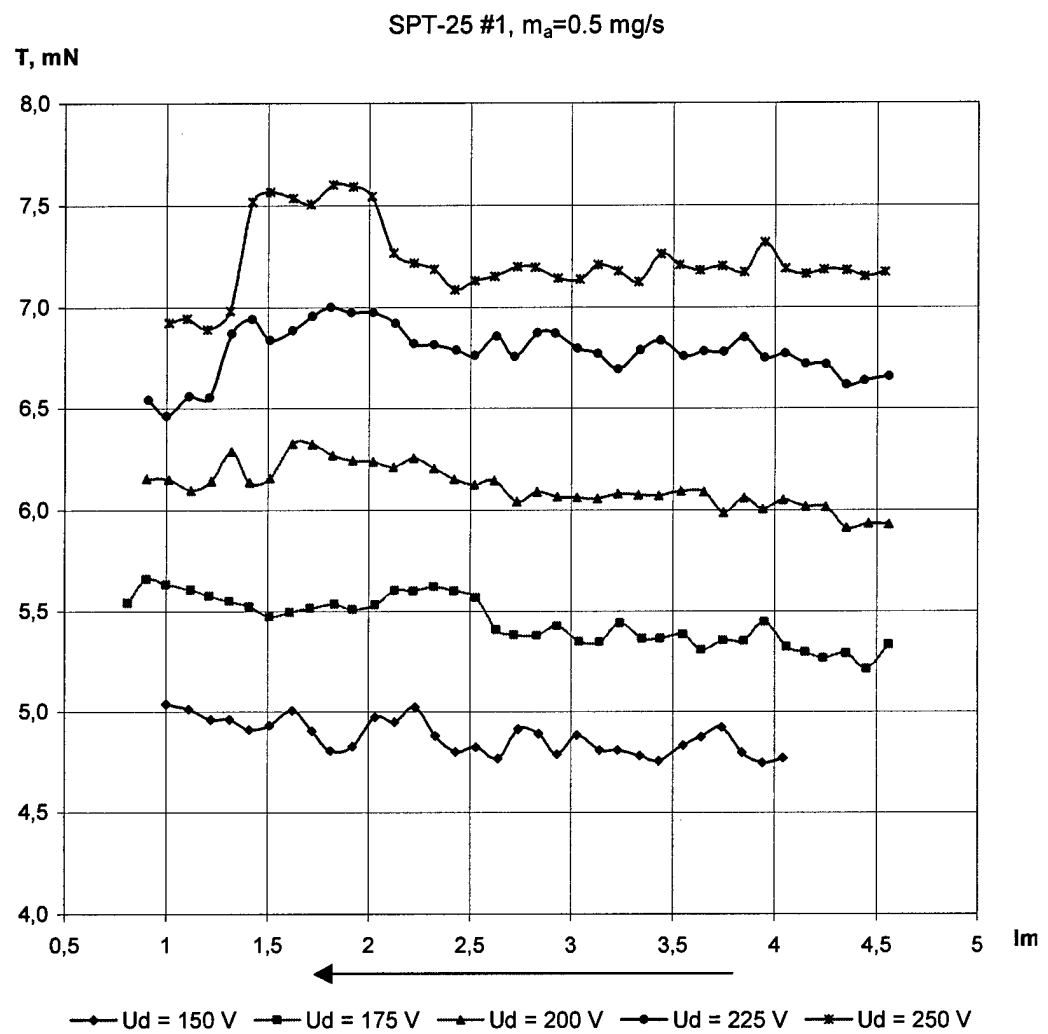


Fig.1.7. Thrust versus the magnetization current

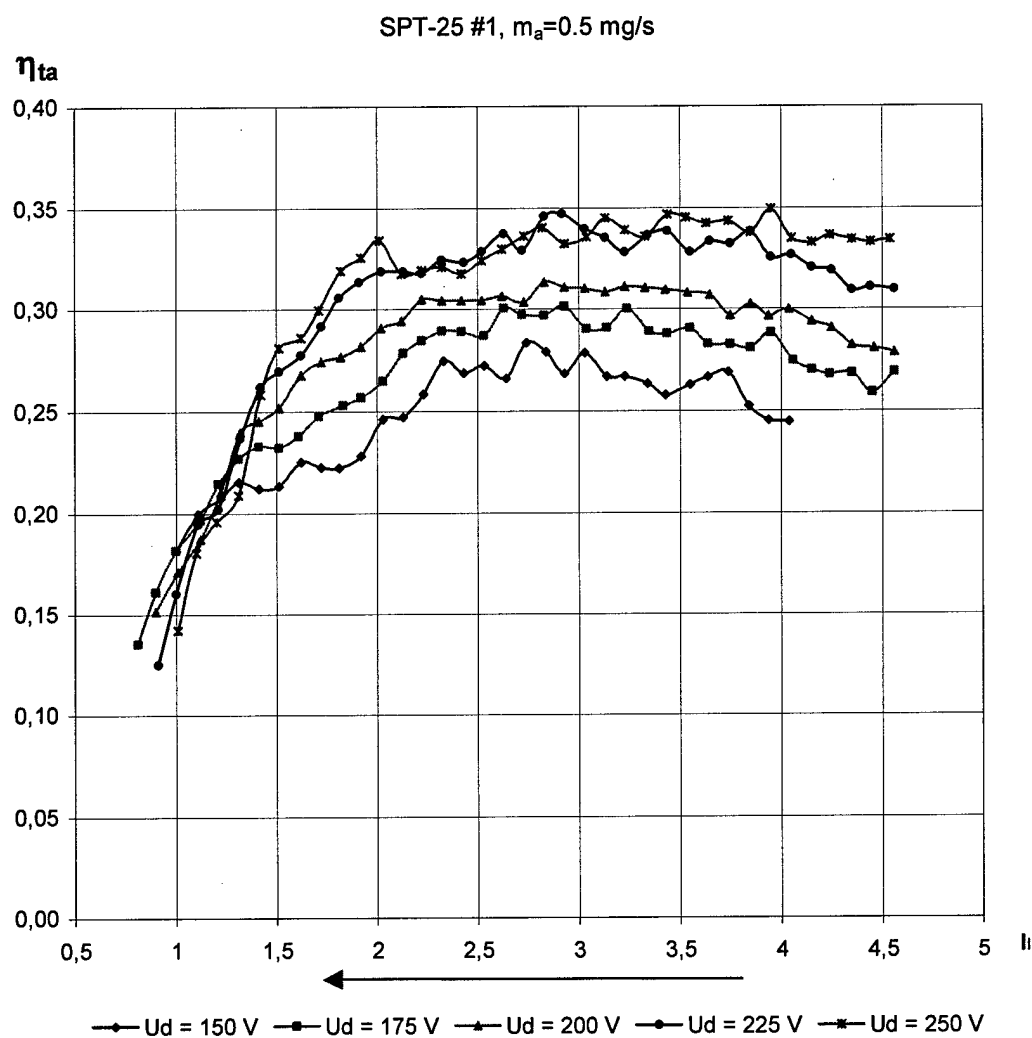


Fig.1.8. Thrust efficiency versus the magnetization current

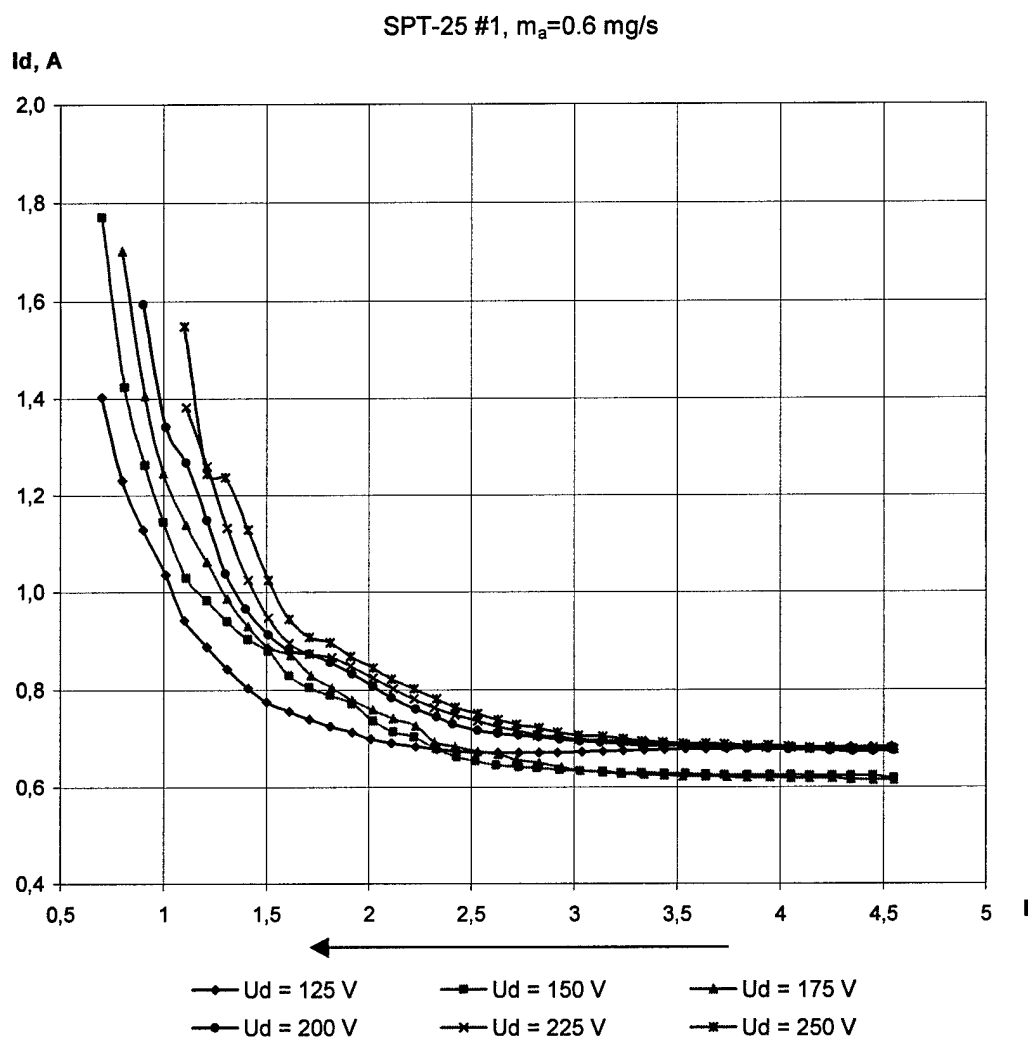


Fig.1.9. Discharge current versus the magnetization current

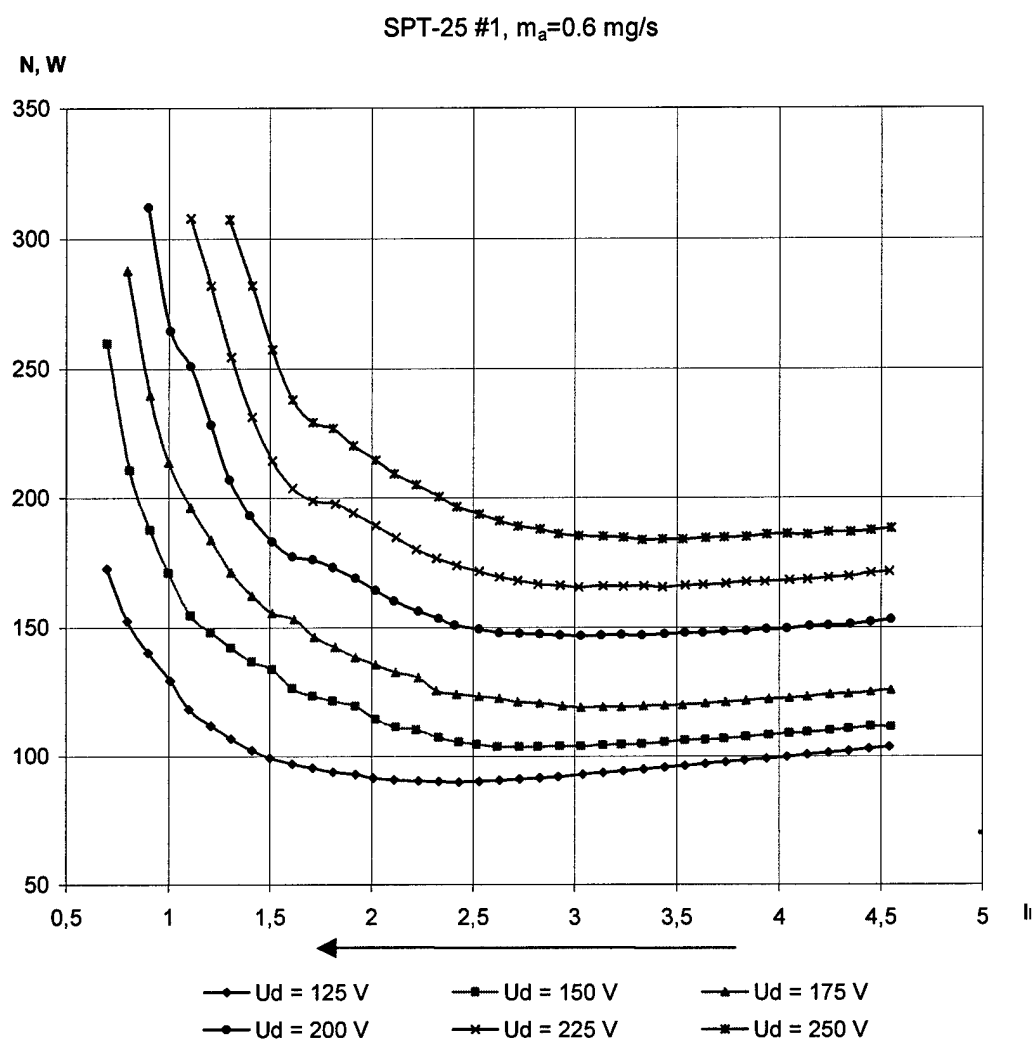


Fig.1.10. Discharge power versus the magnetization current

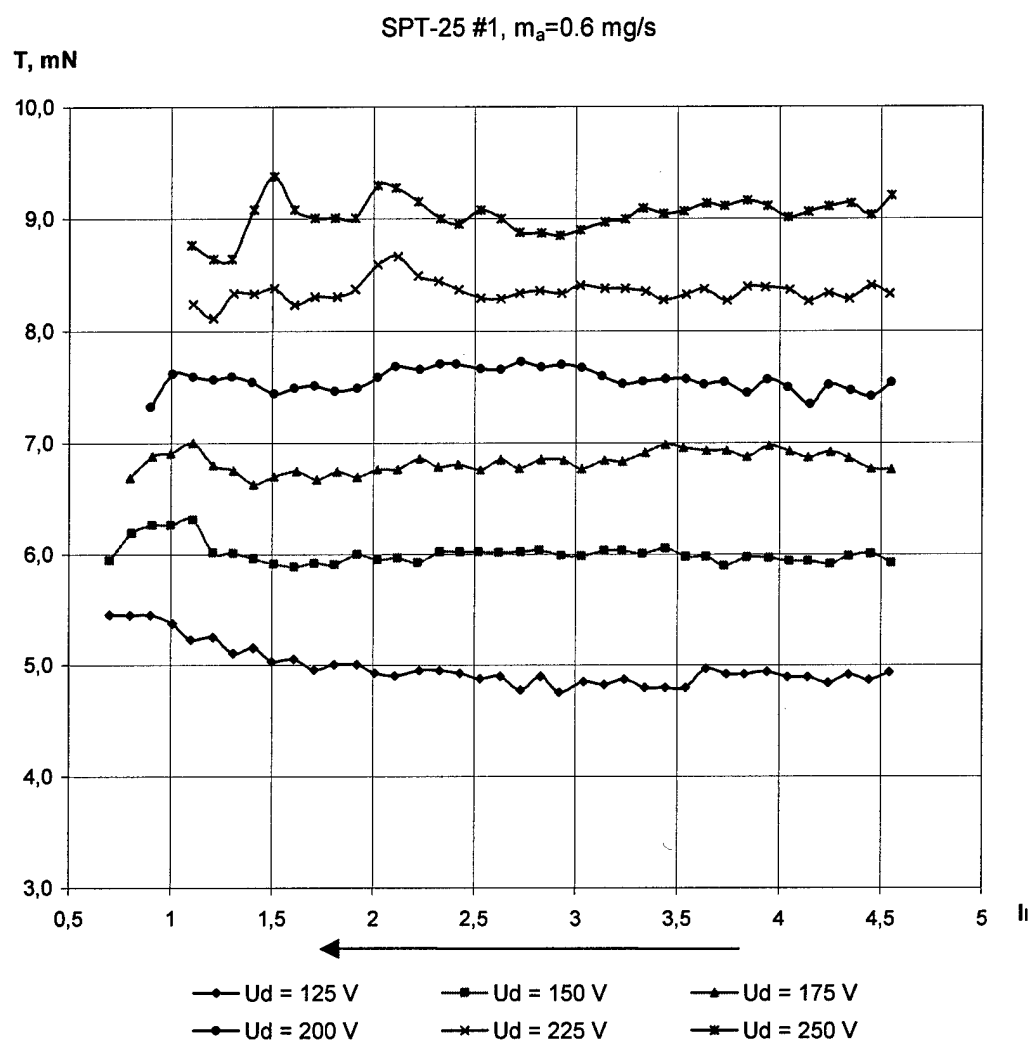


Fig.1.11. Thrust versus the magnetization current

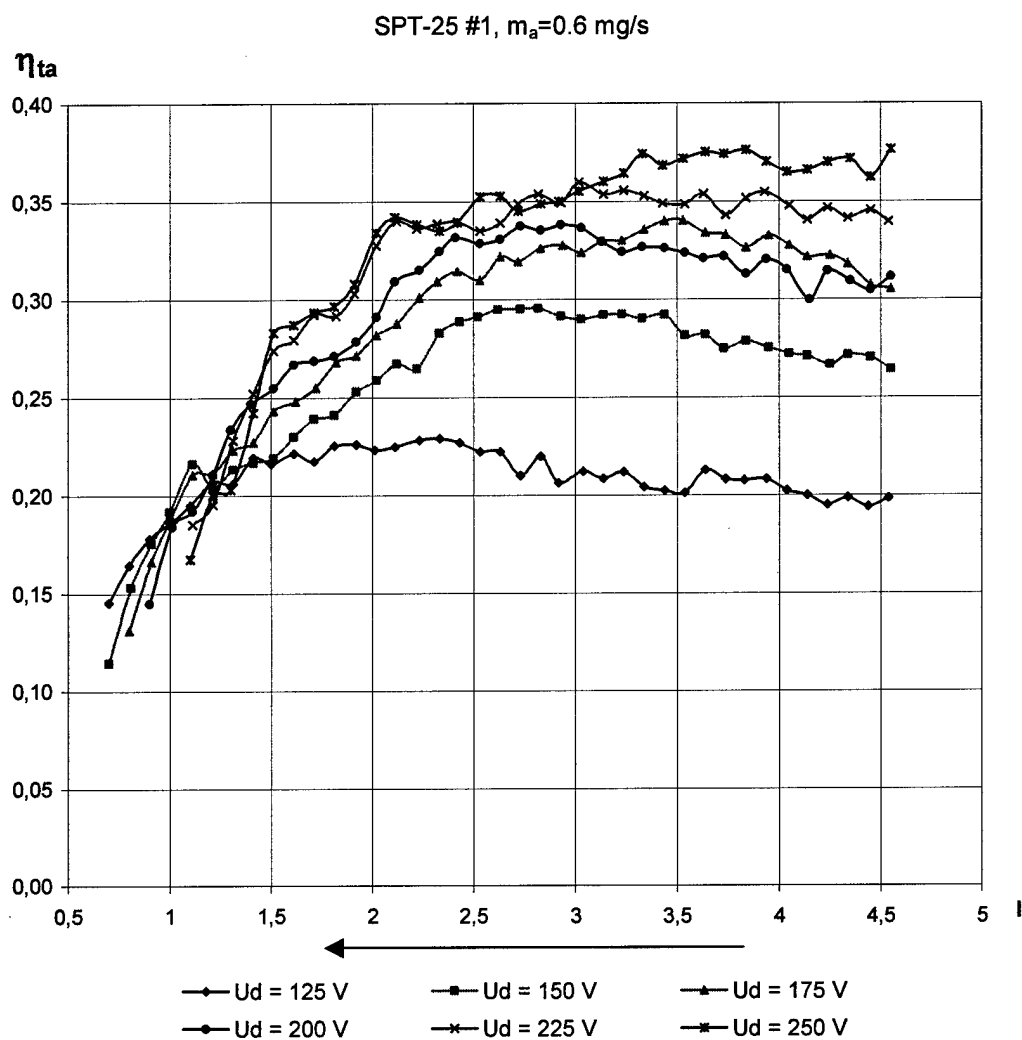


Fig.1.12. Thrust efficiency versus the magnetization current

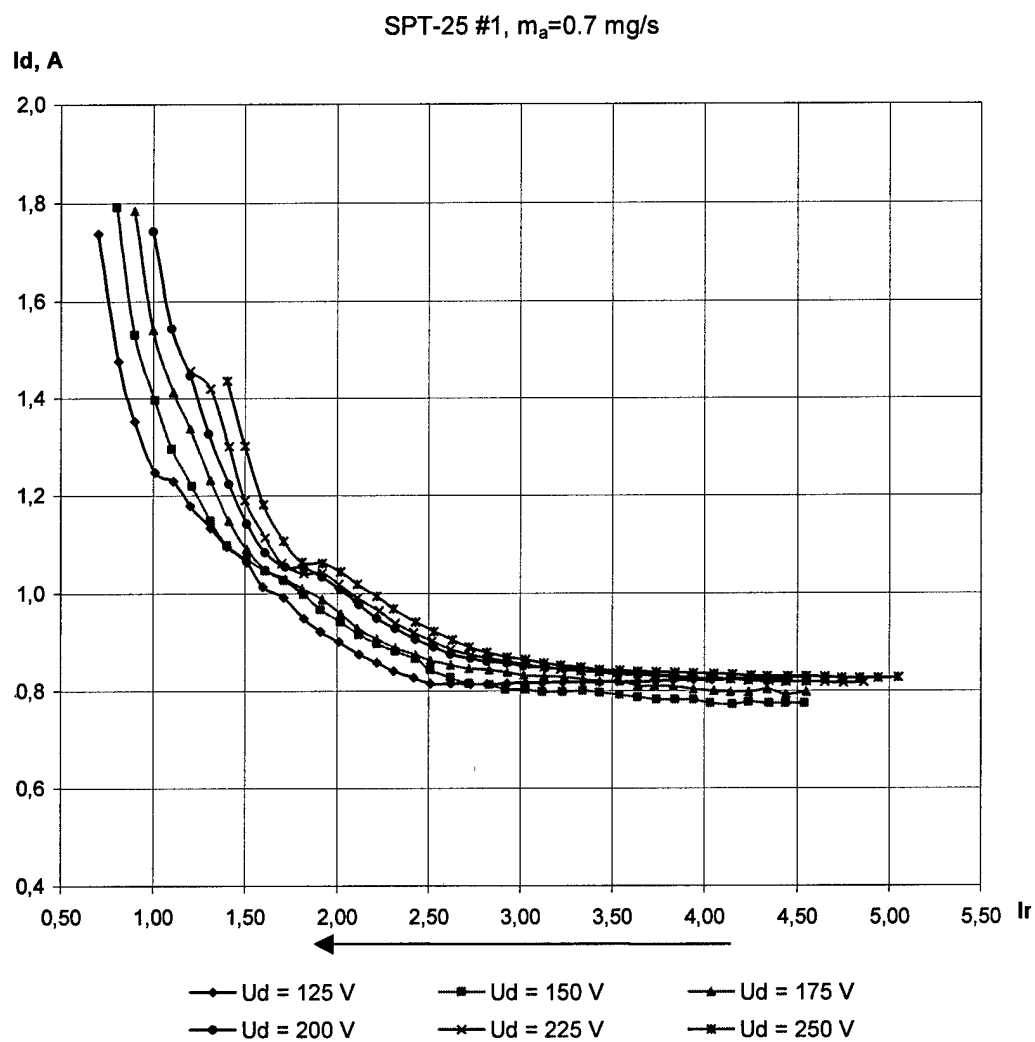


Fig.1.13. Discharge current versus the magnetization current

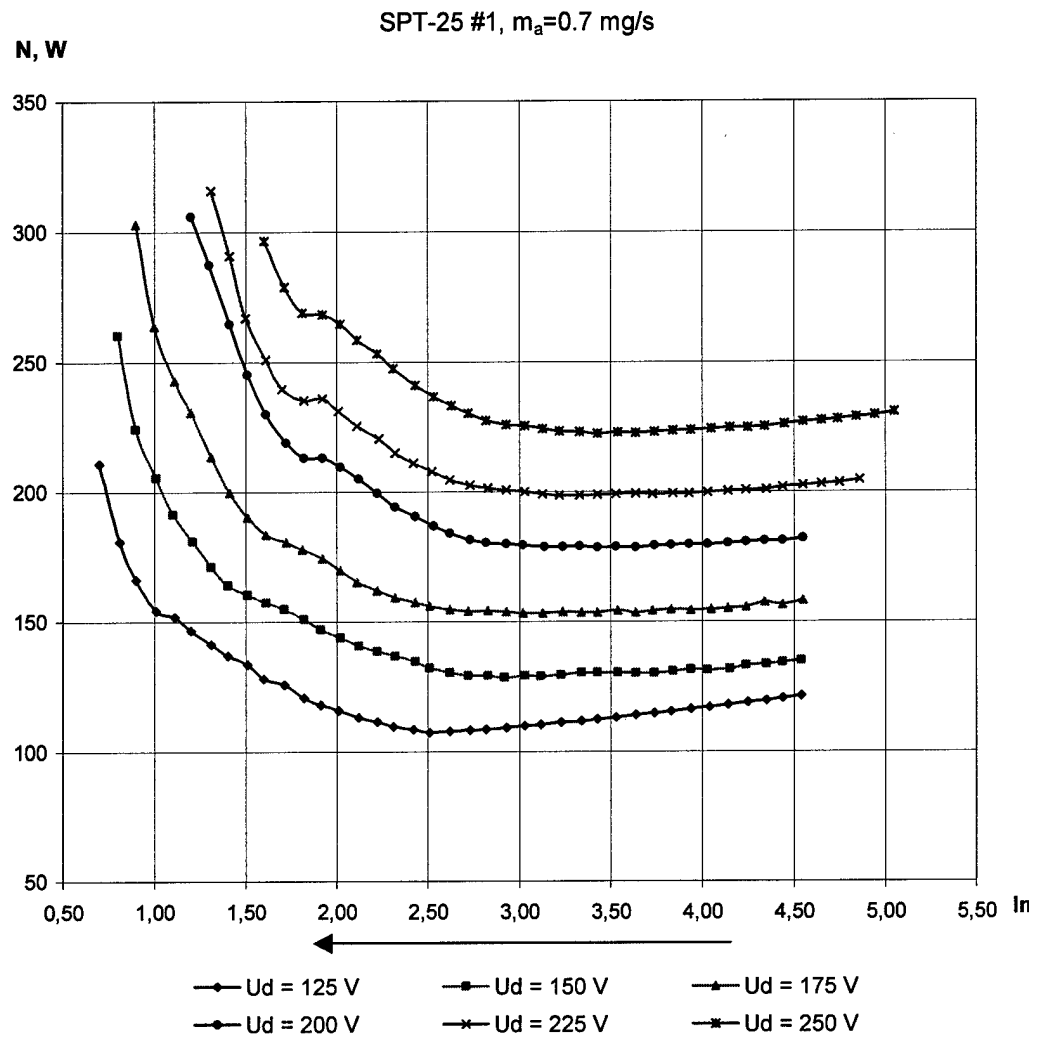


Fig.1.14. Discharge power versus the magnetization current

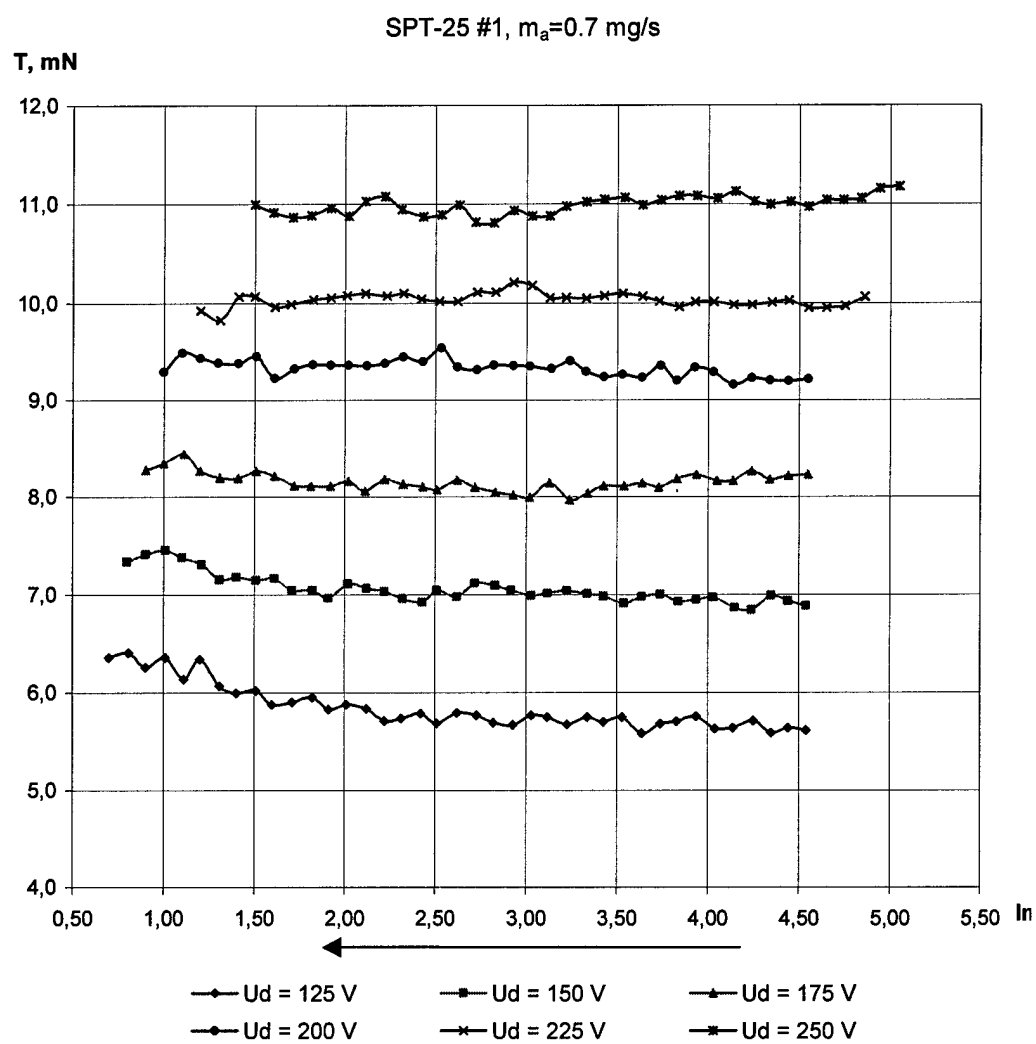


Fig.1.15. Thrust versus the magnetization current

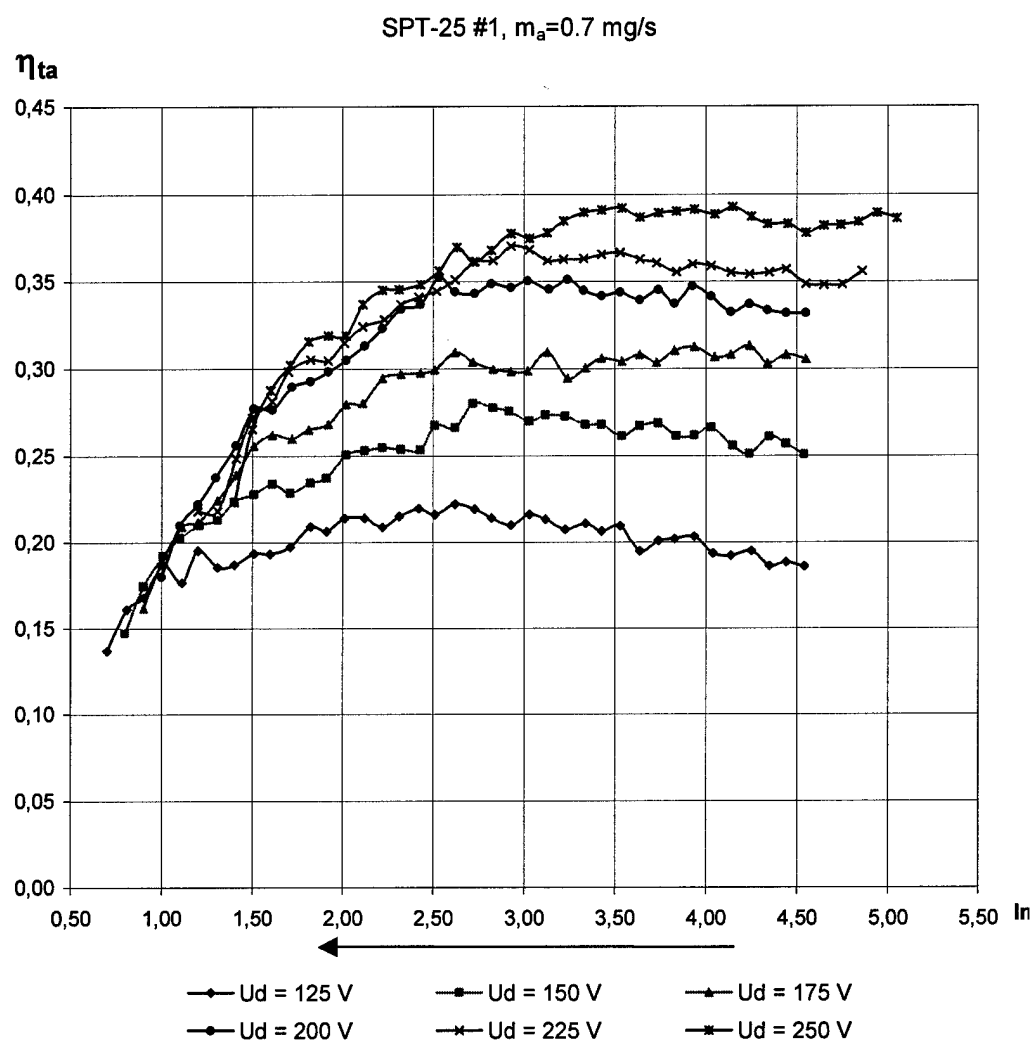


Fig.1.16. Thrust efficiency versus the magnetization current

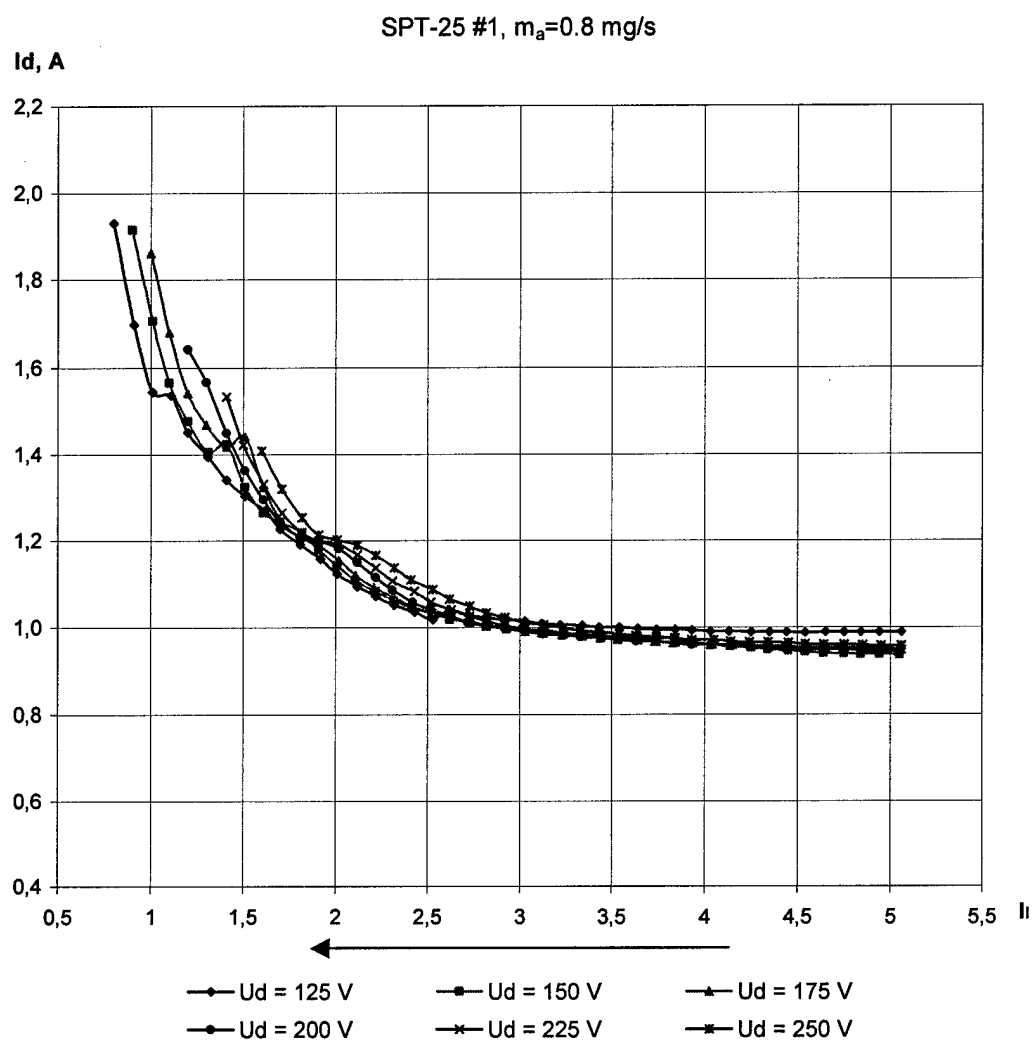


Fig.1.17. Discharge current versus the magnetization current

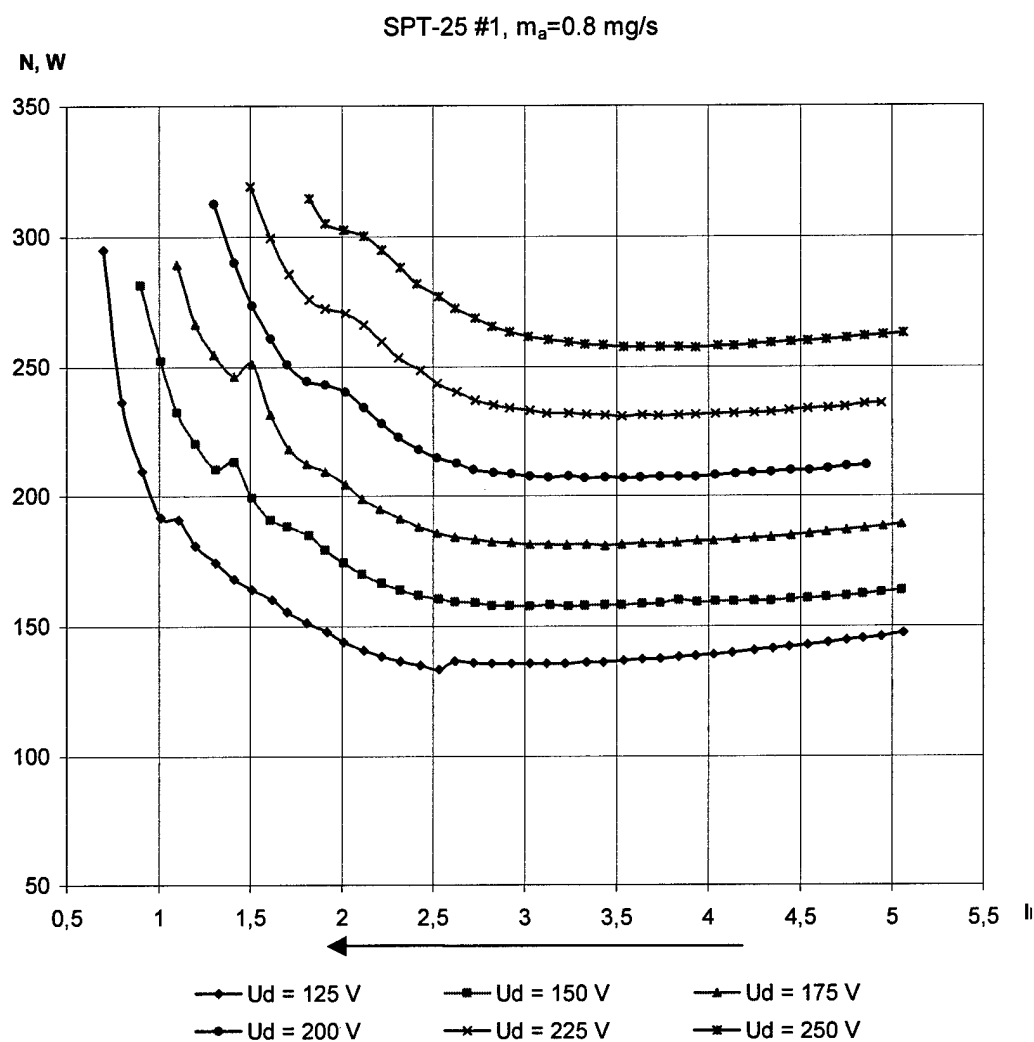


Fig.1.18. Discharge power versus the magnetization current

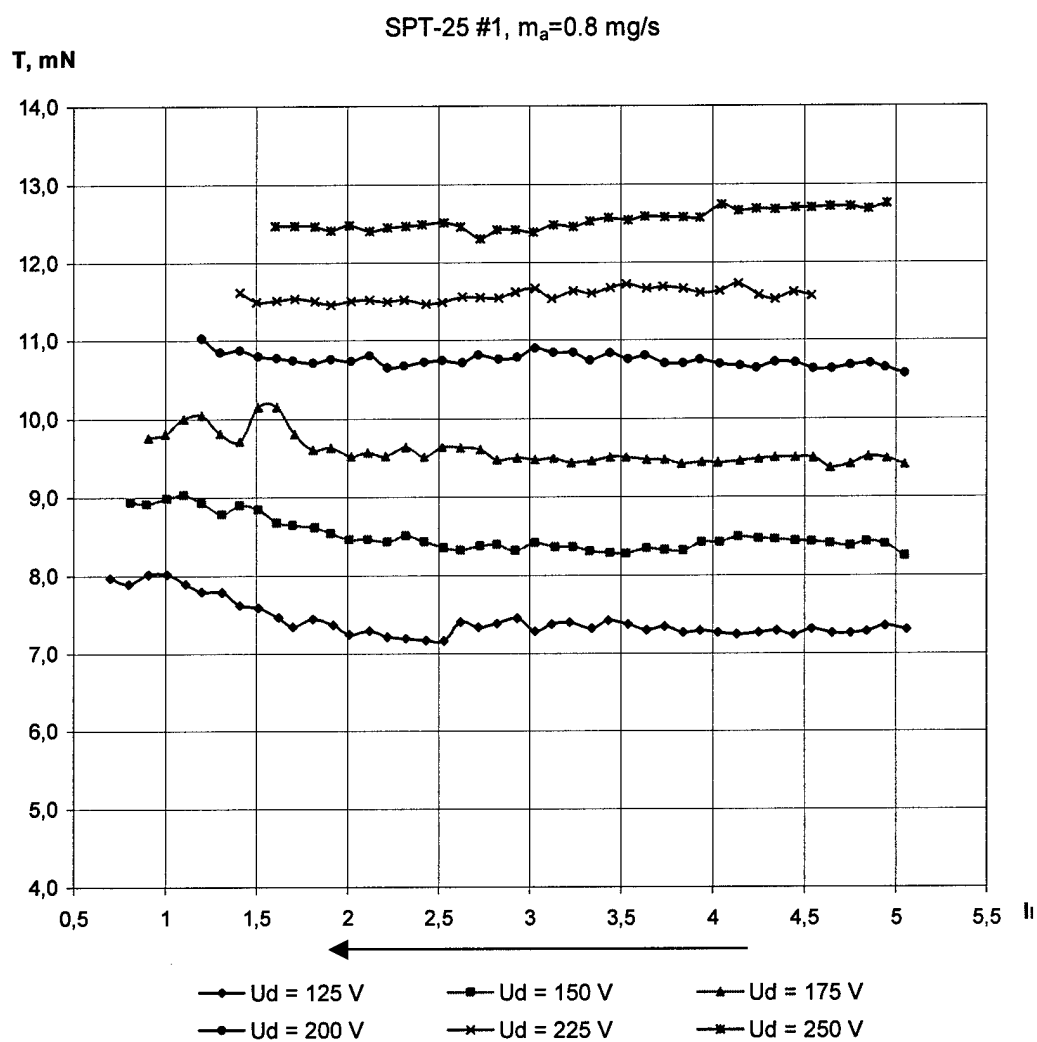


Fig.1.19. Thrust versus the magnetization current

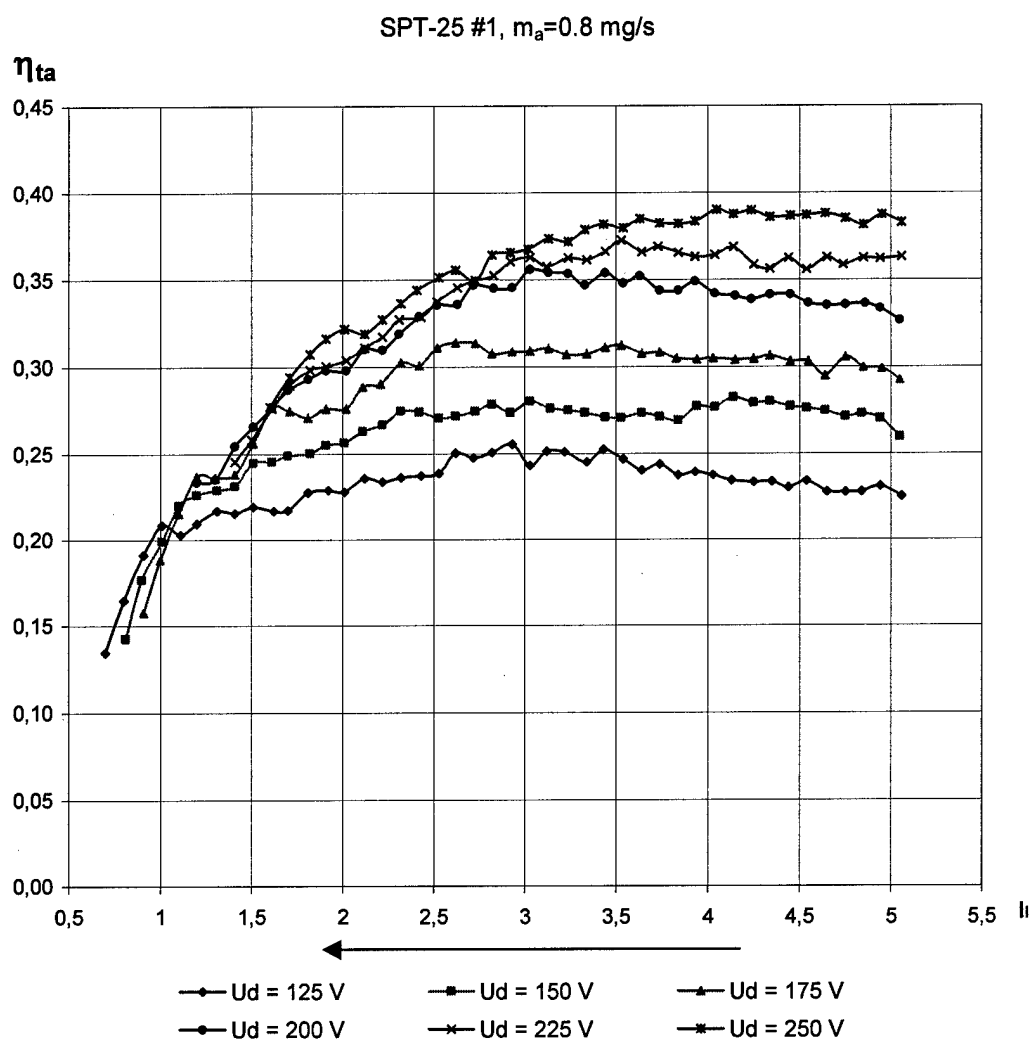


Fig.1.20. Thrust efficiency versus the magnetization current

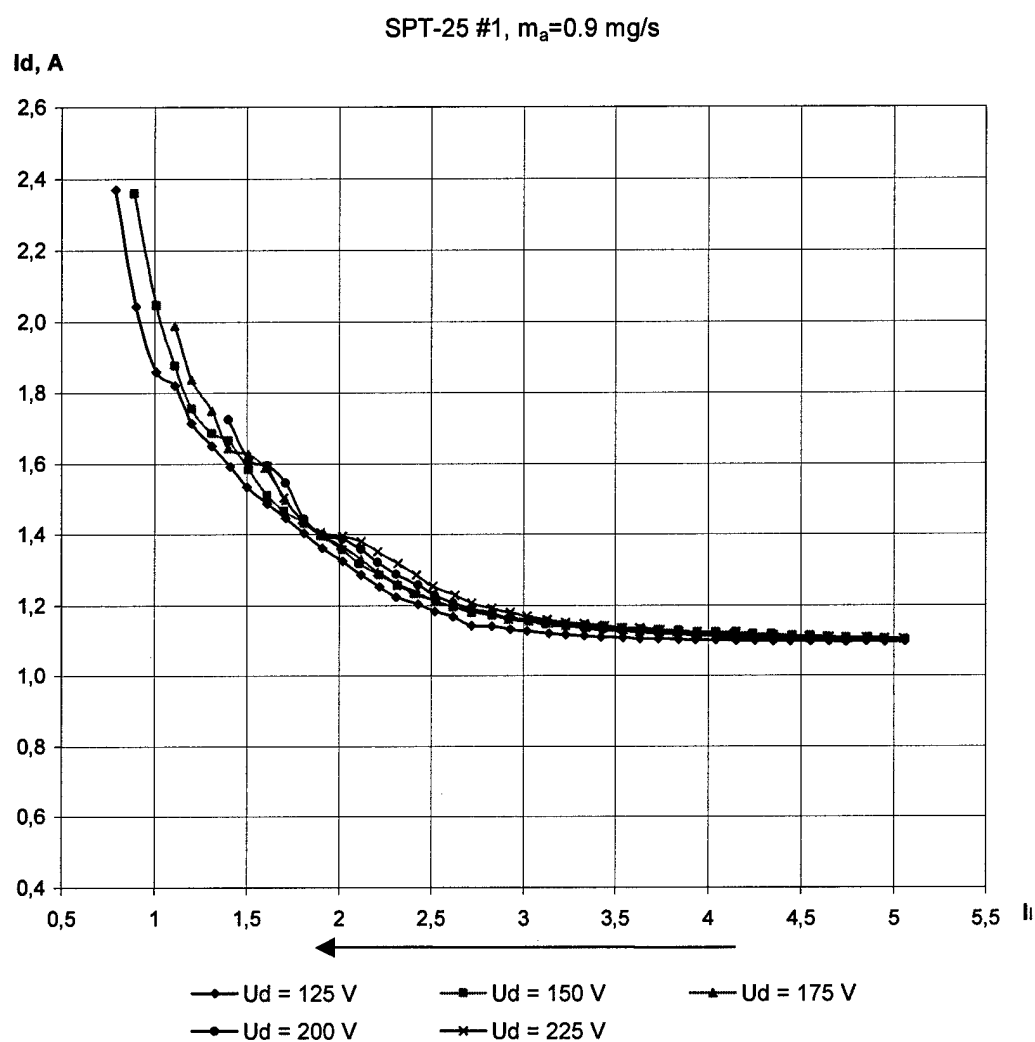


Fig.1.21. Discharge current versus the magnetization current

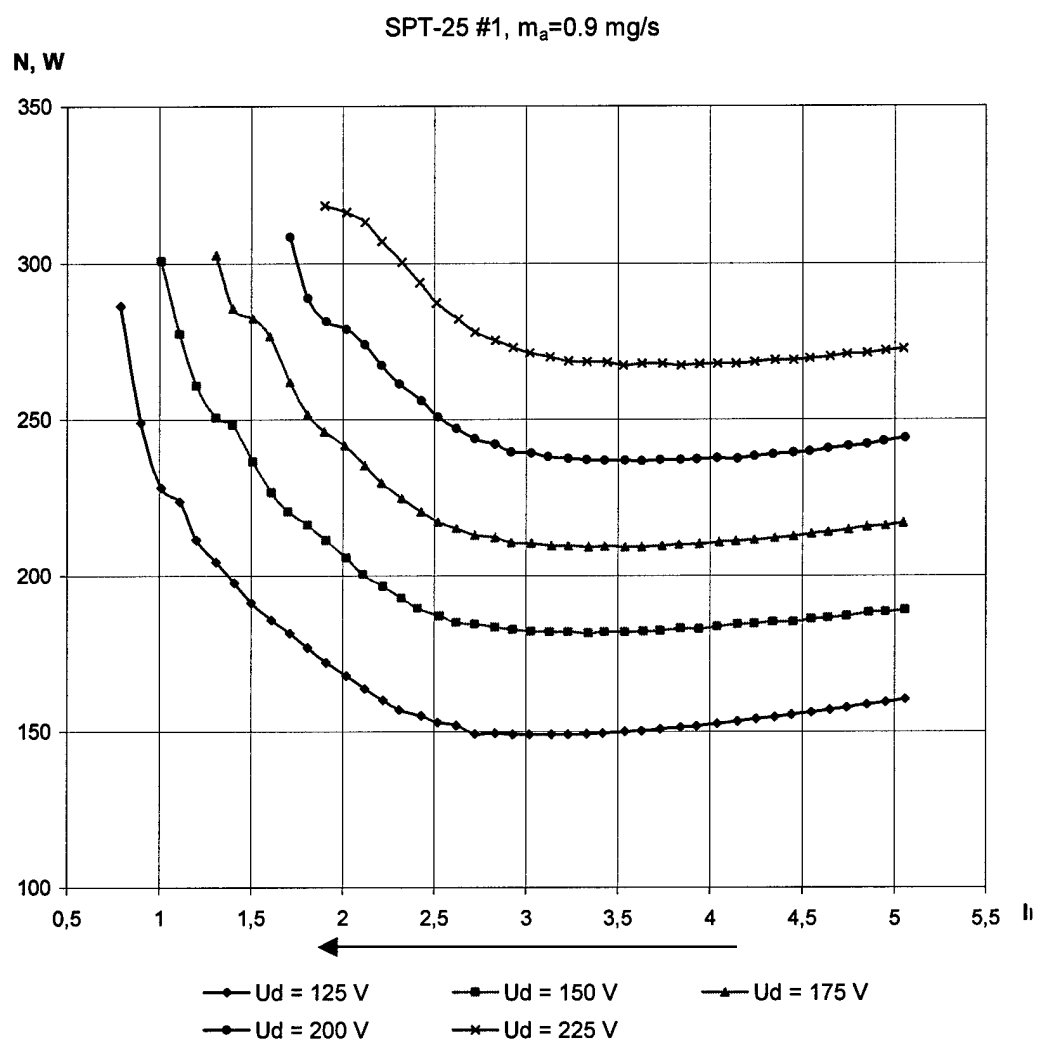


Fig.1.22. Discharge power versus the magnetization current

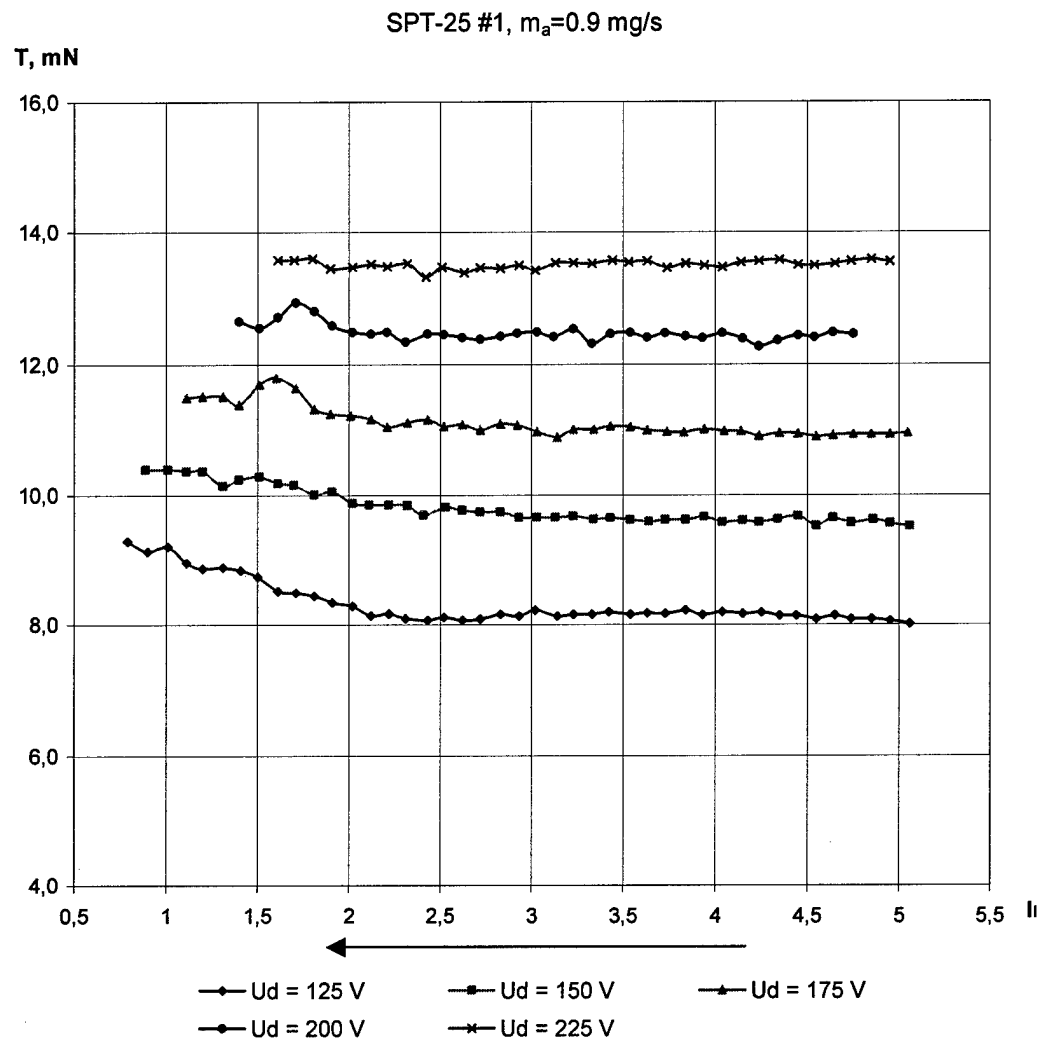


Fig.1.23. Thrust versus the magnetization current

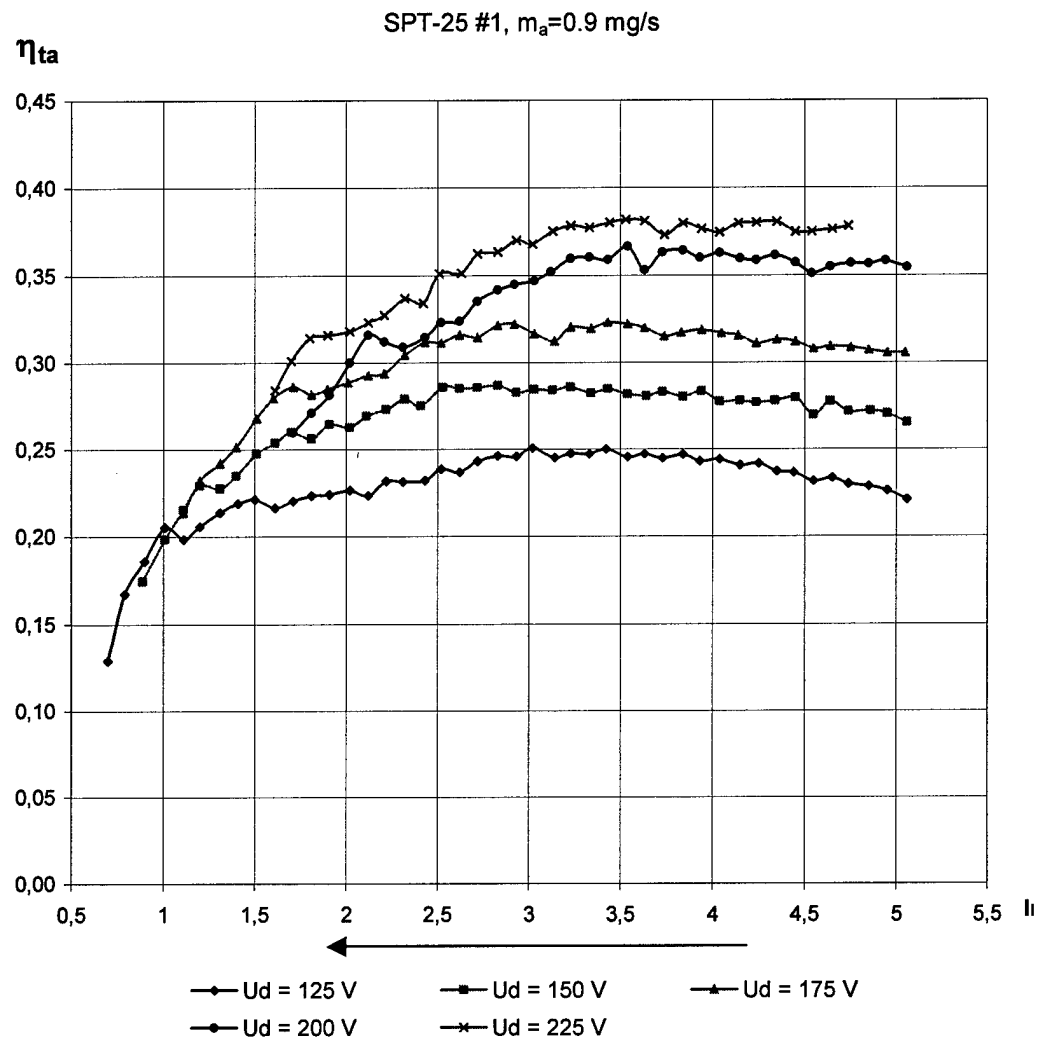


Fig.1.24. Thrust efficiency versus the magnetization current

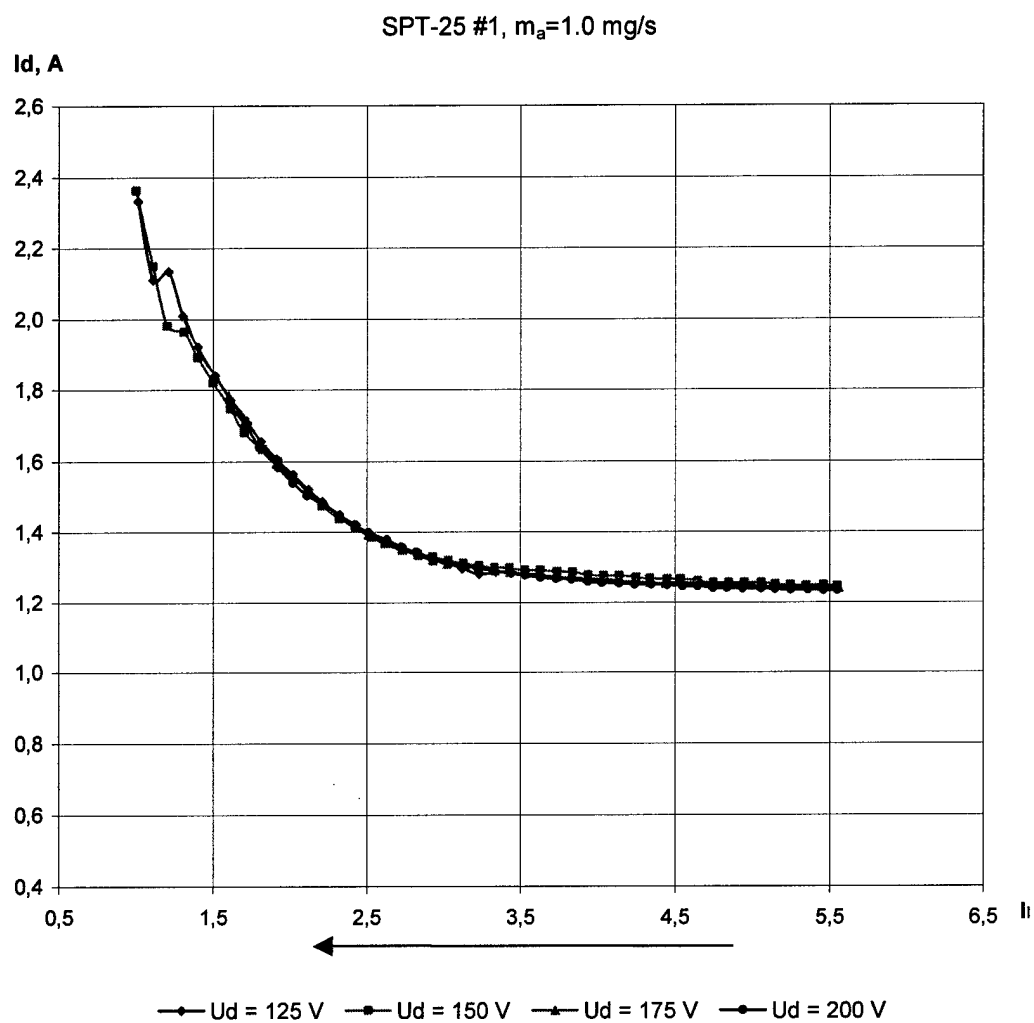


Fig.1.25. Discharge current versus the magnetization current

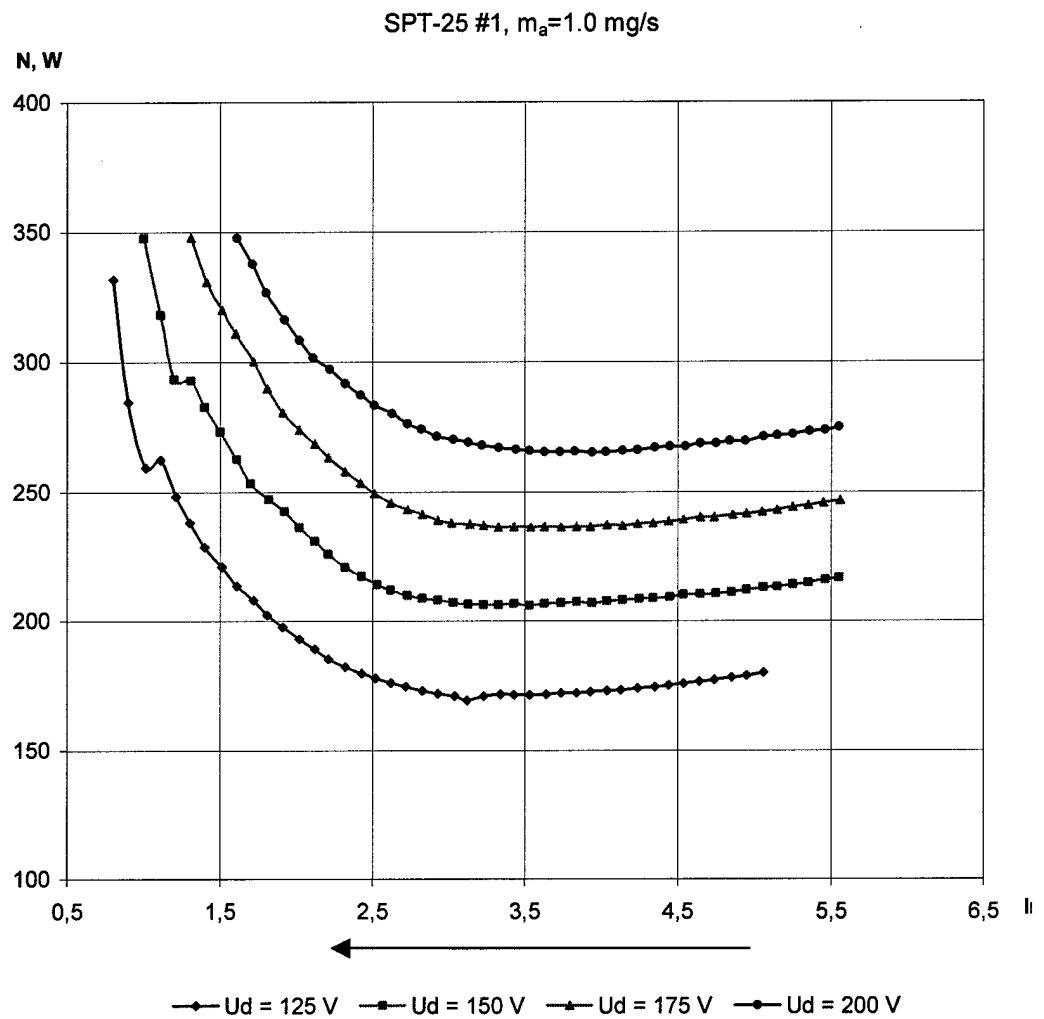


Fig.1.26. Discharge power versus the magnetization current

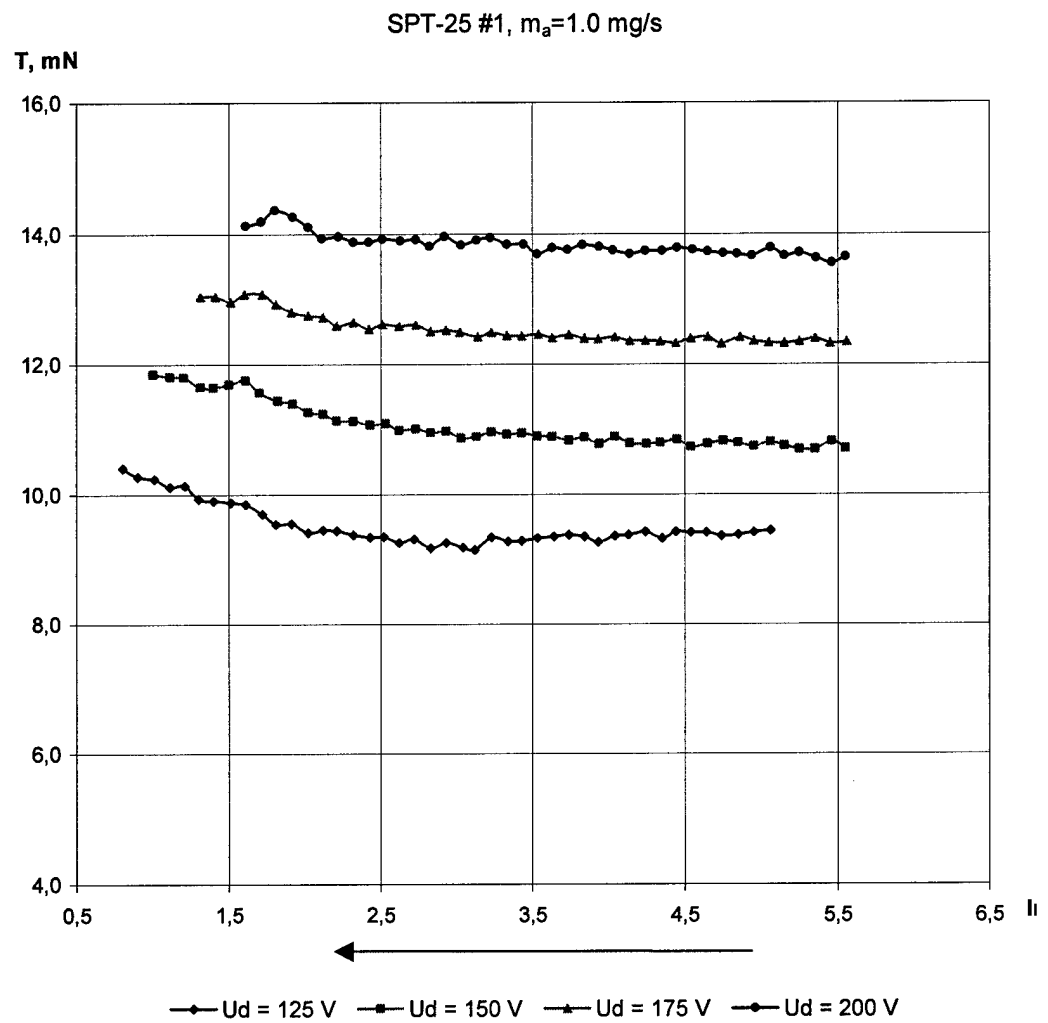


Fig.1.27. Thrust versus the magnetization current

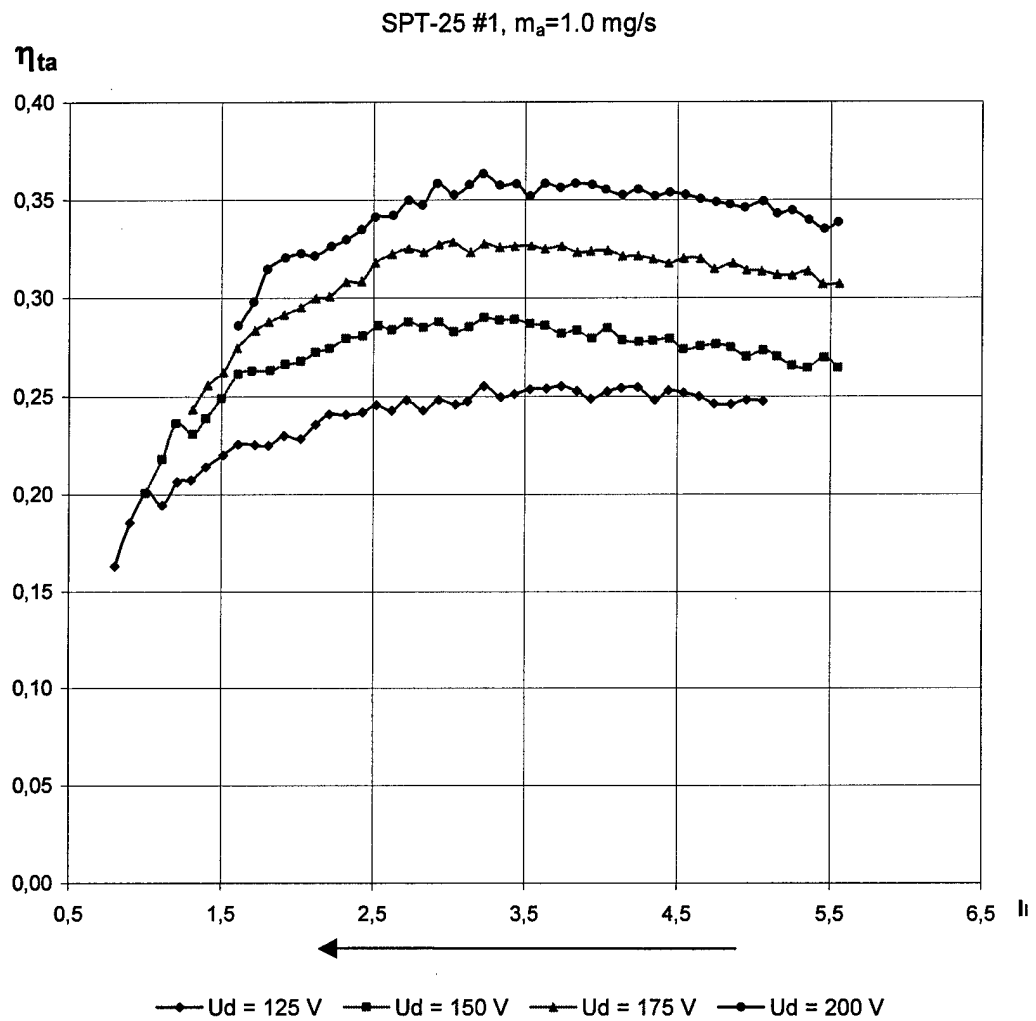


Fig.1.28. Thrust efficiency versus the magnetization current

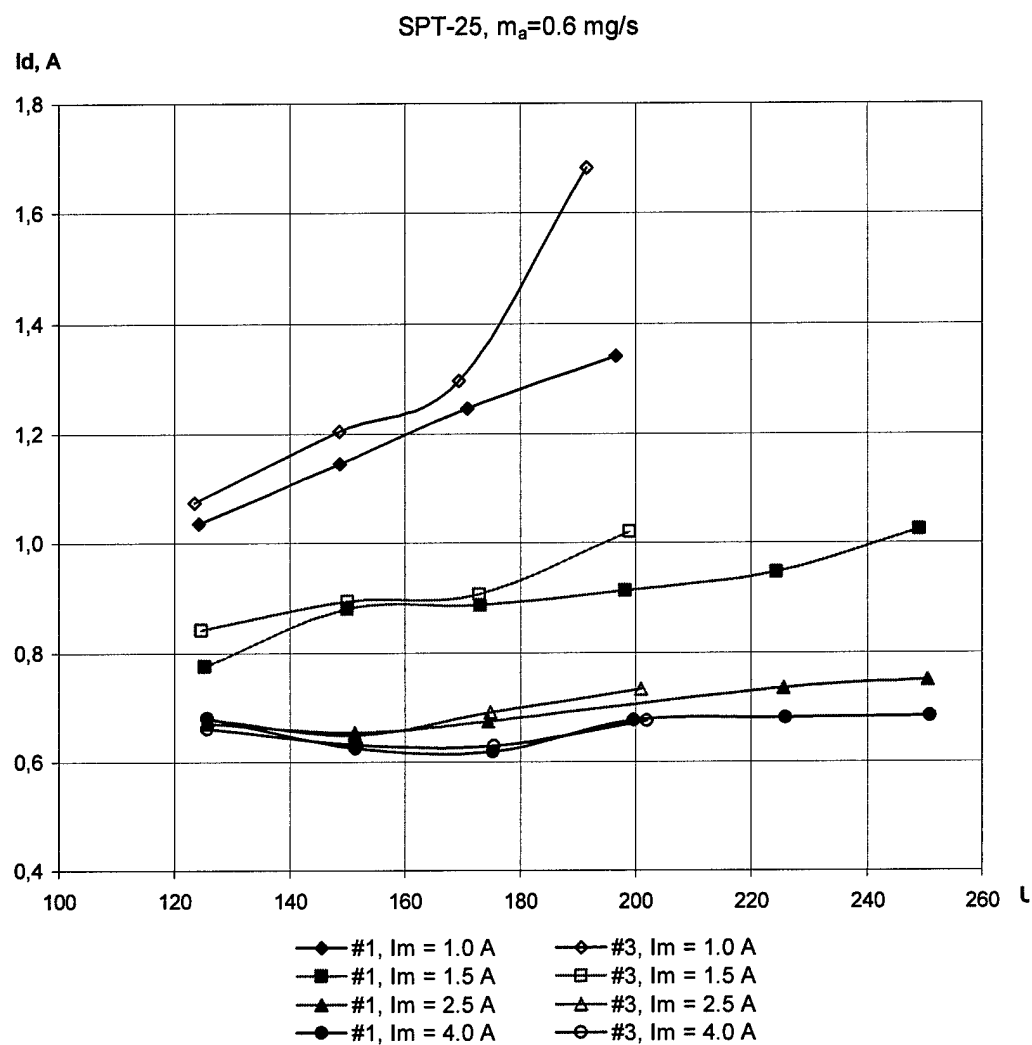


Fig.1.29. Voltage-current characteristics of the SPT-25 with discharge chamber exit rings made of borosil (#1) and ABN (#3)

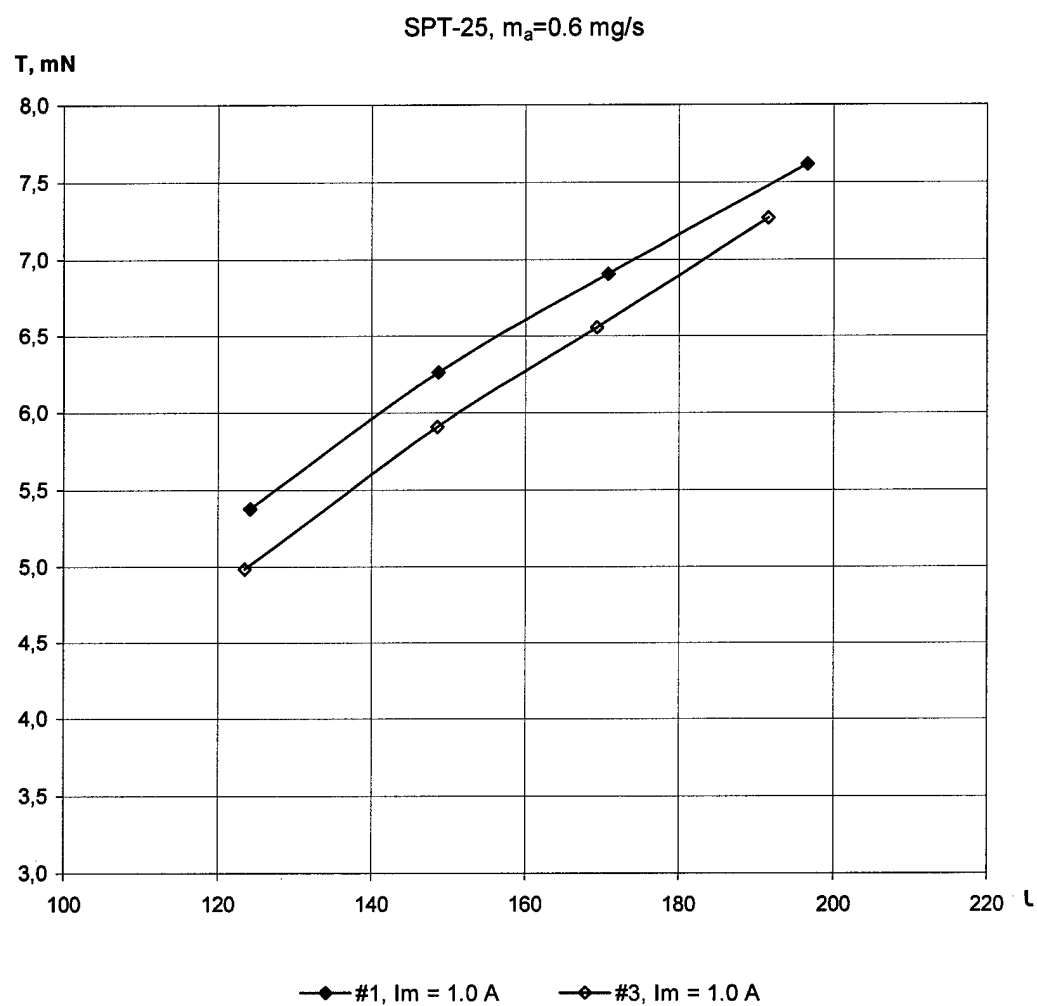


Fig.1.30. Thrust versus the discharge voltage

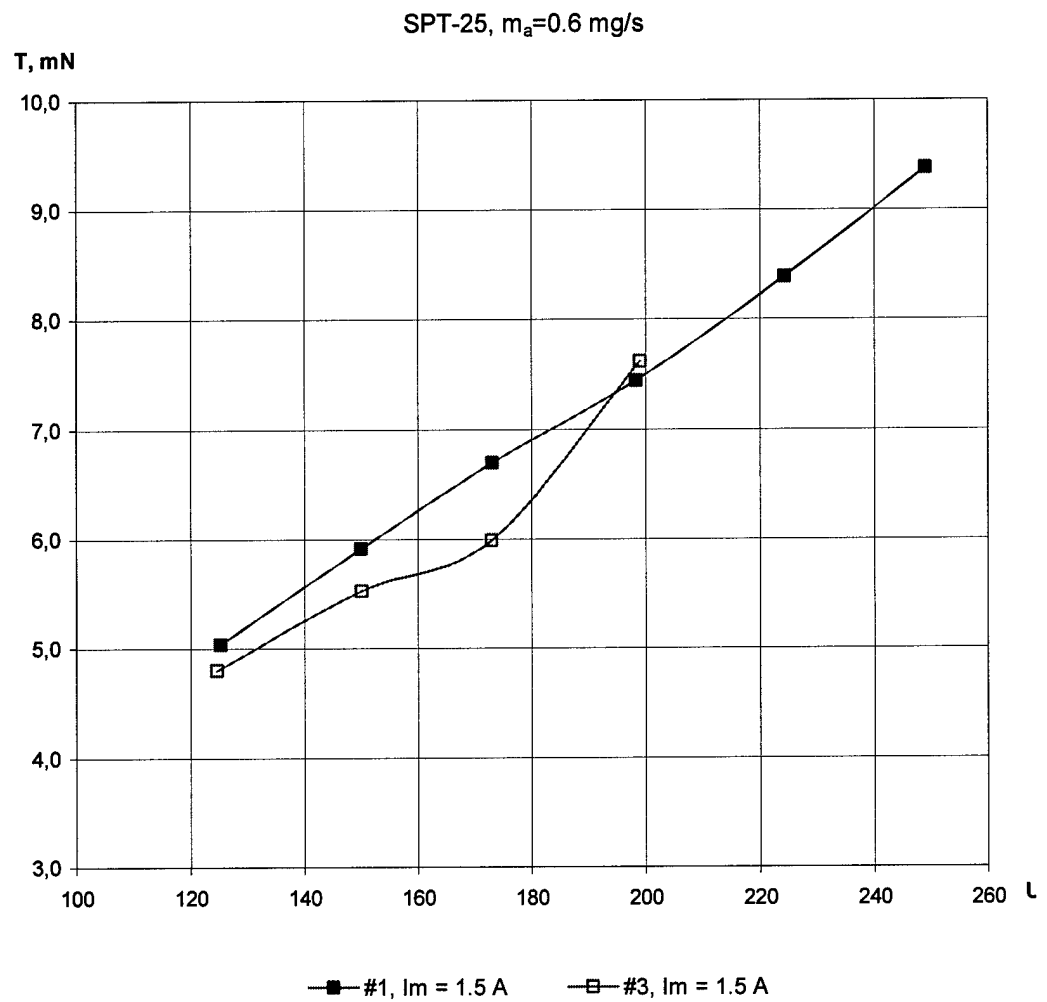


Fig.1.31. Thrust versus the discharge voltage

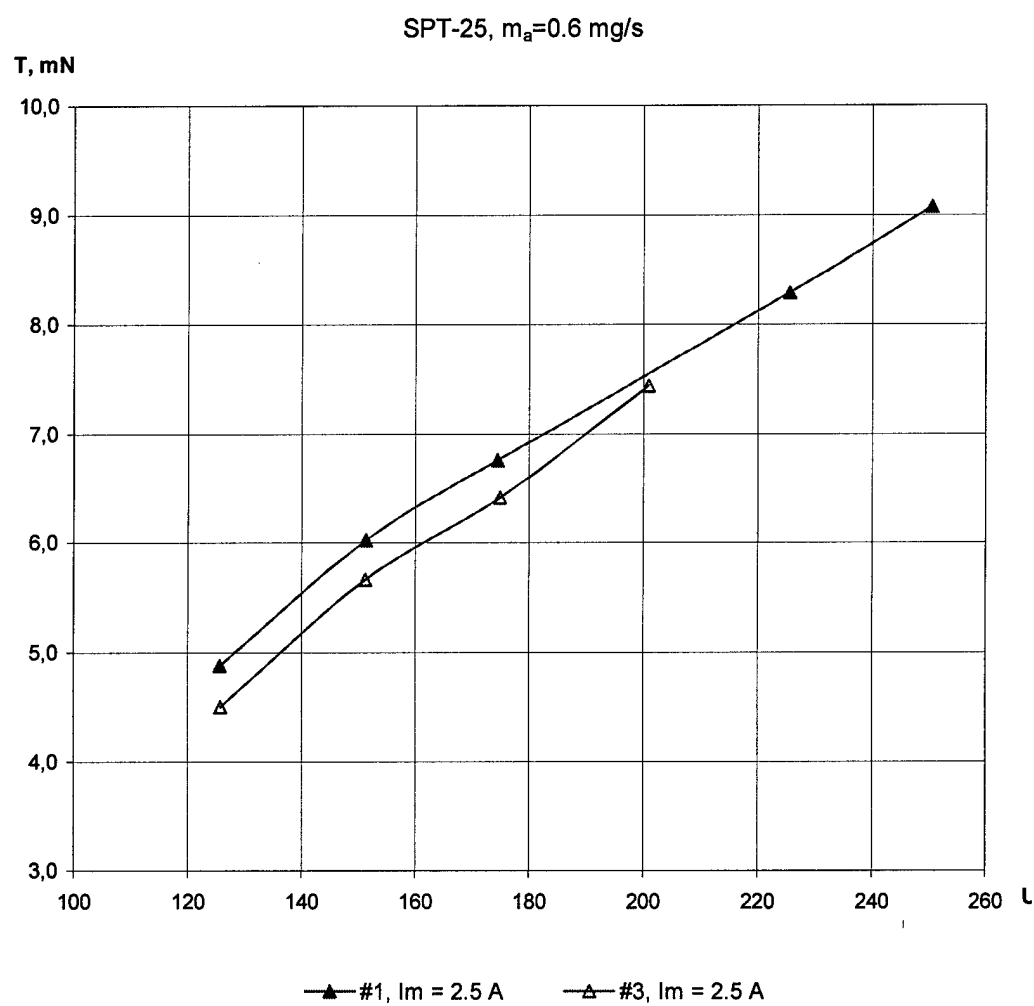


Fig.1.32. Thrust versus the discharge voltage

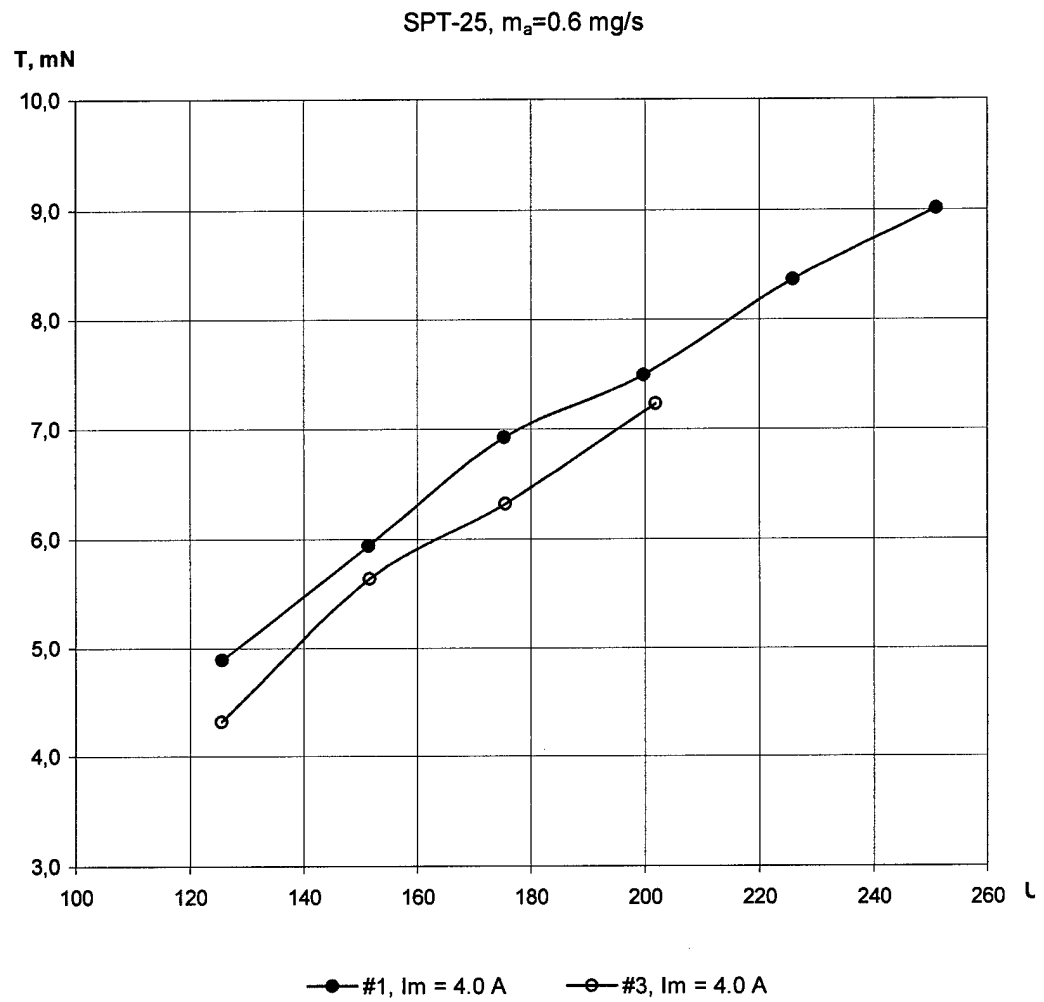


Fig.1.33. Thrust versus the discharge voltage

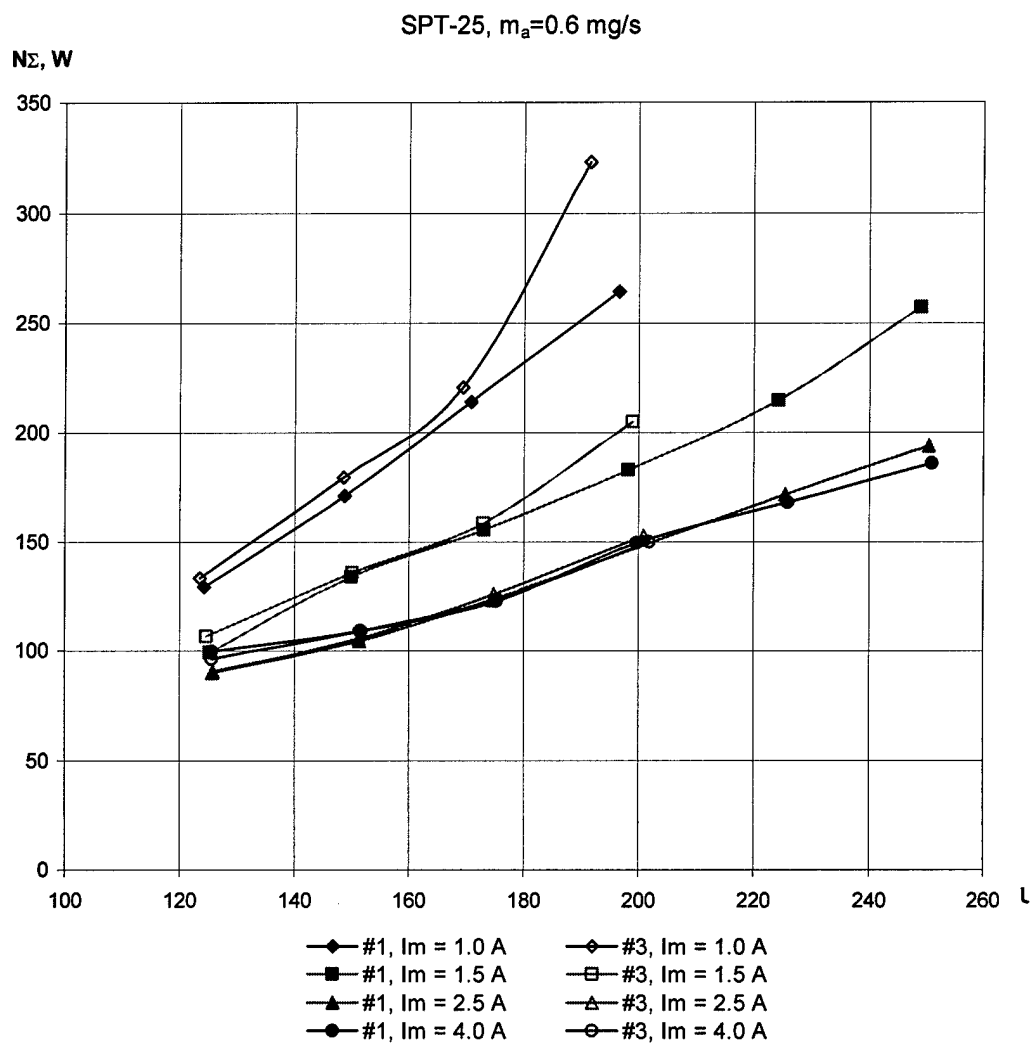


Fig.1.34. Discharge power versus the discharge voltage

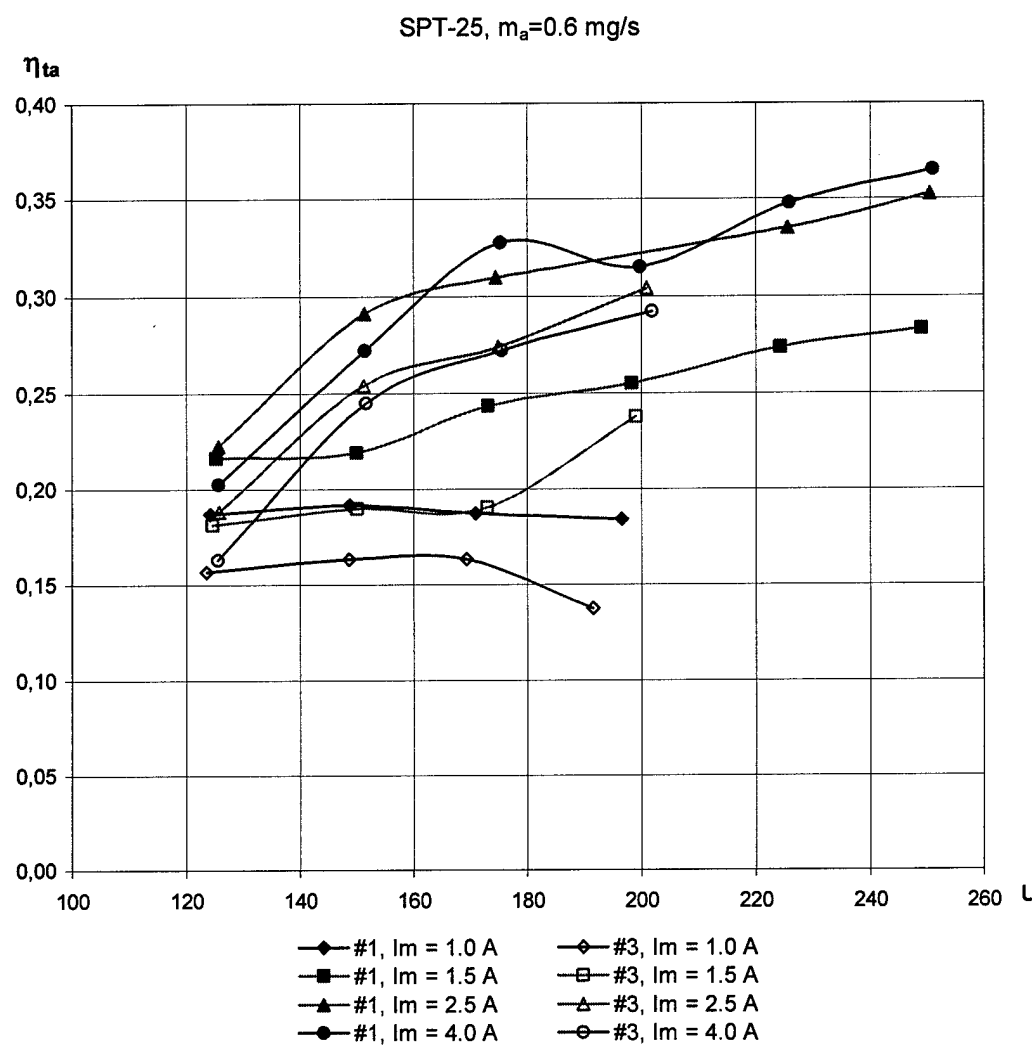


Fig.1.35. Thrust efficiency versus the discharge voltage

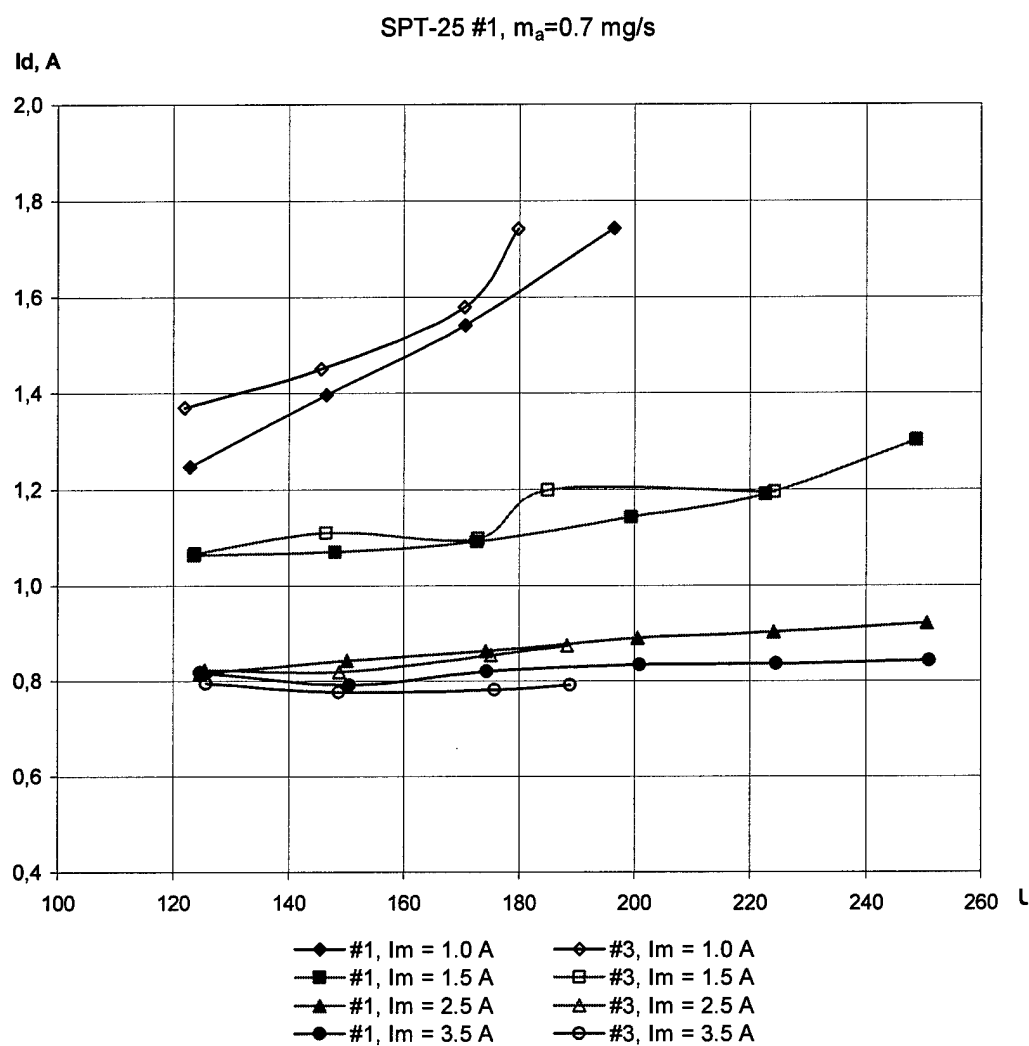


Fig.1.36. Discharge current versus the discharge voltage

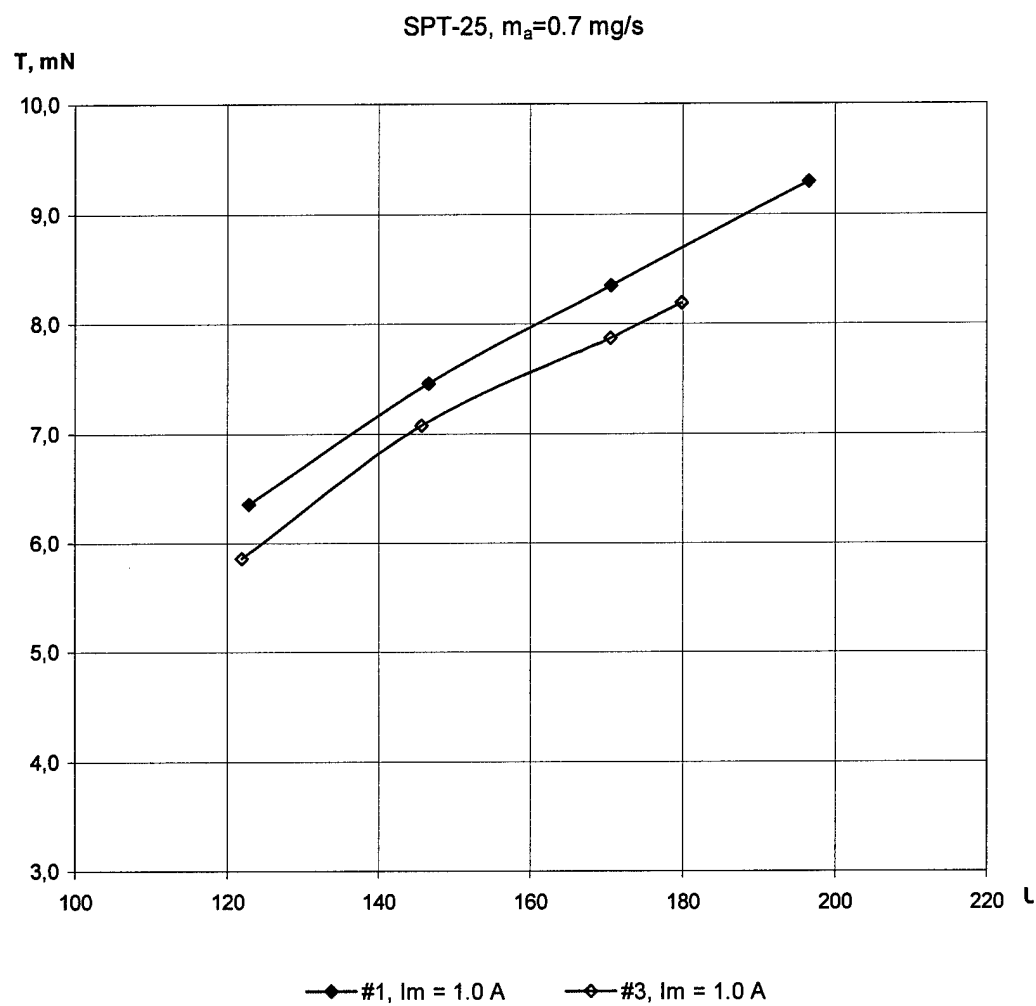


Fig.1.37. Thrust versus the discharge voltage

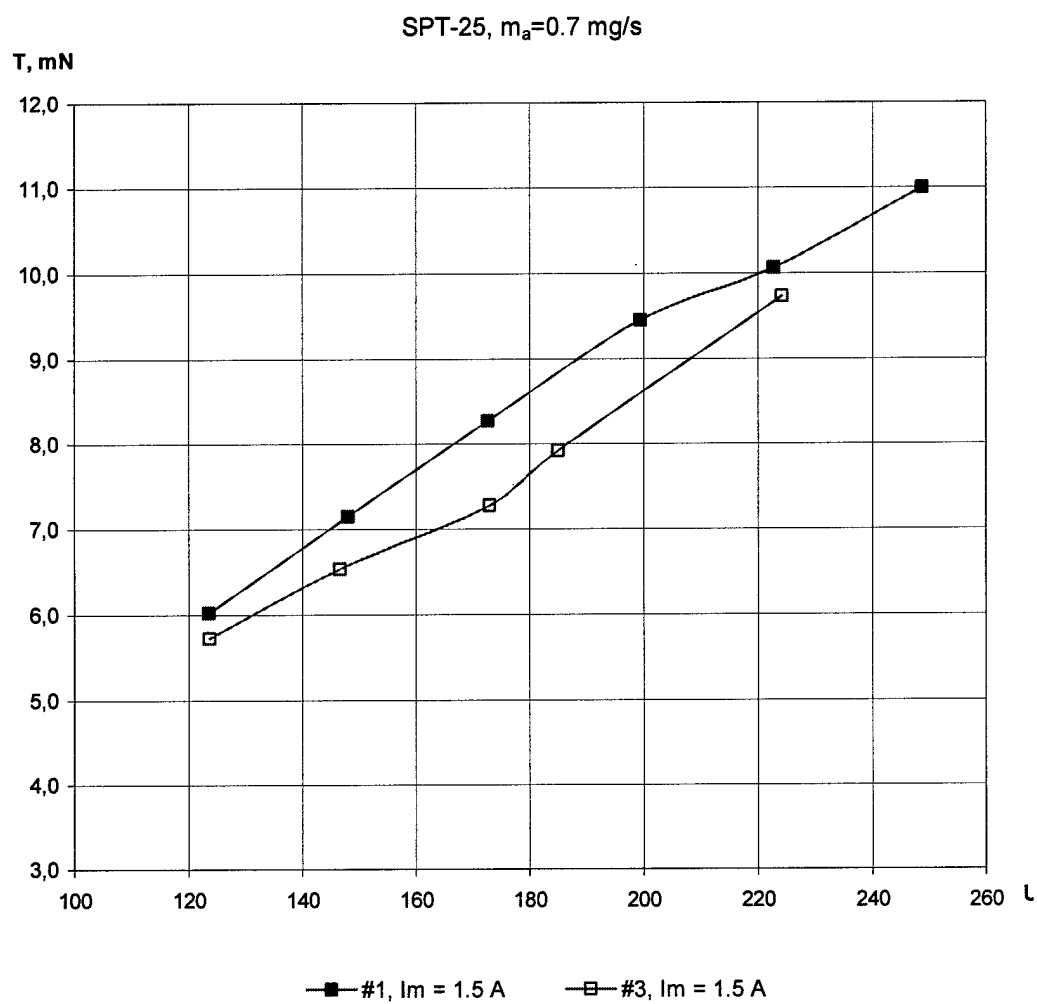


Fig.1.38. Thrust versus the discharge voltage

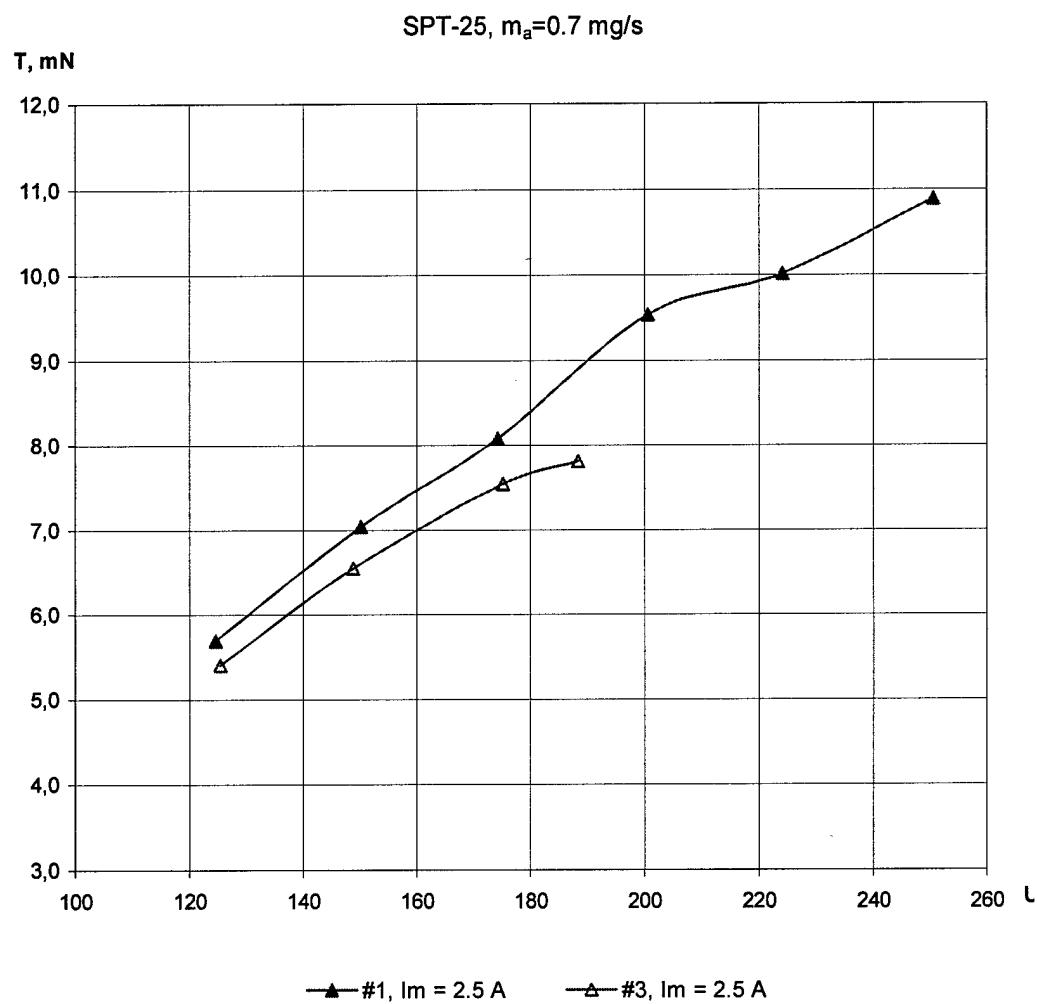


Fig.1.39. Thrust versus the discharge voltage

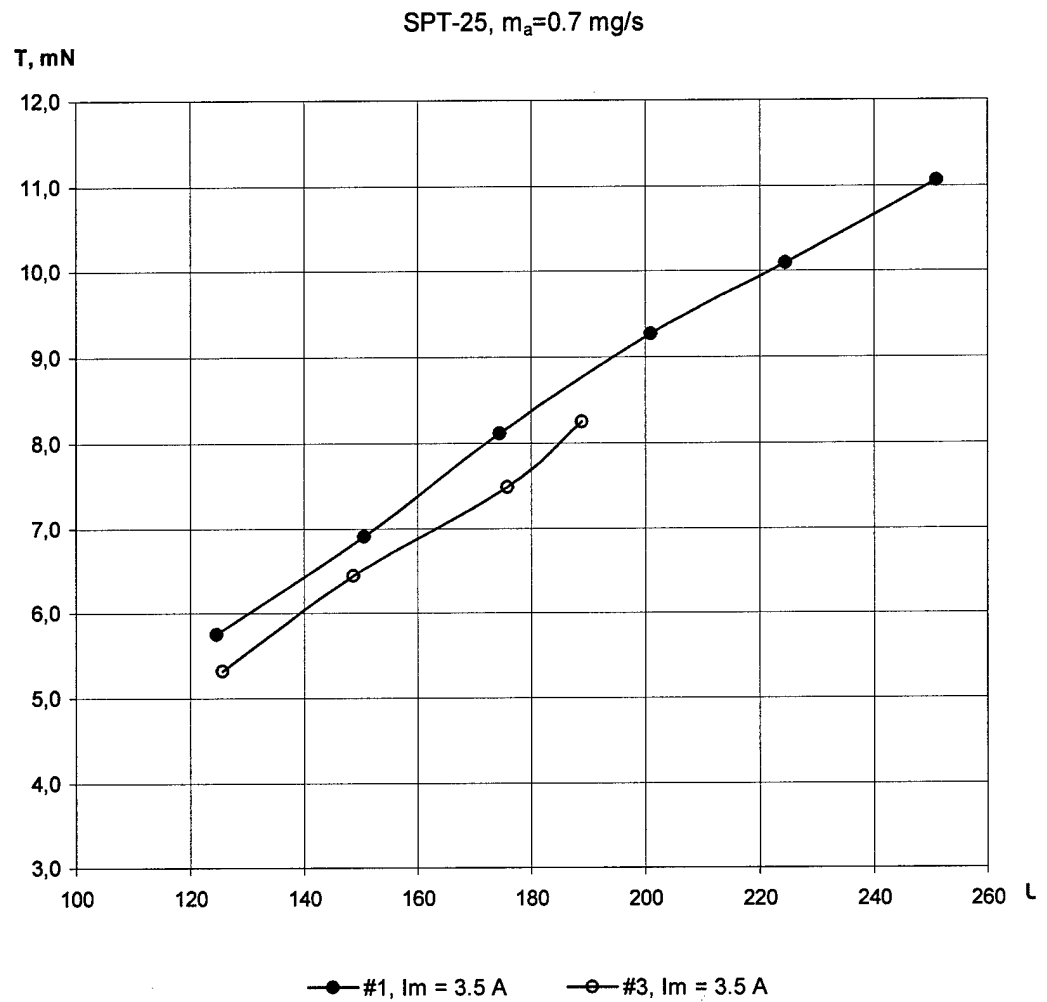


Fig.1.40. Thrust versus the discharge voltage

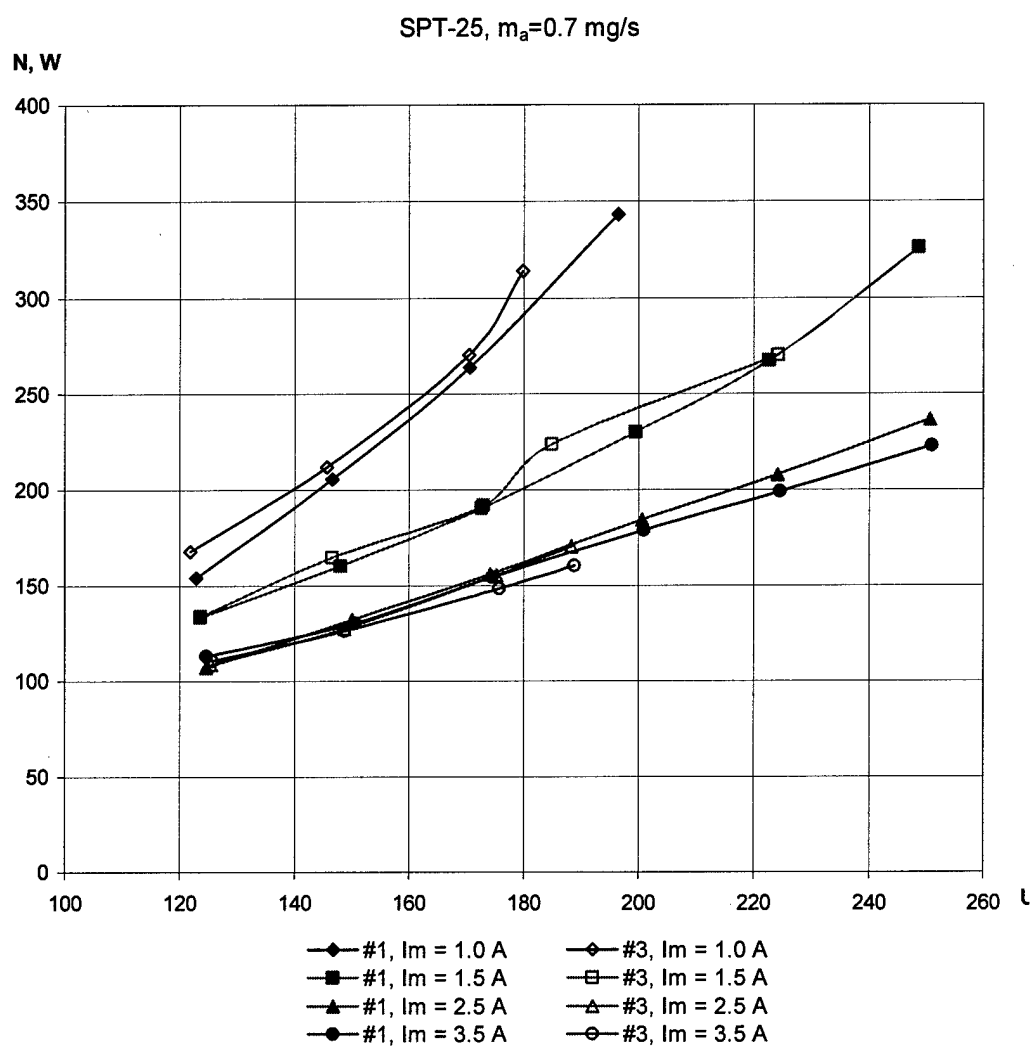


Fig.1.41. Discharge power versus the discharge voltage

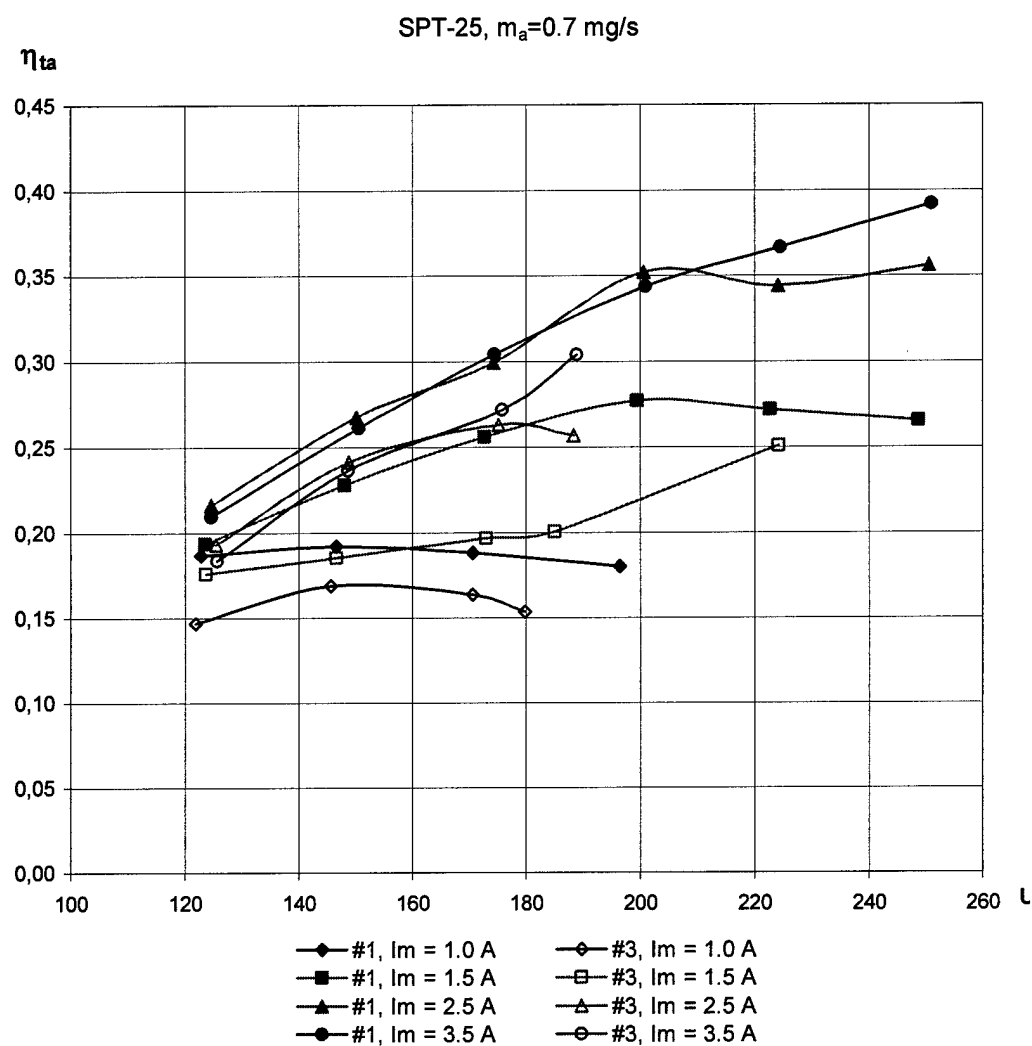


Fig.1.42. Thrust efficiency versus the discharge voltage

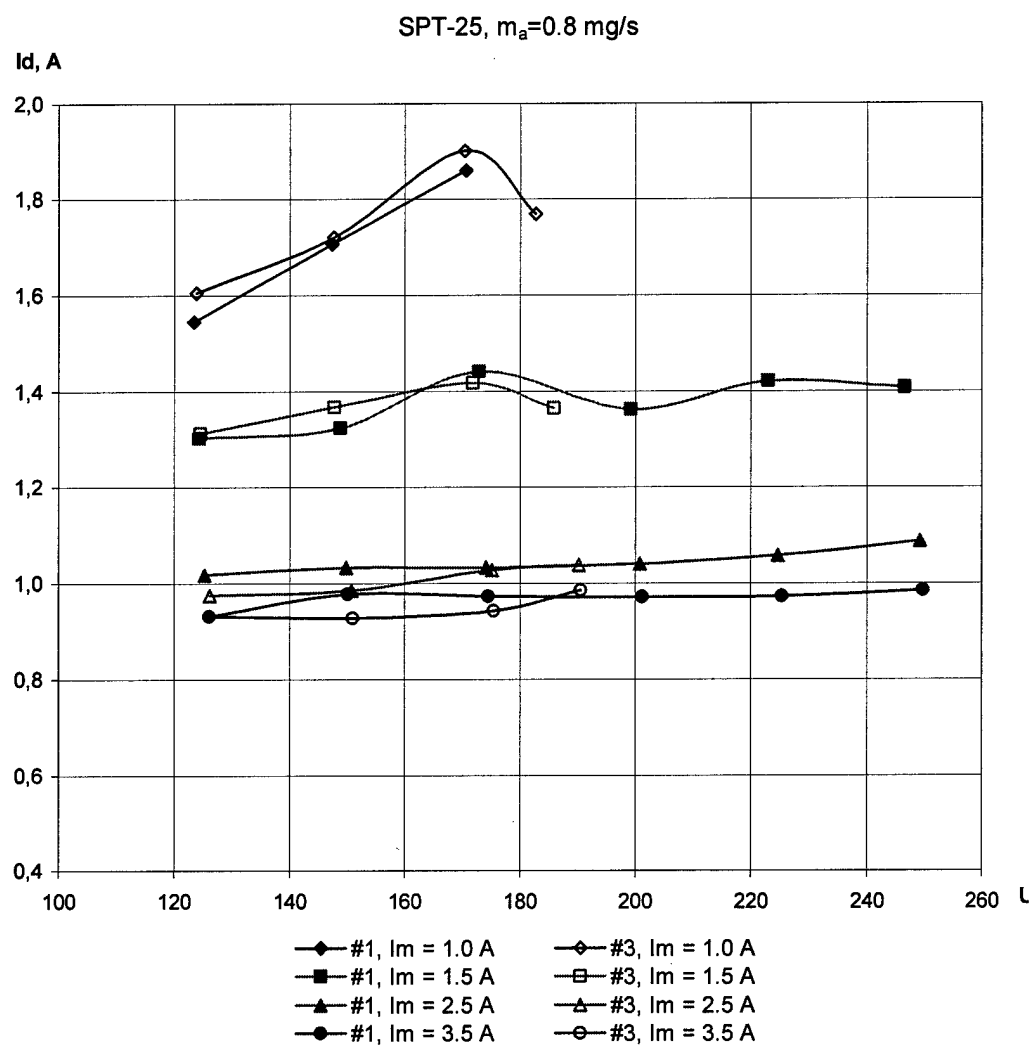


Fig.1.43. Discharge current versus the discharge voltage

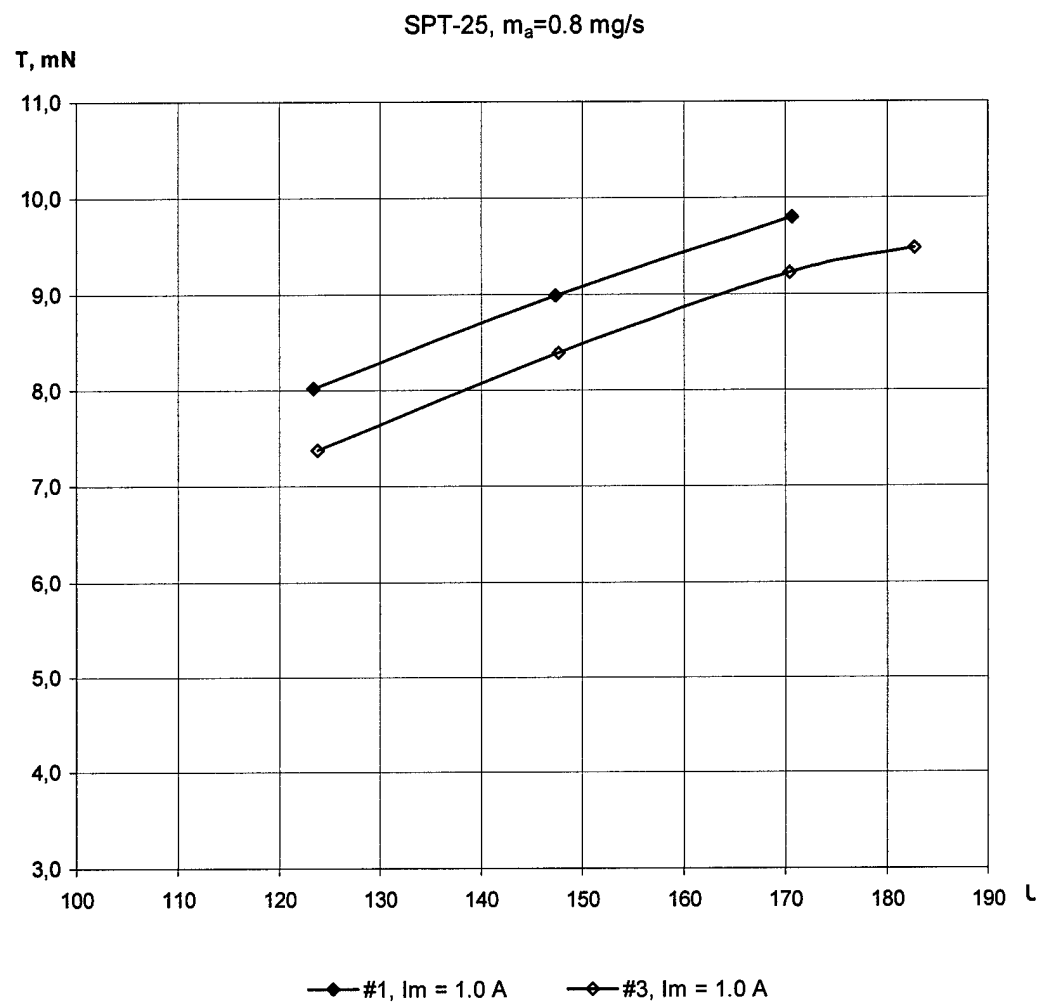


Fig.1.44. Thrust versus the discharge voltage

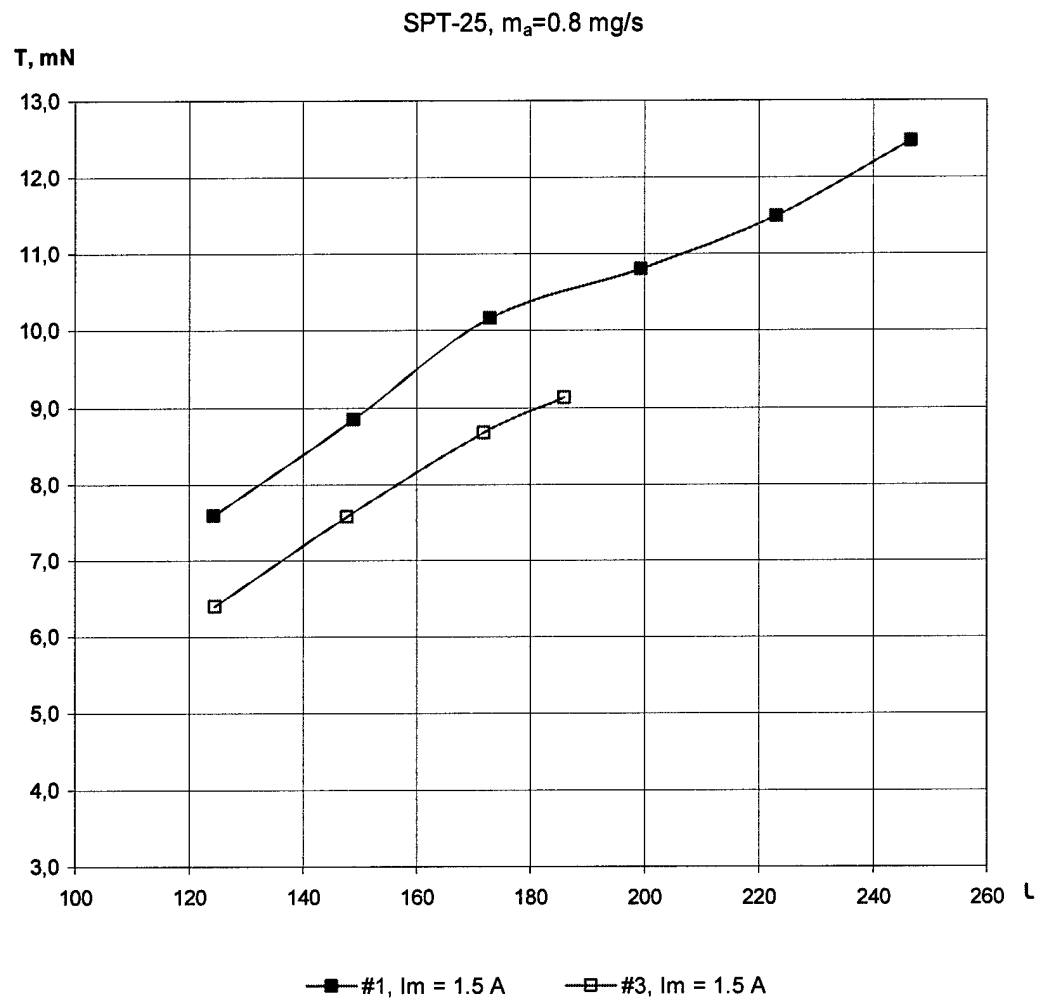


Fig.1.45. Thrust versus the discharge voltage

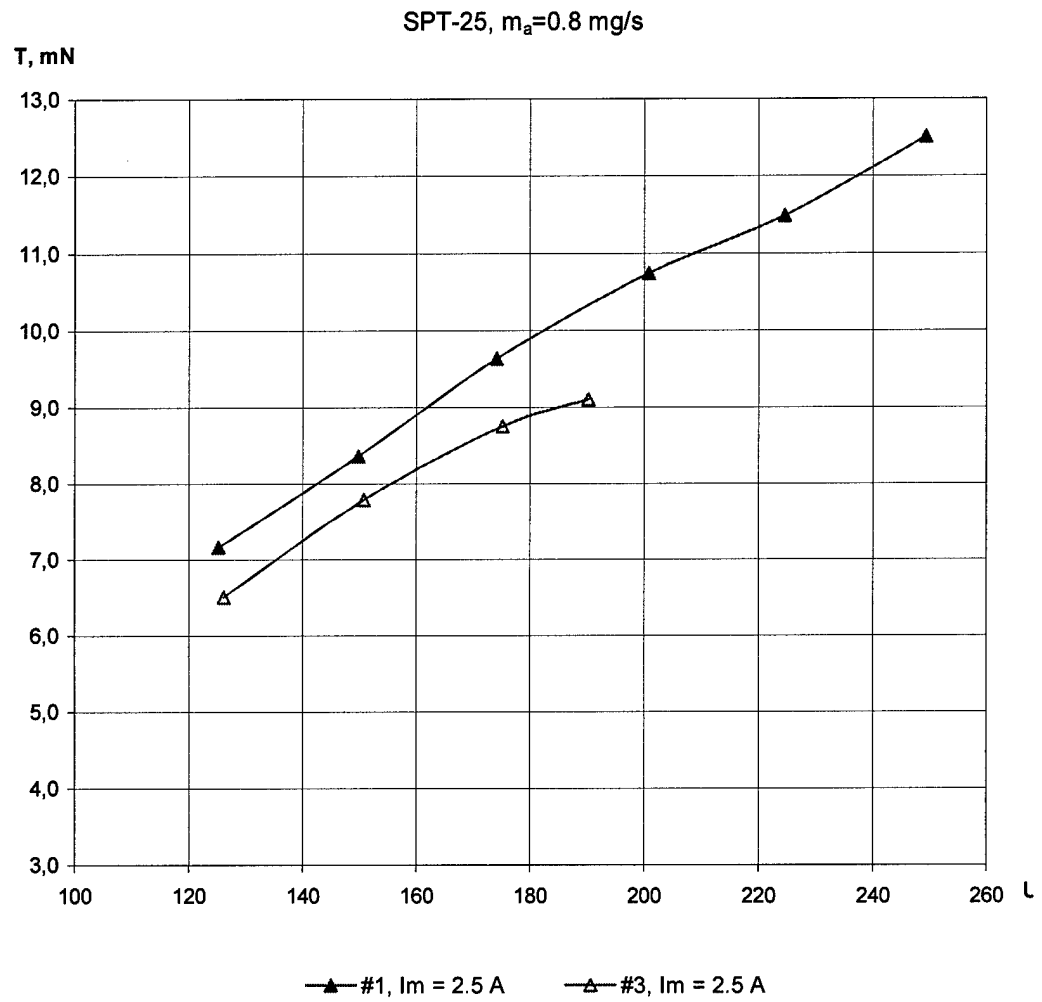


Fig.1.46. Thrust versus the discharge voltage

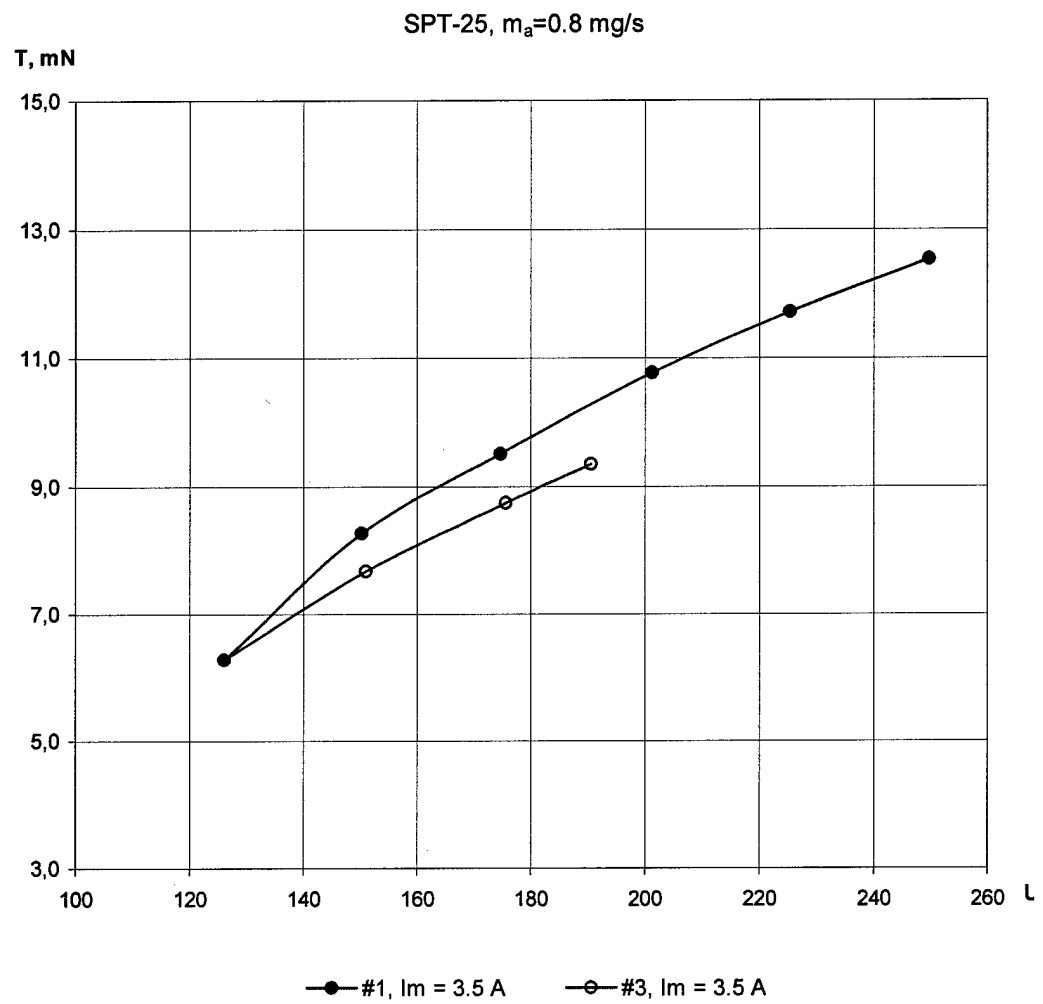


Fig.1.47. Thrust versus the discharge voltage

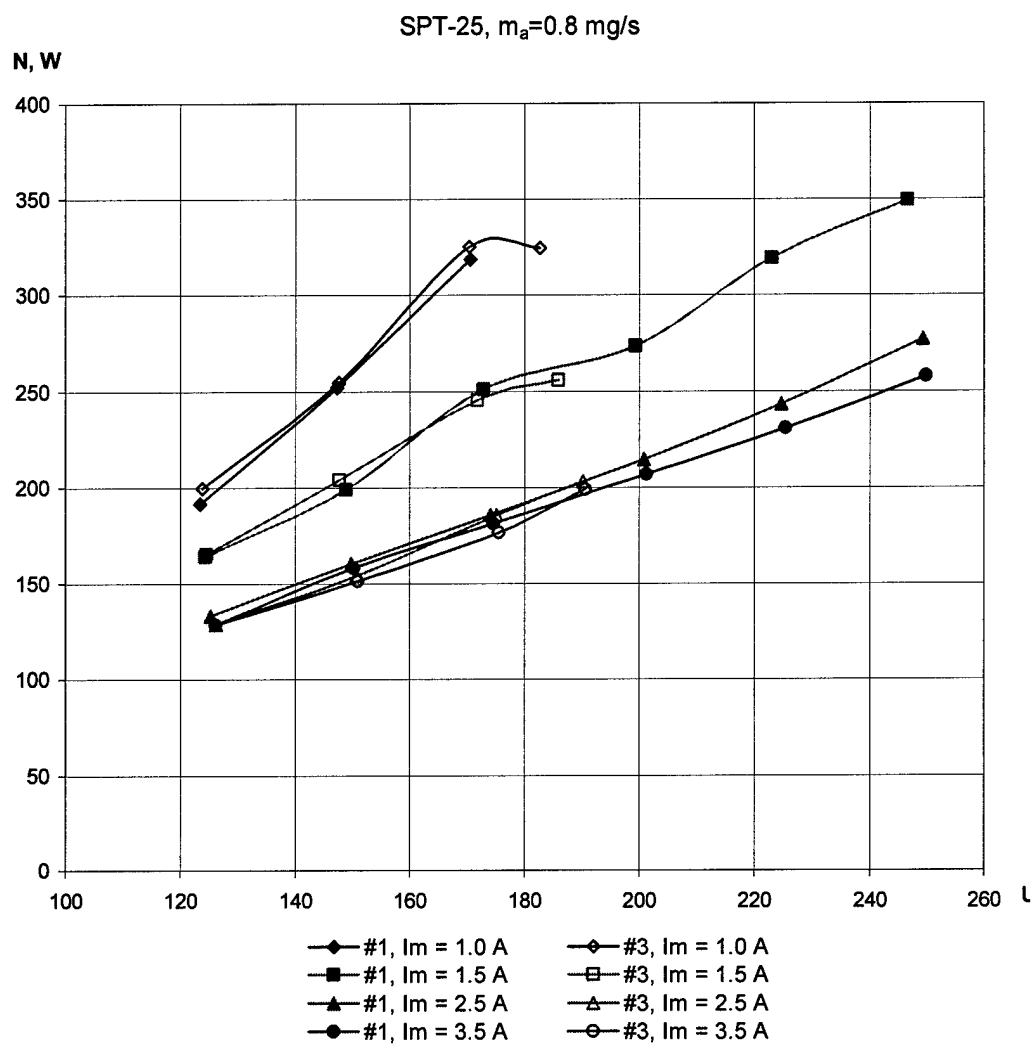


Fig.1.48. Discharge power versus the discharge voltage

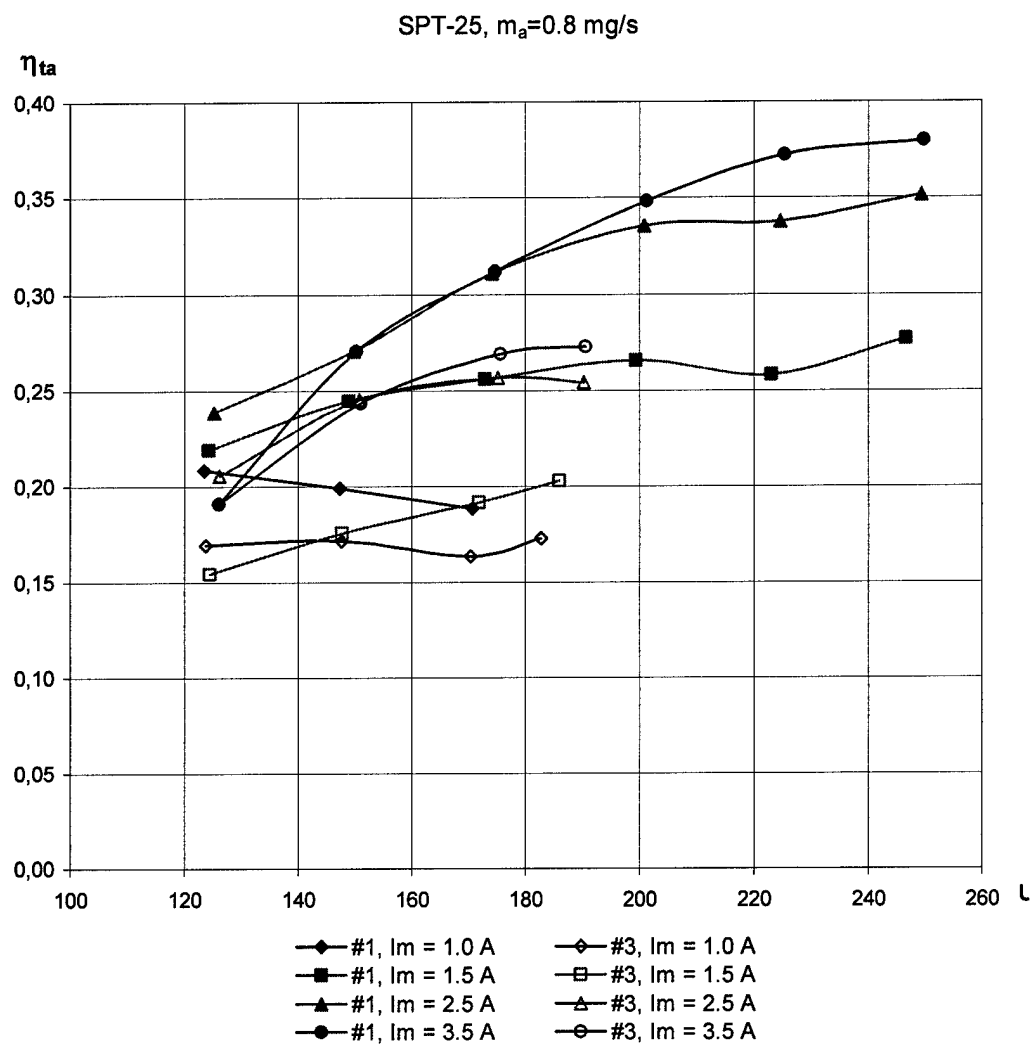


Fig.1.49. Thrust efficiency versus the discharge voltage

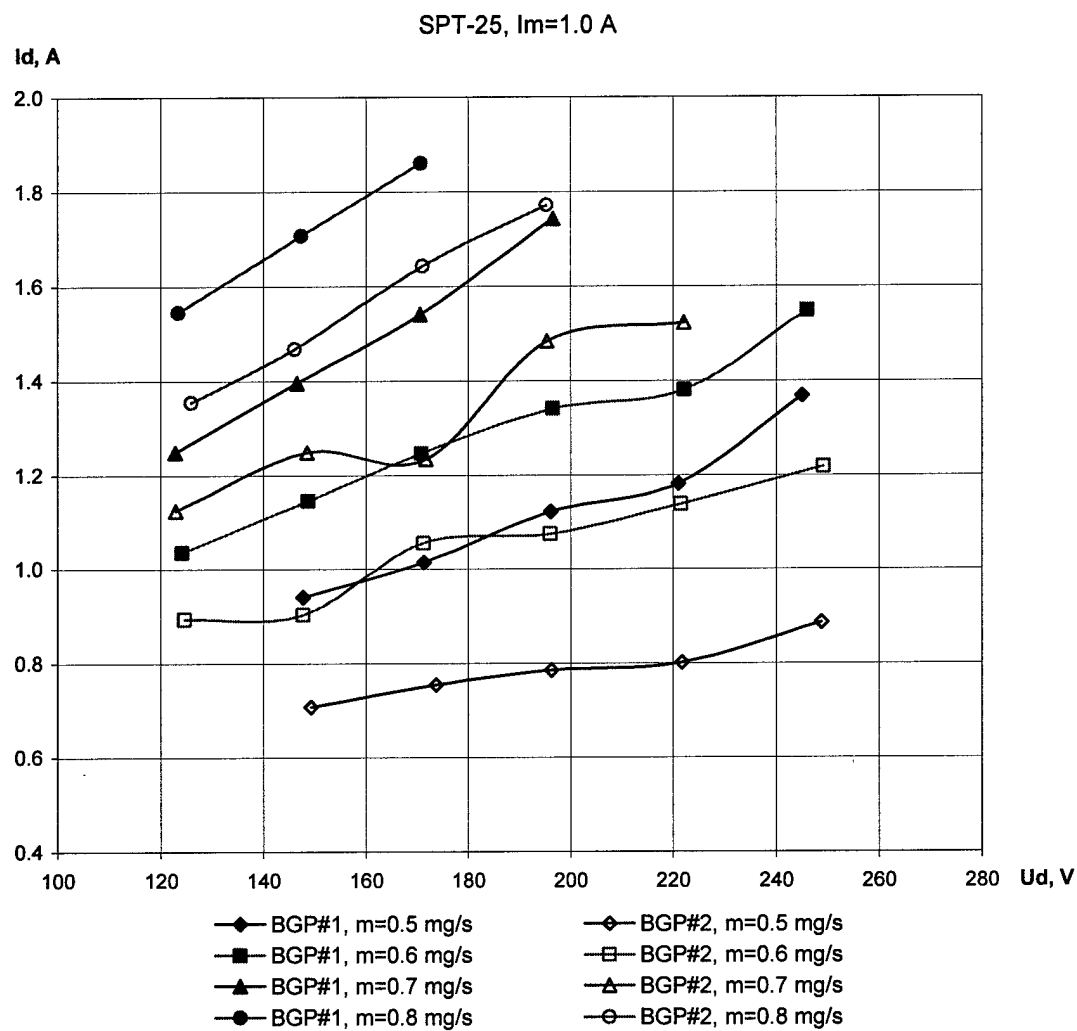


Fig.1.50. Voltage-current characteristics with cathode #1 and cathode #2.

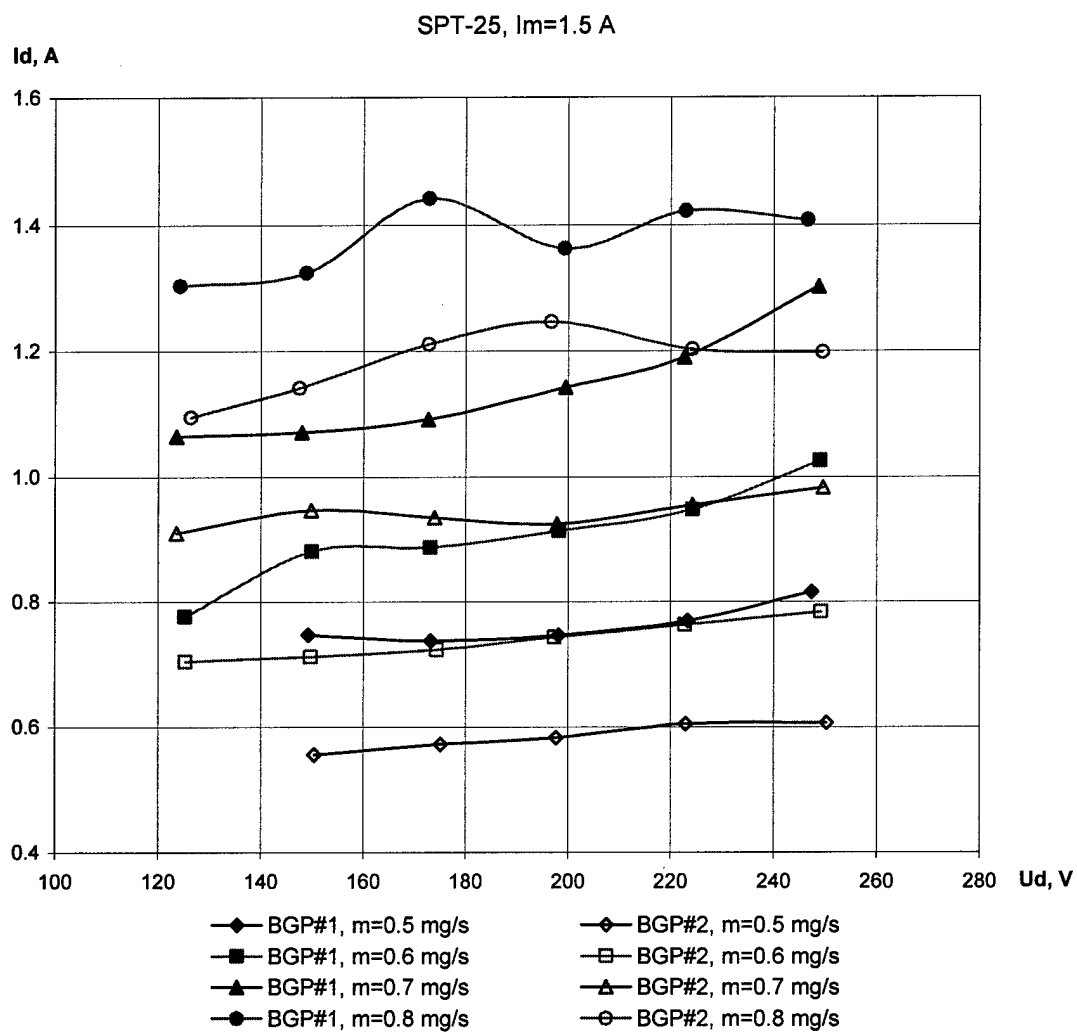


Fig.1.51. Voltage-current characteristics with cathode #1 and cathode #2.

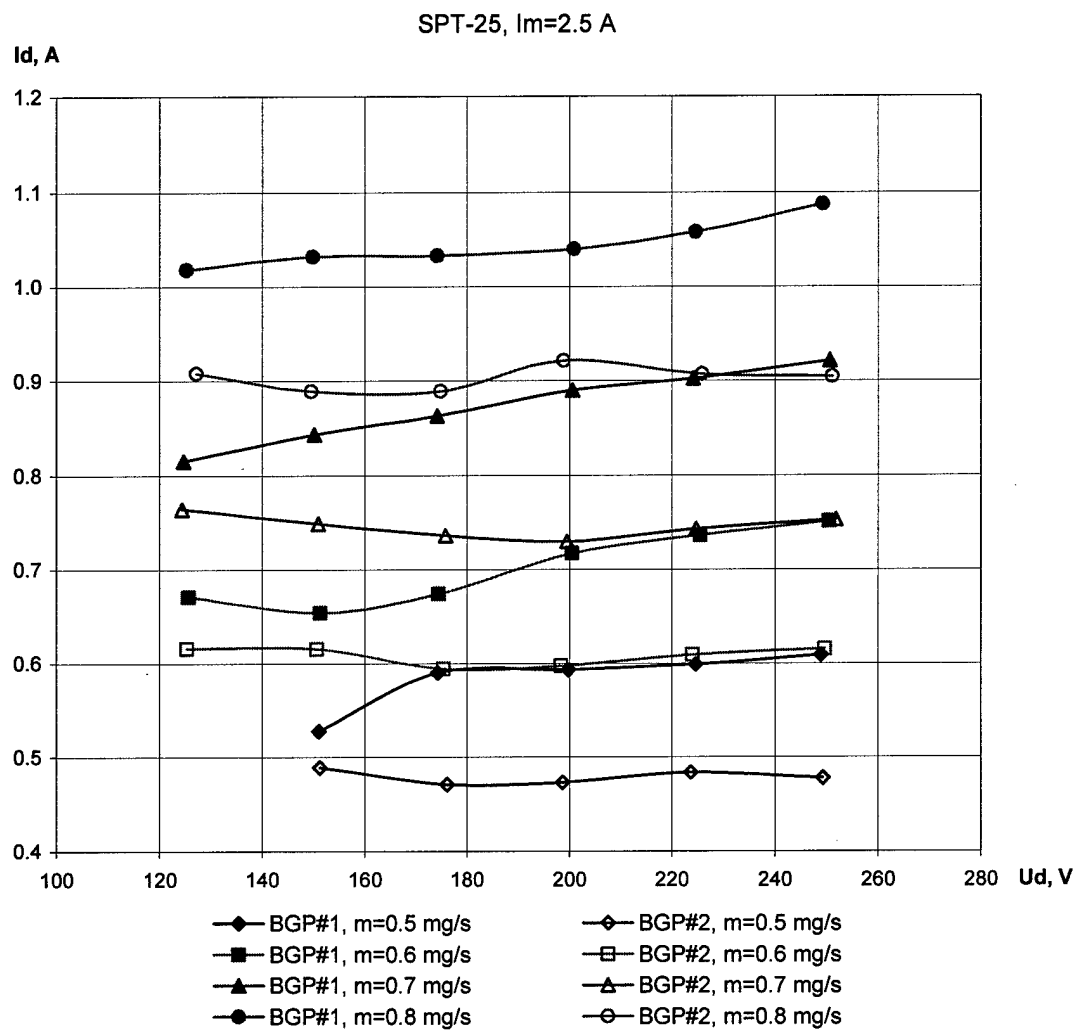


Fig.1.52. Voltage-current characteristics with cathode #1 and cathode #2.

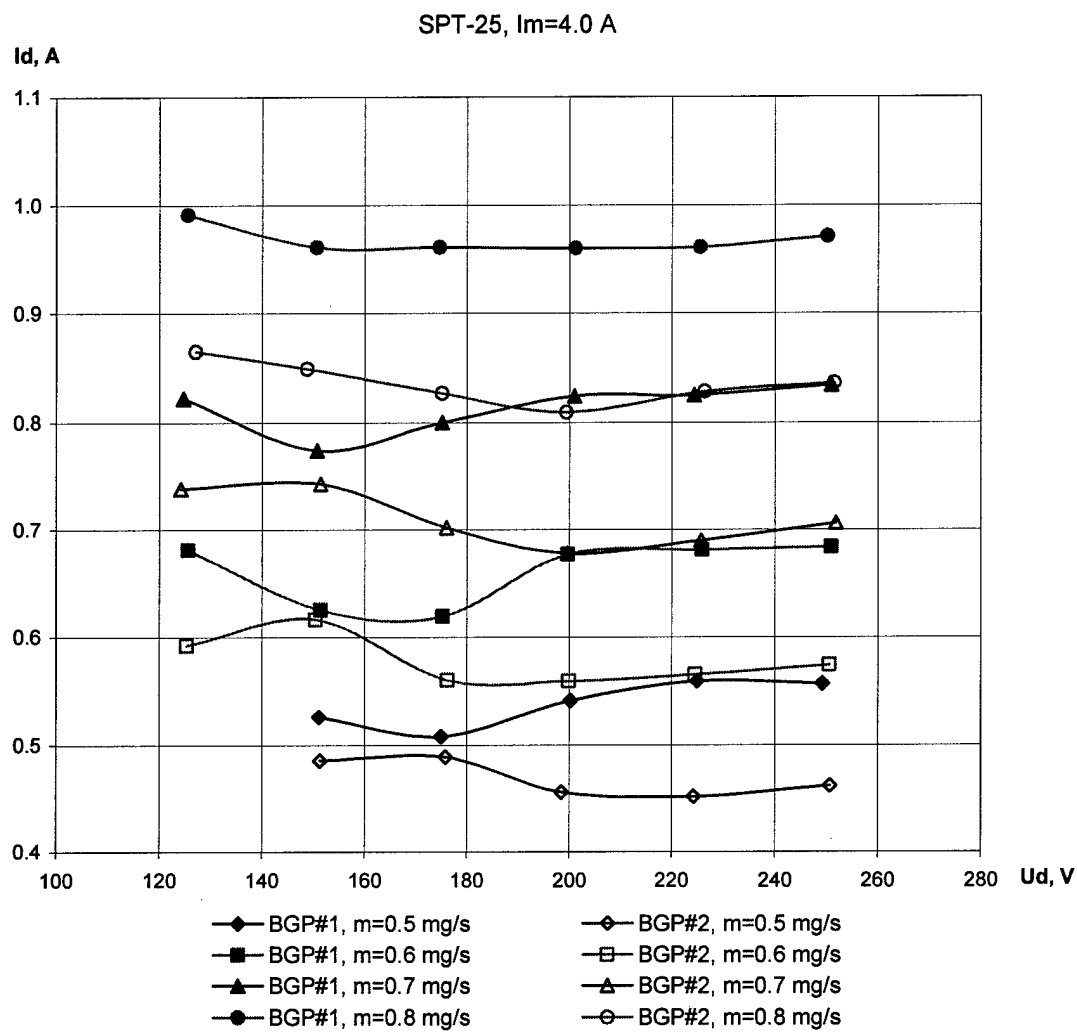


Fig.1.53. Voltage-current characteristics with cathode #1 and cathode #2.

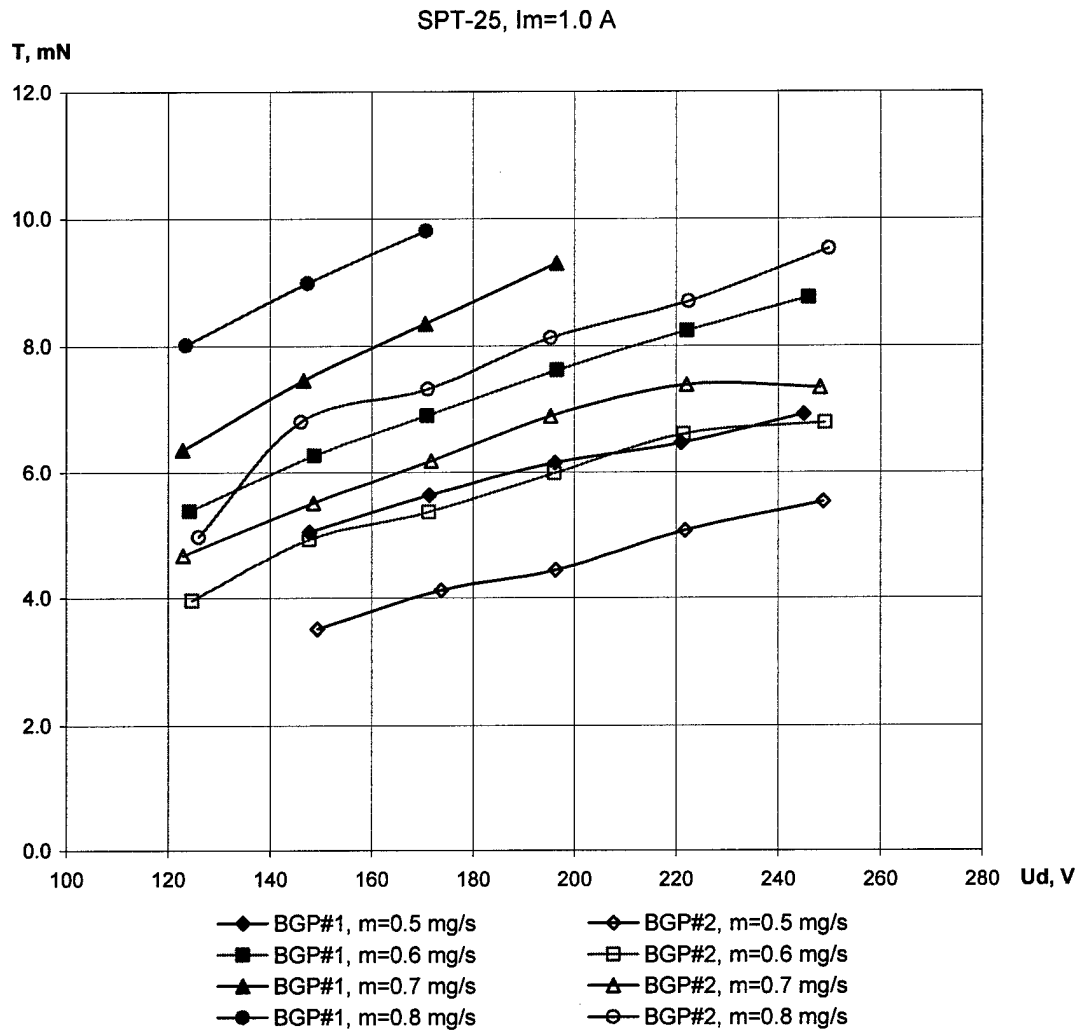


Fig.1.54. Thrust versus the discharge voltage with cathode #1 and cathode #2.

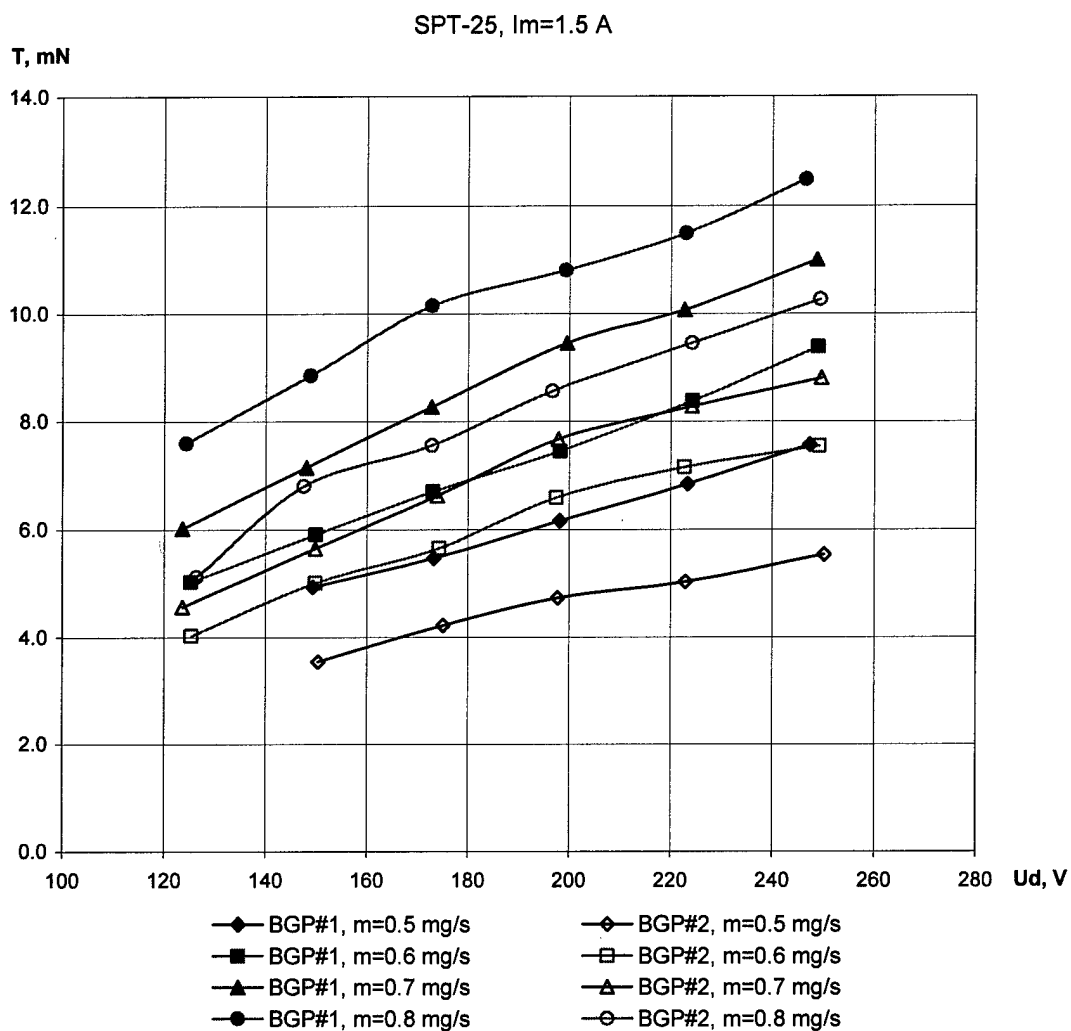


Fig.1.55. Thrust versus the discharge voltage with cathode #1 and cathode #2.

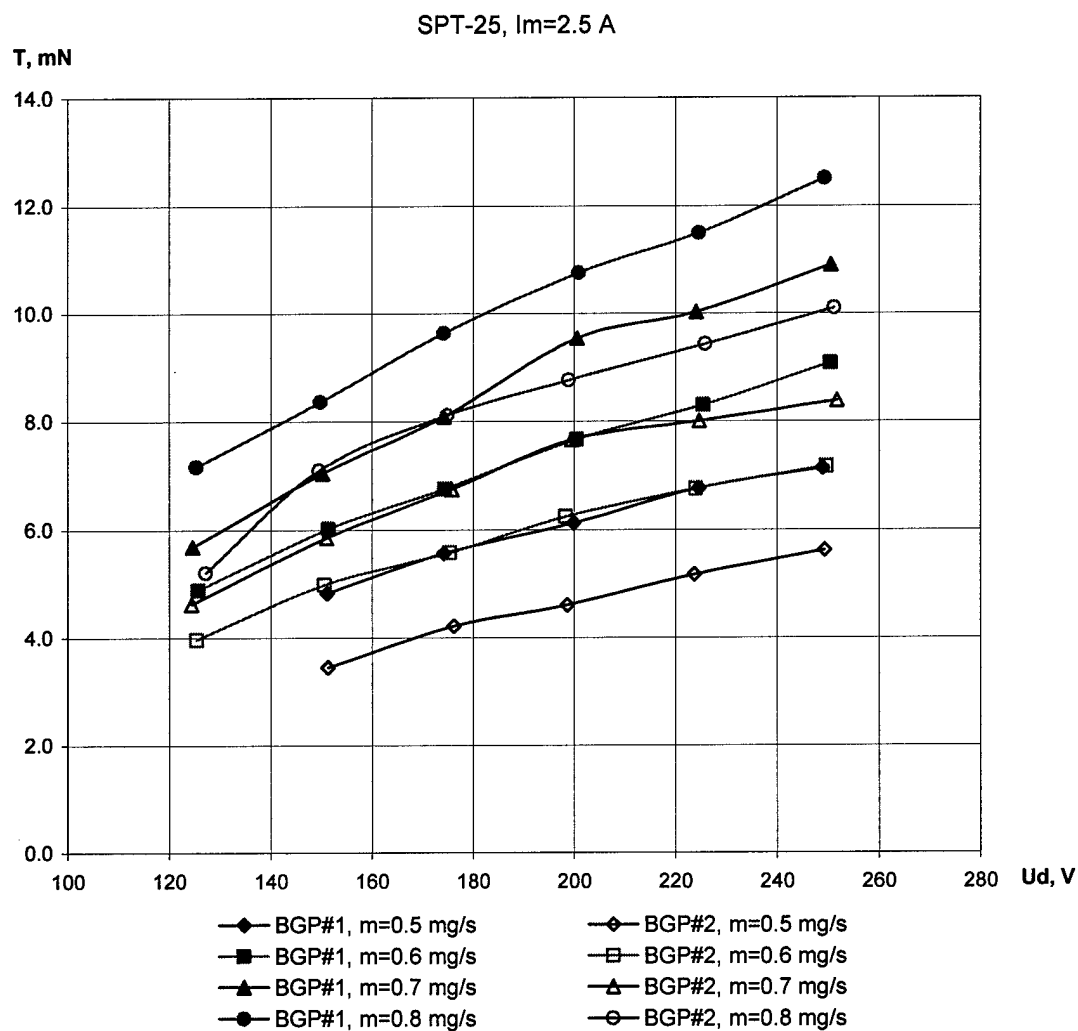


Fig.1.56. Thrust versus the discharge voltage with cathode #1 and cathode #2.

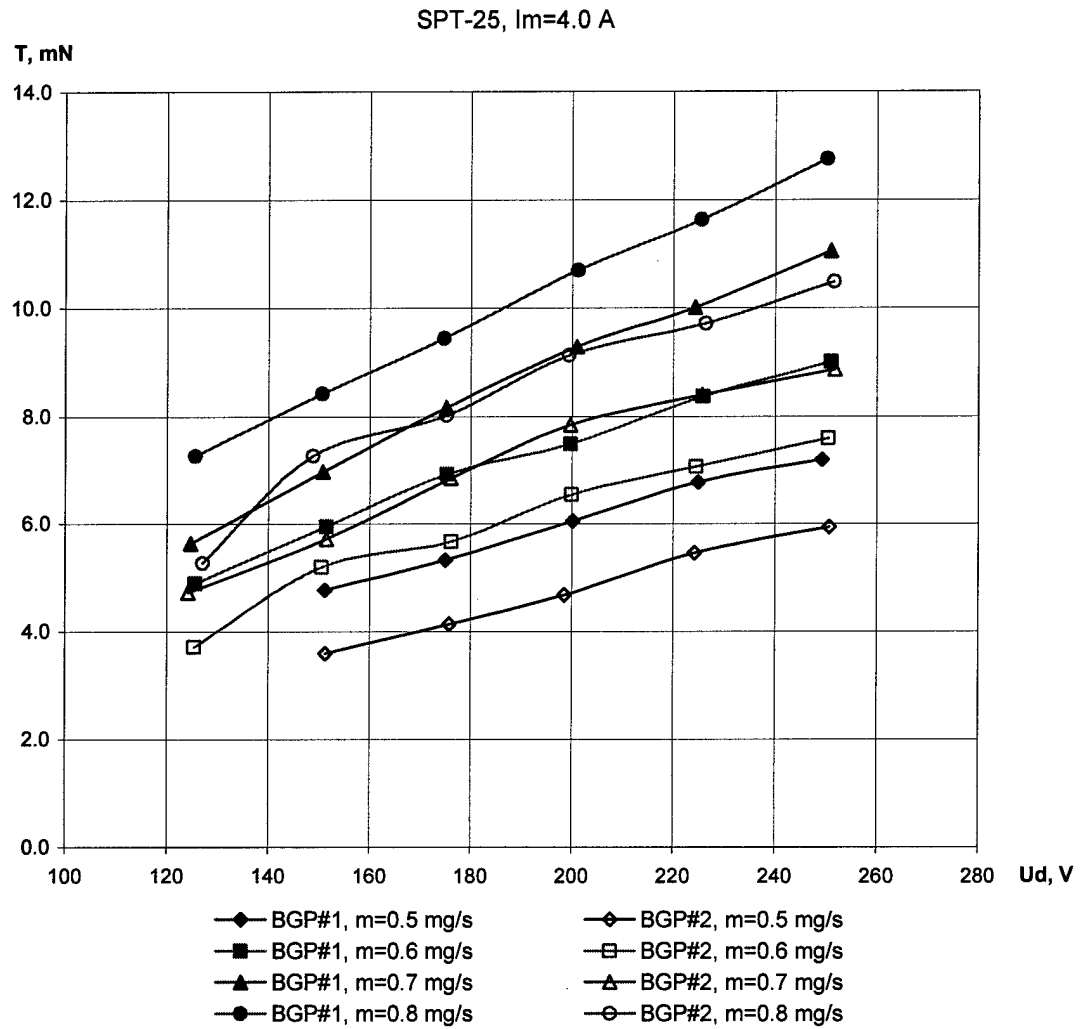


Fig.1.57. Thrust versus the discharge voltage with cathode #1 and cathode #2.

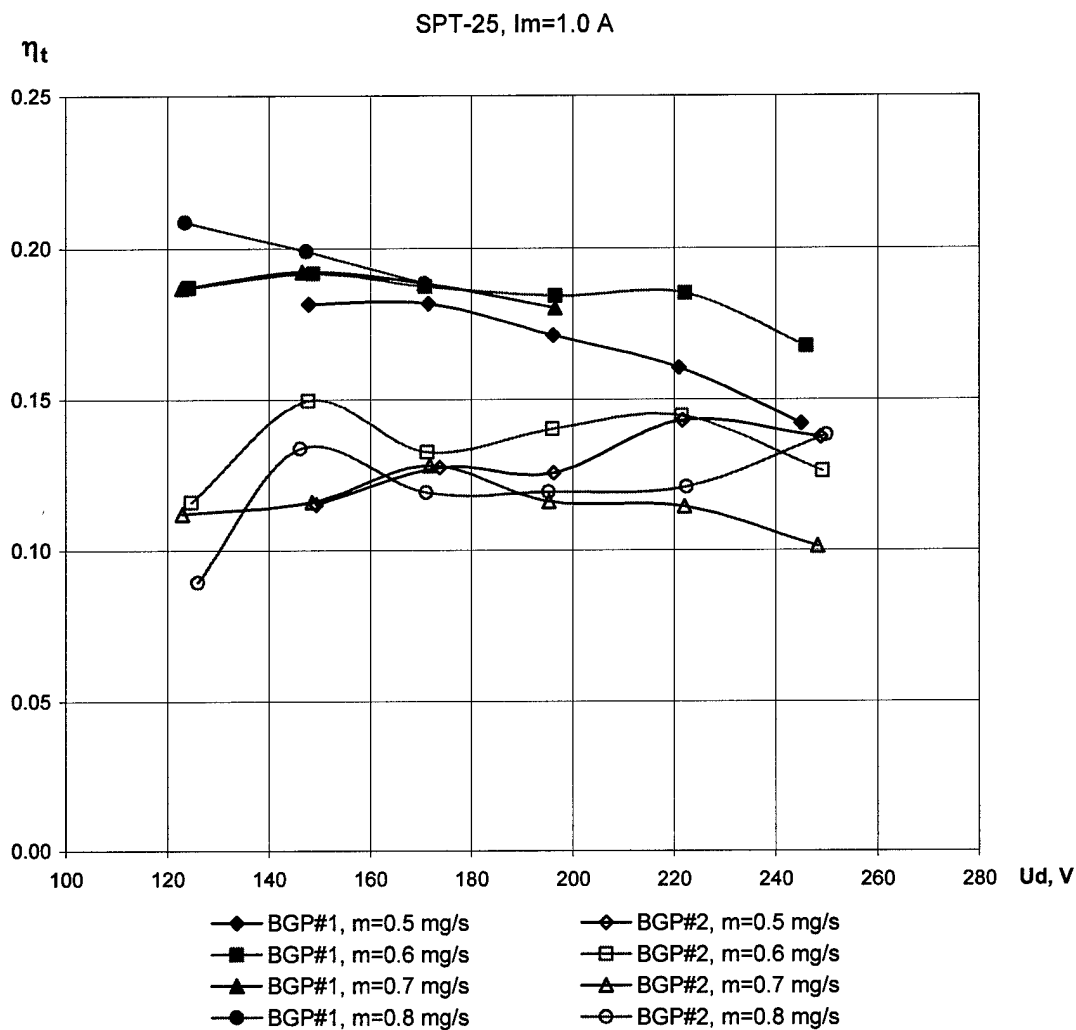


Fig.1.58. Thrust efficiency versus the discharge voltage with cathode #1 and cathode #2.

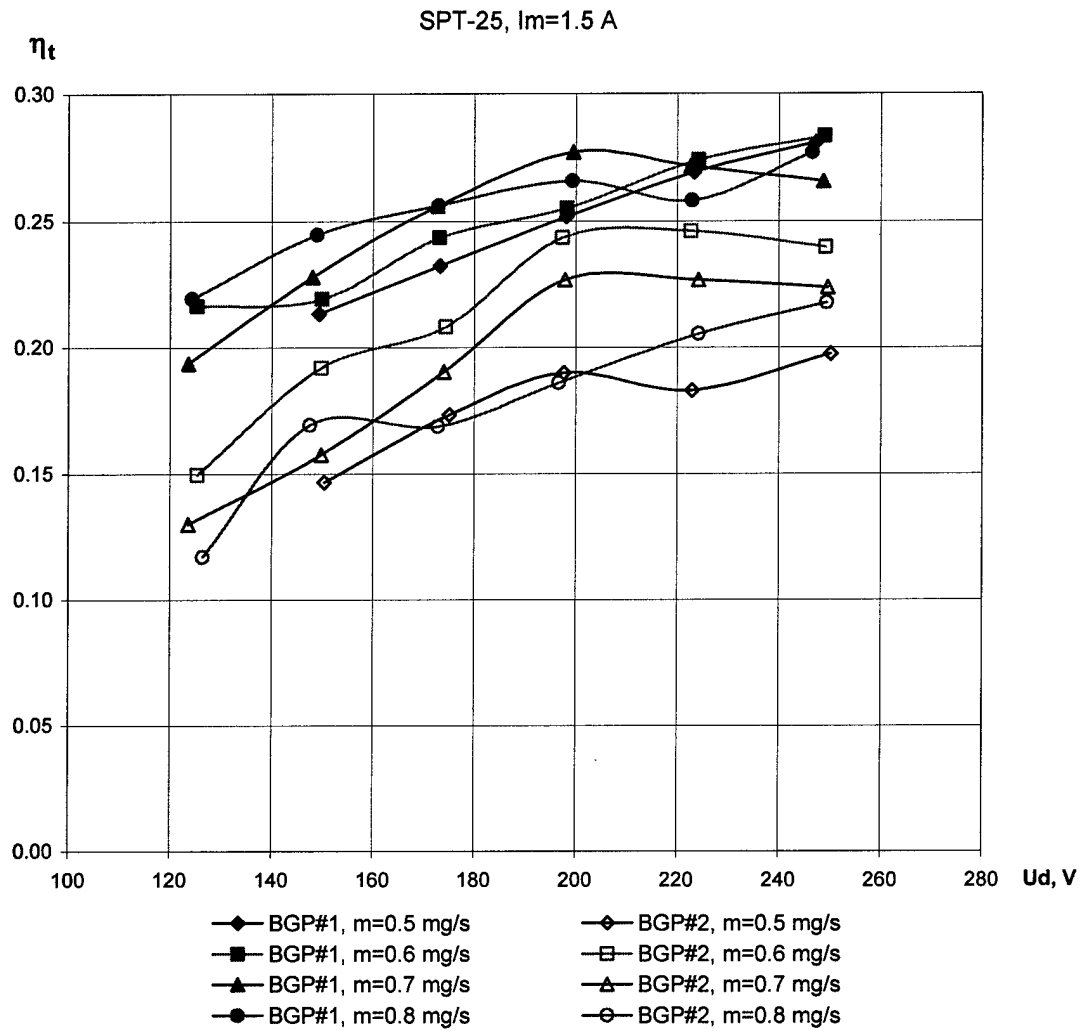


Fig.1.59. Thrust efficiency versus the discharge voltage with cathode #1 and cathode #2.

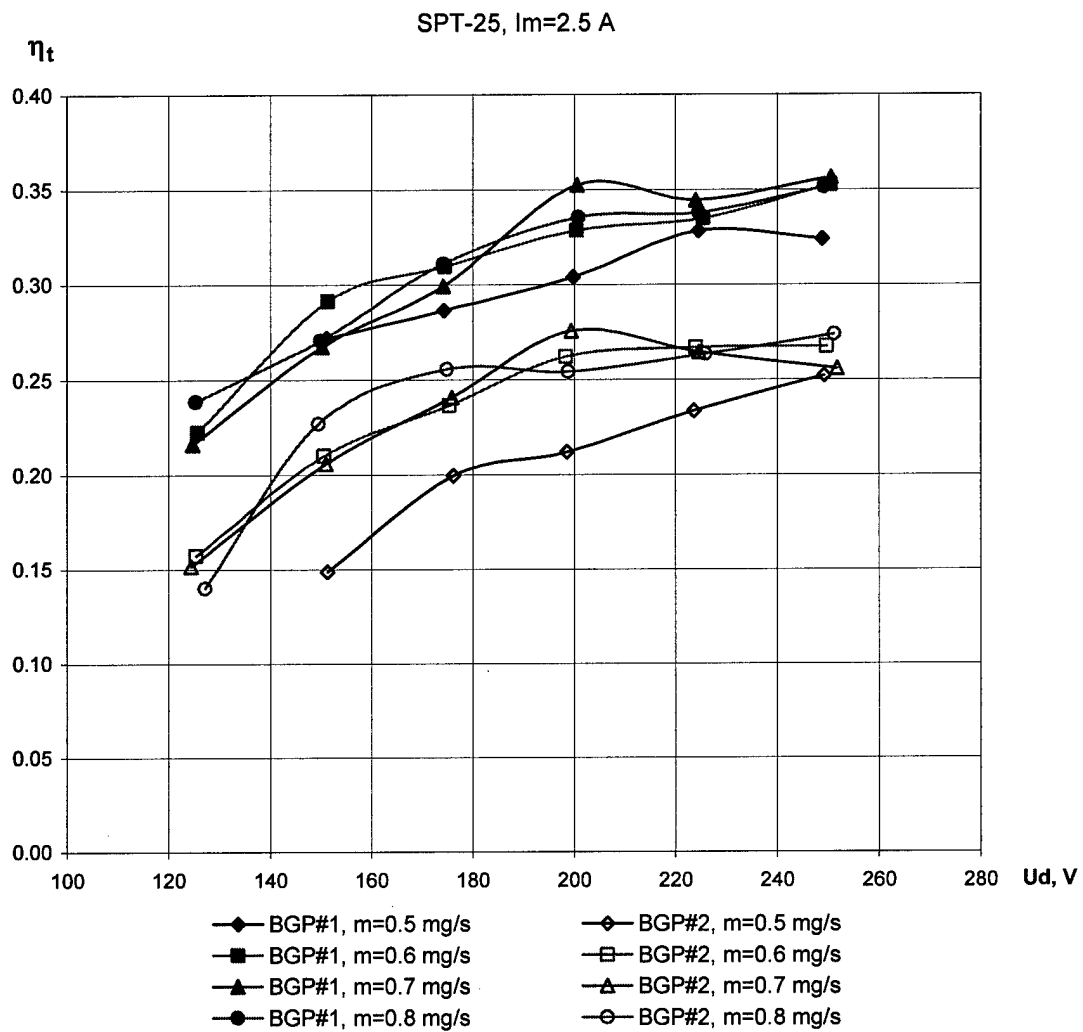


Fig.1.60. Thrust efficiency versus the discharge voltage with cathode #1 and cathode #2.

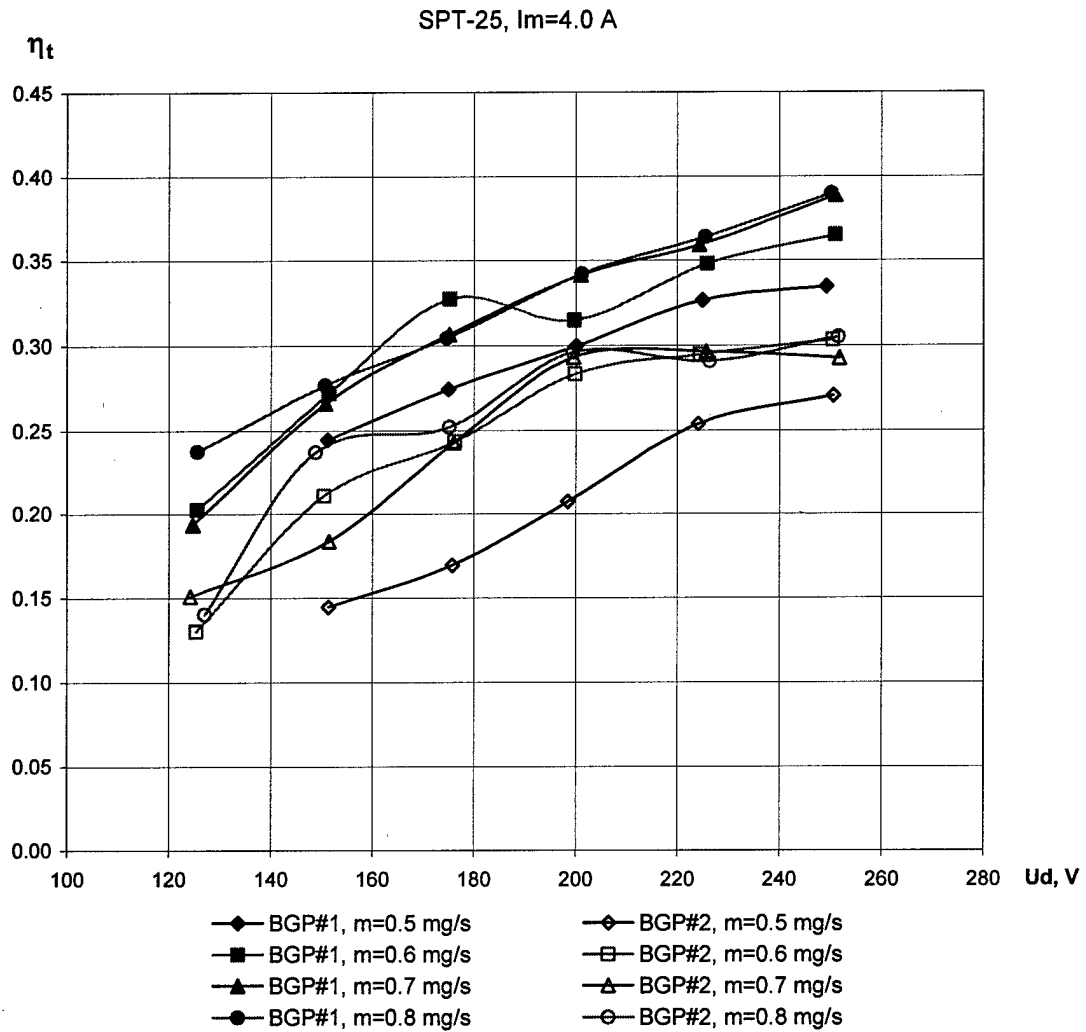


Fig.1.61. Thrust efficiency versus the discharge voltage with cathode #1 and cathode #2.

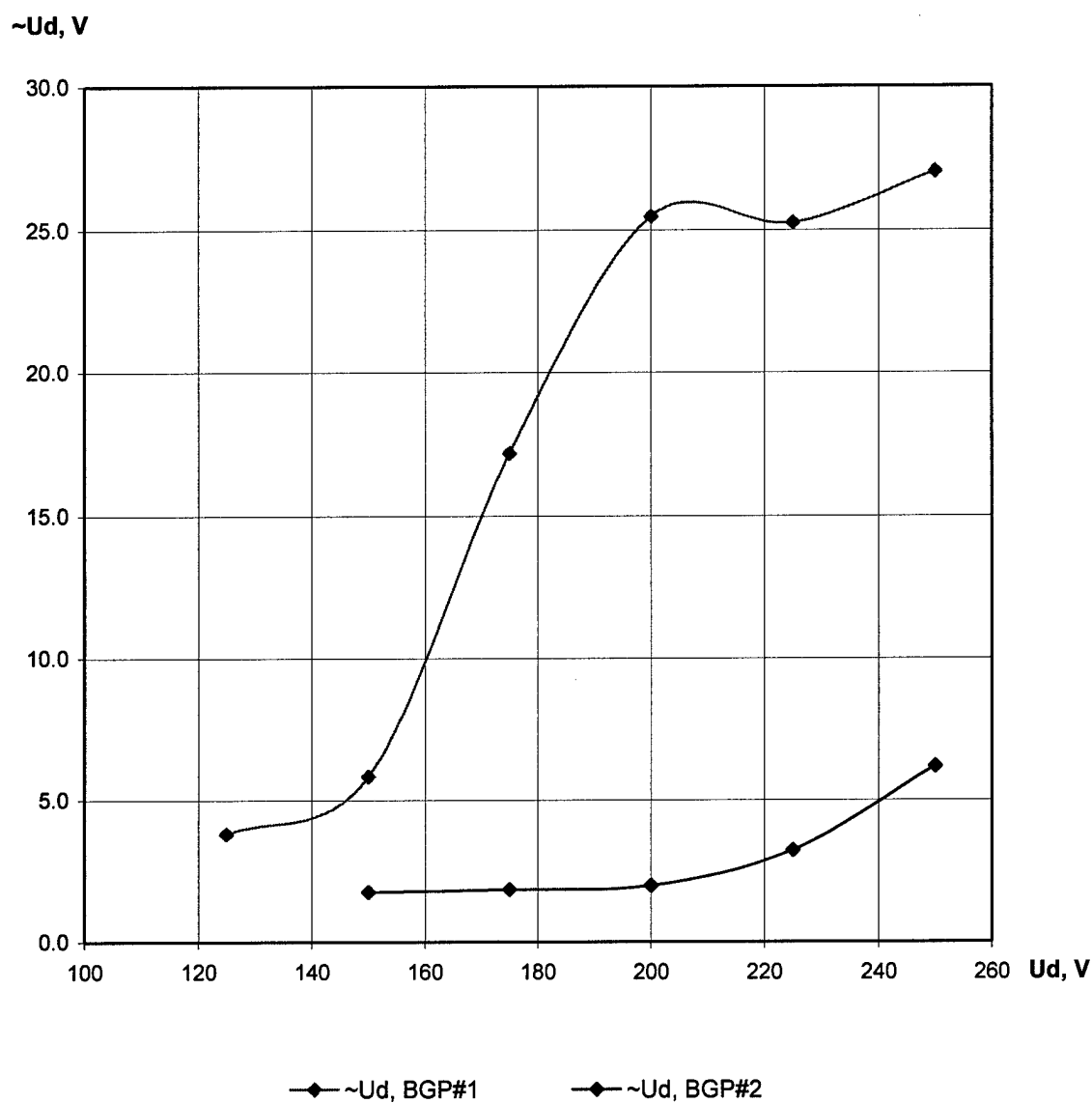
SPT-25, $m=0.6$ mg/s, $I_m=1.5$ A.

Fig.1.62. The discharge voltage oscillations RMS amplitude versus the discharge voltage with cathode #1 and cathode #2.

SPT-25, $m=0.6$ mg/s, $I_m=1.5$ A.

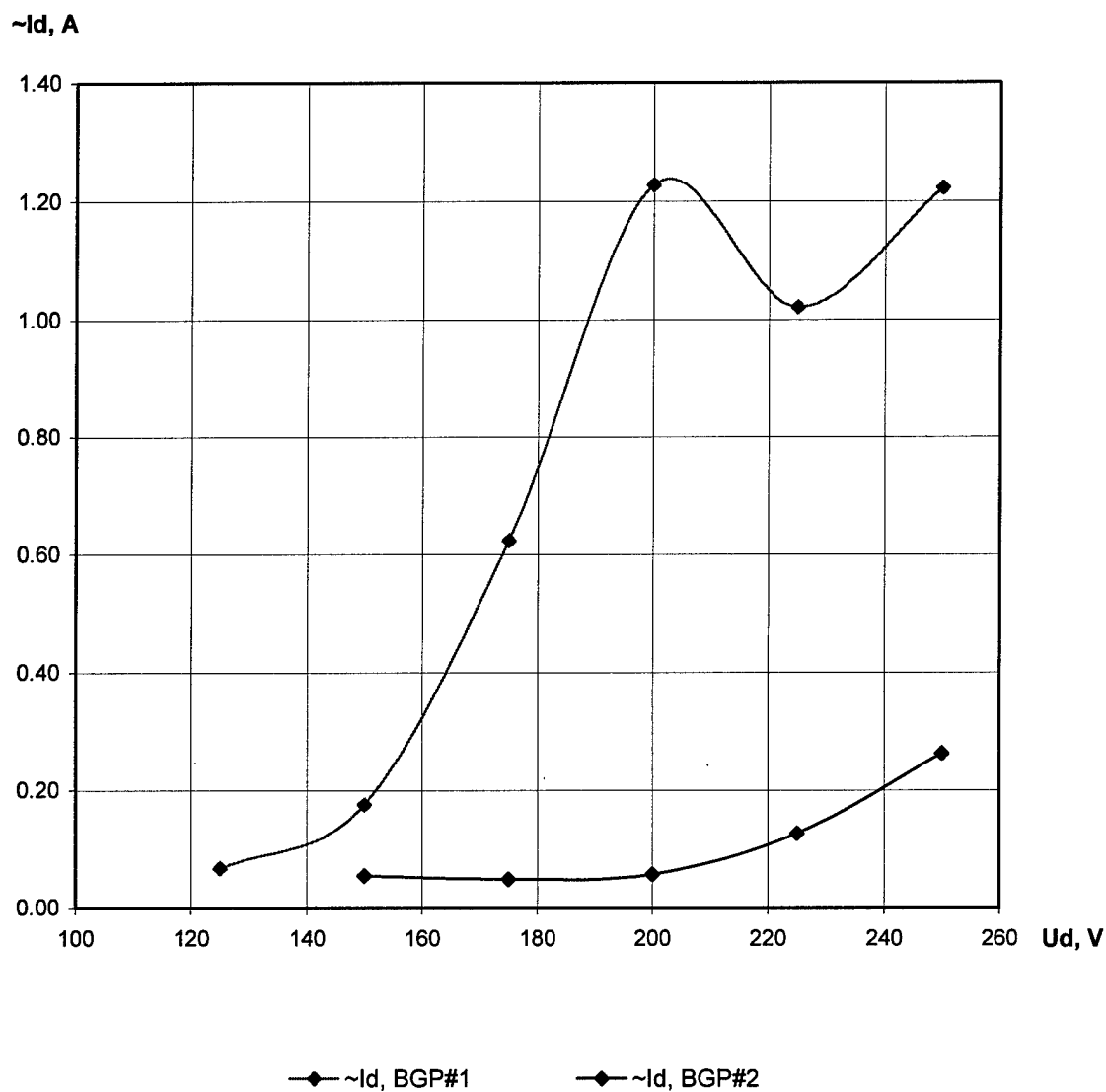


Fig.1.63. The discharge current oscillations RMS amplitude versus the discharge voltage with cathode #1 and cathode #2.

SPT-25, $m=0.6$ mg/s, $I_m=2.7$ A.

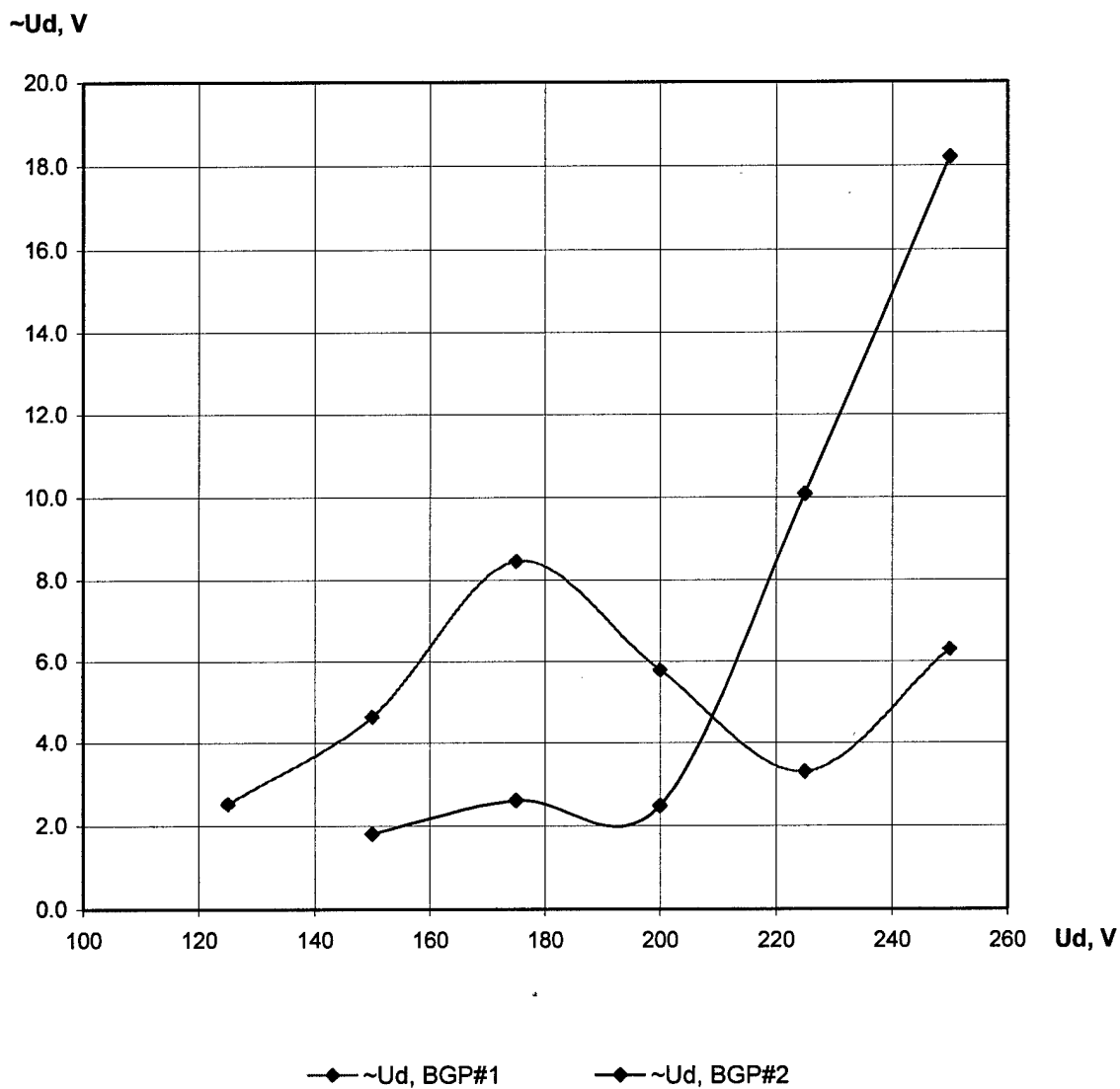


Fig.1.64. The discharge voltage oscillations RMS amplitude versus the discharge voltage with cathode #1 and cathode #2.

SPT-25, $m=0.6$ mg/s, $I_m=2.7$ A.

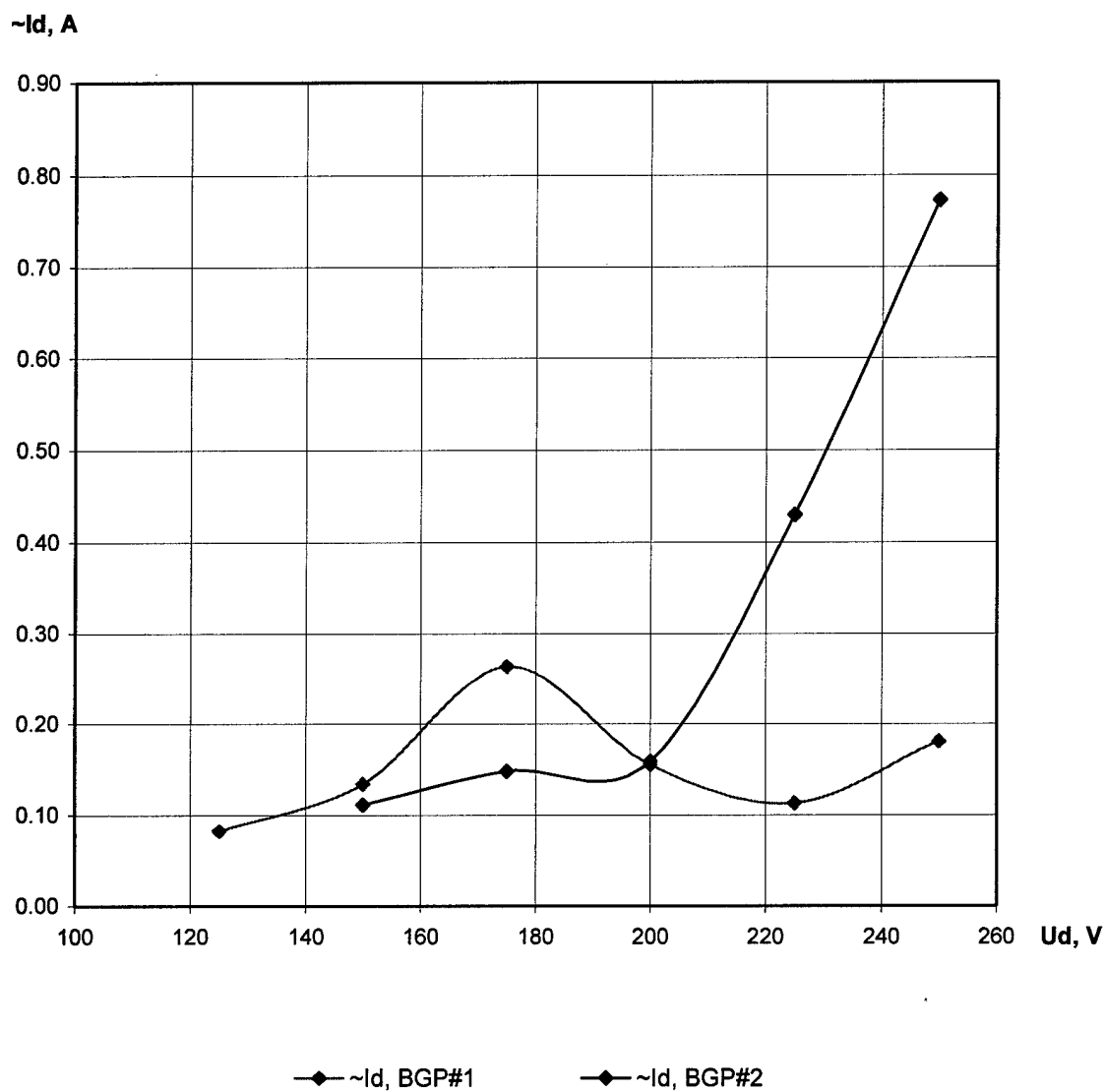


Fig.1.65. The discharge current oscillations RMS amplitude versus the discharge voltage with cathode #1 and cathode #2.

SPT-25, $m=0.6$ mg/s, $I_m=4.0$ A.

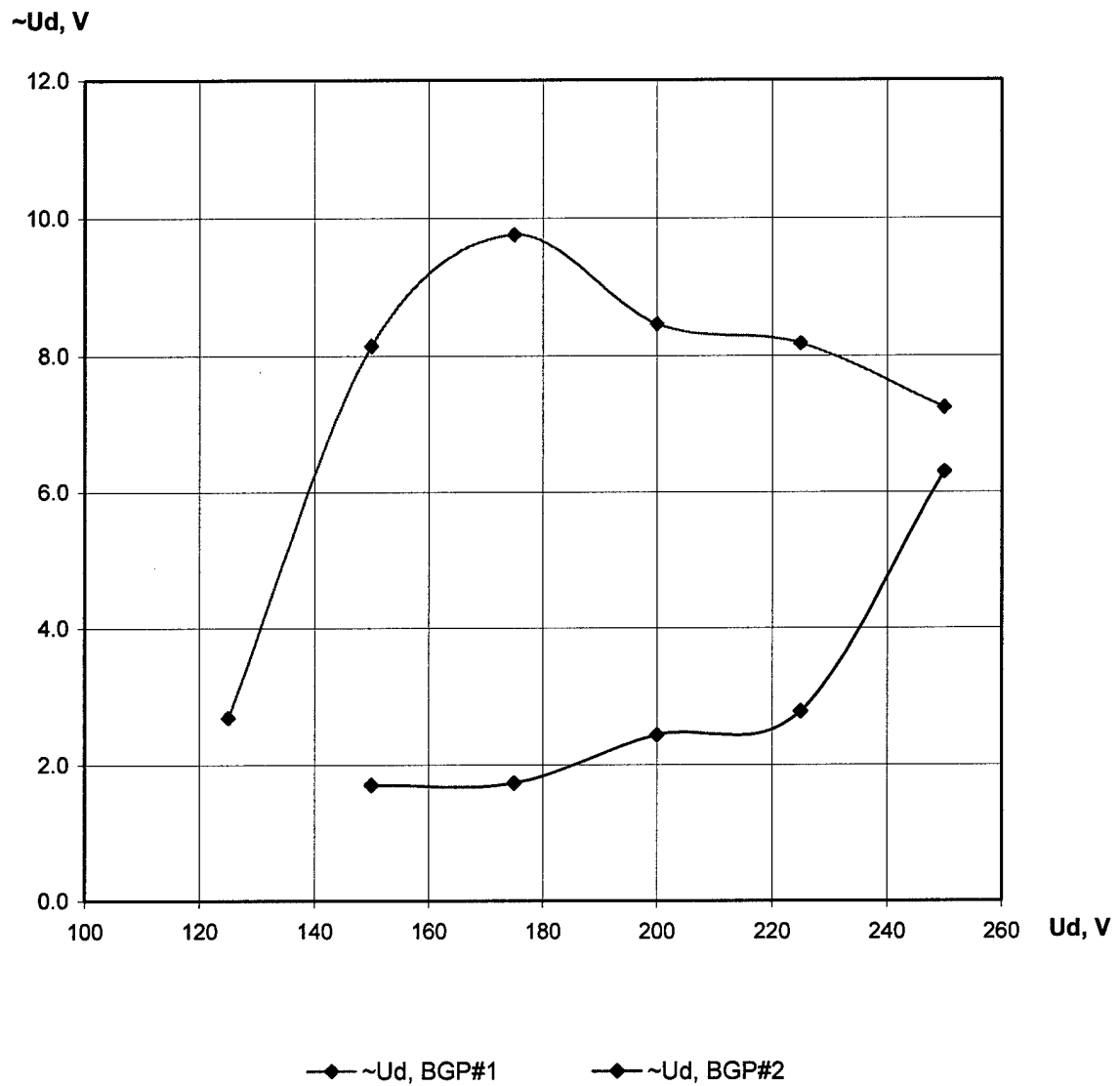


Fig.1.66. The discharge voltage oscillations RMS amplitude versus the discharge voltage with cathode #1 and cathode #2.

SPT-25, $m=0.6$ mg/s, $I_m=4.0$ A.

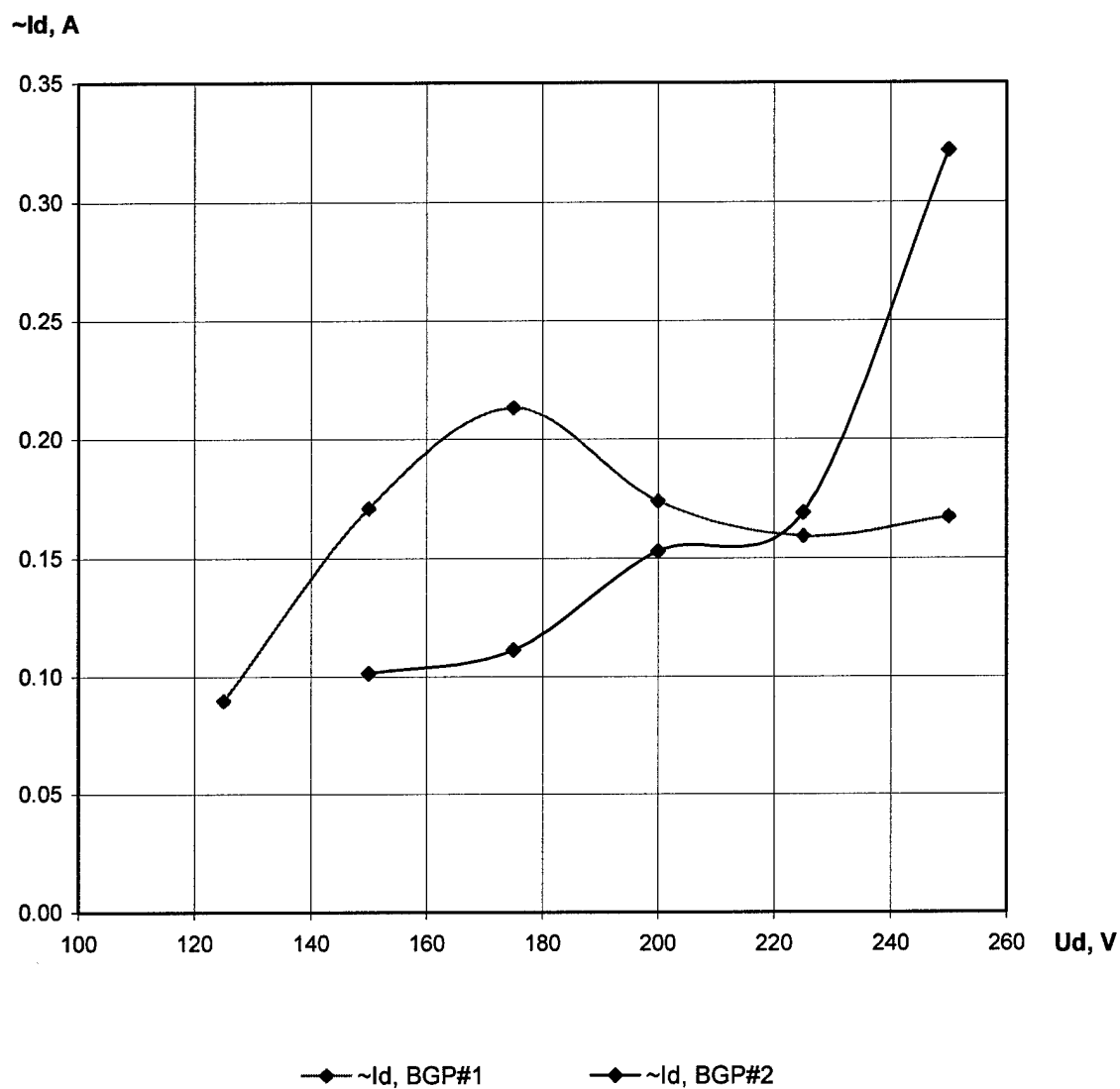


Fig.1.67. The discharge current oscillations RMS amplitude versus the discharge voltage with cathode #1 and cathode #2.

SPT-25, $m=0.7$ mg/s, $I_m=2.7$ A.

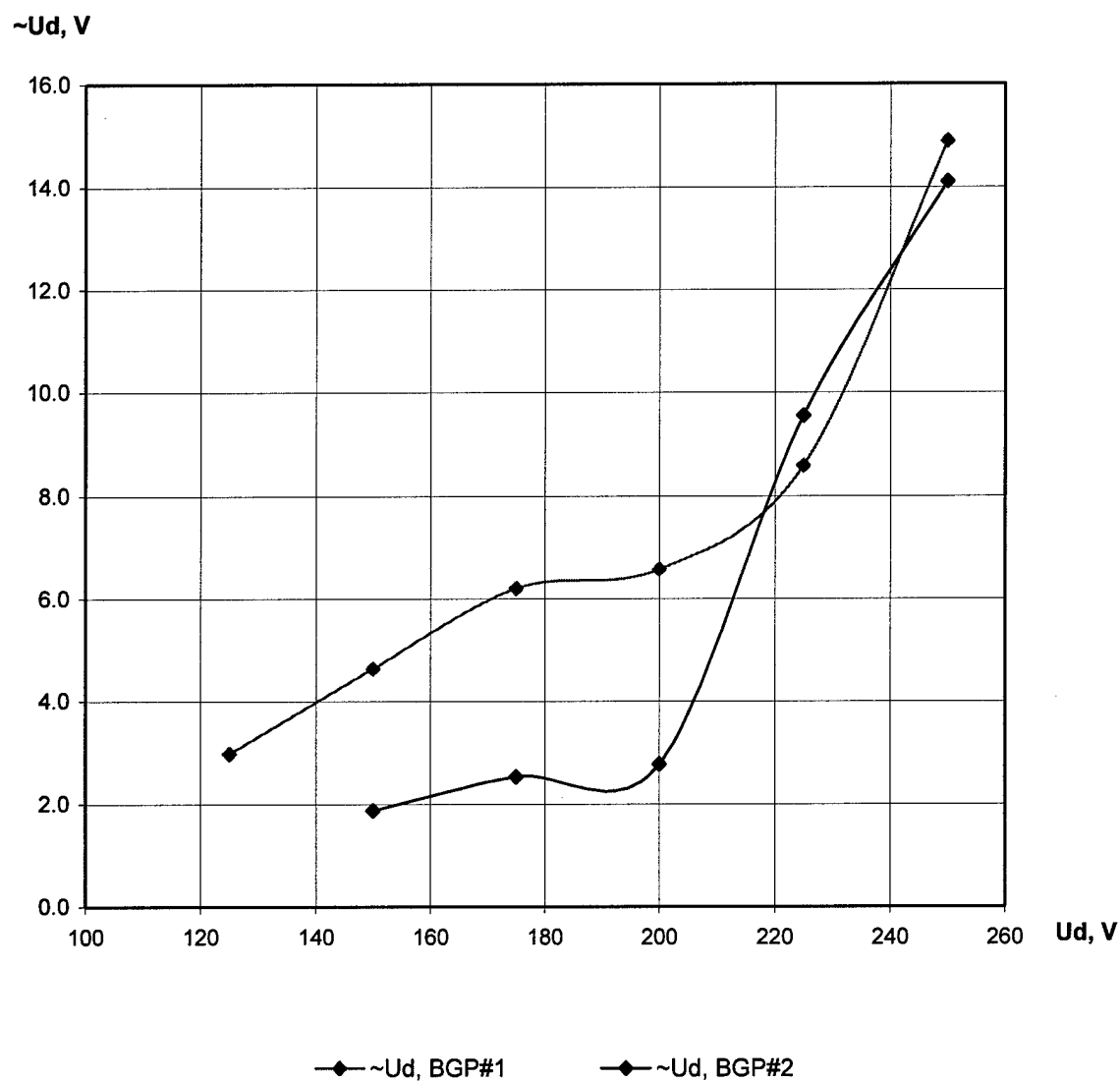


Fig.1.68. The discharge voltage oscillations RMS amplitude versus the discharge voltage with cathode #1 and cathode #2.

SPT-25, $m=0.7$ mg/s, $I_m=2.7$ A.

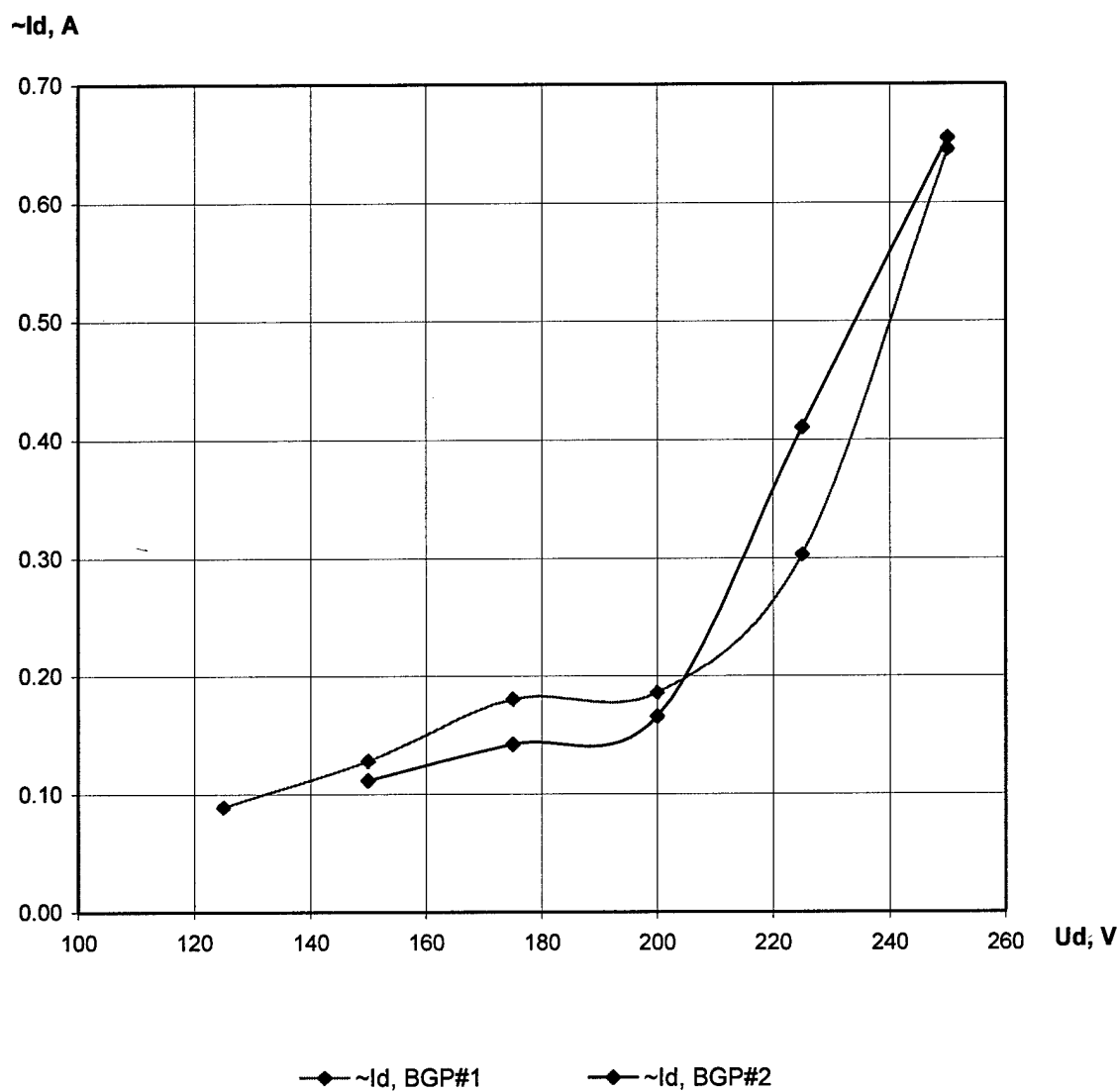


Fig.1.69. The discharge current oscillations RMS amplitude versus the discharge voltage with cathode #1 and cathode #2.

SPT-25, $m=0.6$ mg/s, $I_m=1.5$ A .

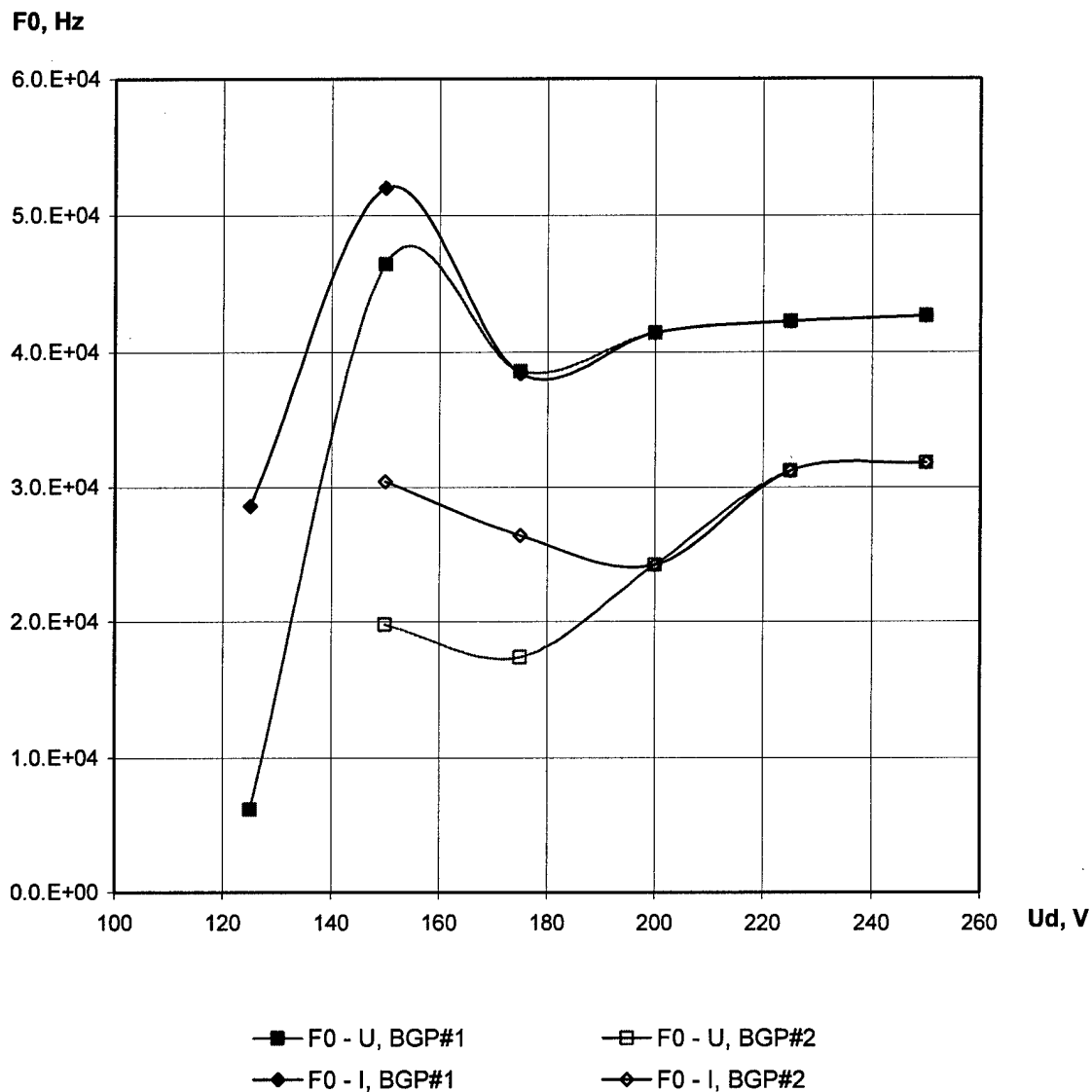


Fig.1.70. The frequency of the dominating discharge voltage (F0-U) and discharge current (F0-I) oscillation mode versus the discharge voltage with cathode #1 and cathode #2.

SPT-25, $m=0.6$ mg/s, $I_m=2.7$ A .

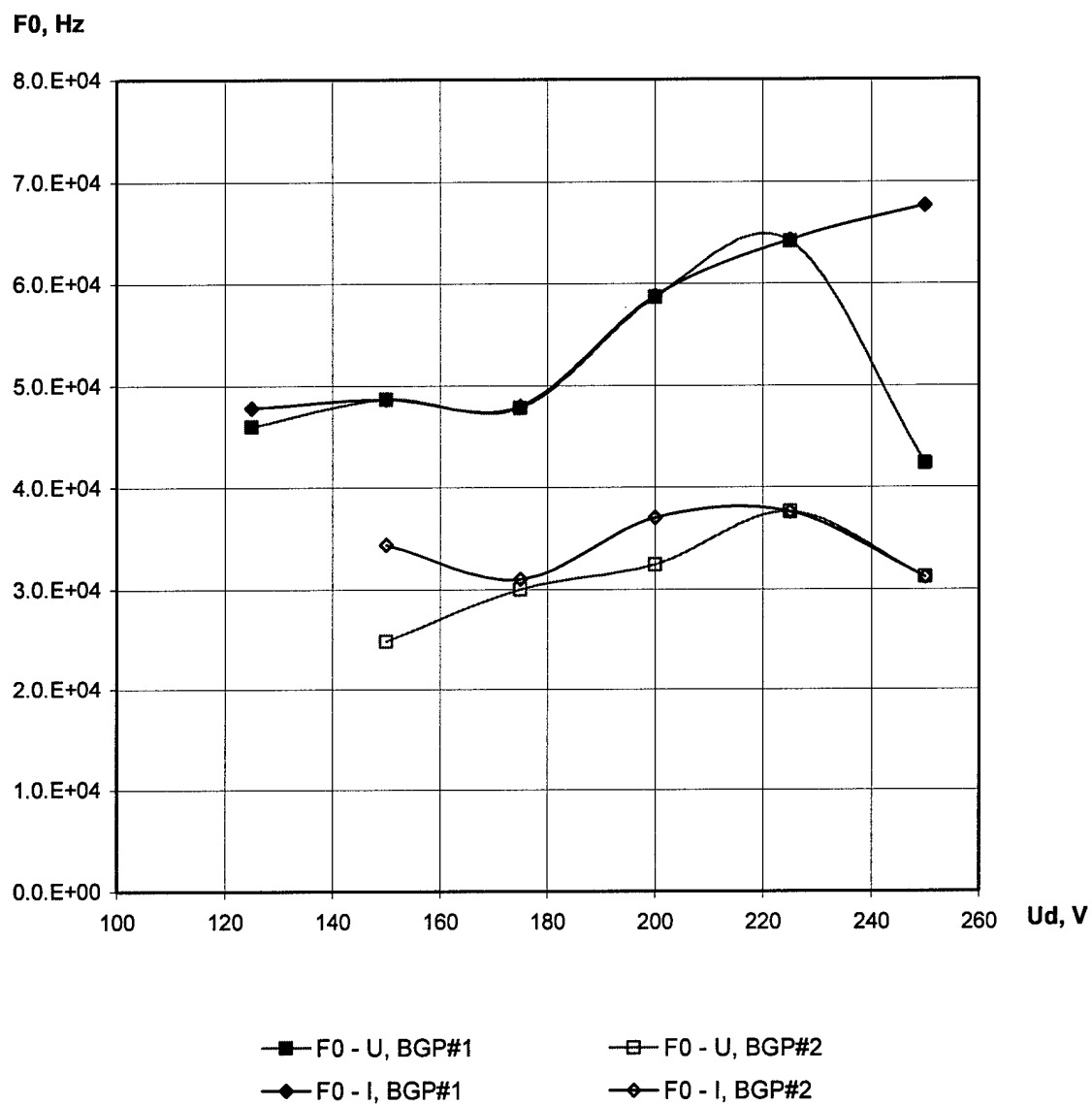


Fig.1.71. The frequency of the dominating discharge voltage (F0-U) and discharge current (F0-I) oscillation mode versus the discharge voltage with cathode #1 and cathode #2.

SPT-25, $m=0.6$ mg/s, $I_m=4.0$ A .

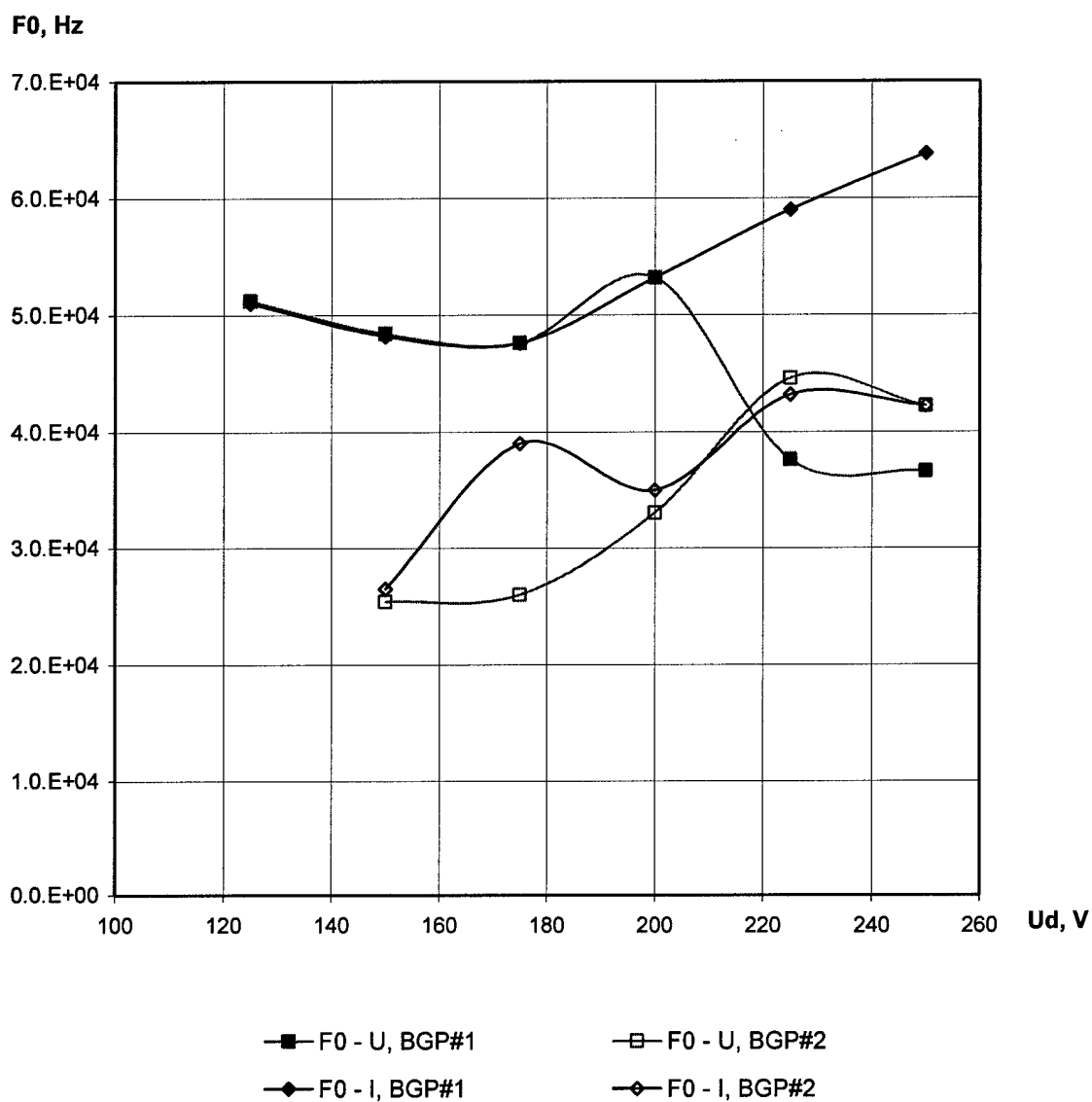


Fig.1.72. The frequency of the dominating discharge voltage (F0-U) and discharge current (F0-I) oscillation mode versus the discharge voltage with cathode #1 and cathode #2.

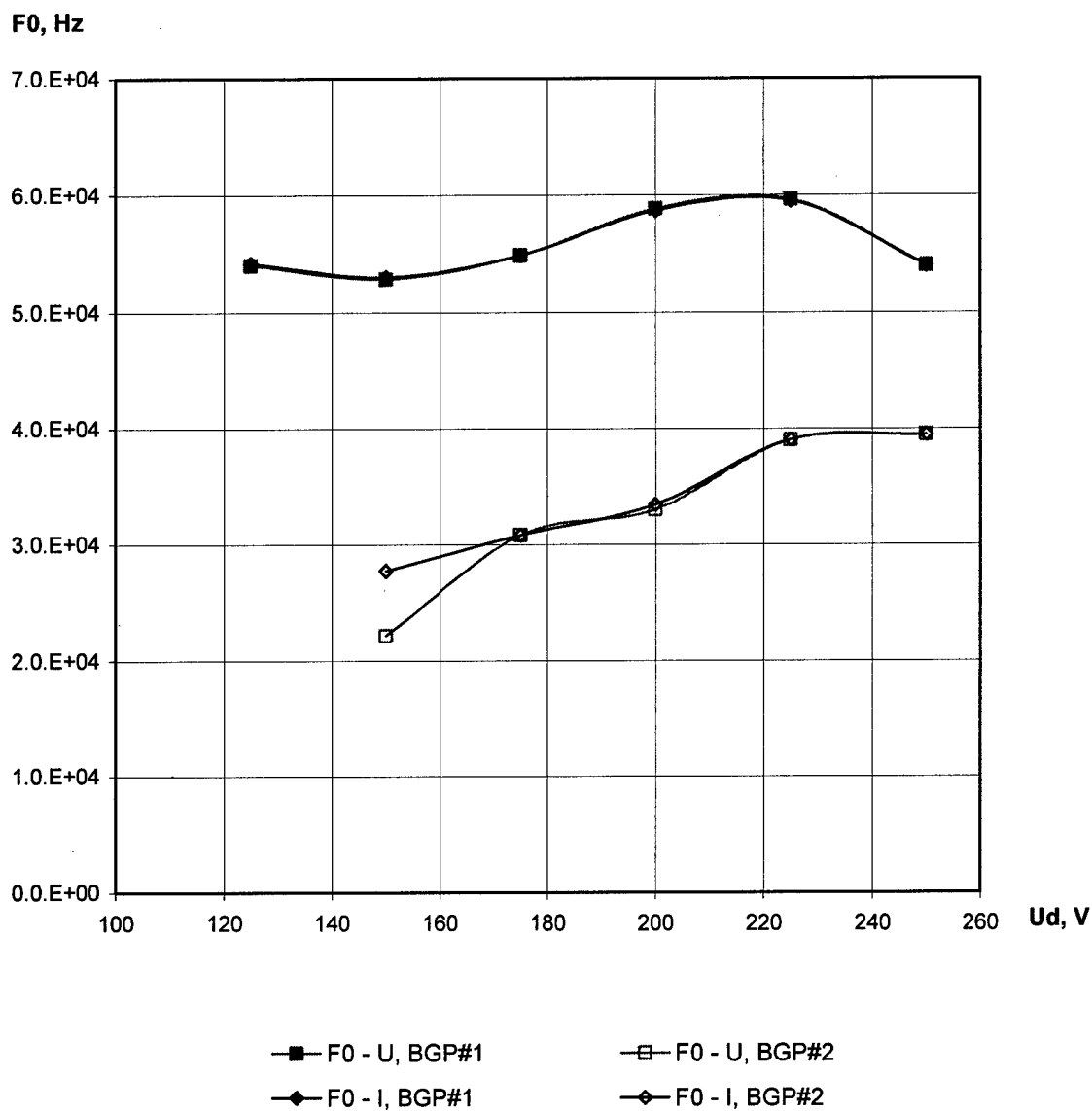
SPT-25, $m=0.7$ mg/s, $I_m=2.7$ A.

Fig.1.73. The frequency of the dominating discharge voltage (F0-U) and discharge current (F0-I) oscillation mode versus the discharge voltage with cathode #1 and cathode #2.

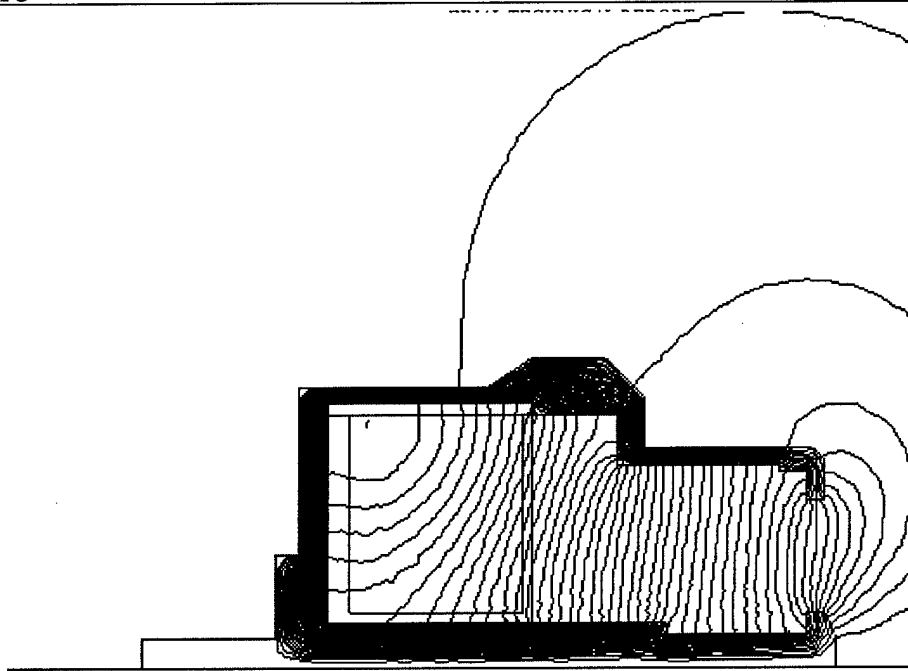


Fig.1.74. The SPT-25 magnetic field topology ($I_m=2.5$ A).

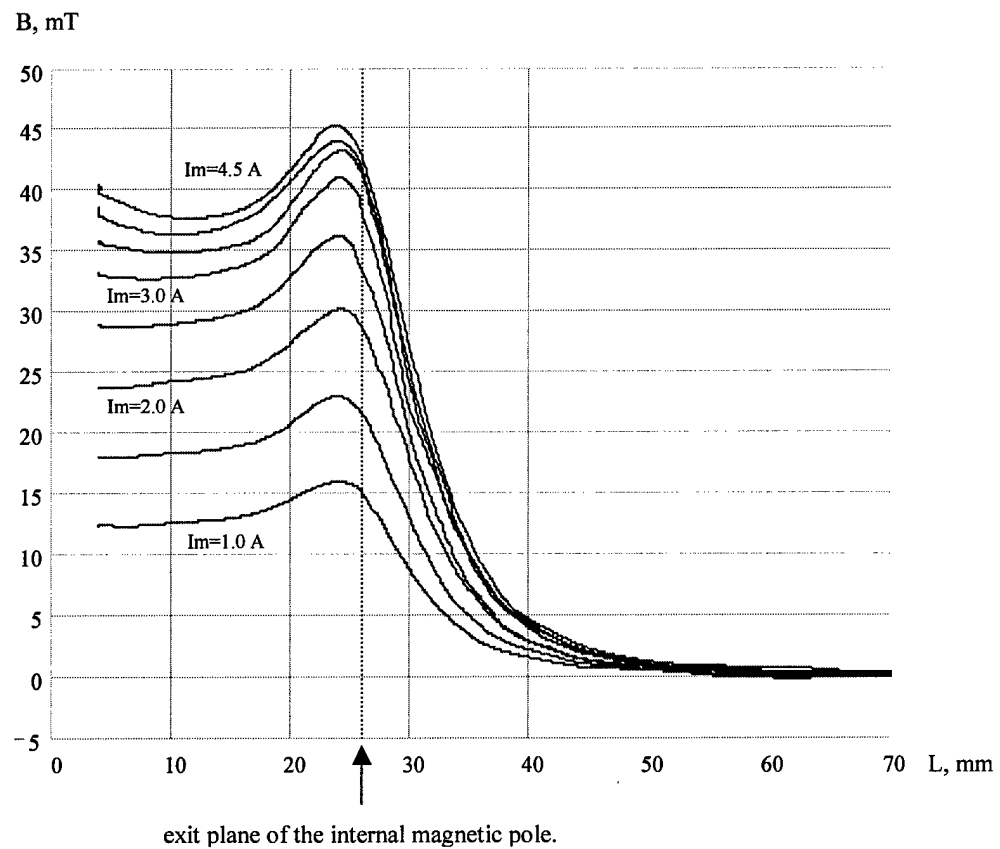


Fig.1.75. The radial magnetic field distribution along the accelerating channel mid surface.

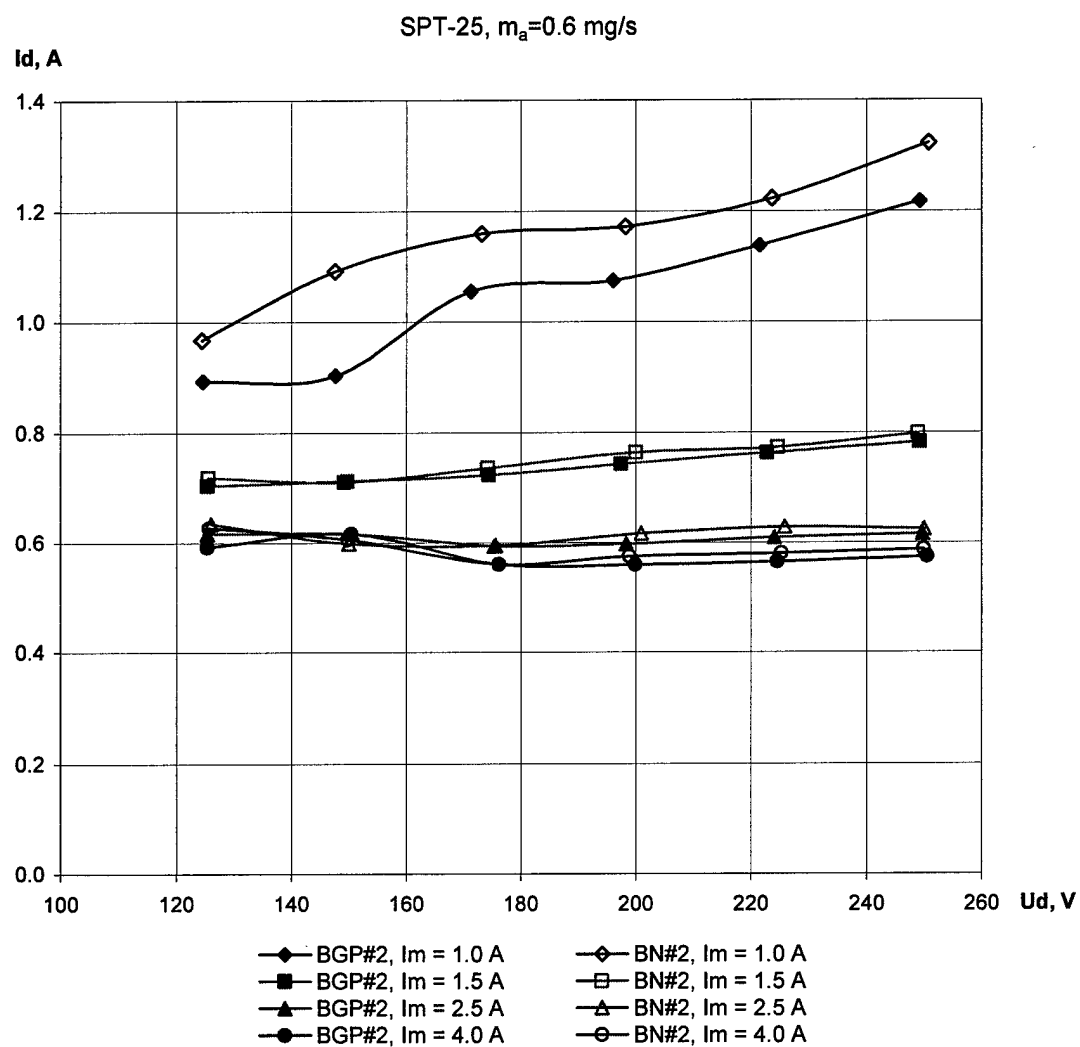


Fig.1.76. Comparative voltage-current characteristics with cathode #2.

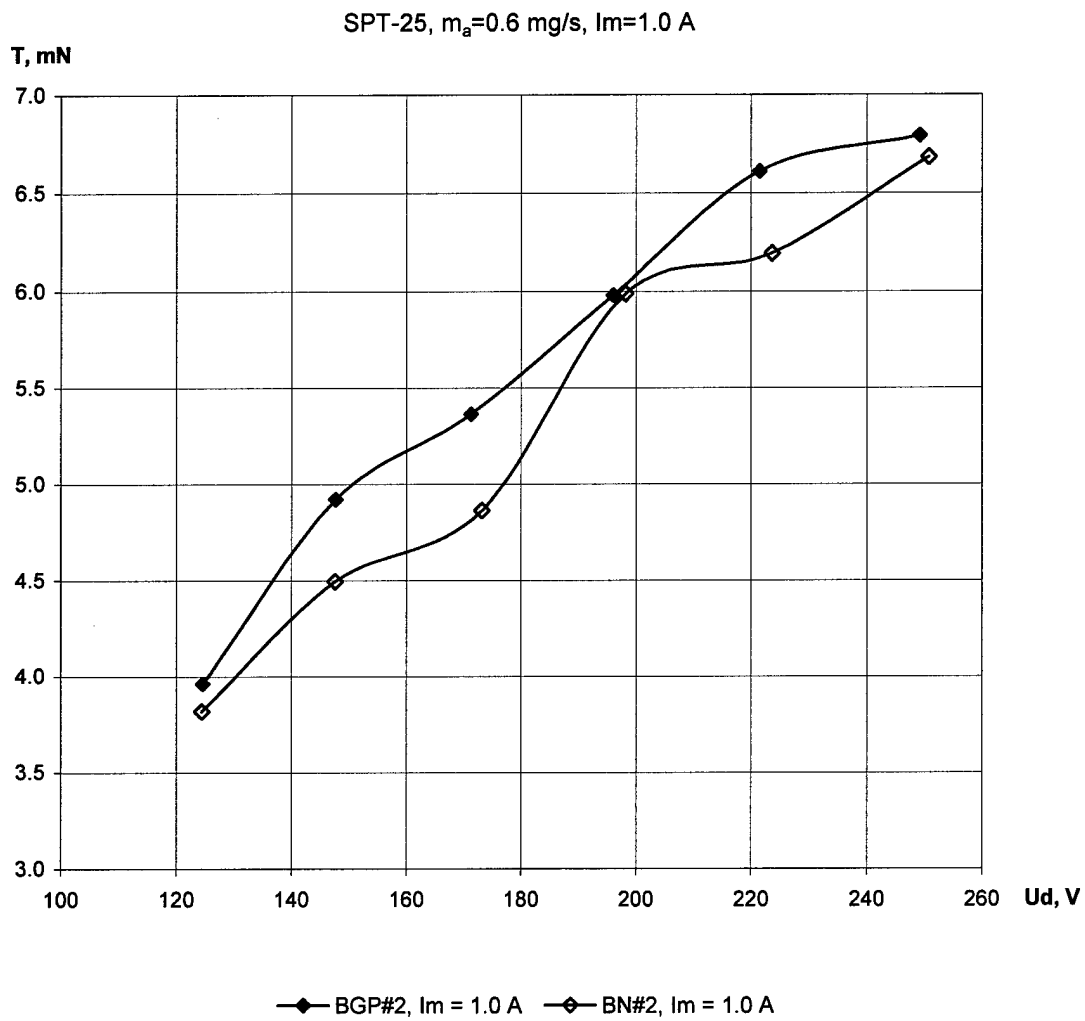


Fig.1.77. Thrust versus the discharge voltage with cathode #2.

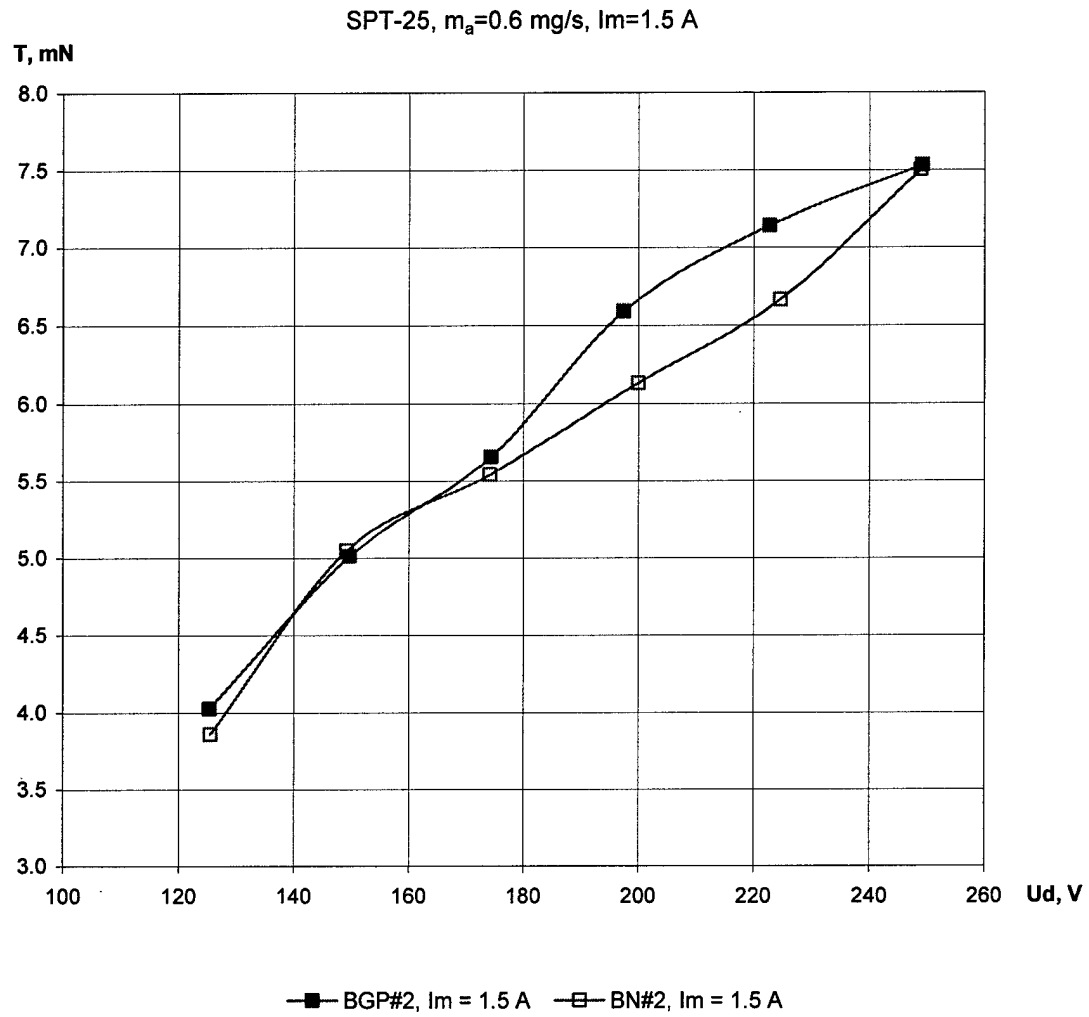


Fig.1.78. Thrust versus the discharge voltage with cathode #2.

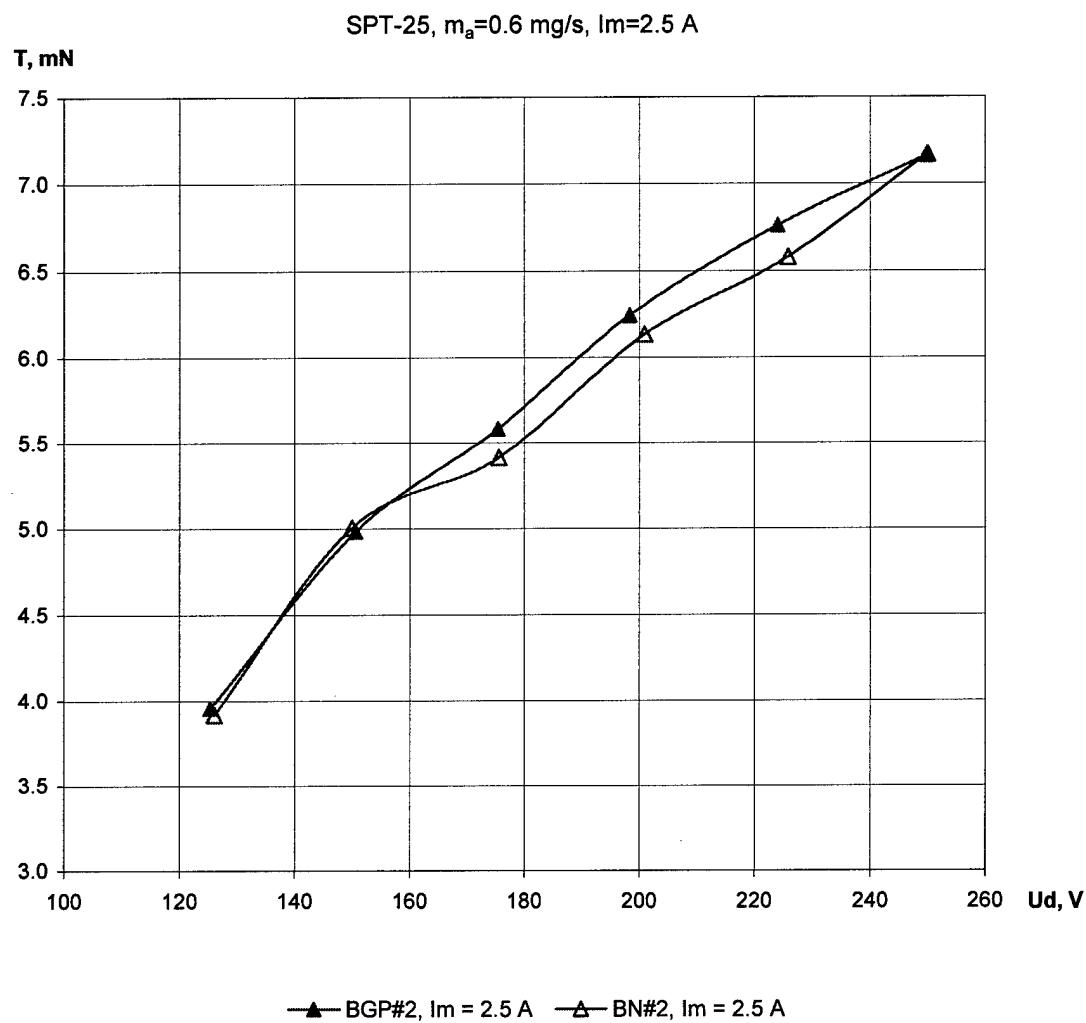


Fig.1.79. Thrust versus the discharge voltage with cathode #2.

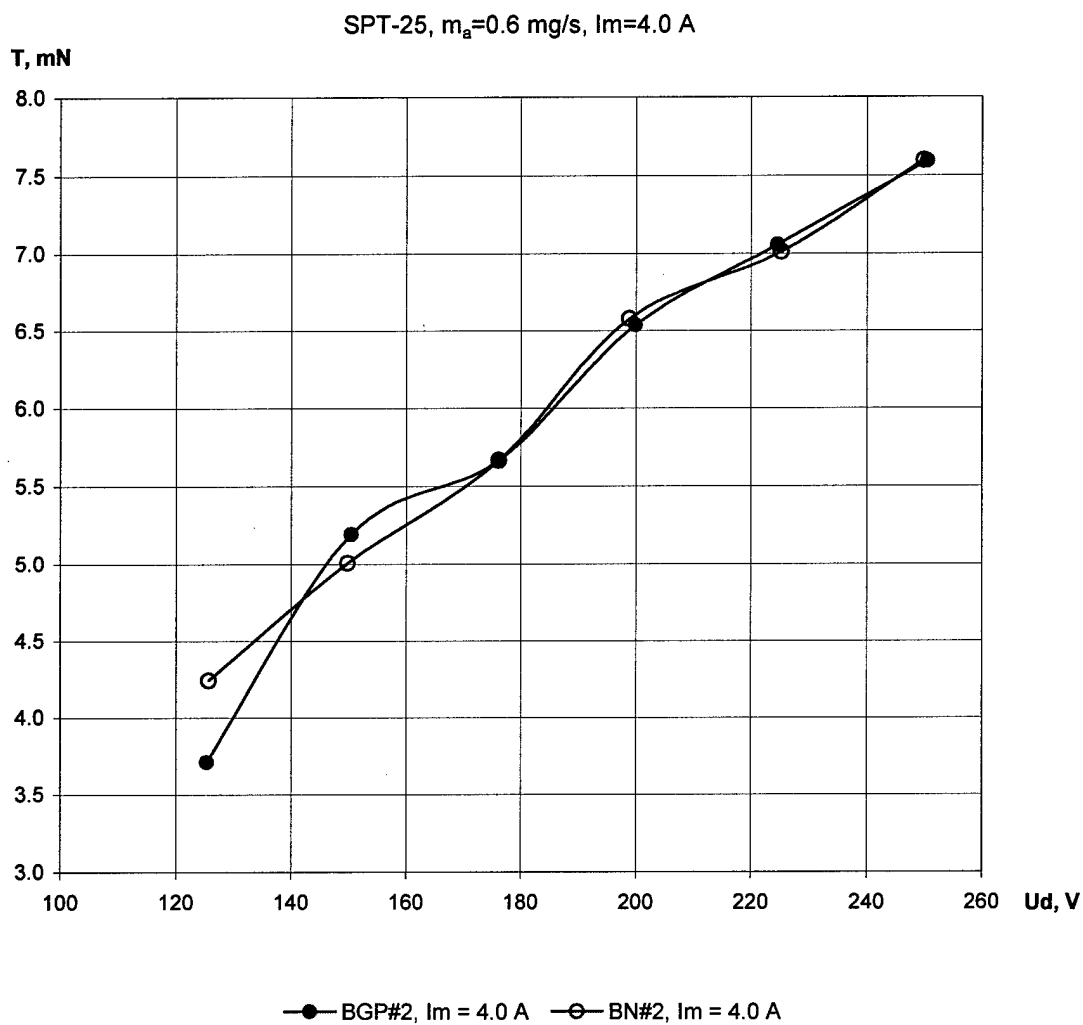


Fig.1.80. Thrust versus the discharge voltage with cathode #2.

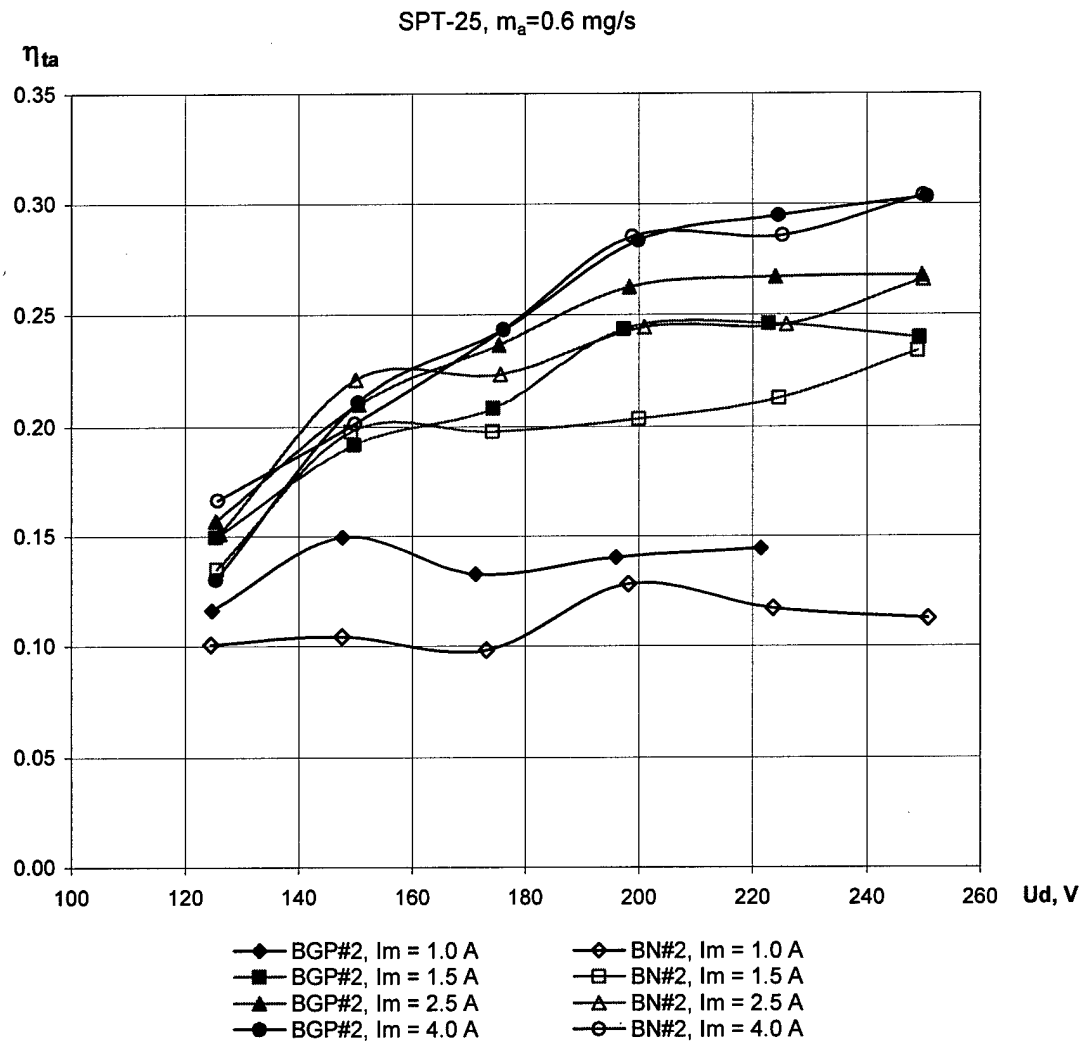


Fig.1.81. Thrust efficiency versus the discharge voltage with cathode #2.

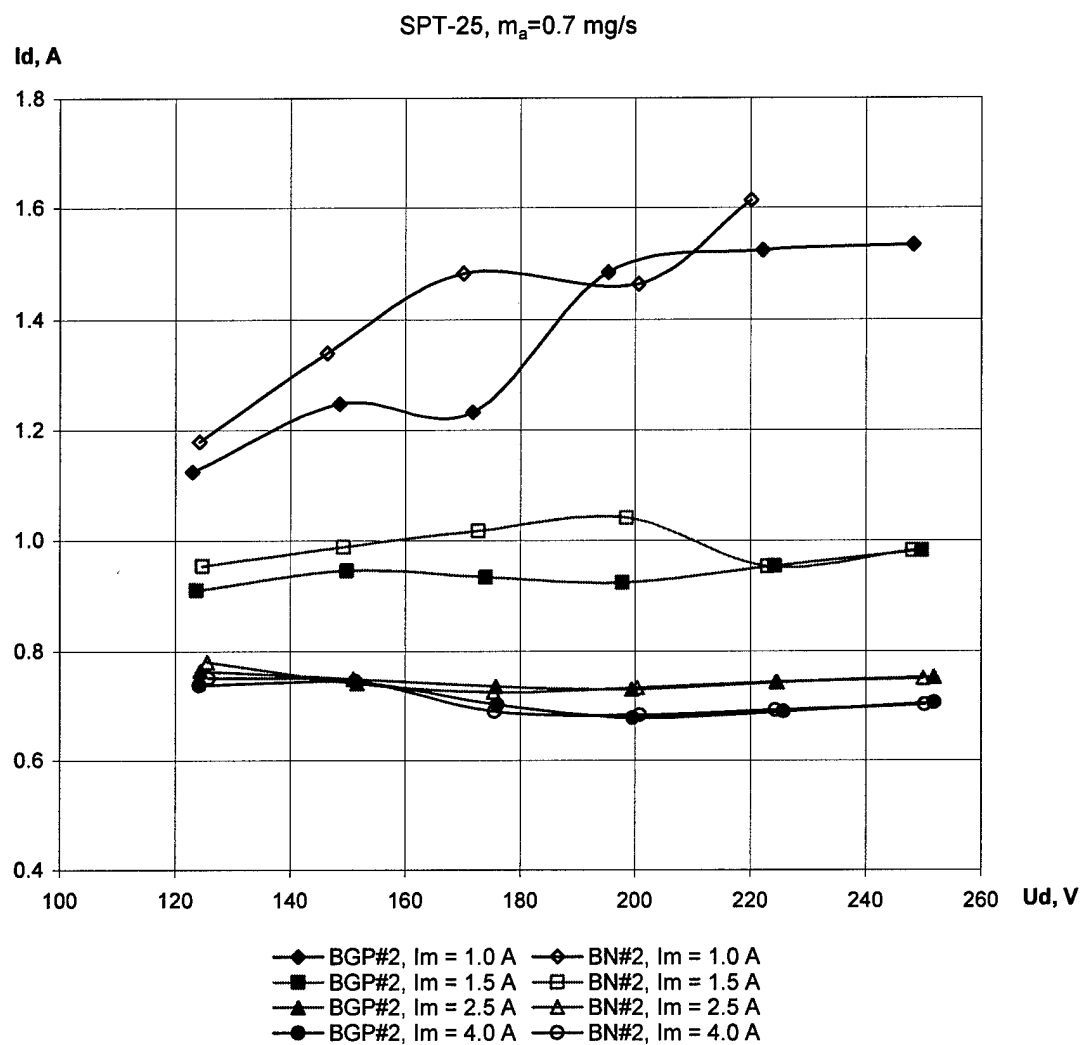


Fig.1.82. Comparative voltage-current characteristics with cathode #2.

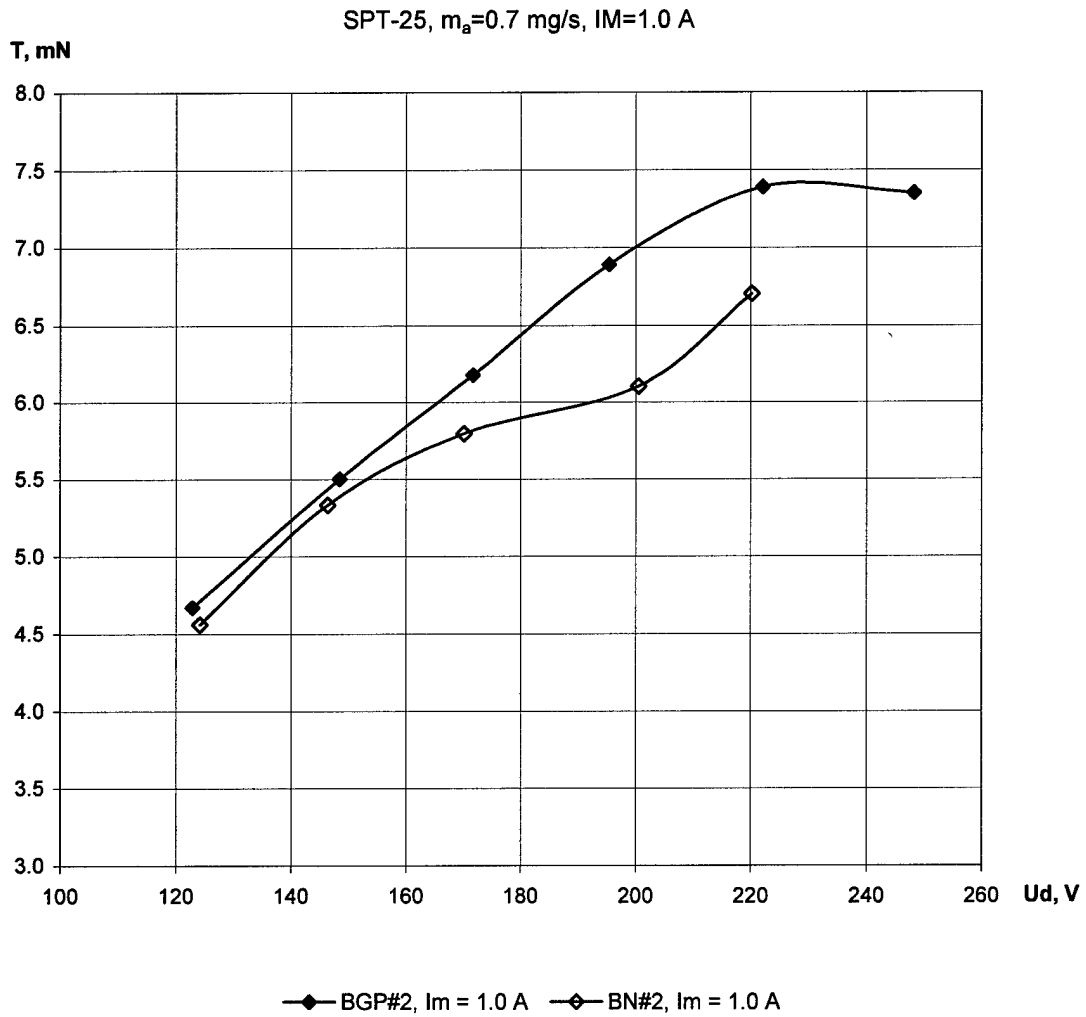


Fig.1.83. Thrust versus the discharge voltage with cathode #2.

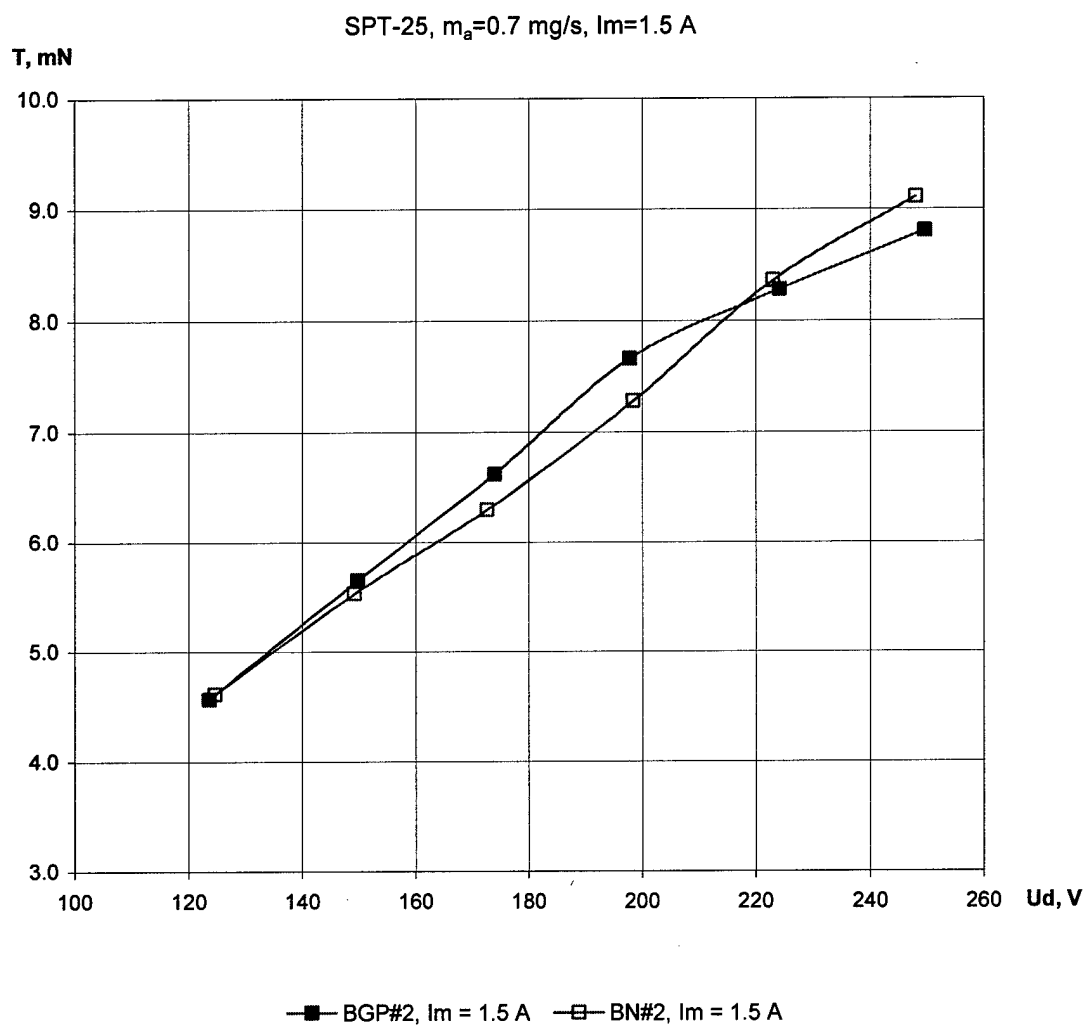


Fig.1.84. Thrust versus the discharge voltage with cathode #2.

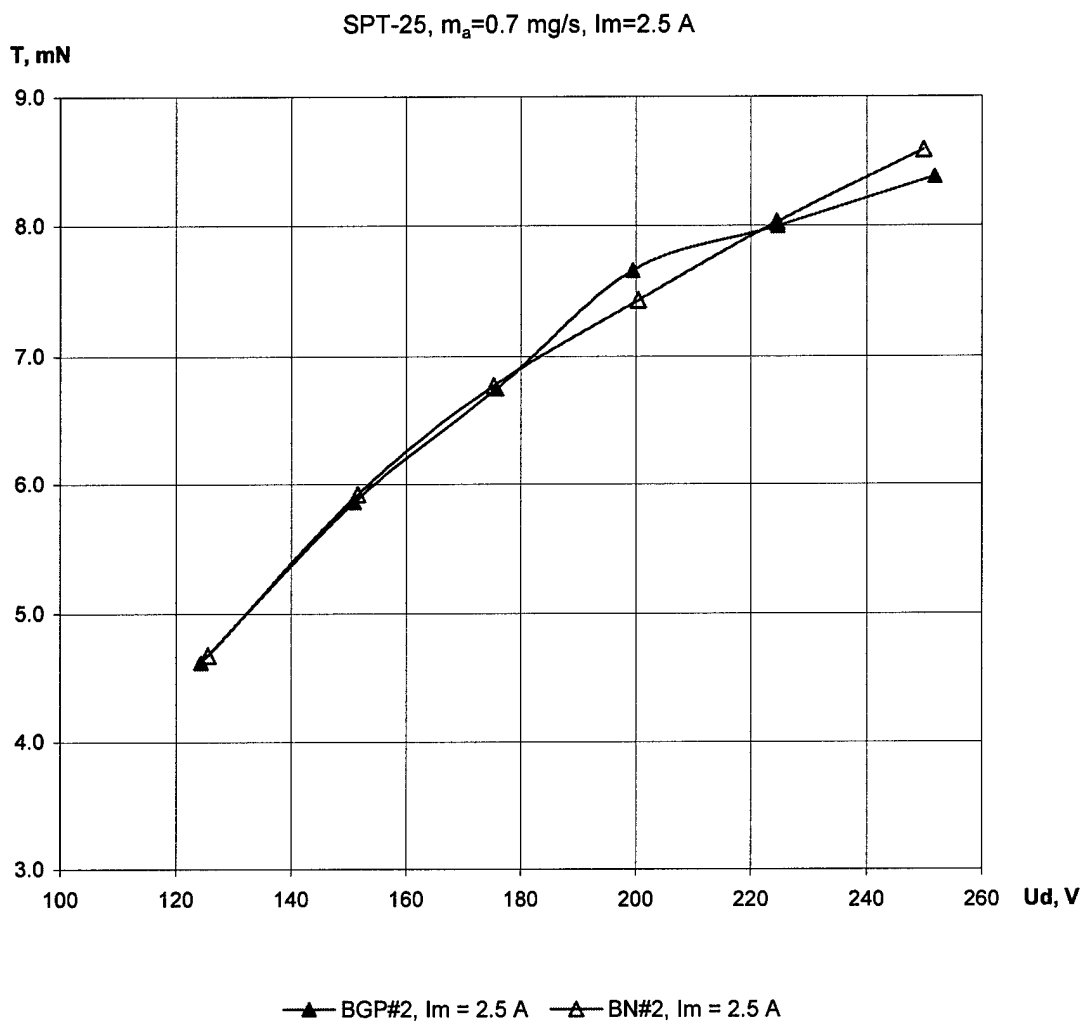


Fig.1.85. Thrust versus the discharge voltage with cathode #2.

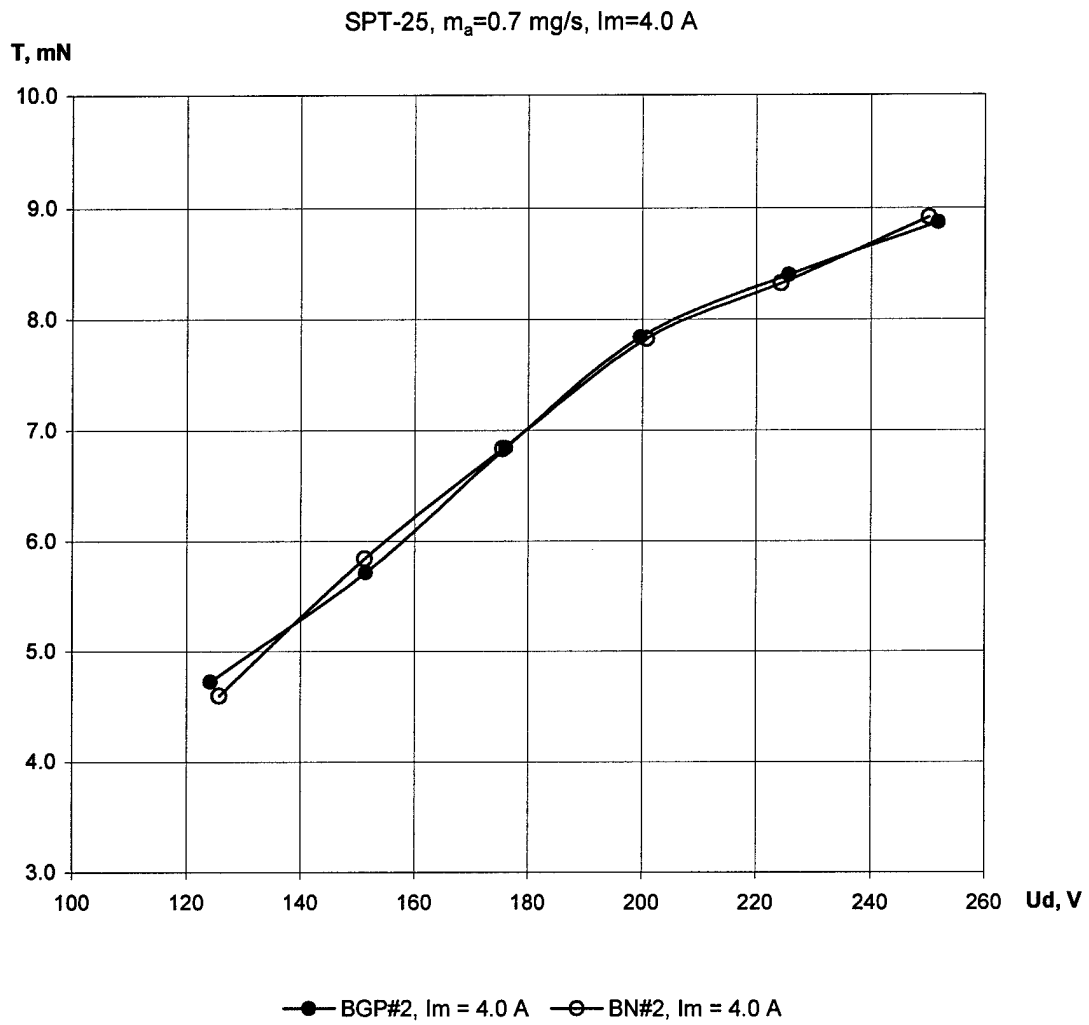


Fig.1.86. Thrust versus the discharge voltage with cathode #2.

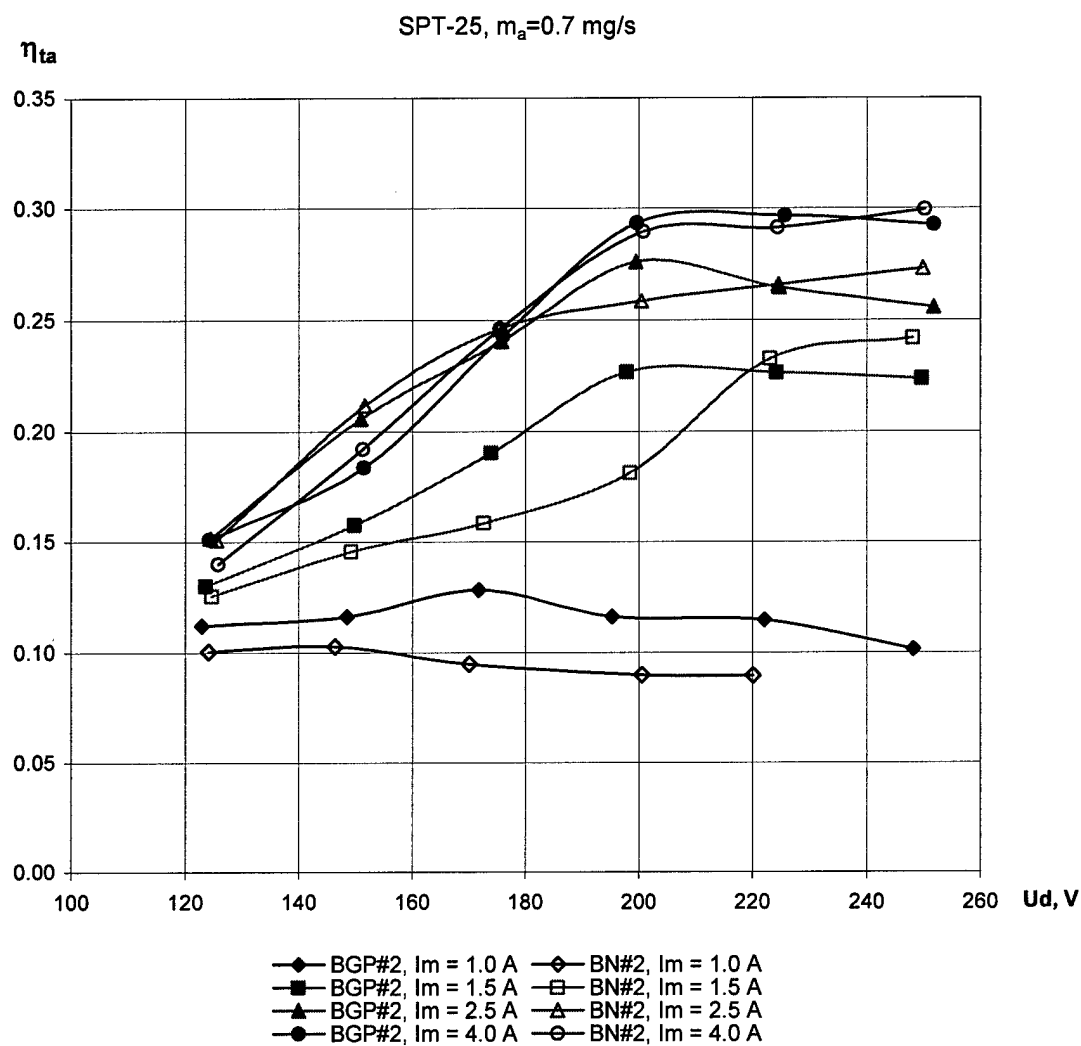


Fig.1.87. Thrust efficiency versus the discharge voltage with cathode #2.

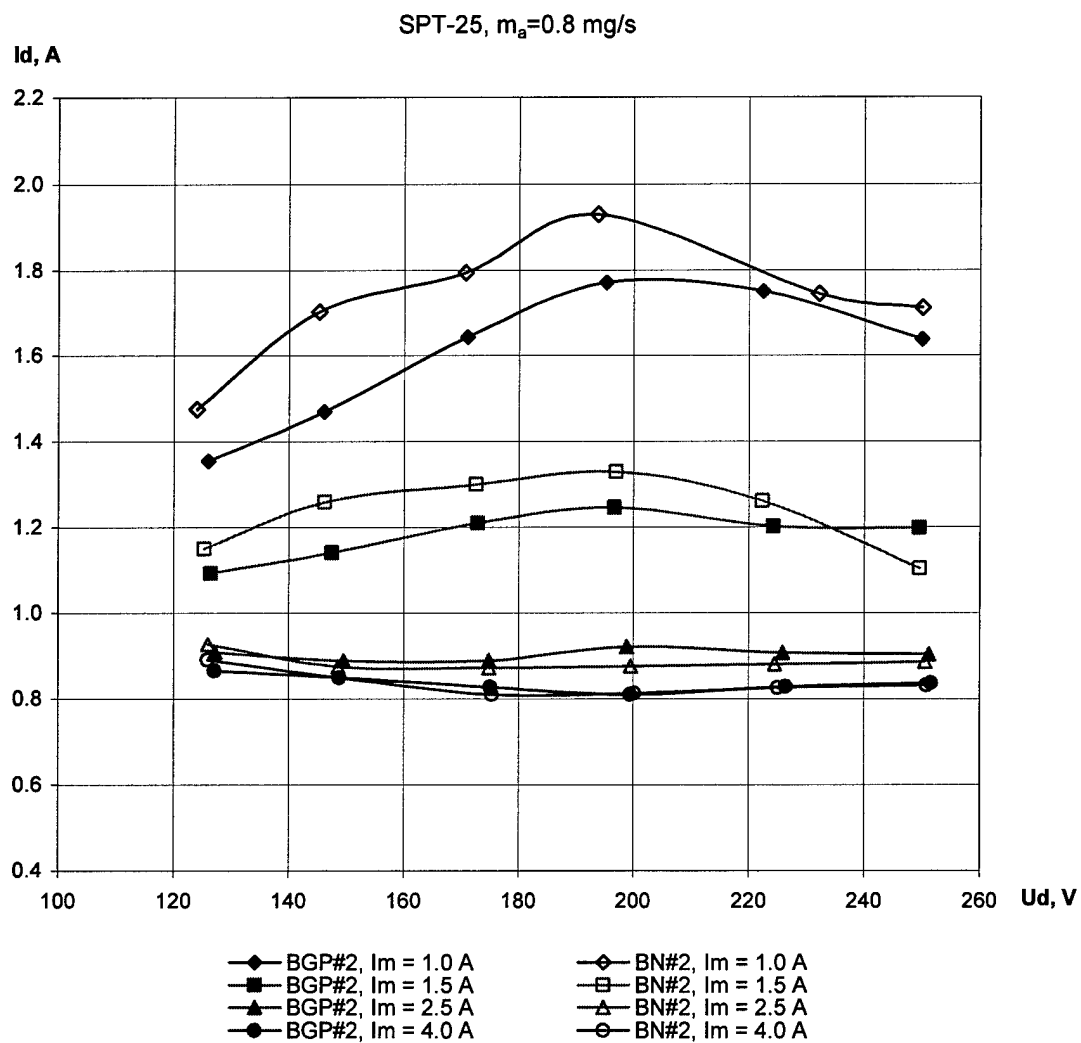


Fig.1.88. Comparative voltage-current characteristics with cathode #2.

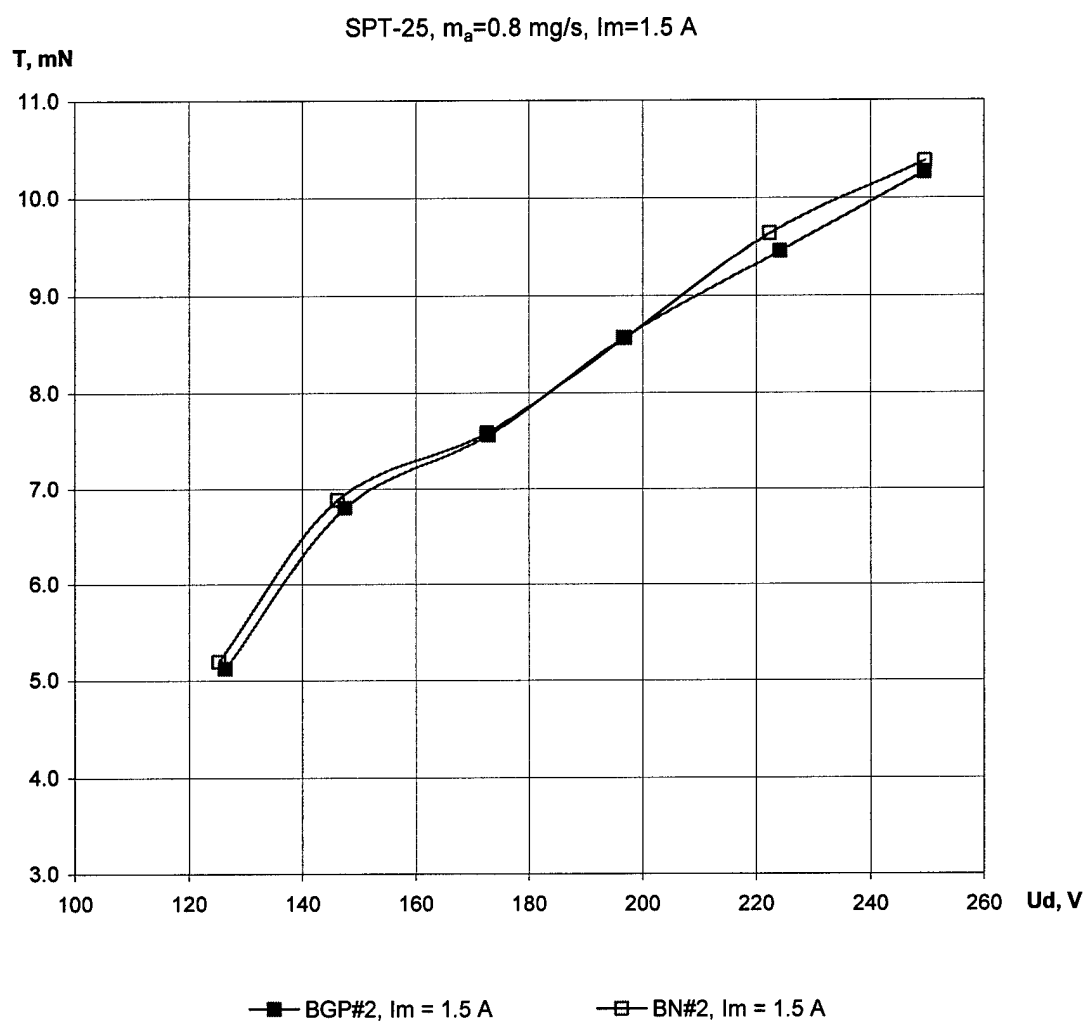


Fig.1.89. Thrust versus the discharge voltage with cathode #2.

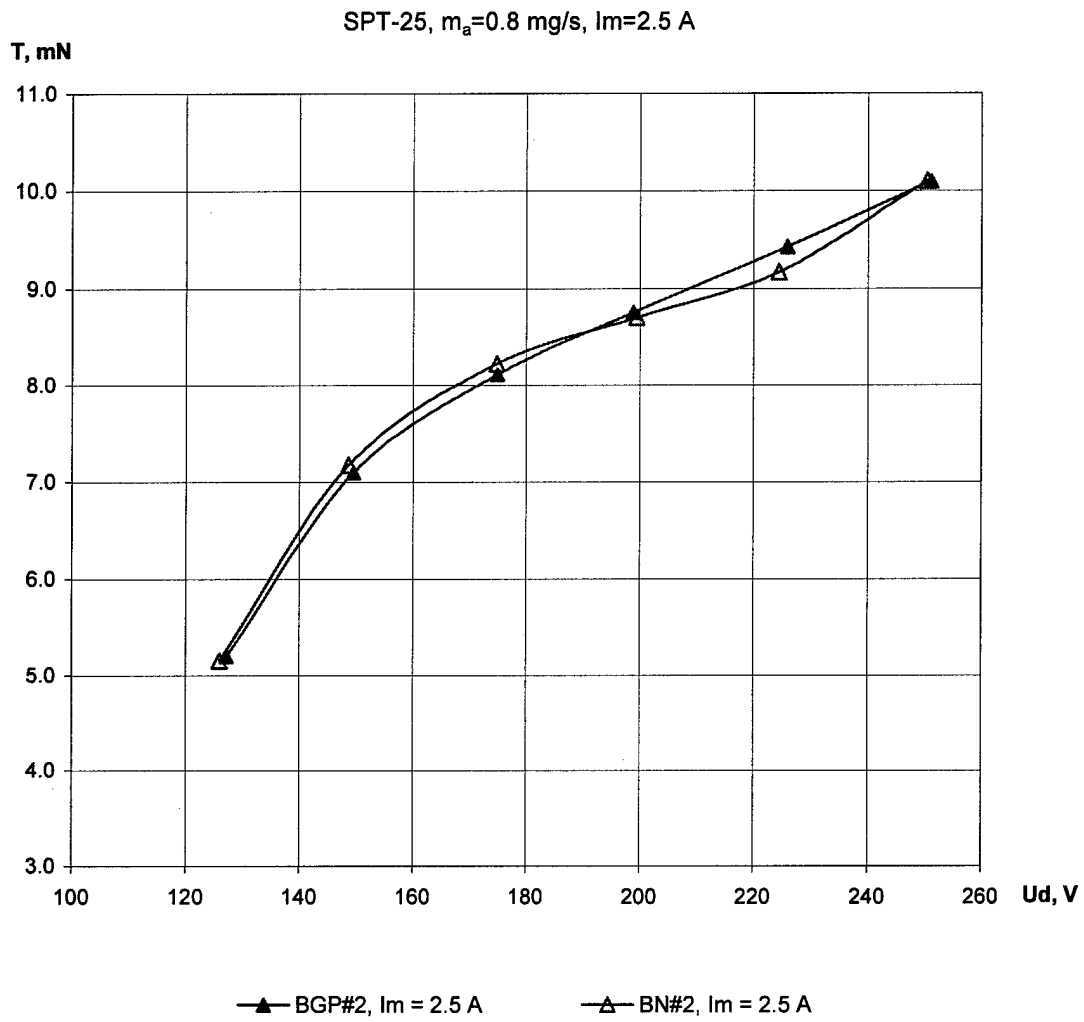


Fig.1.90. Thrust versus the discharge voltage with cathode #2.

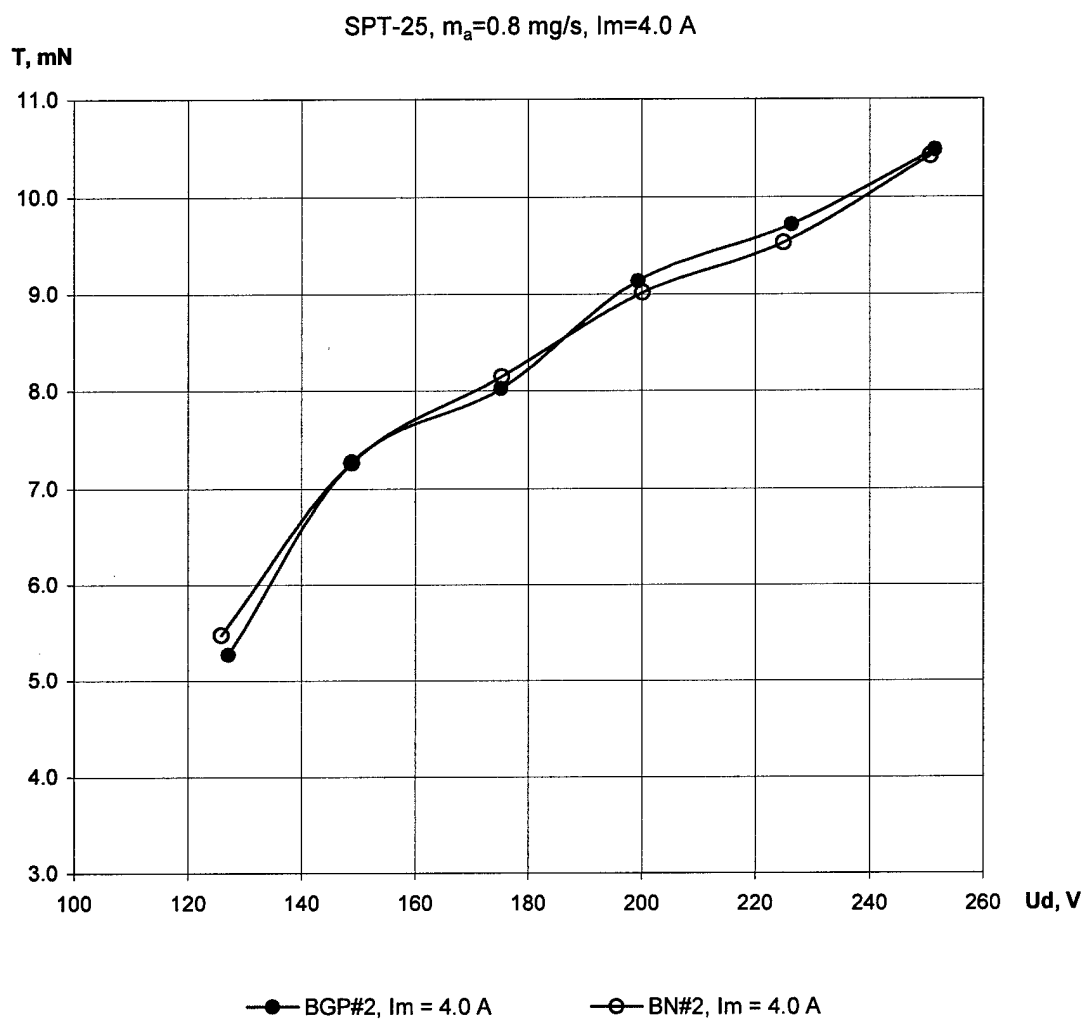


Fig.1.91. Thrust versus the discharge voltage with cathode #2.

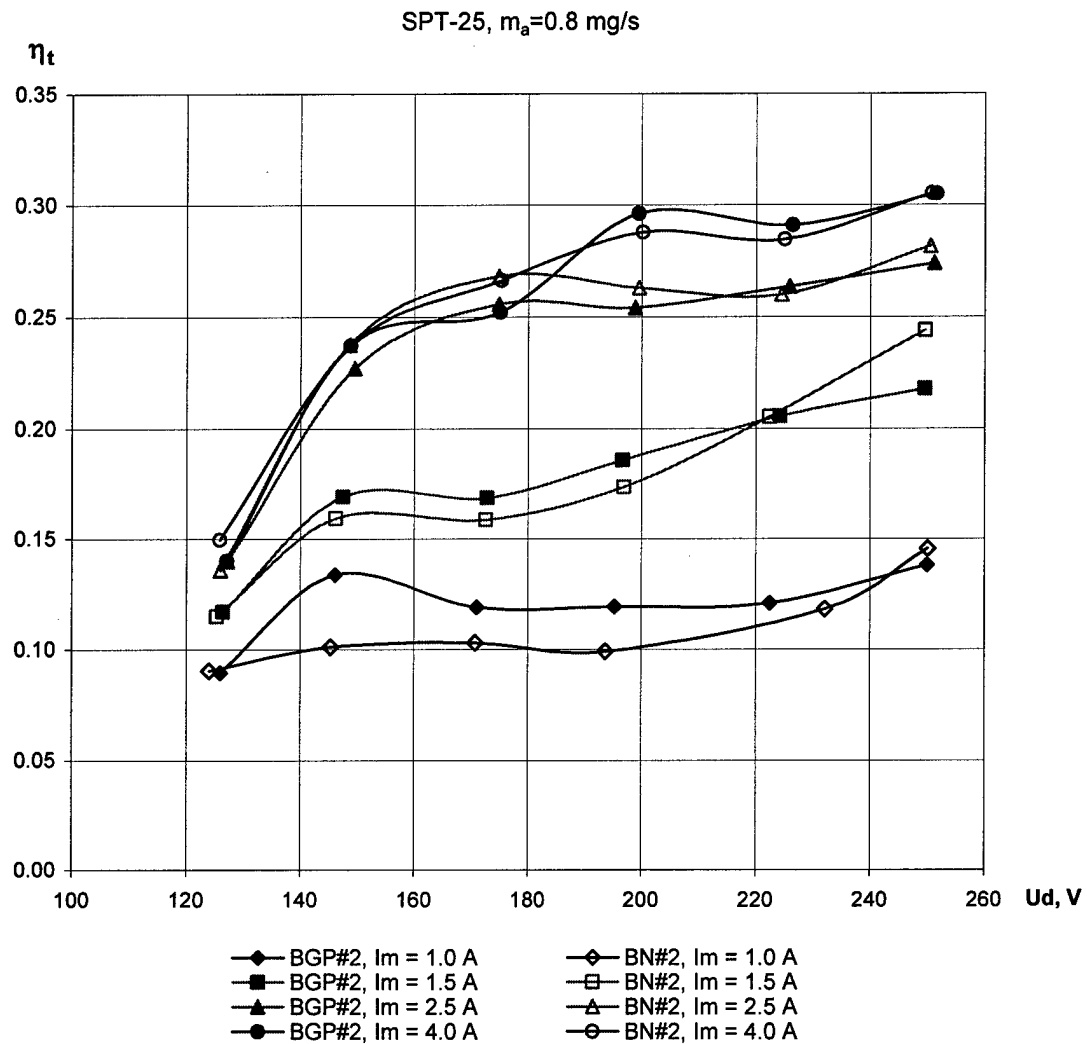


Fig.1.92. Thrust efficiency versus the discharge voltage with cathode #2.

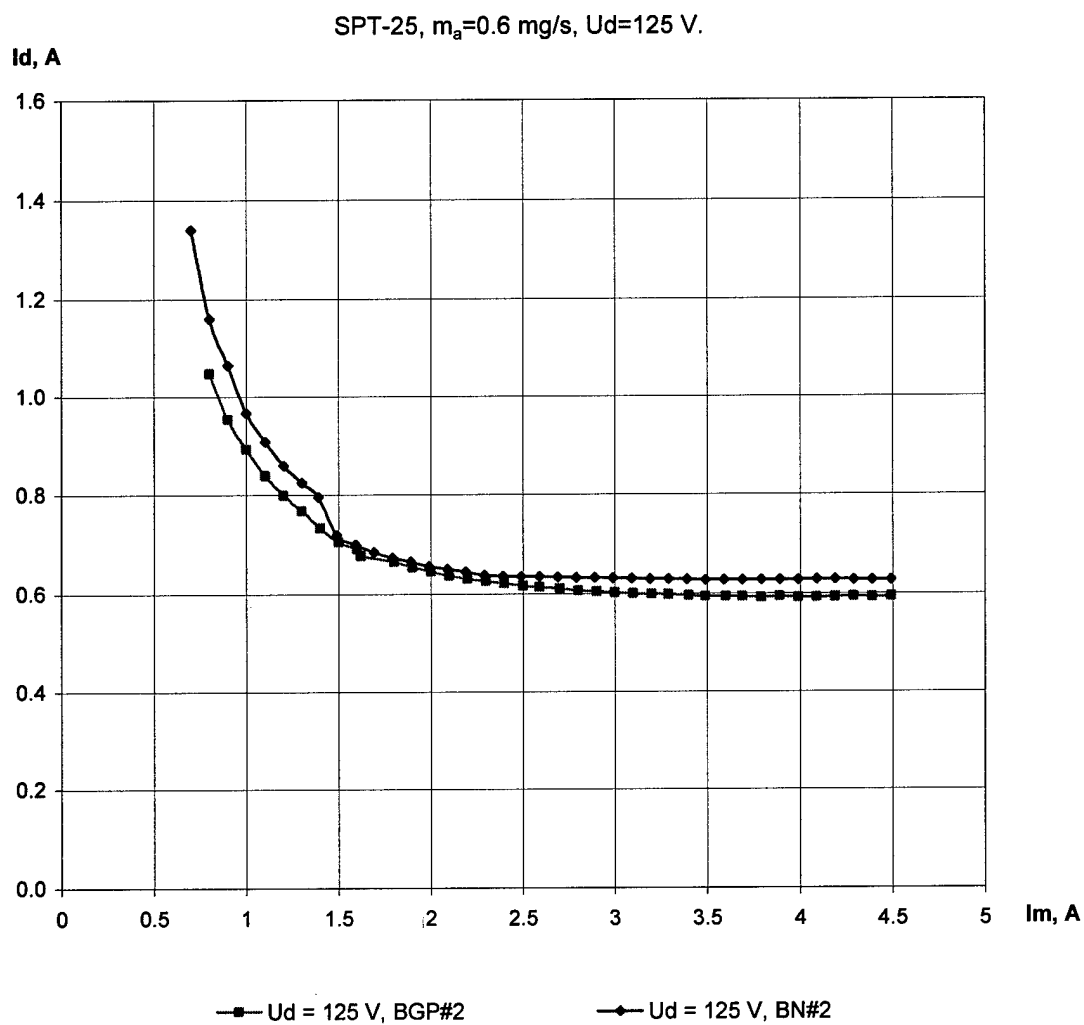


Fig.1.93. Discharge current versus the magnetization current.

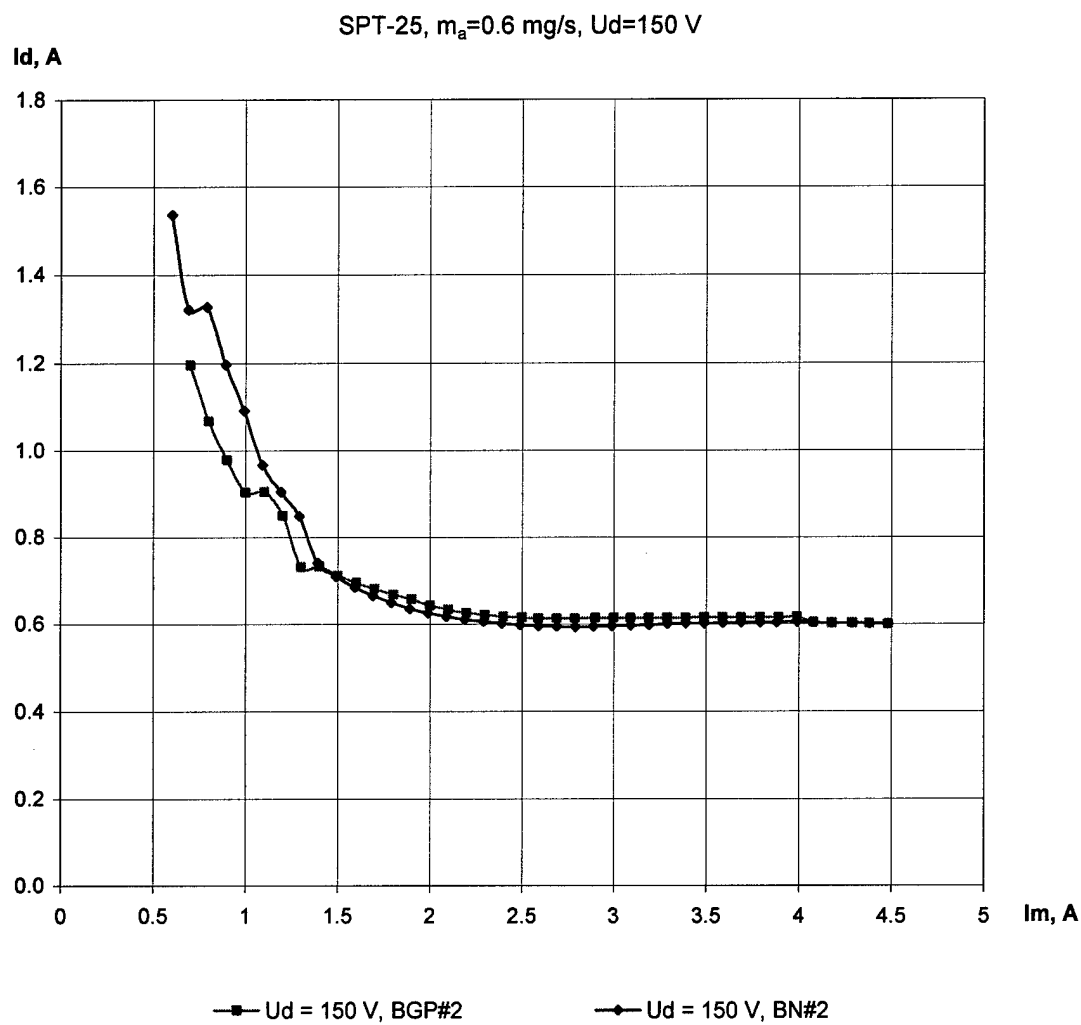


Fig.1.94. Discharge current versus the magnetization current.

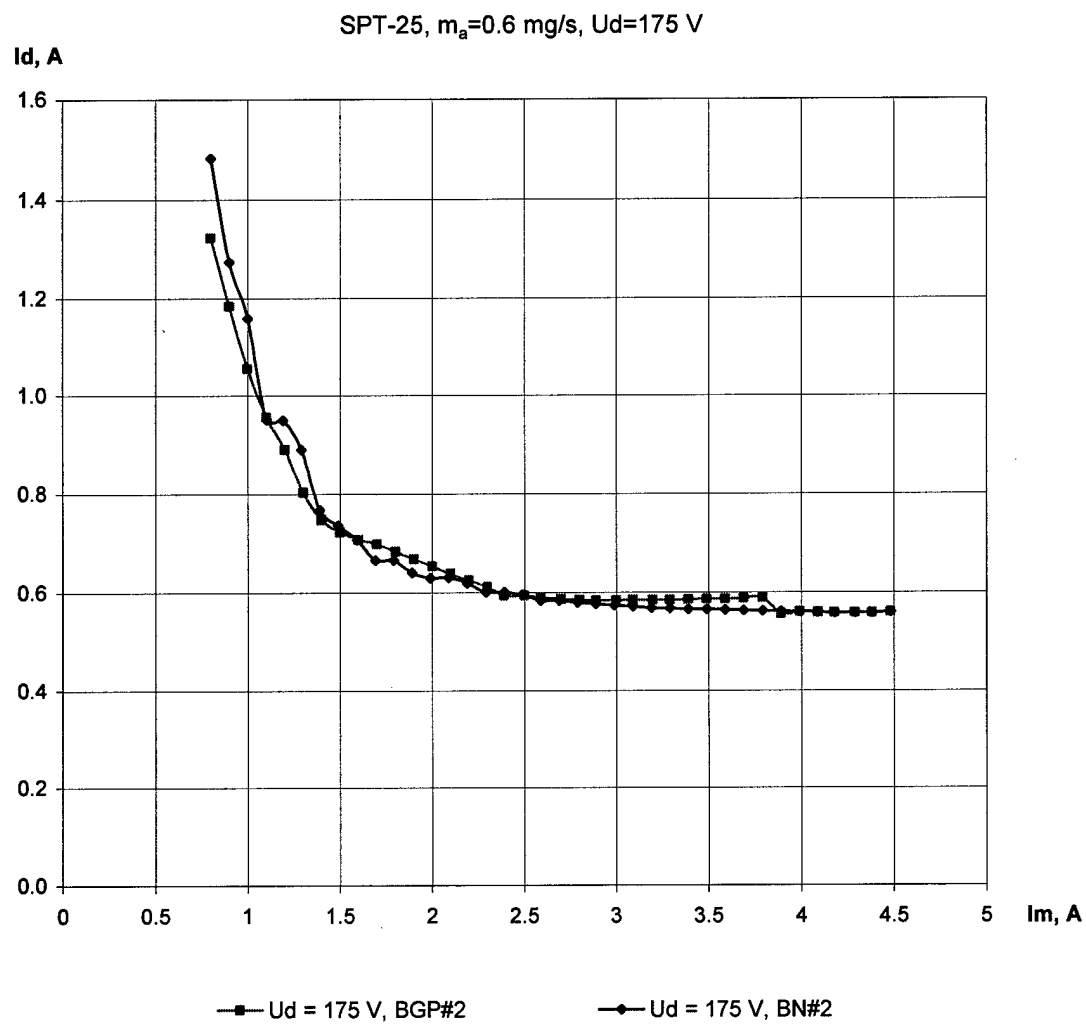


Fig.1.95. Discharge current versus the magnetization current.

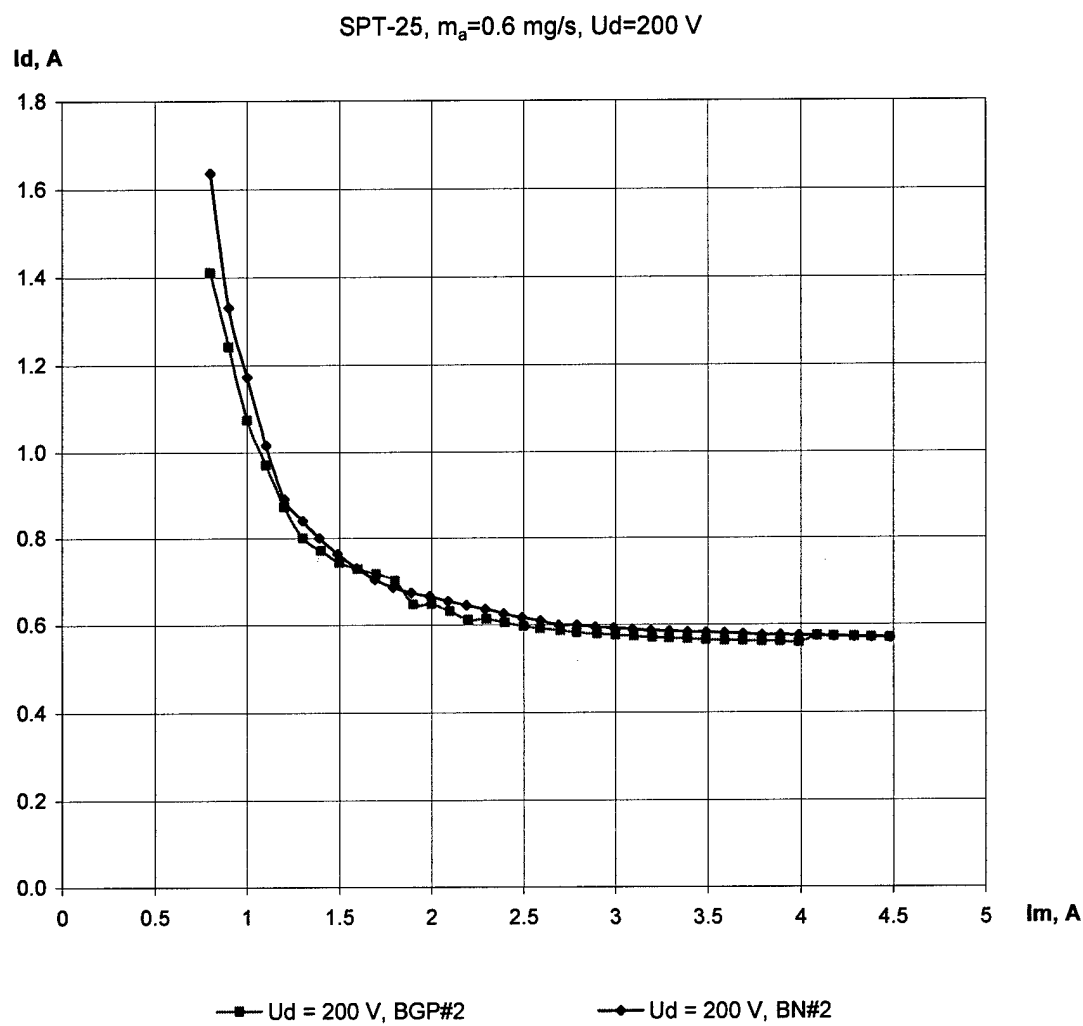


Fig.1.96. Discharge current versus the magnetization current.

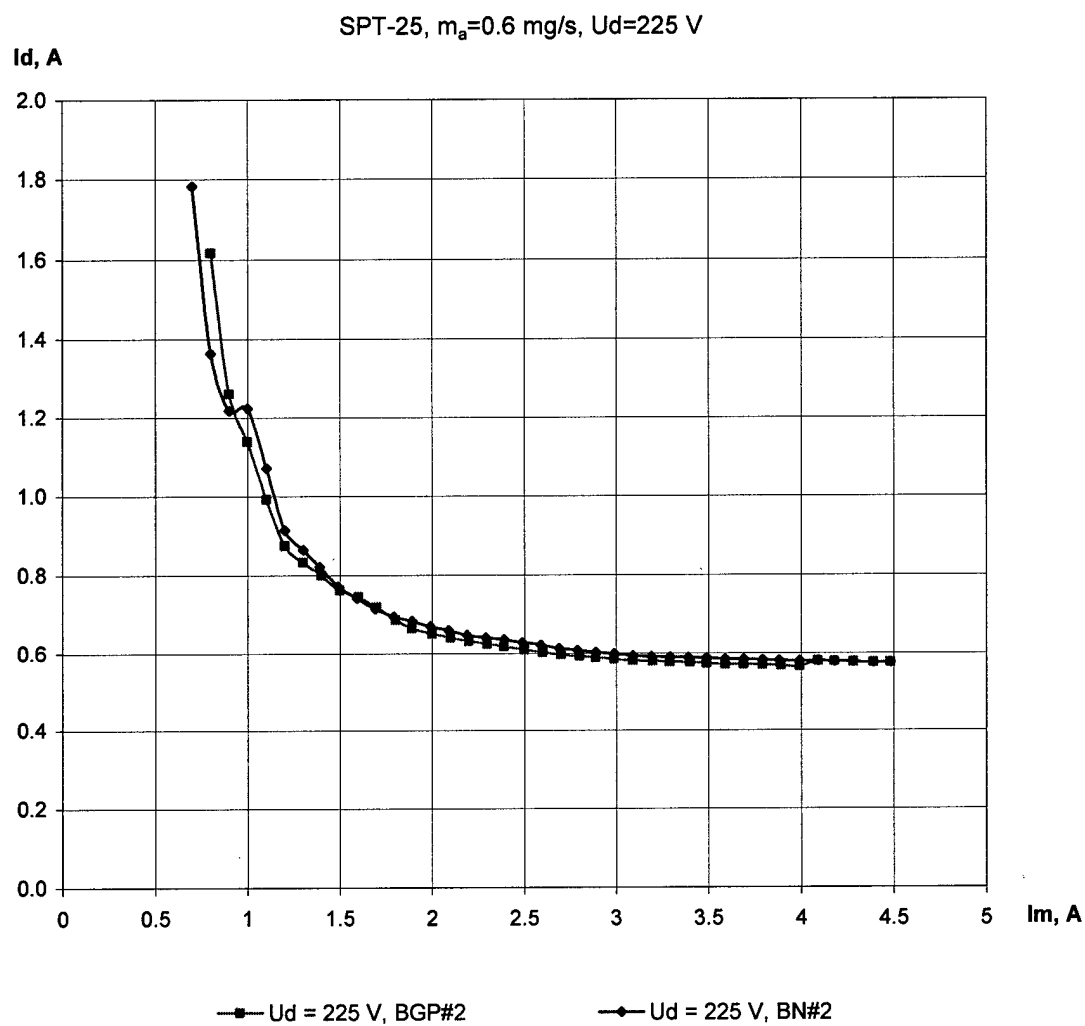


Fig.1.97. Discharge current versus the magnetization current.

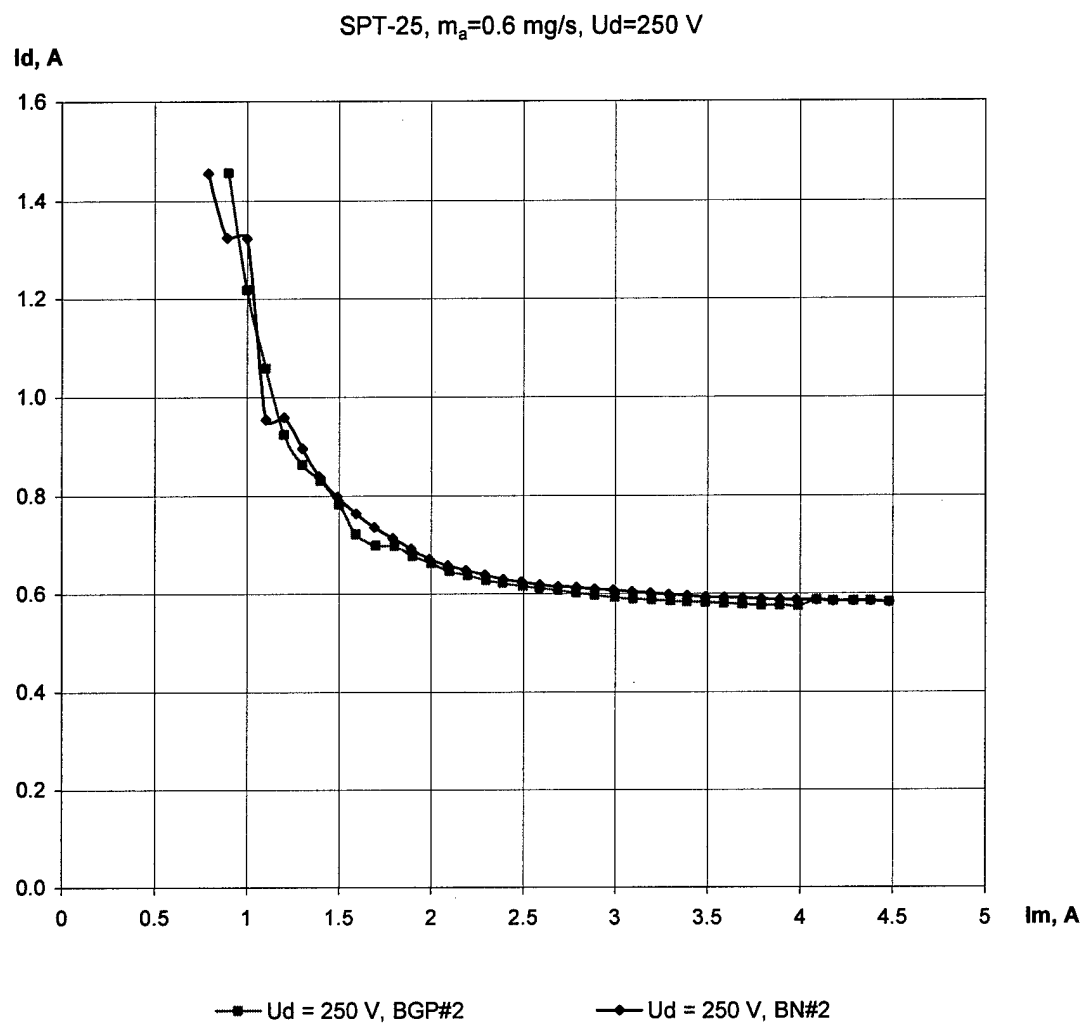


Fig.1.98. Discharge current versus the magnetization current.

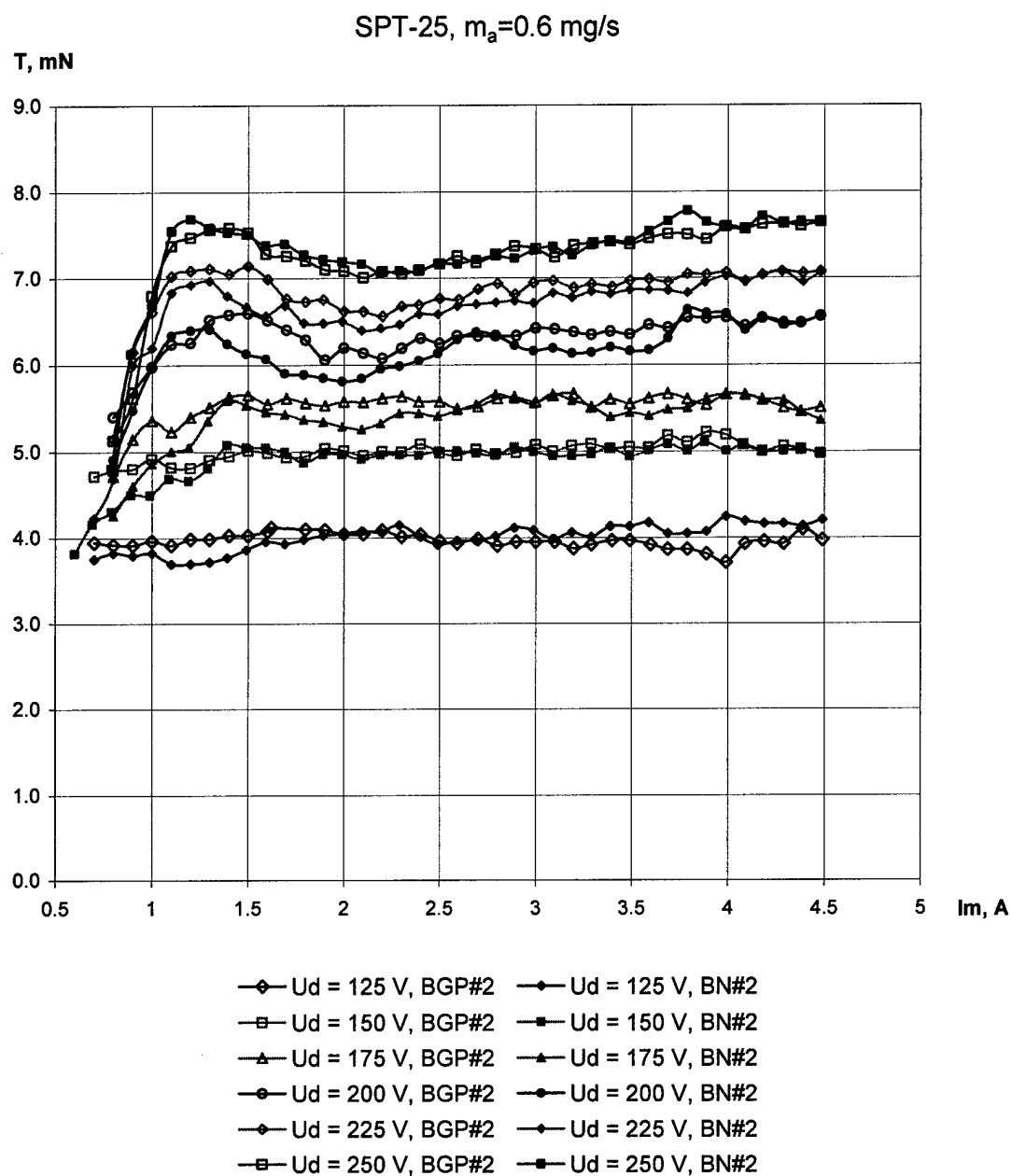


Fig.1.99. Thrust versus the magnetization current.

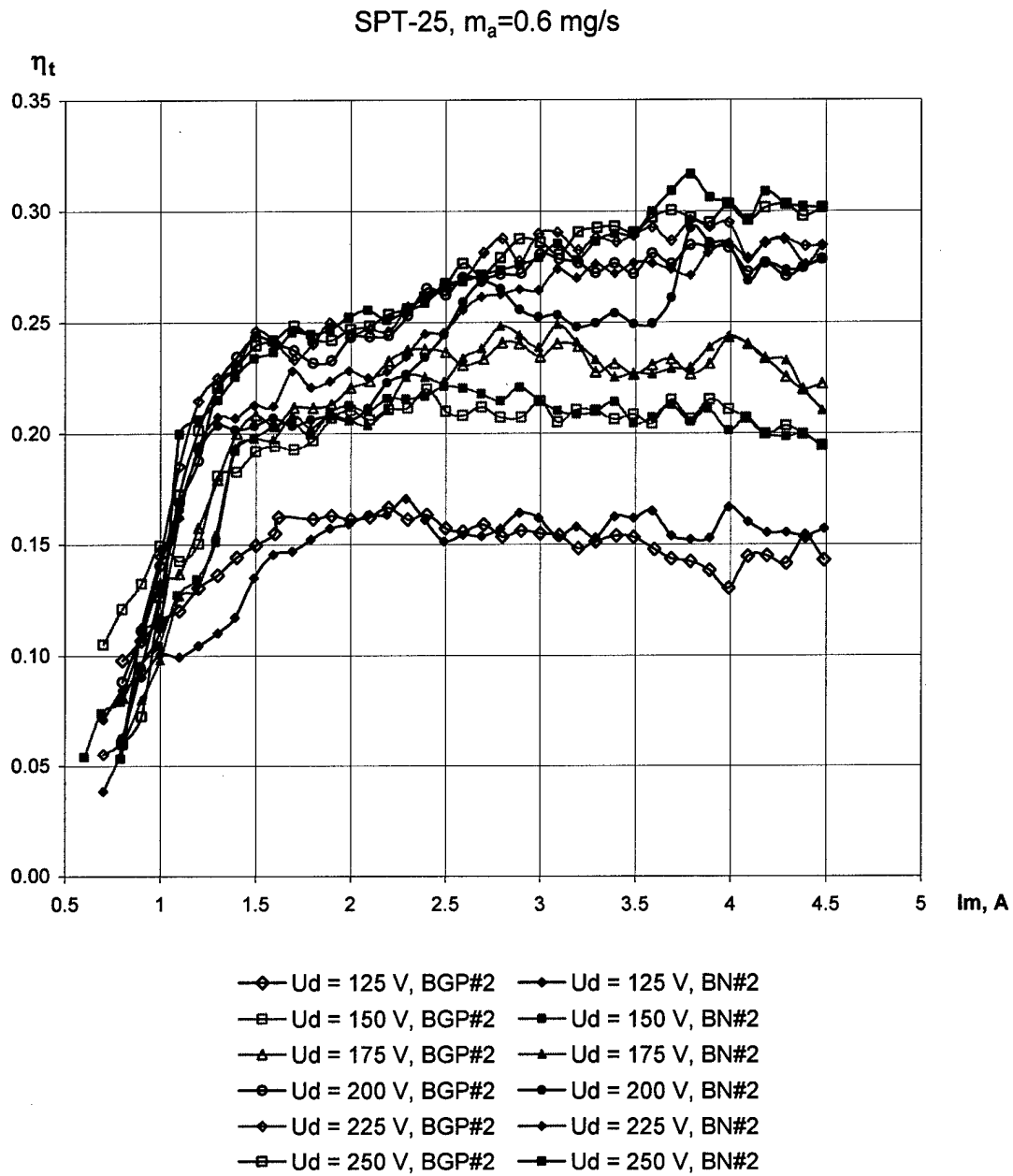


Fig.1.100. Thrust efficiency versus the magnetization current.

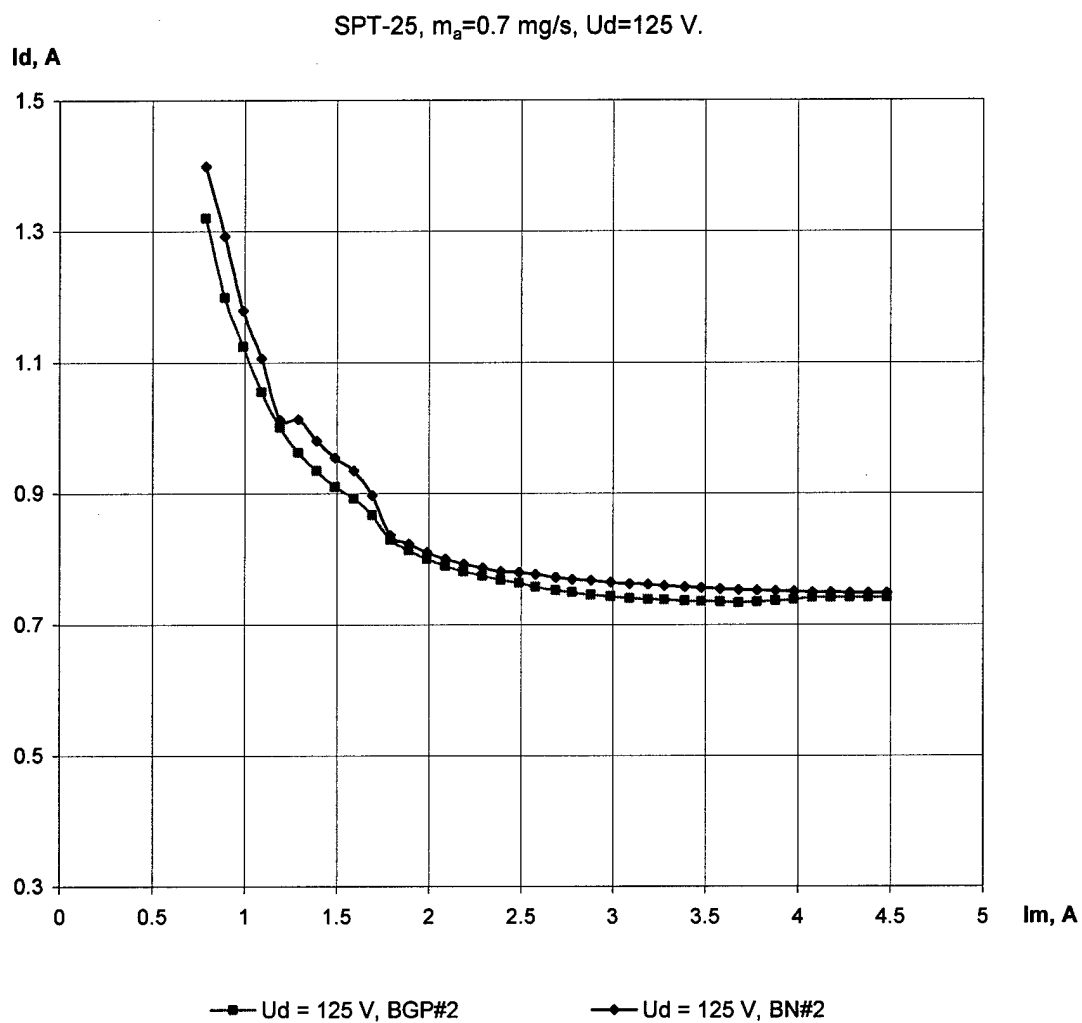


Fig.1.101. Discharge current versus the magnetization current.

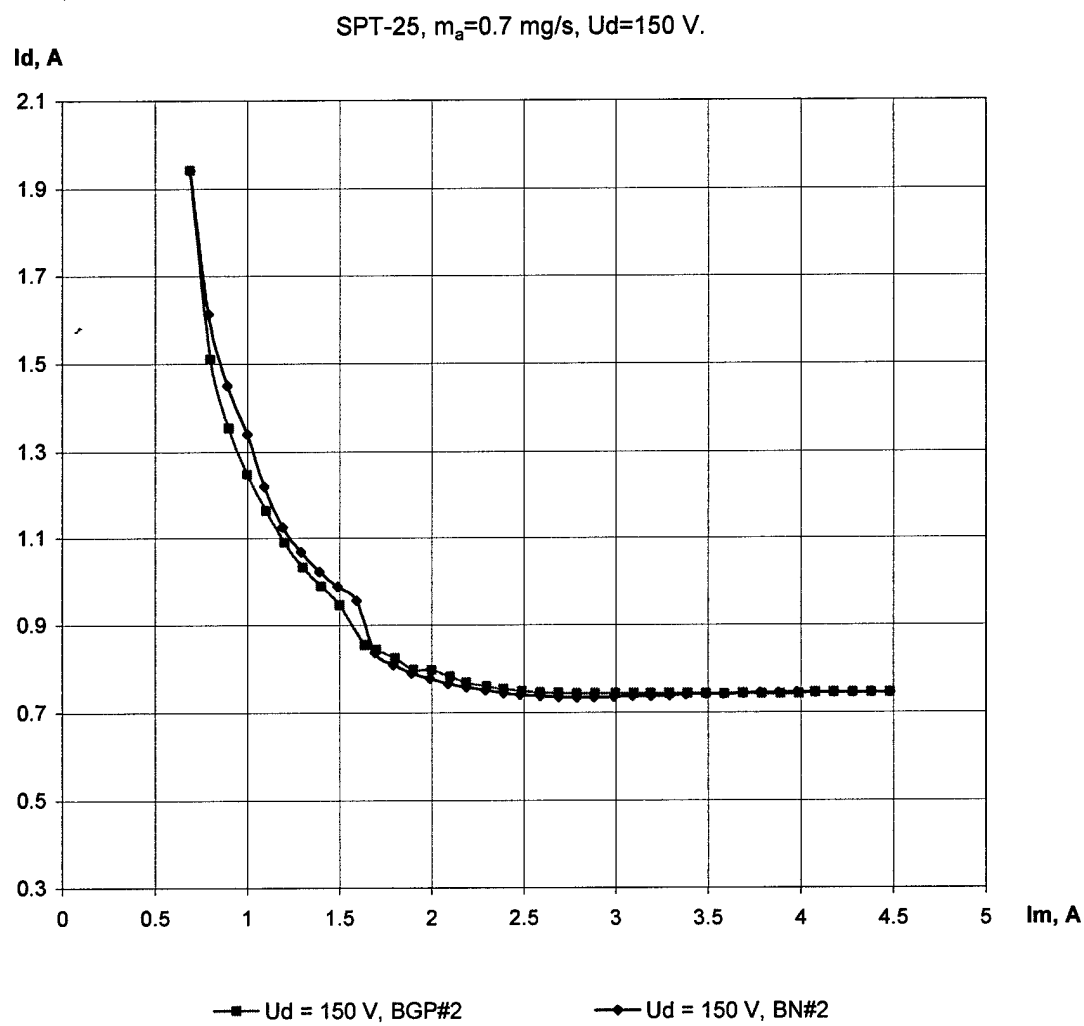


Fig.1.102. Discharge current versus the magnetization current.

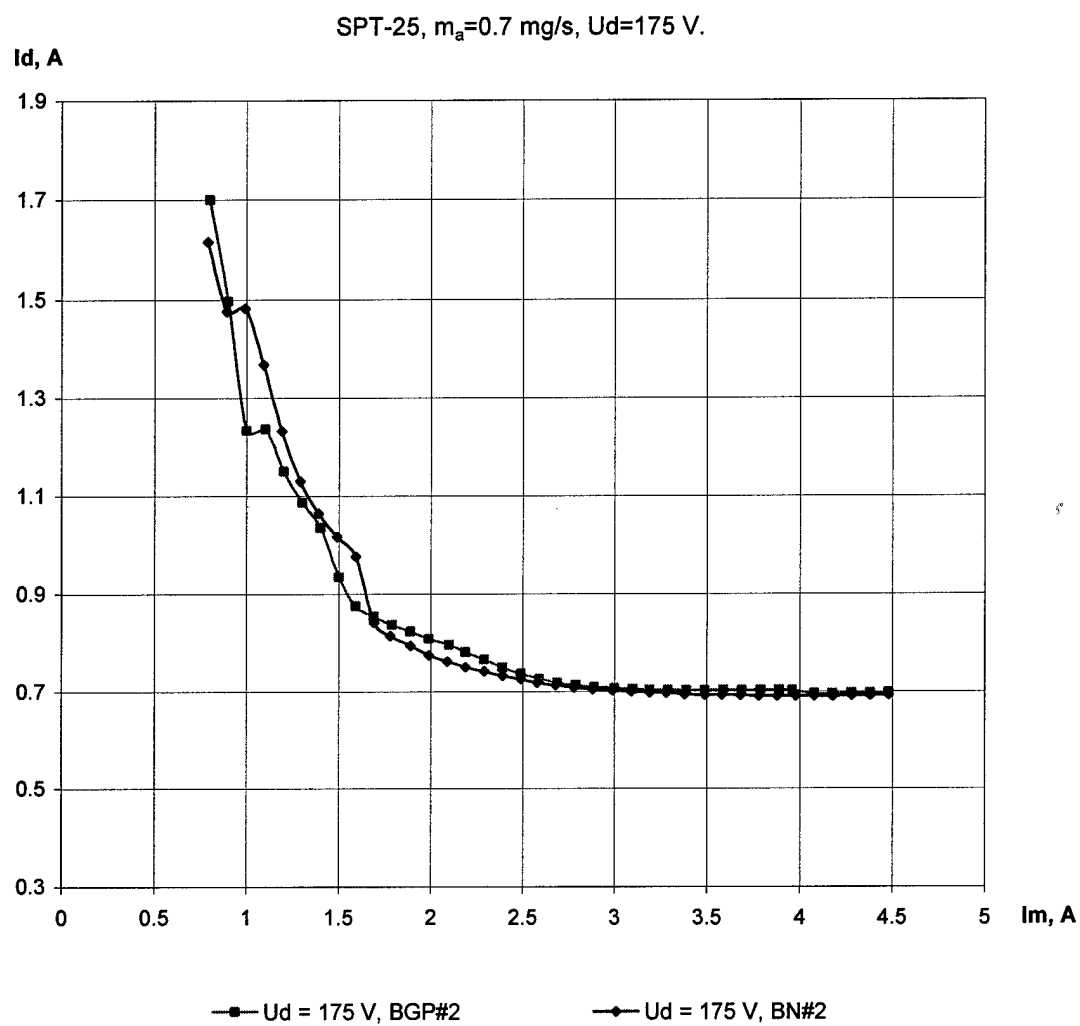


Fig.1.103. Discharge current versus the magnetization current.

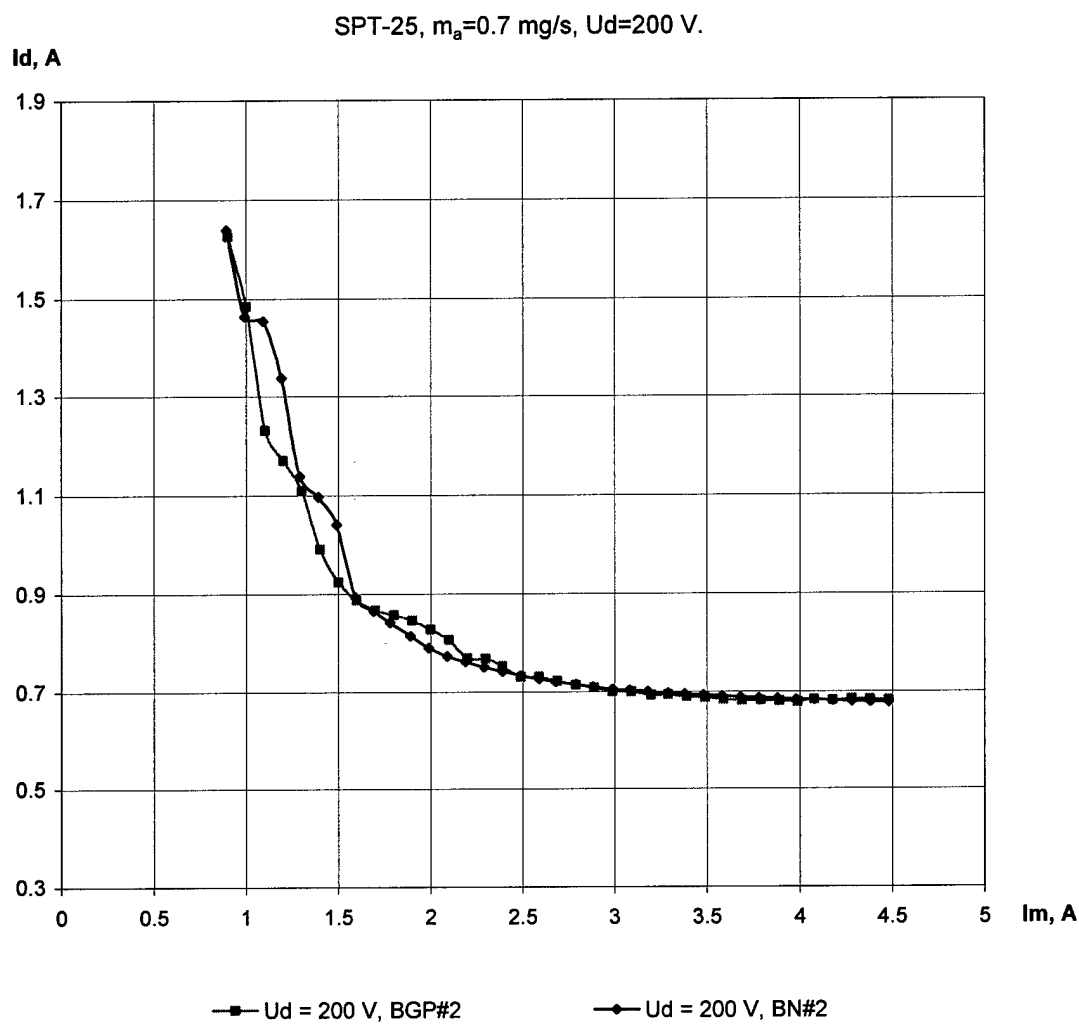


Fig.1.104. Discharge current versus the magnetization current.

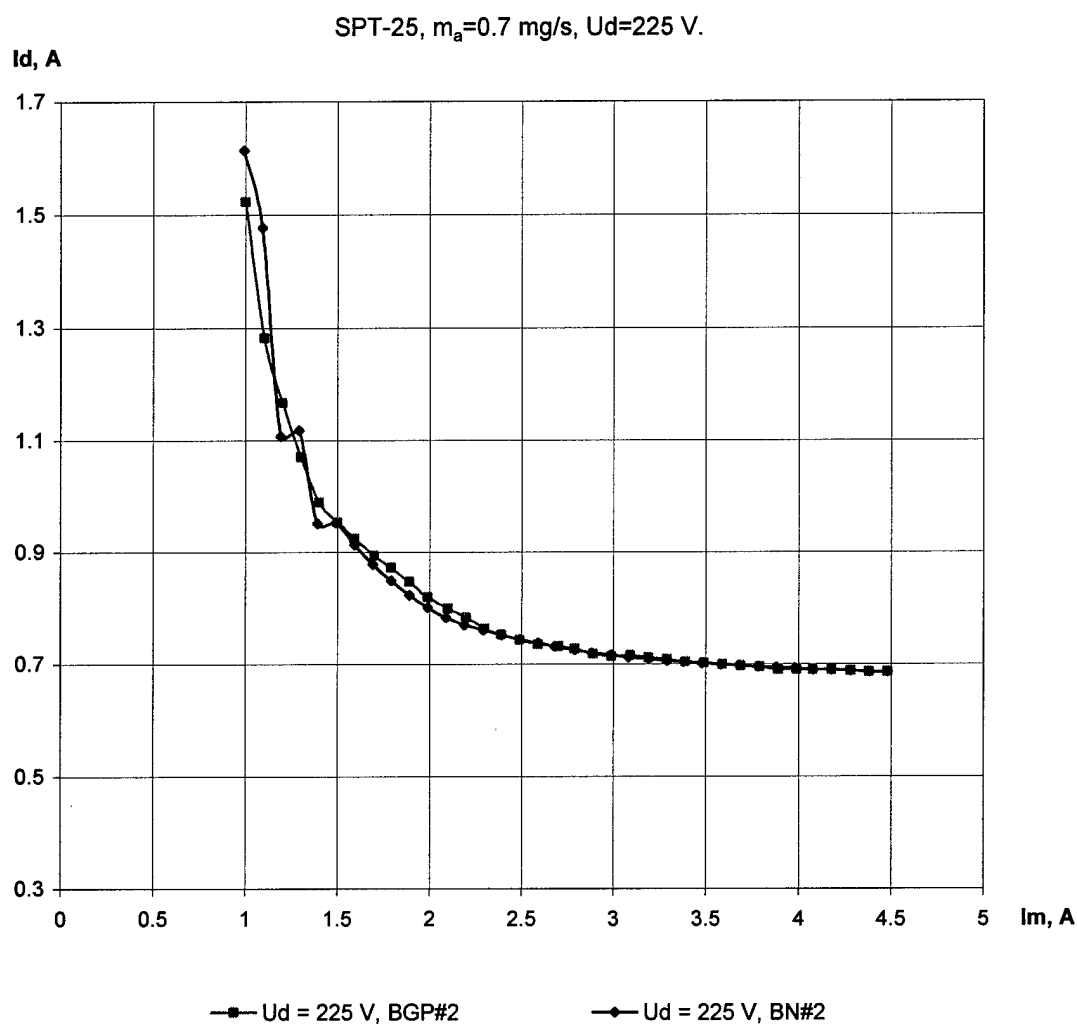


Fig.1.105. Discharge current versus the magnetization current.

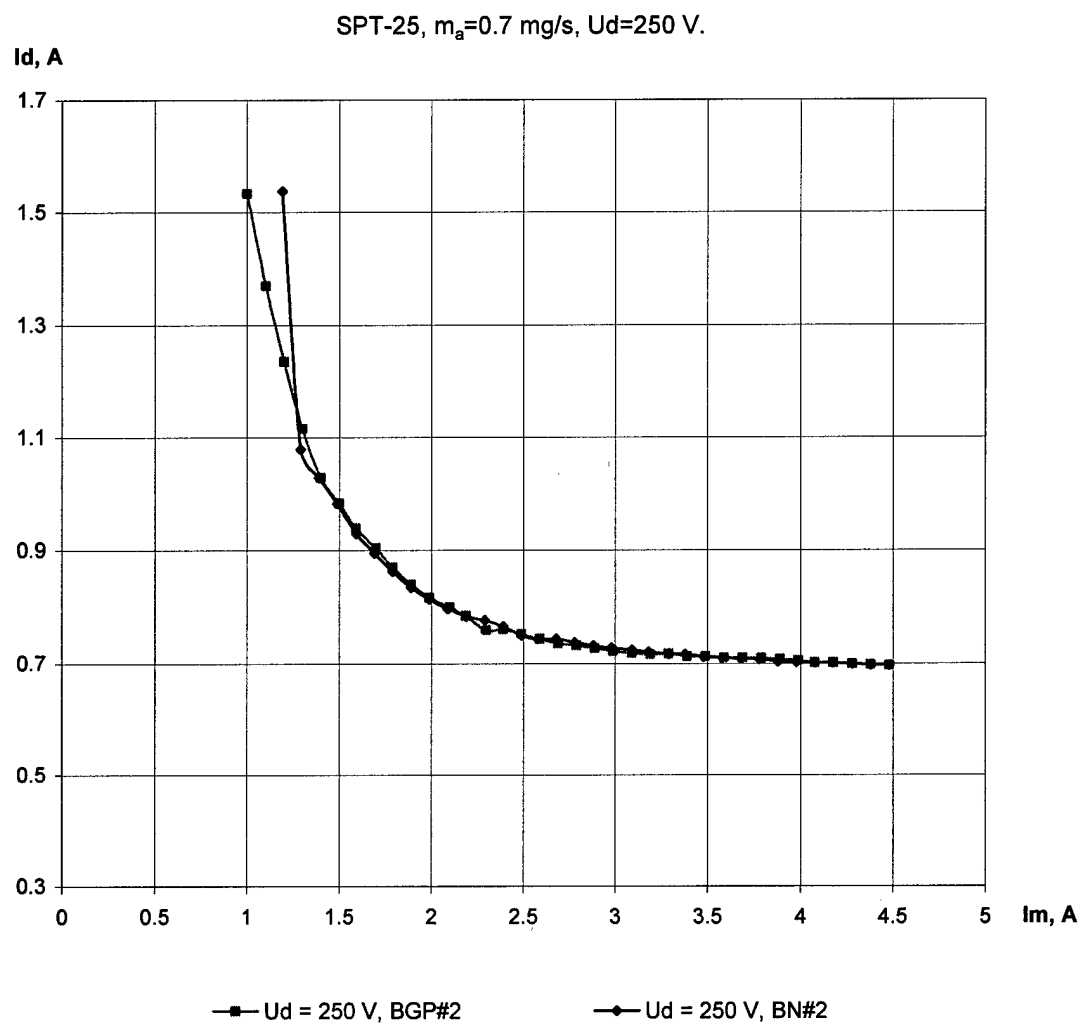


Fig.1.106. Discharge current versus the magnetization current.

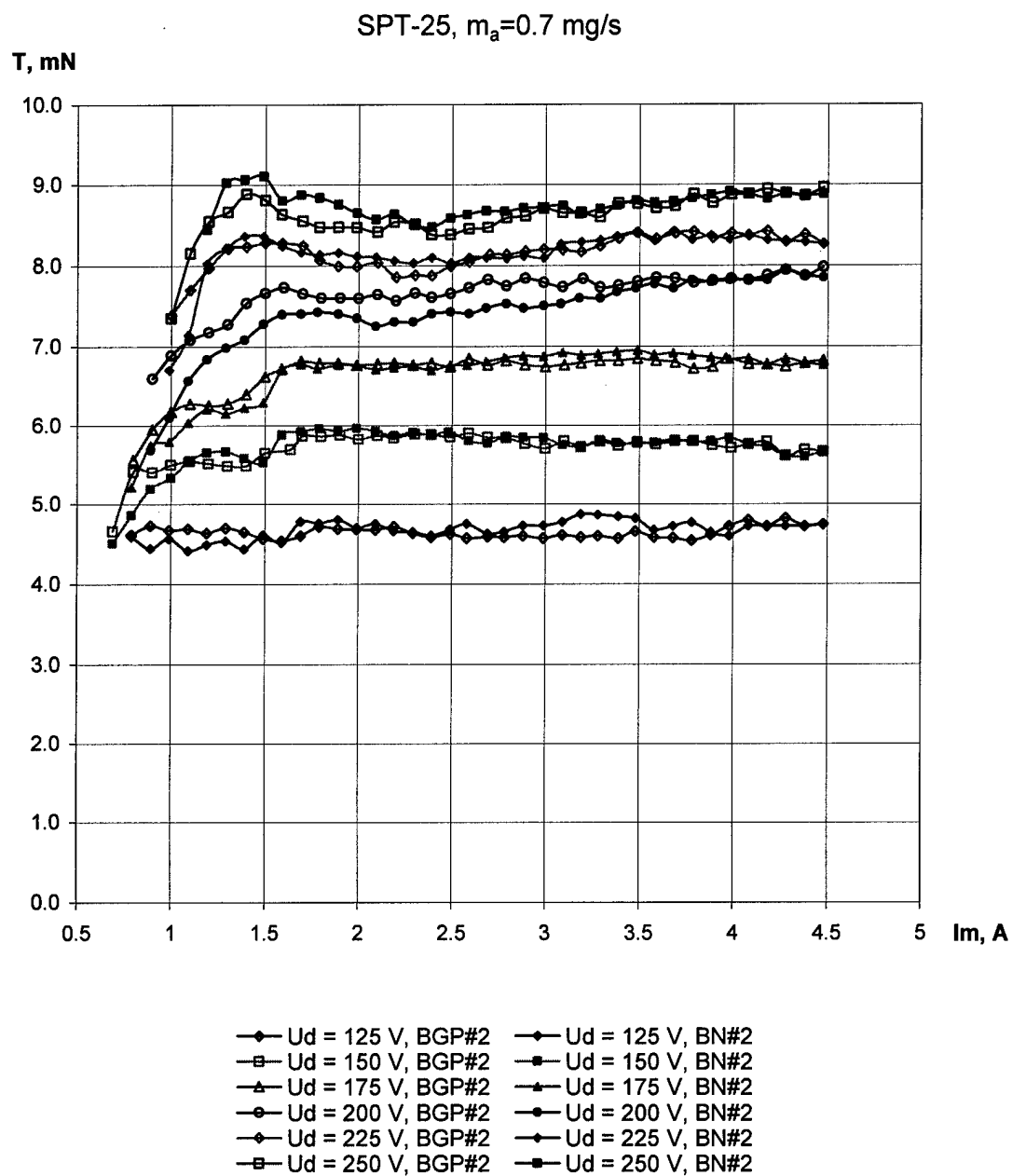


Fig.1.107. Thrust versus the magnetization current.

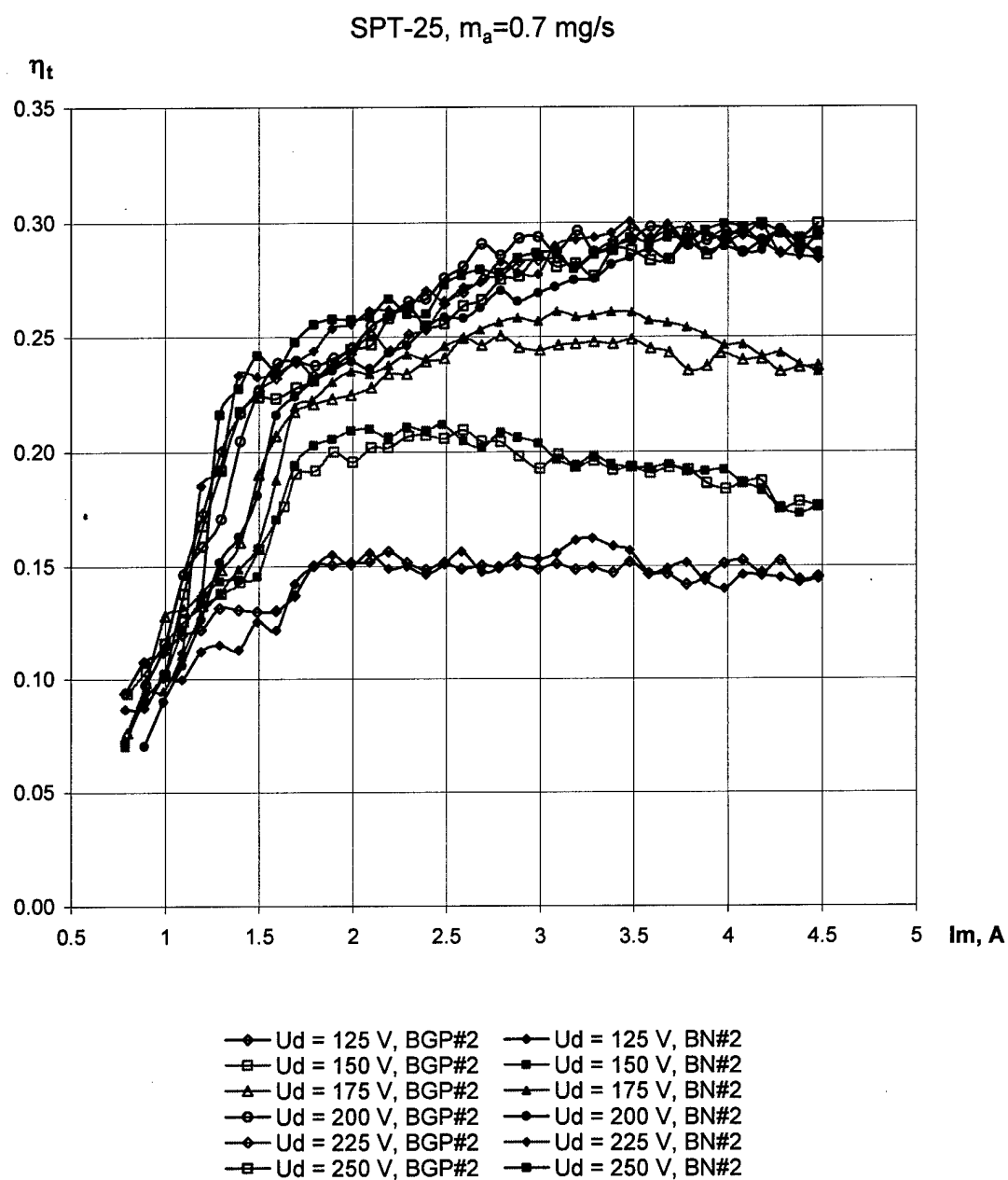


Fig.1.108. Thrust efficiency versus the magnetization current.

SPT-25, $m=0.6$ mg/s, $I_m=1.5$ A.

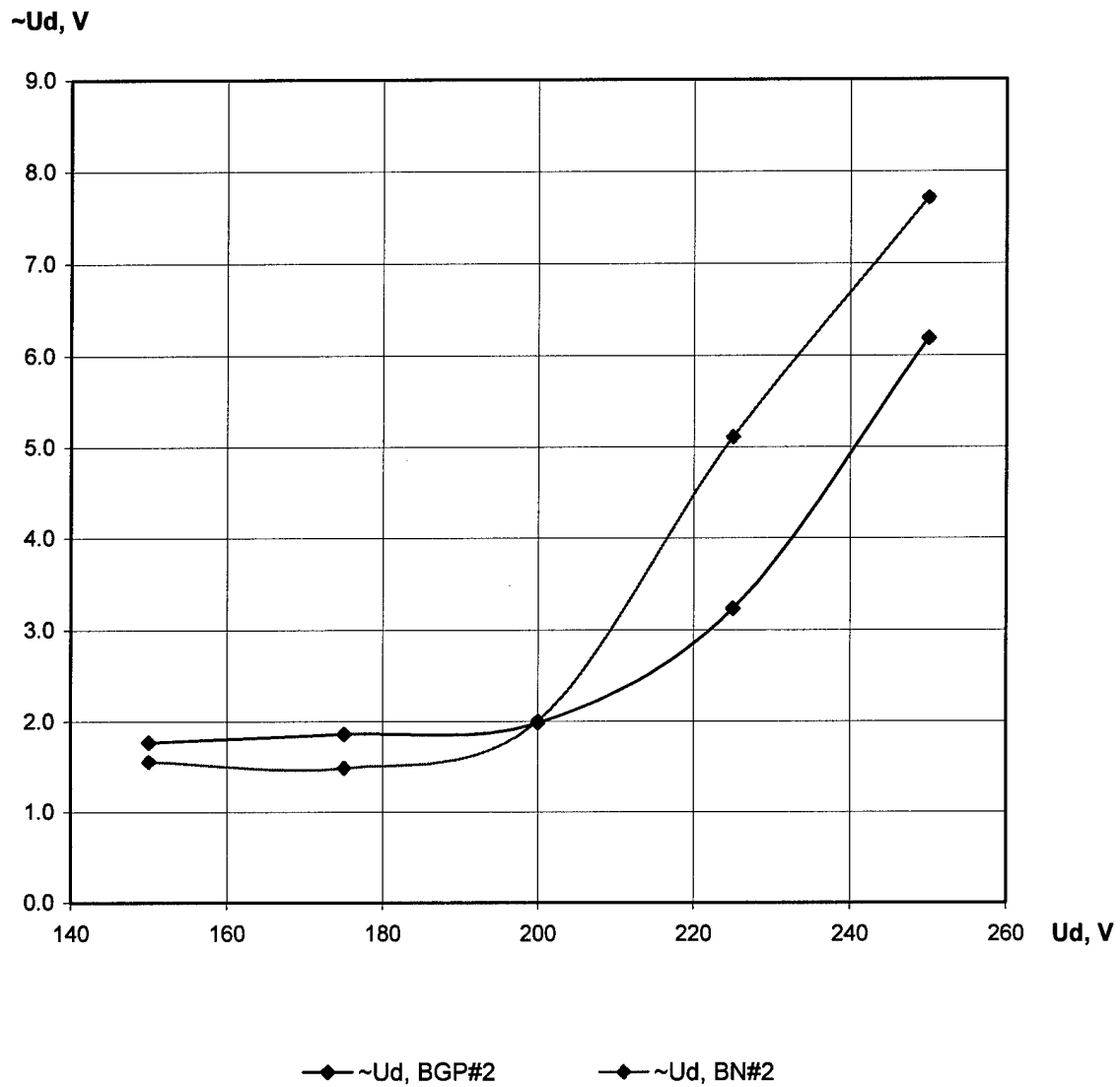


Fig.1.109. The discharge voltage oscillations RMS amplitude versus the discharge voltage.

SPT-25, $m=0.6$ mg/s, $I_m=1.5$ A.

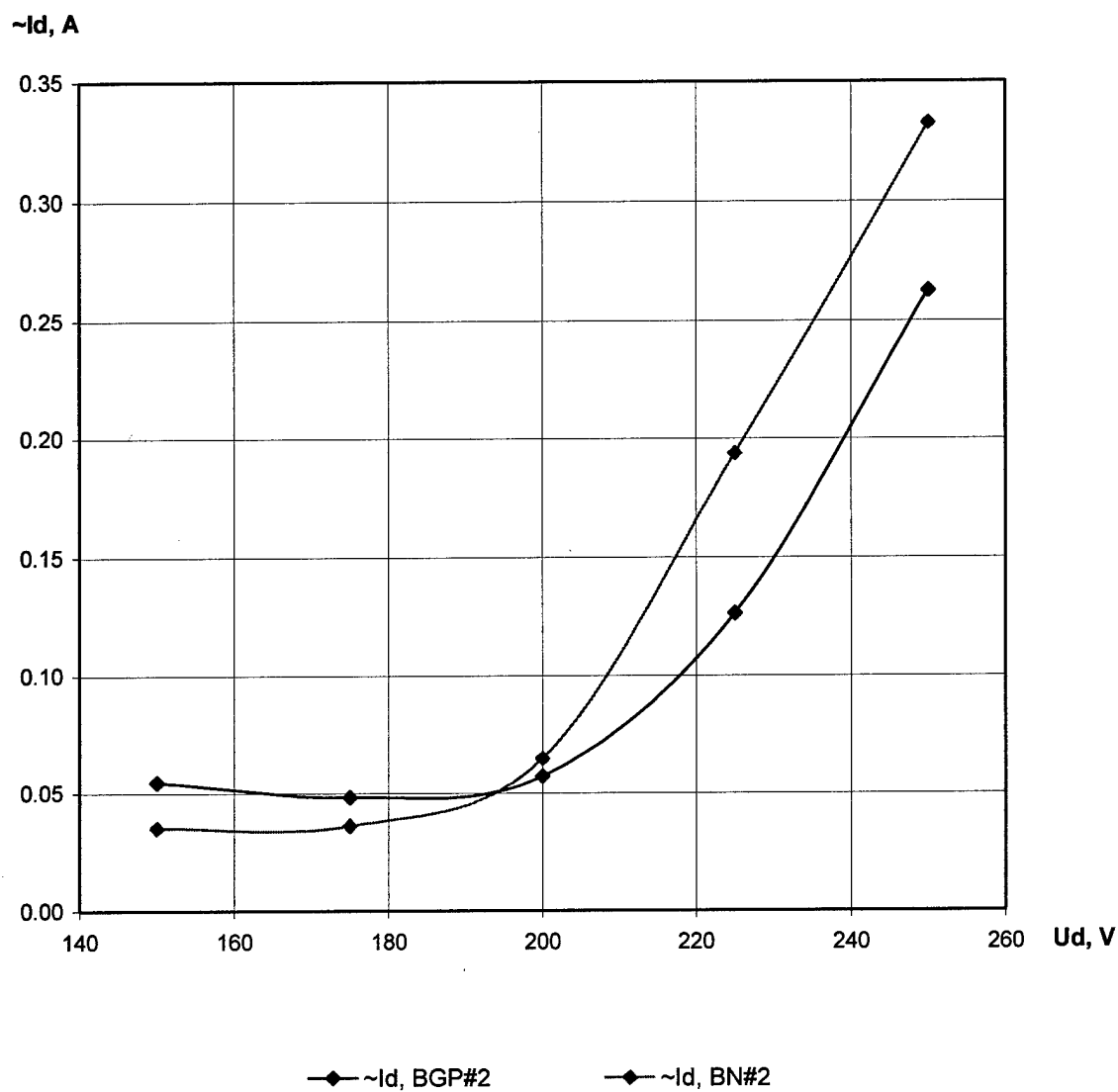


Fig.1.110. The discharge current oscillations RMS amplitude versus the discharge voltage.

SPT-25, $m=0.6$ mg/s, $I_m=2.7$ A.

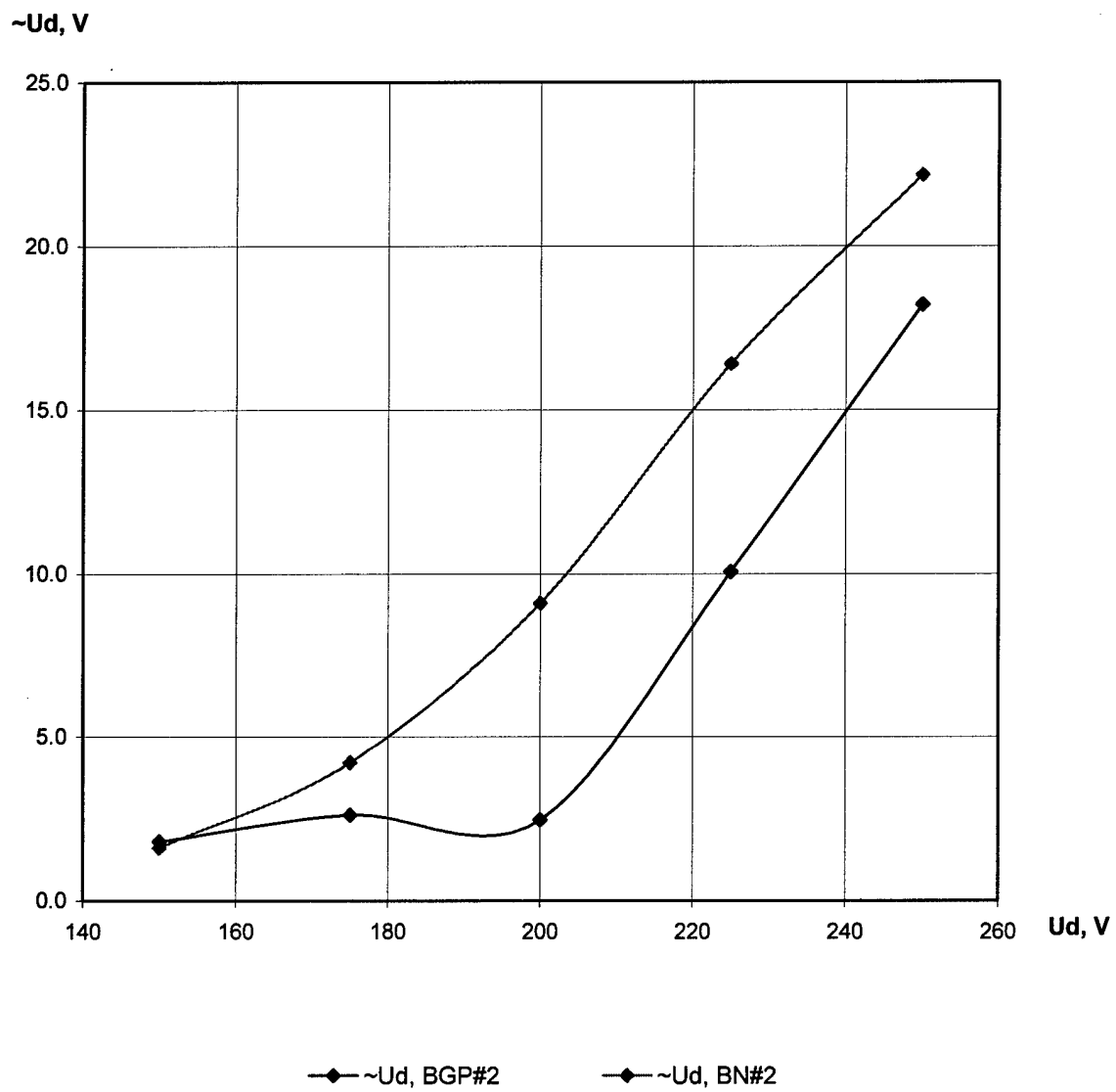


Fig.1.111. The discharge voltage oscillations RMS amplitude versus the discharge voltage.

SPT-25, $m=0.6$ mg/s, $I_m=2.7$ A.

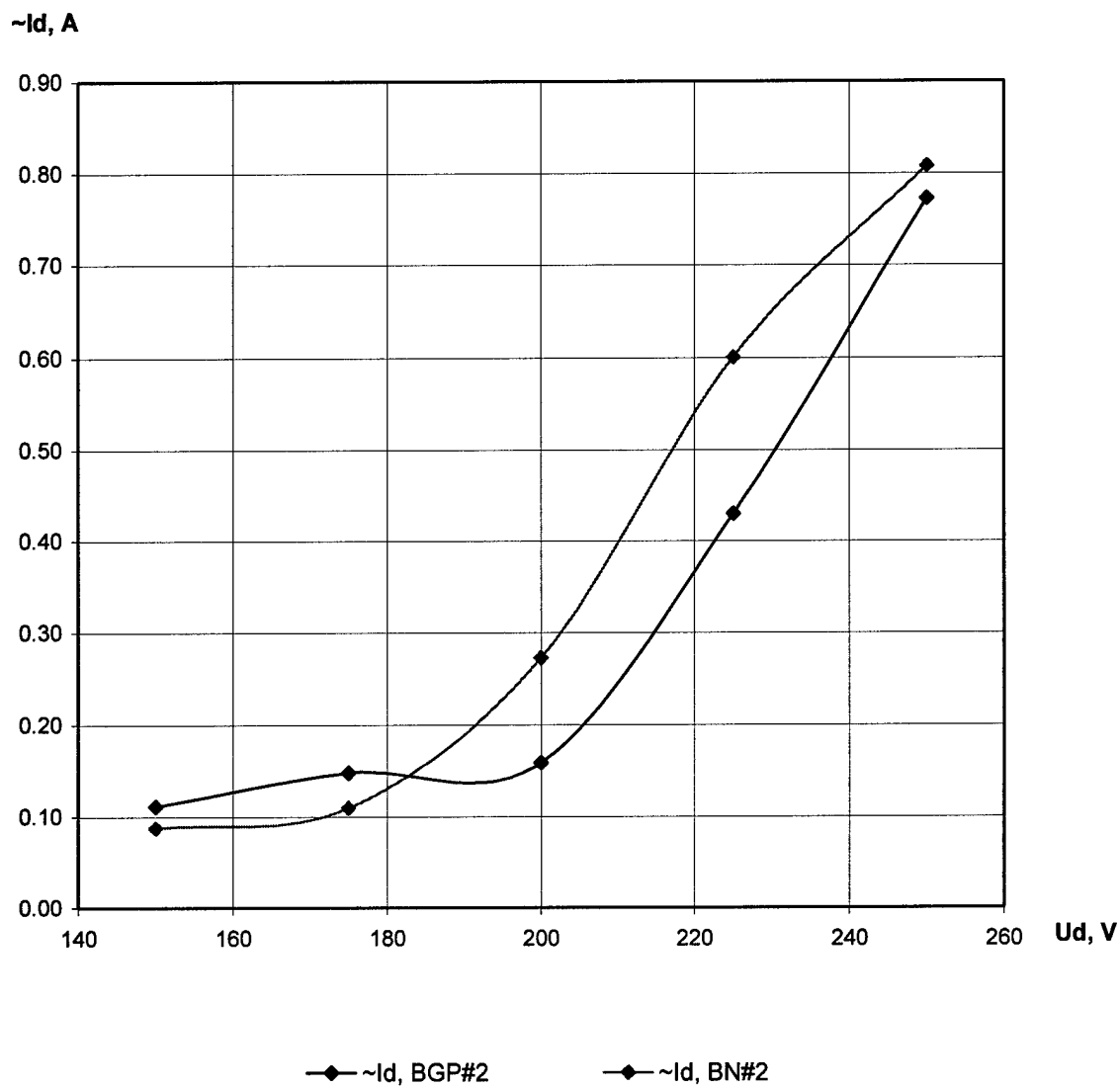


Fig.1.112. The discharge current oscillations RMS amplitude versus the discharge voltage.

SPT-25, $m=0.6$ mg/s, $I_m=4.0$ A.

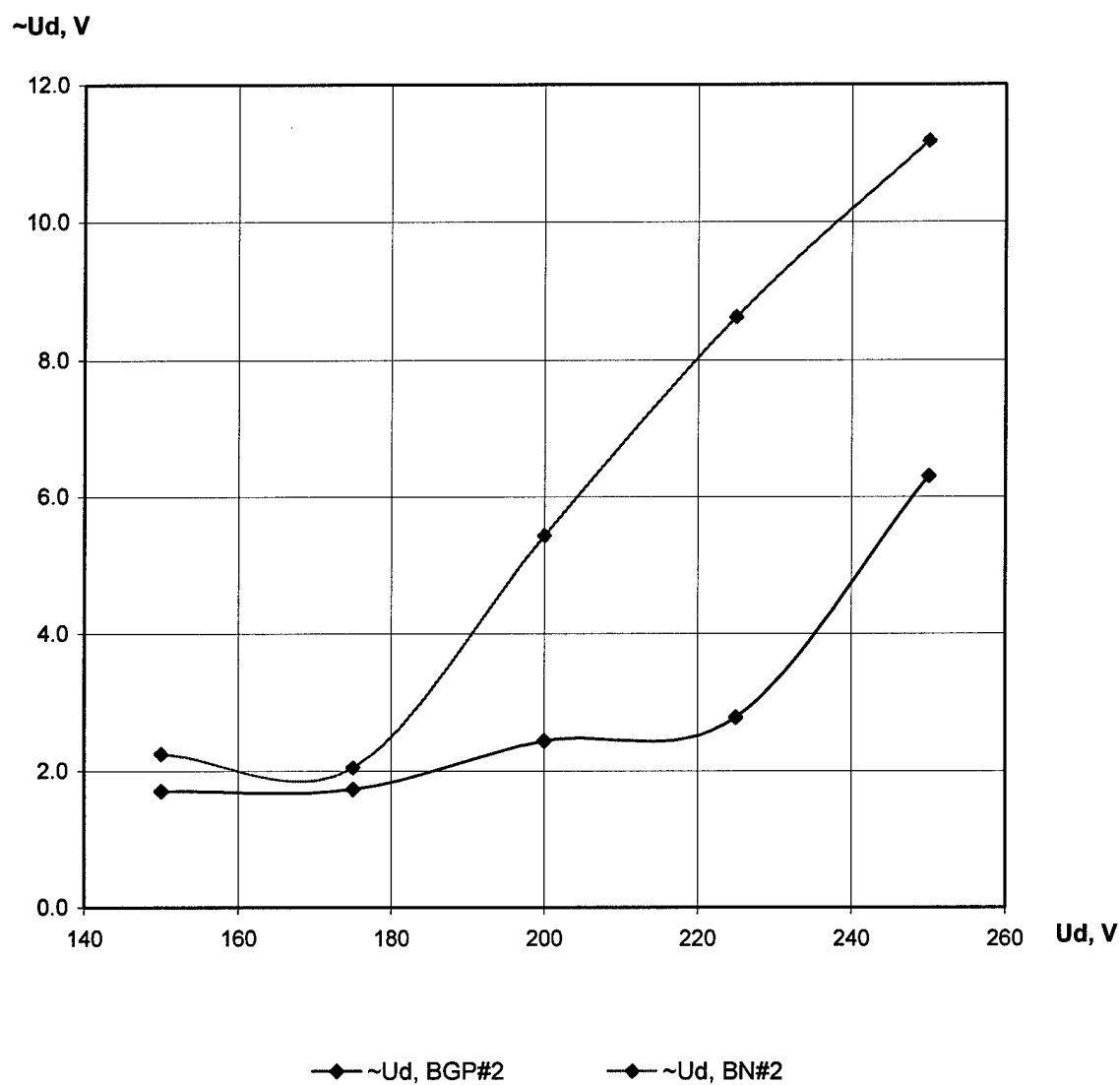


Fig.1.113. The discharge voltage oscillations RMS amplitude versus the discharge voltage.

SPT-25, $m=0.6$ mg/s, $I_m=4.0$ A.

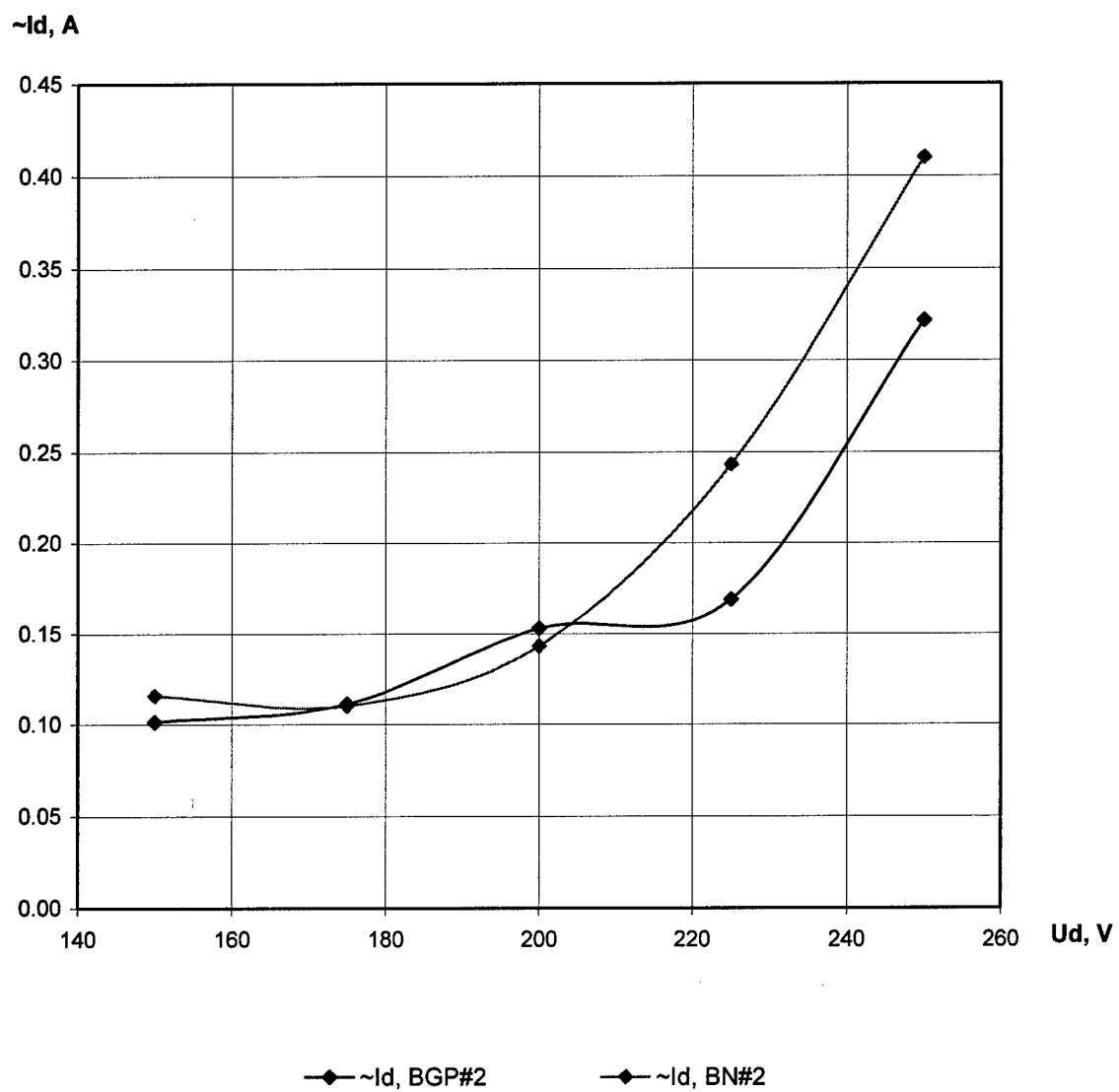


Fig.1.114. The discharge current oscillations RMS amplitude versus the discharge voltage.

SPT-25, $m=0.7$ mg/s, $I_m=1.5$ A.

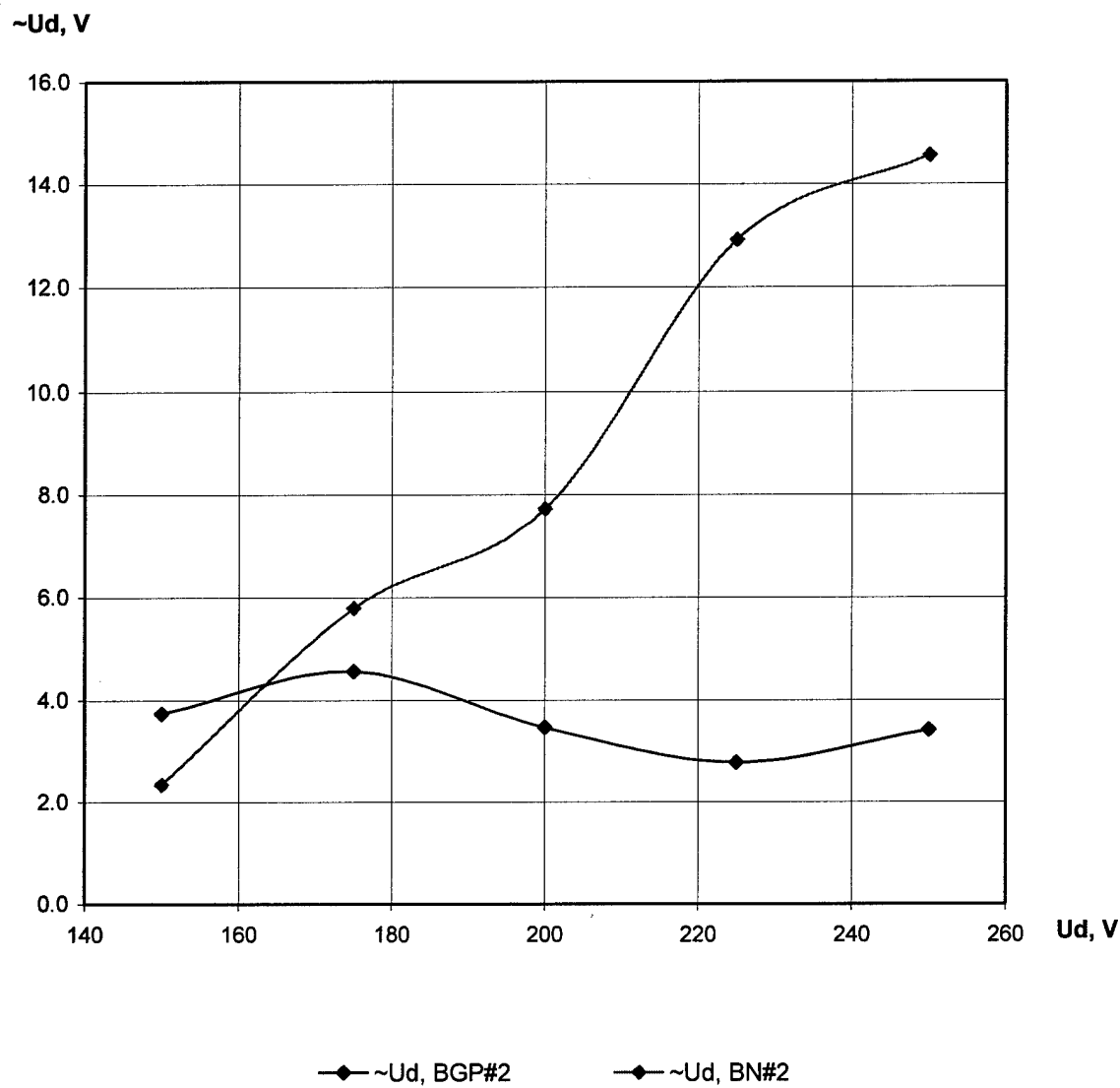


Fig.1.115. The discharge voltage oscillations RMS amplitude versus the discharge voltage.

SPT-25, $m=0.7$ mg/s, $I_m=1.5$ A.

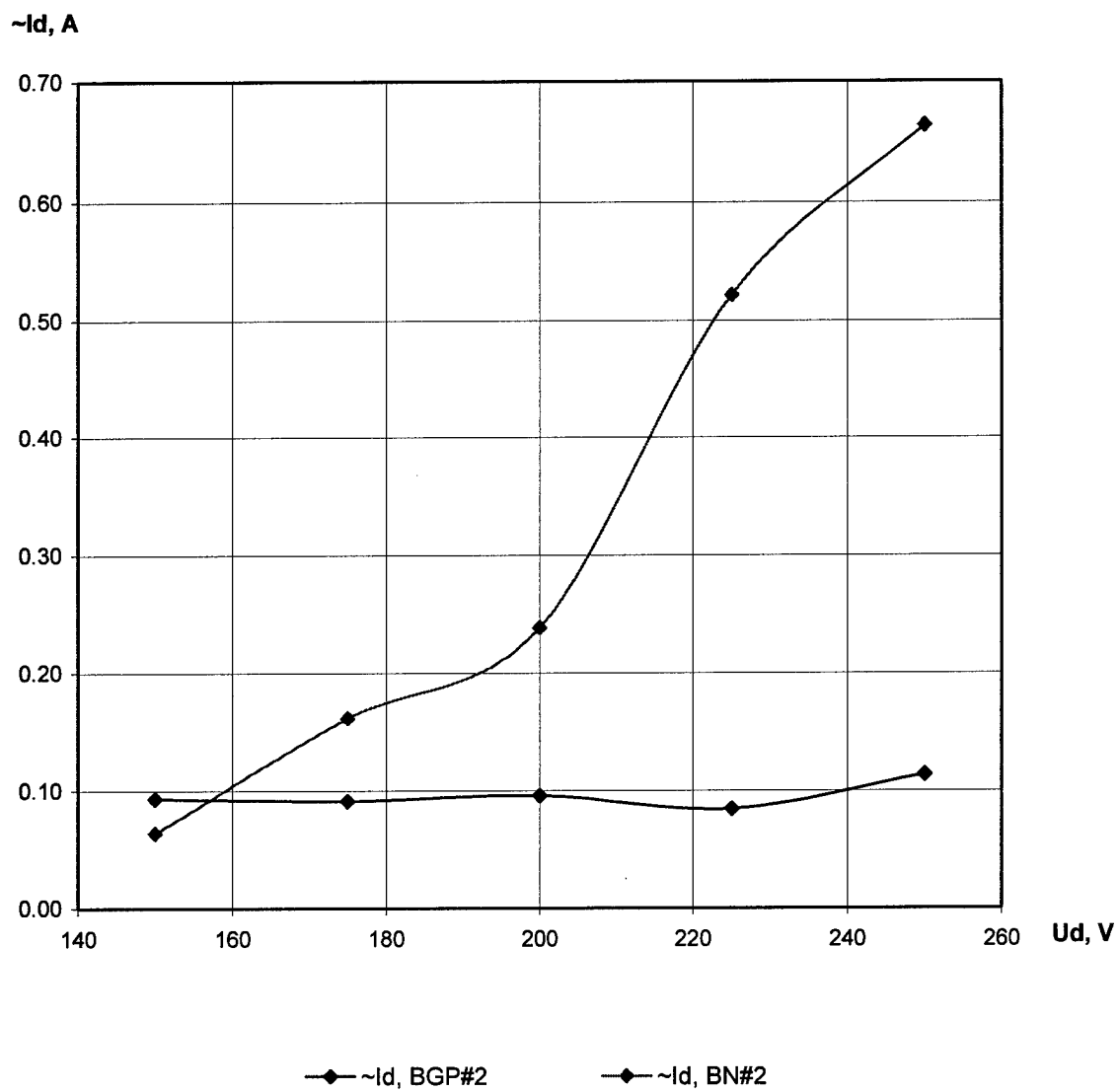


Fig.1.116. The discharge current oscillations RMS amplitude versus the discharge voltage.

SPT-25, $m=0.7$ mg/s, $I_m=2.7$ A.

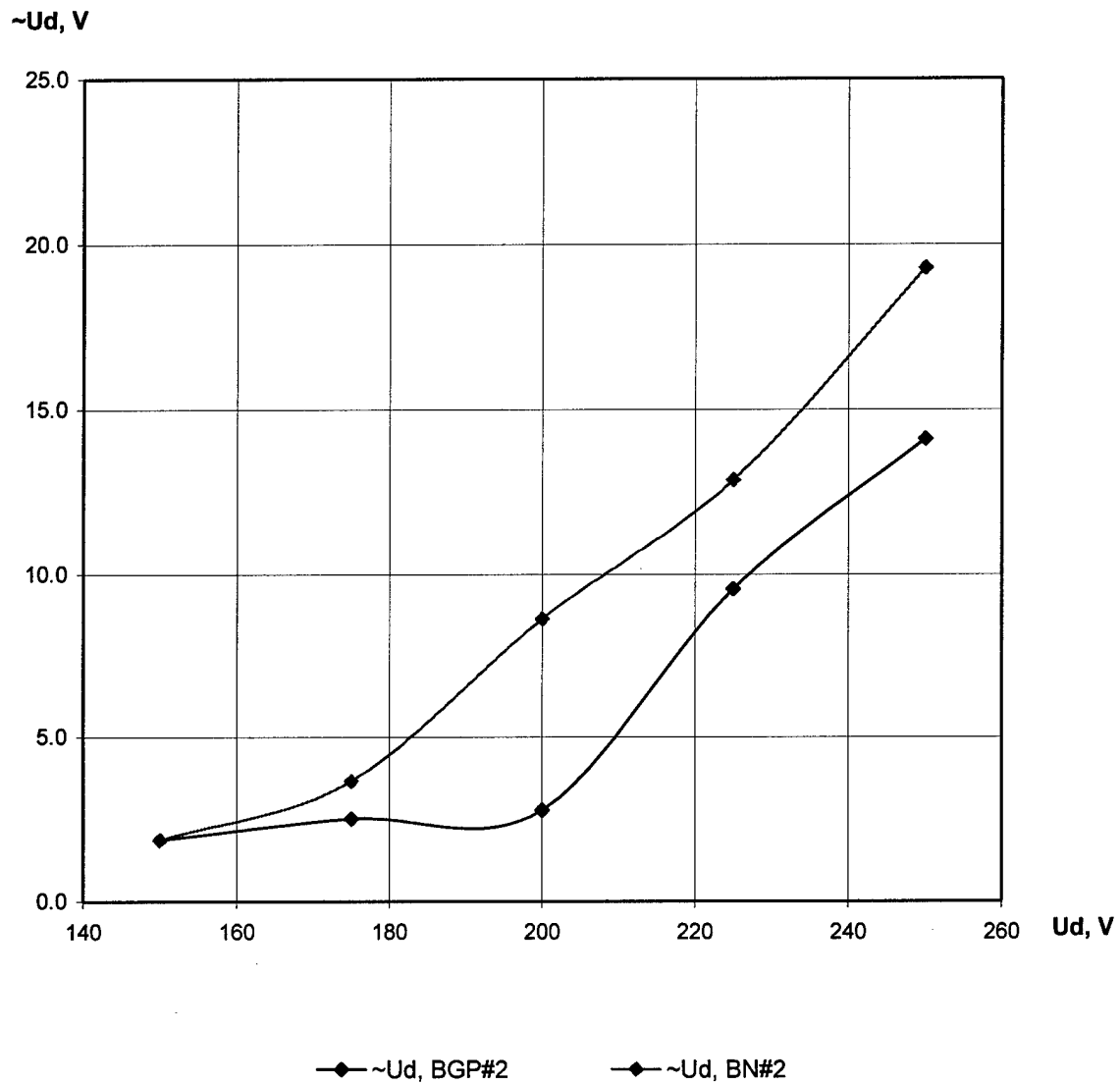


Fig.1.117. The discharge voltage oscillations RMS amplitude versus the discharge voltage.

SPT-25, $m=0.7$ mg/s, $I_m=2.7$ A.

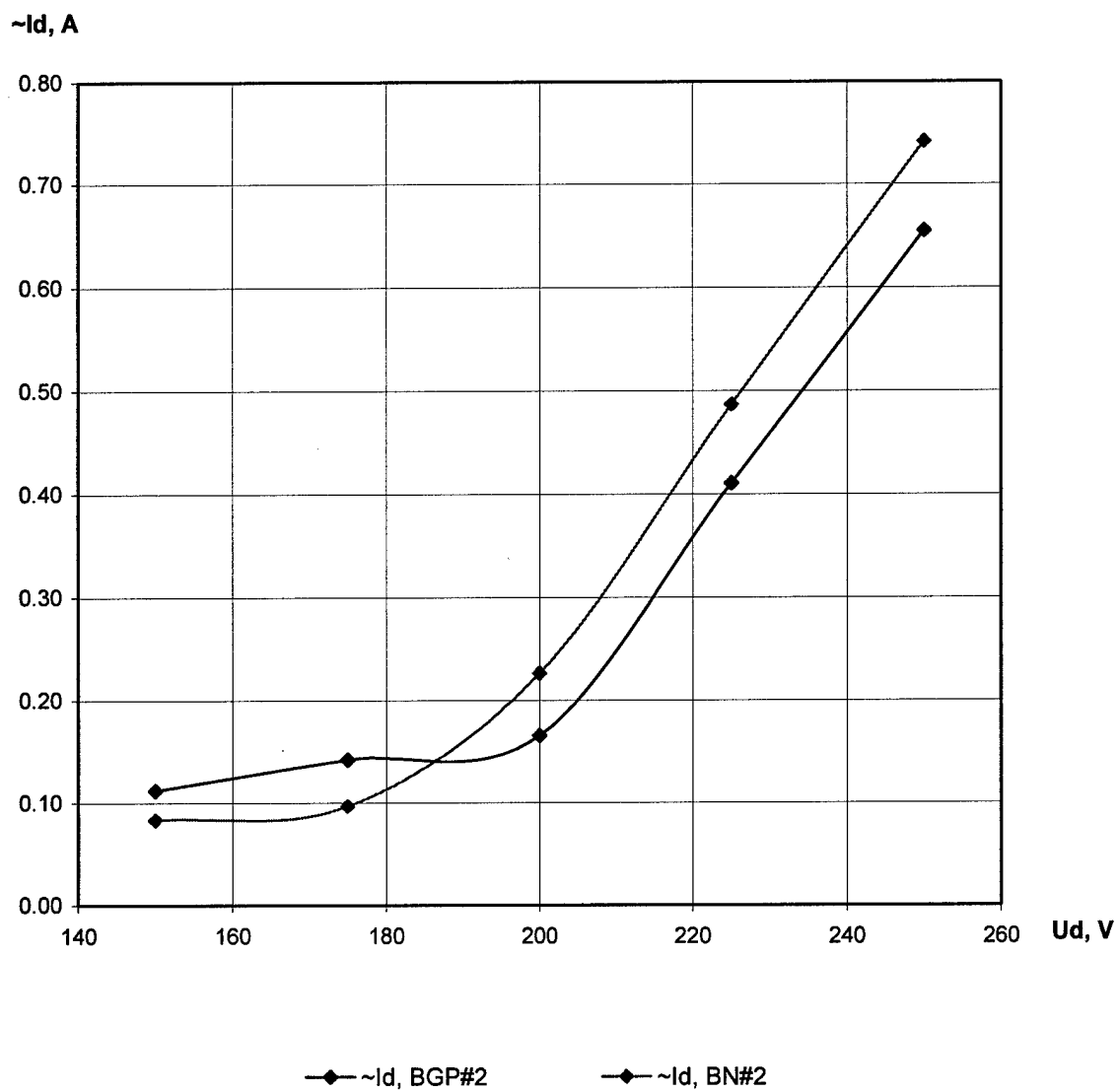


Fig.1.118. The discharge current oscillations RMS amplitude versus the discharge voltage.

SPT-25, $m=0.7$ mg/s, $I_m=4.0$ A.

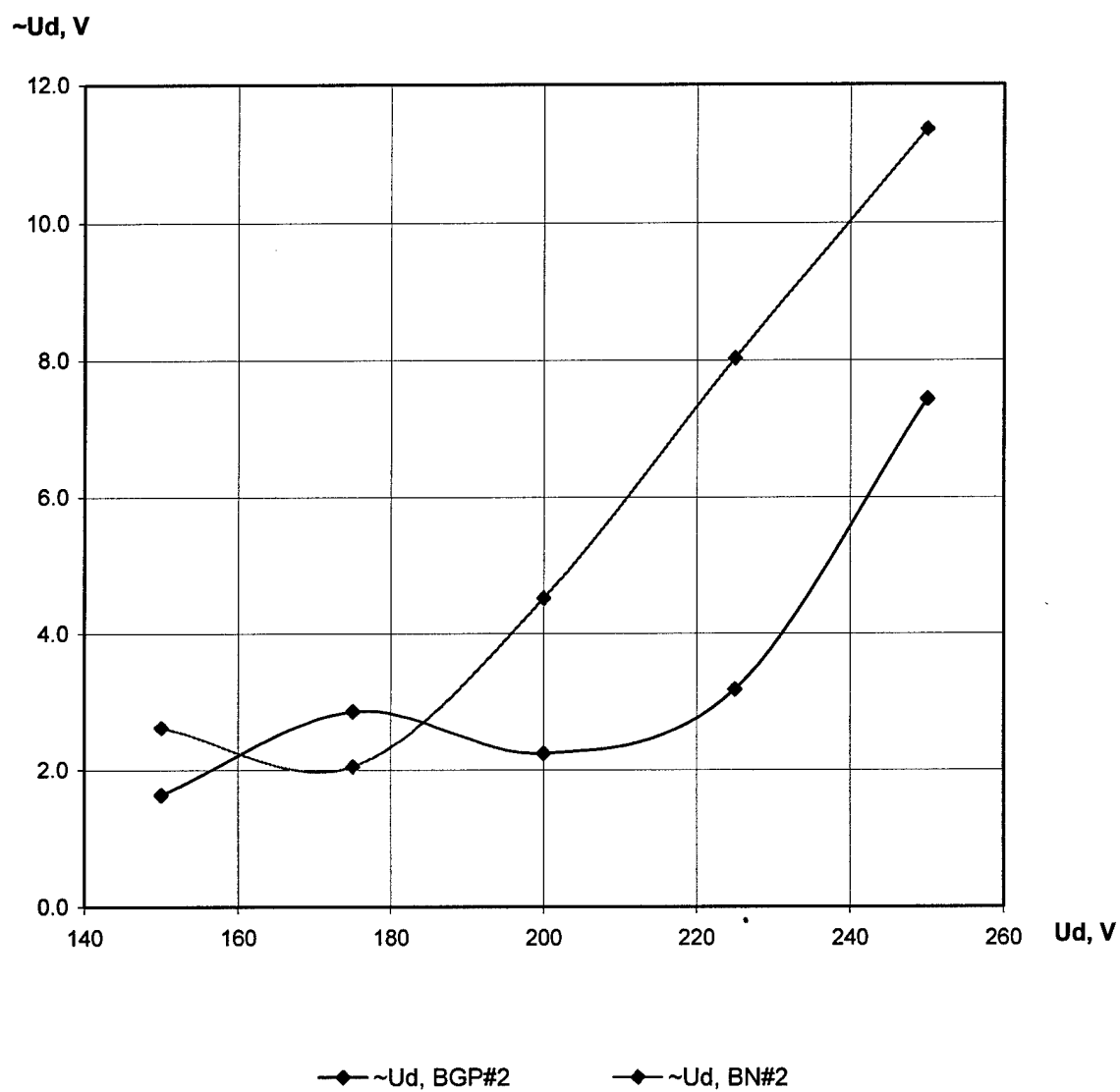


Fig.1.119. The discharge voltage oscillations RMS amplitude versus the discharge voltage.

SPT-25, $m=0.7$ mg/s, $I_m=4.0$ A.

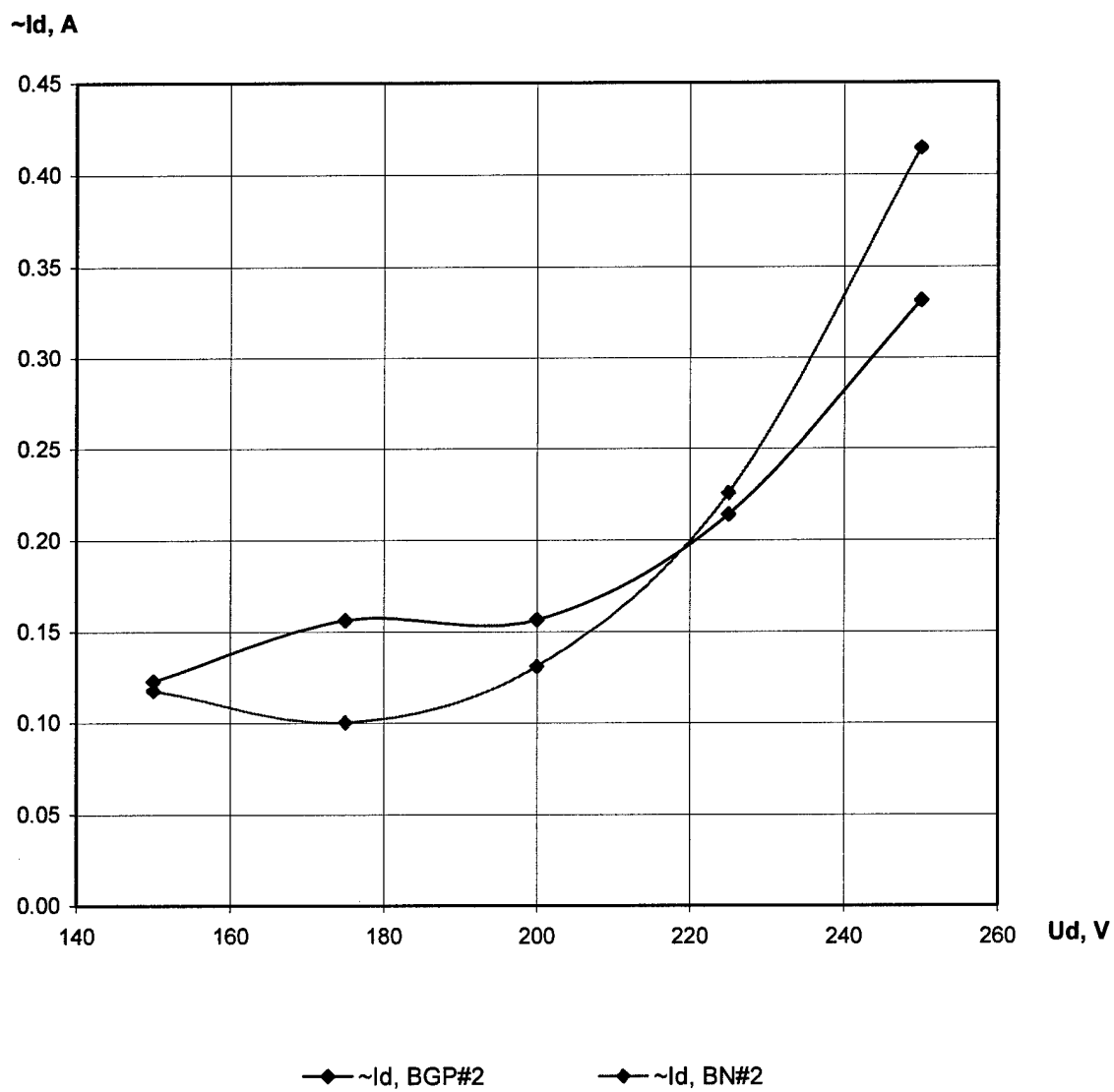


Fig.1.120. The discharge current oscillations RMS amplitude versus the discharge voltage.

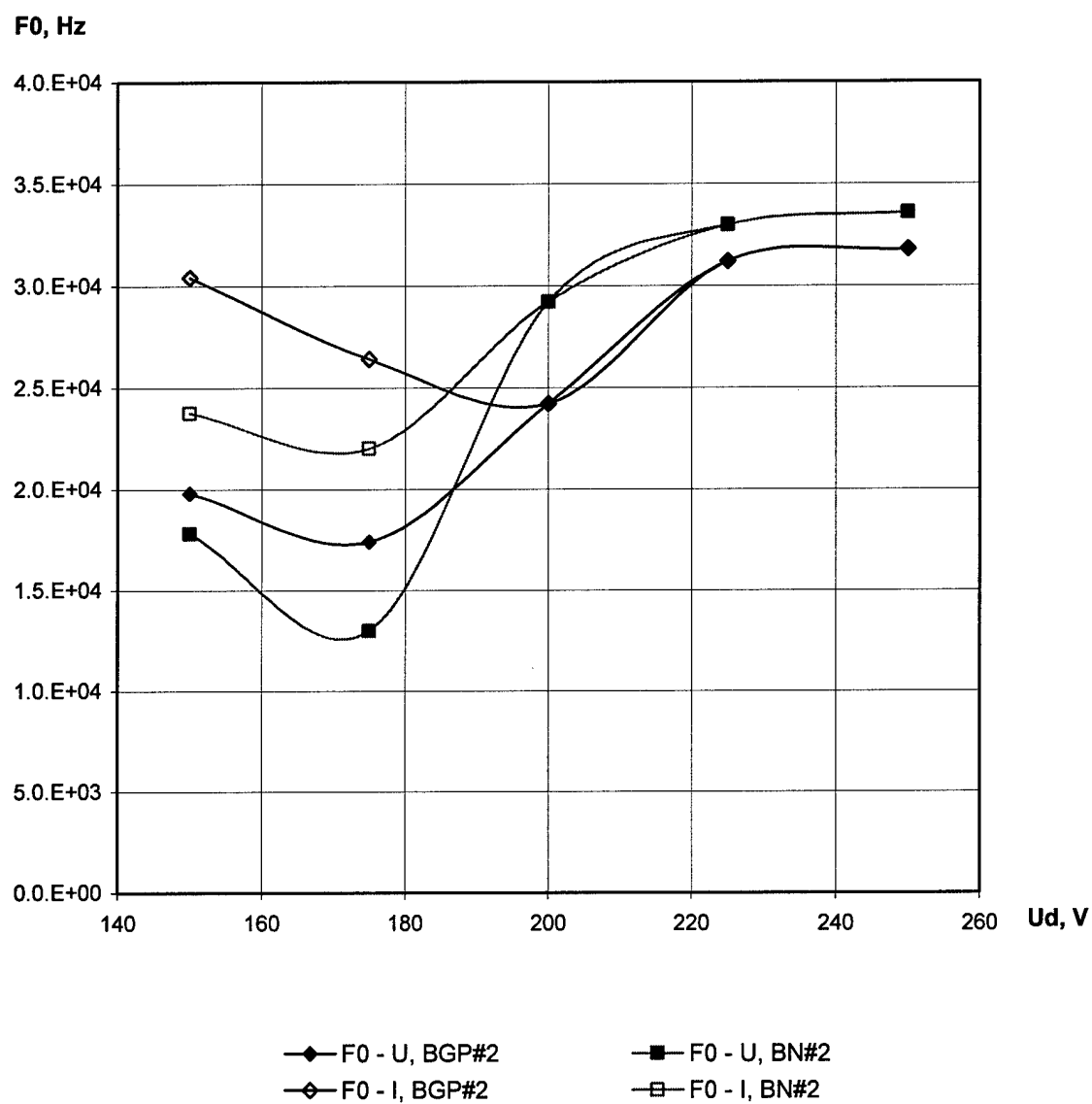
SPT-25, $m=0.6$ mg/s, $I_m=1.5$ A .

Fig.1.121. Dominating discharge voltage (F0-U) and discharge current (F0-I) oscillations mode frequency versus the discharge voltage.

SPT-25, $m=0.6$ mg/s, $I_m=2.7$ A .

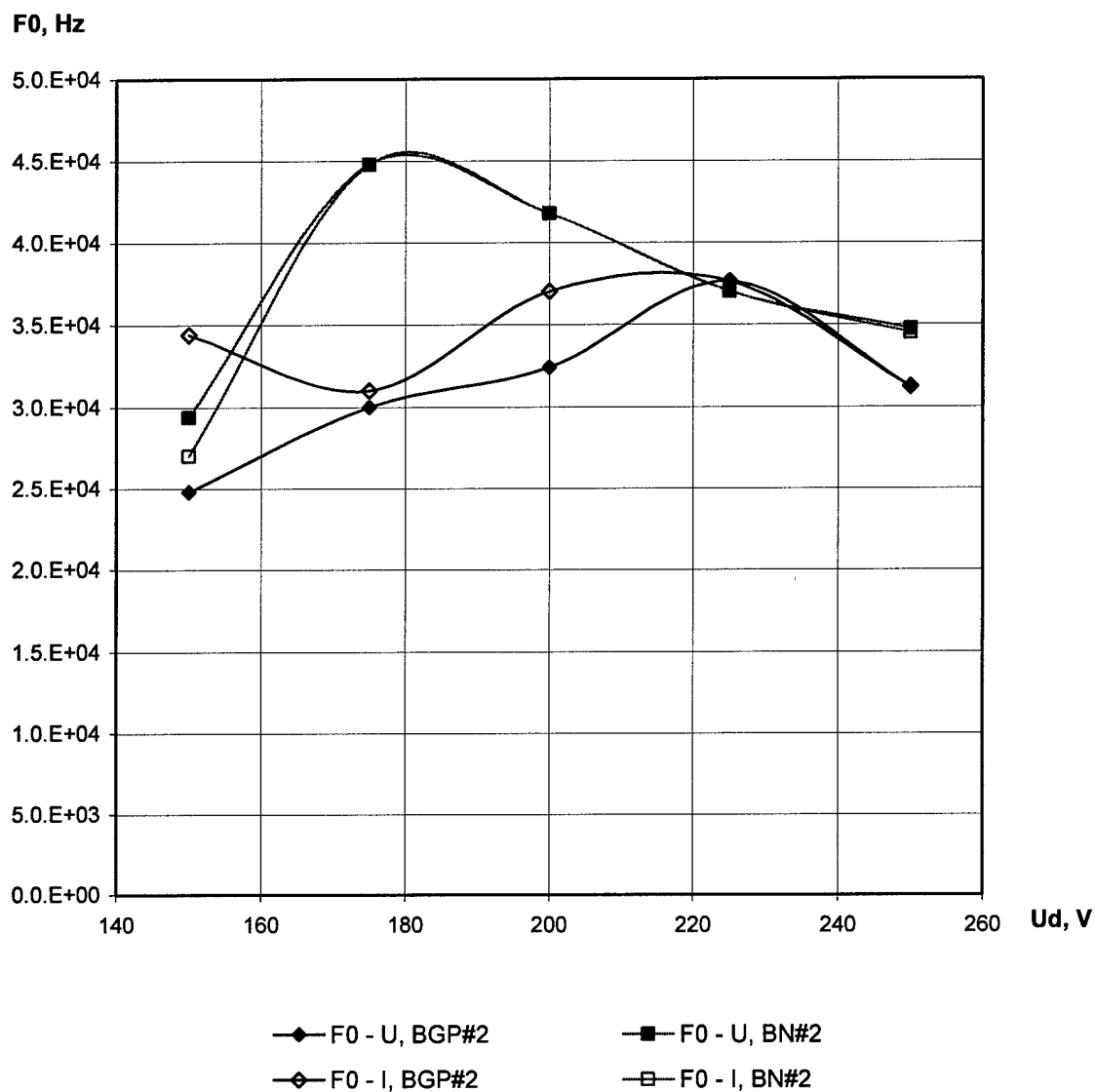


Fig.1.122. Dominating discharge voltage (F0-U) and discharge current (F0-I) oscillations mode frequency versus the discharge voltage.

SPT-25, $m=0.6$ mg/s, $I_m=4.0$ A .

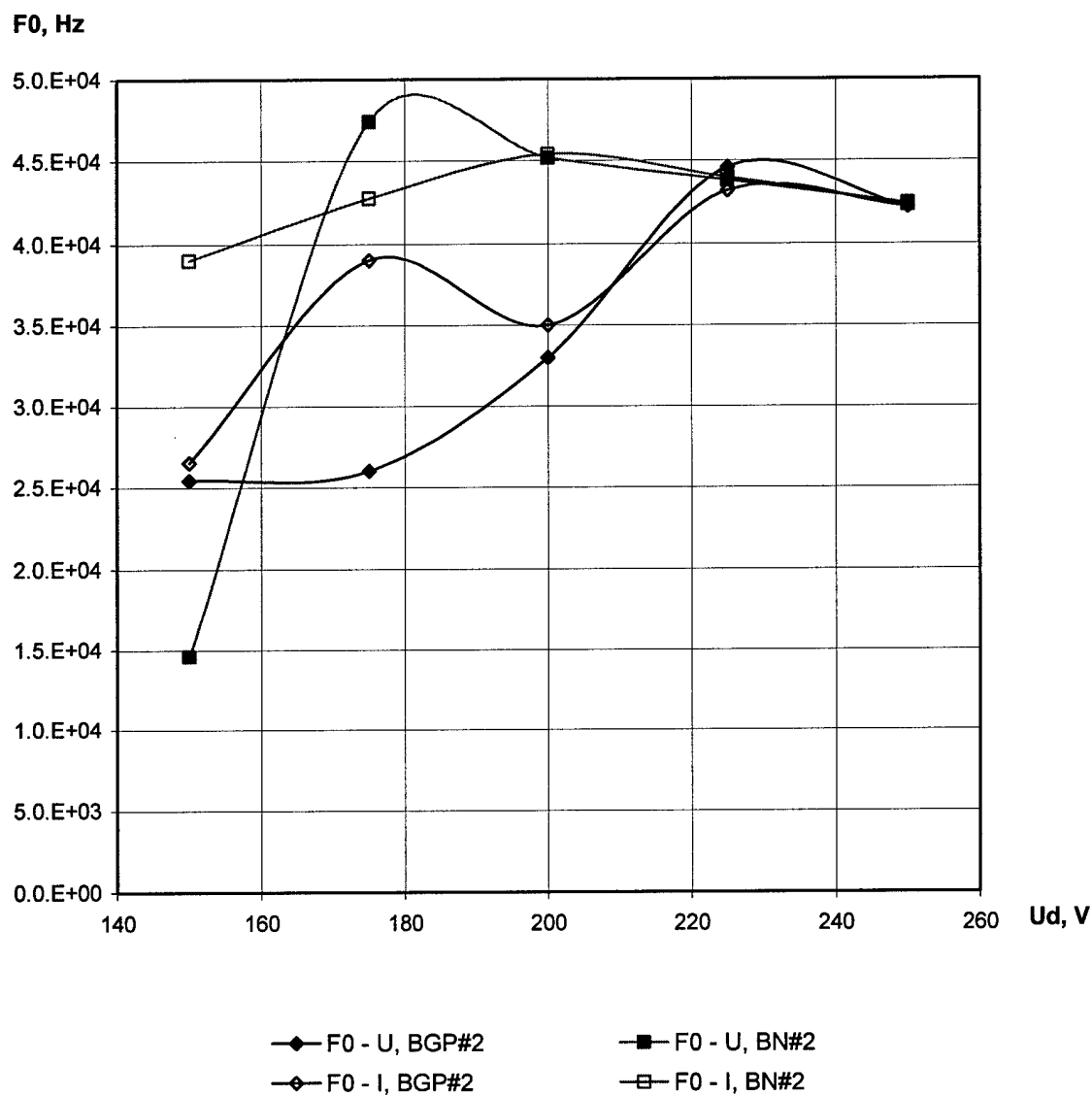


Fig.1.123. Dominating discharge voltage (F0-U) and discharge current (F0-I) oscillations mode frequency versus the discharge voltage.

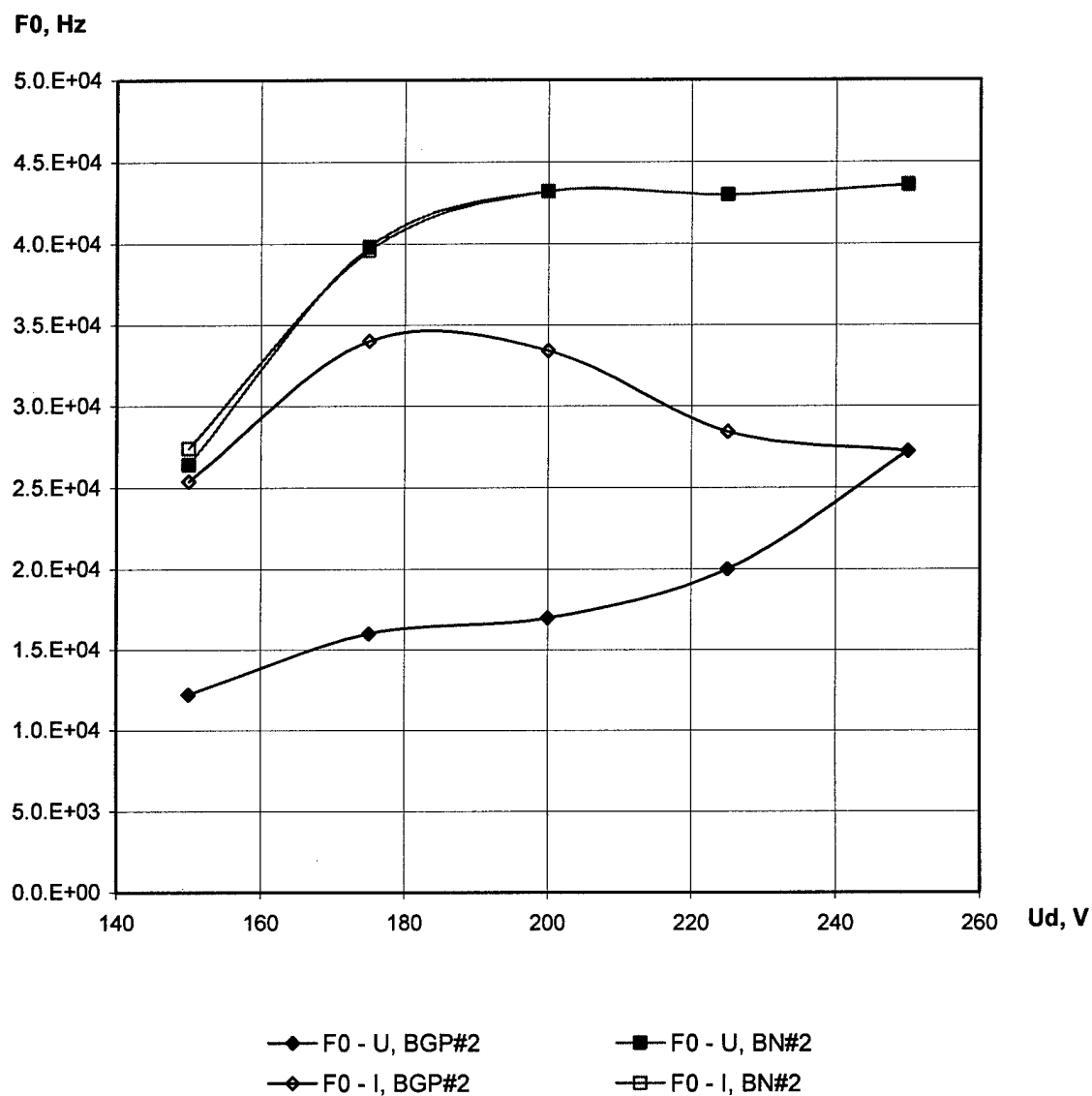
SPT-25, $m=0.7$ mg/s, $I_m=1.5$ A .

Fig.1.124. Dominating discharge voltage (F0-U) and discharge current (F0-I) oscillations mode frequency versus the discharge voltage.

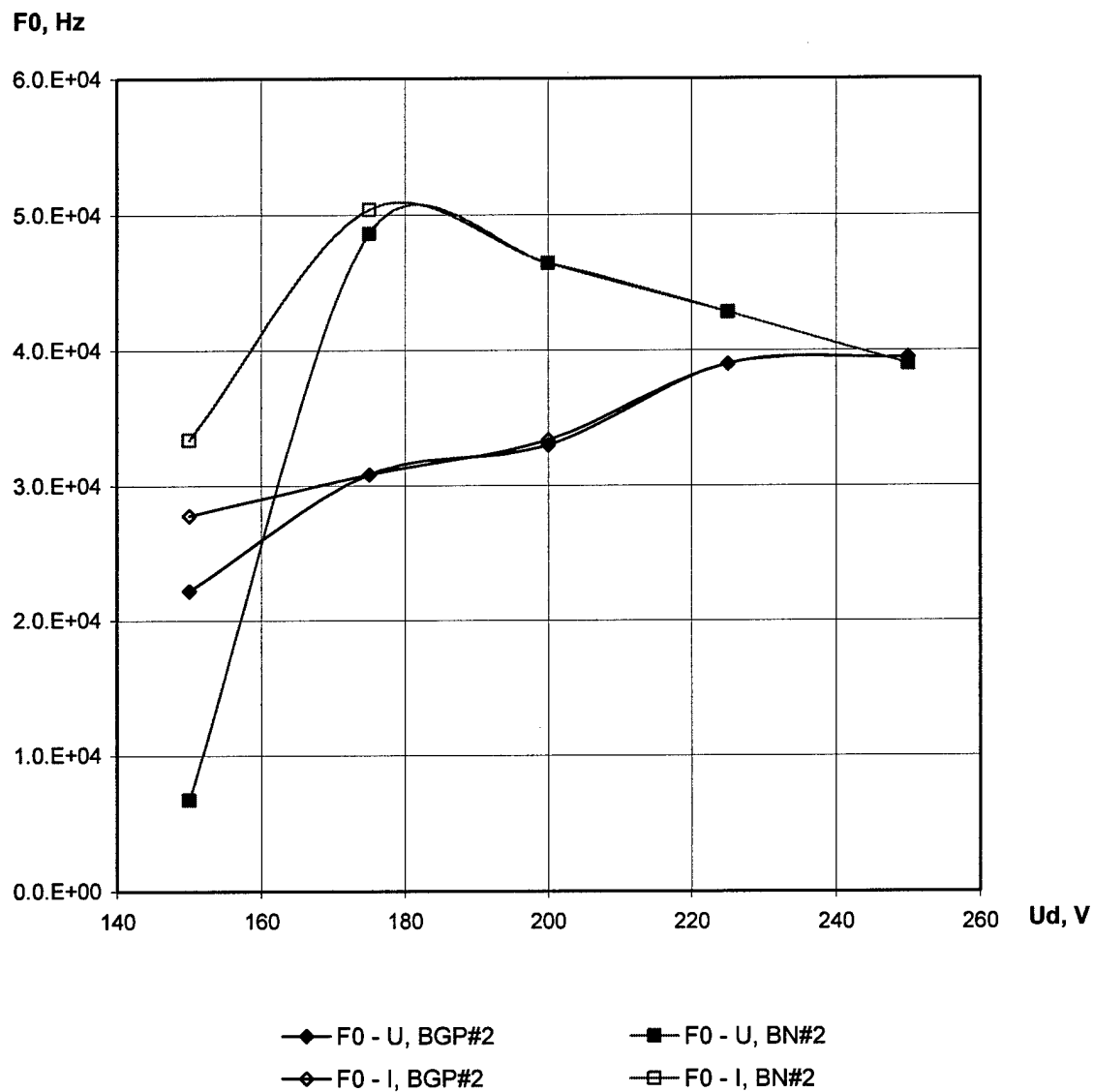
SPT-25, $m=0.7$ mg/s, $I_m=2.7$ A .

Fig.1.125. Dominating discharge voltage (F0-U) and discharge current (F0-I) oscillations mode frequency versus the discharge voltage.

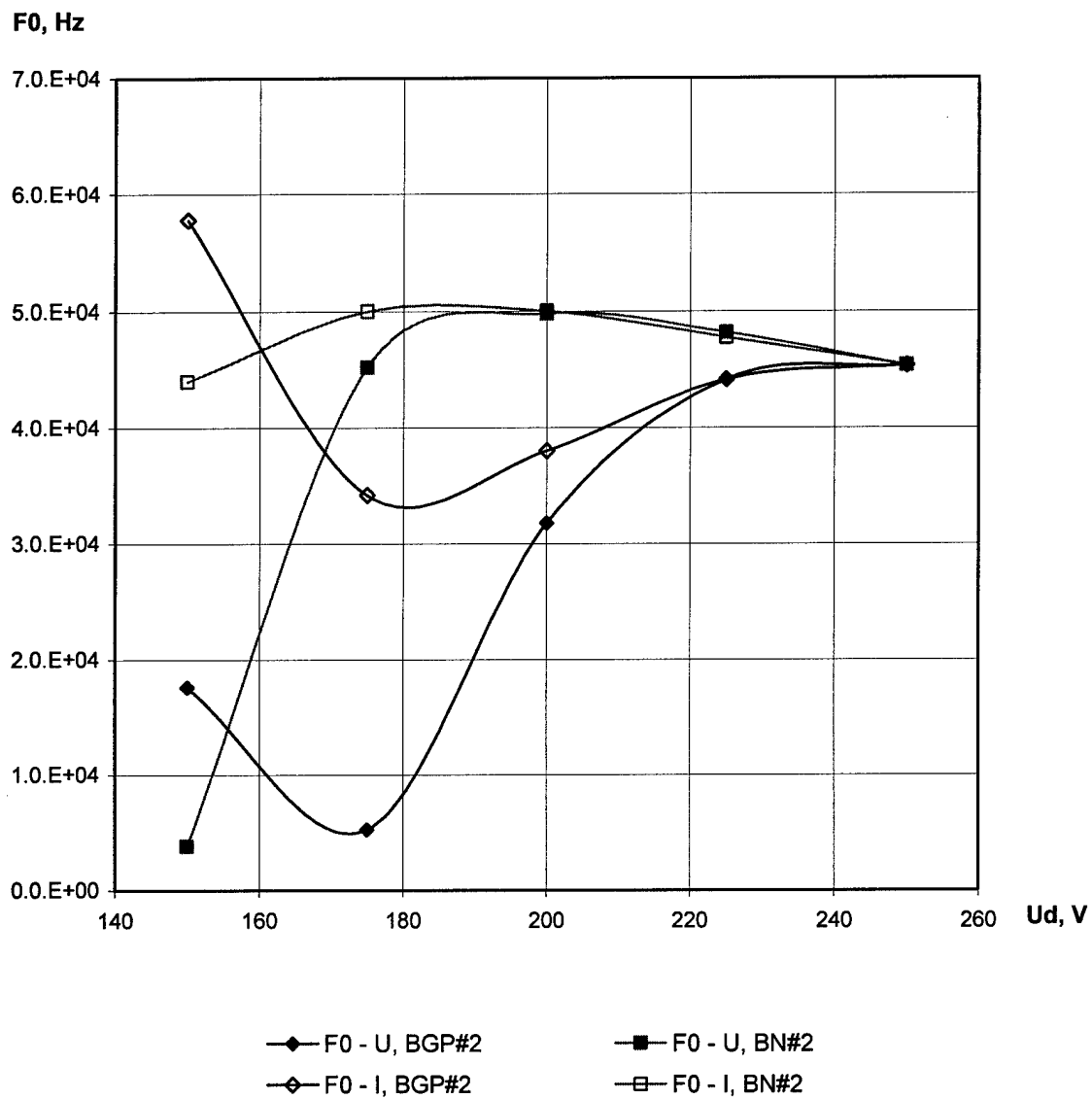
SPT-25, $m=0.7$ mg/s, $I_m=4.0$ A .

Fig.1.126. Dominating discharge voltage (F0-U) and discharge current (F0-I) oscillations mode frequency versus the discharge voltage.

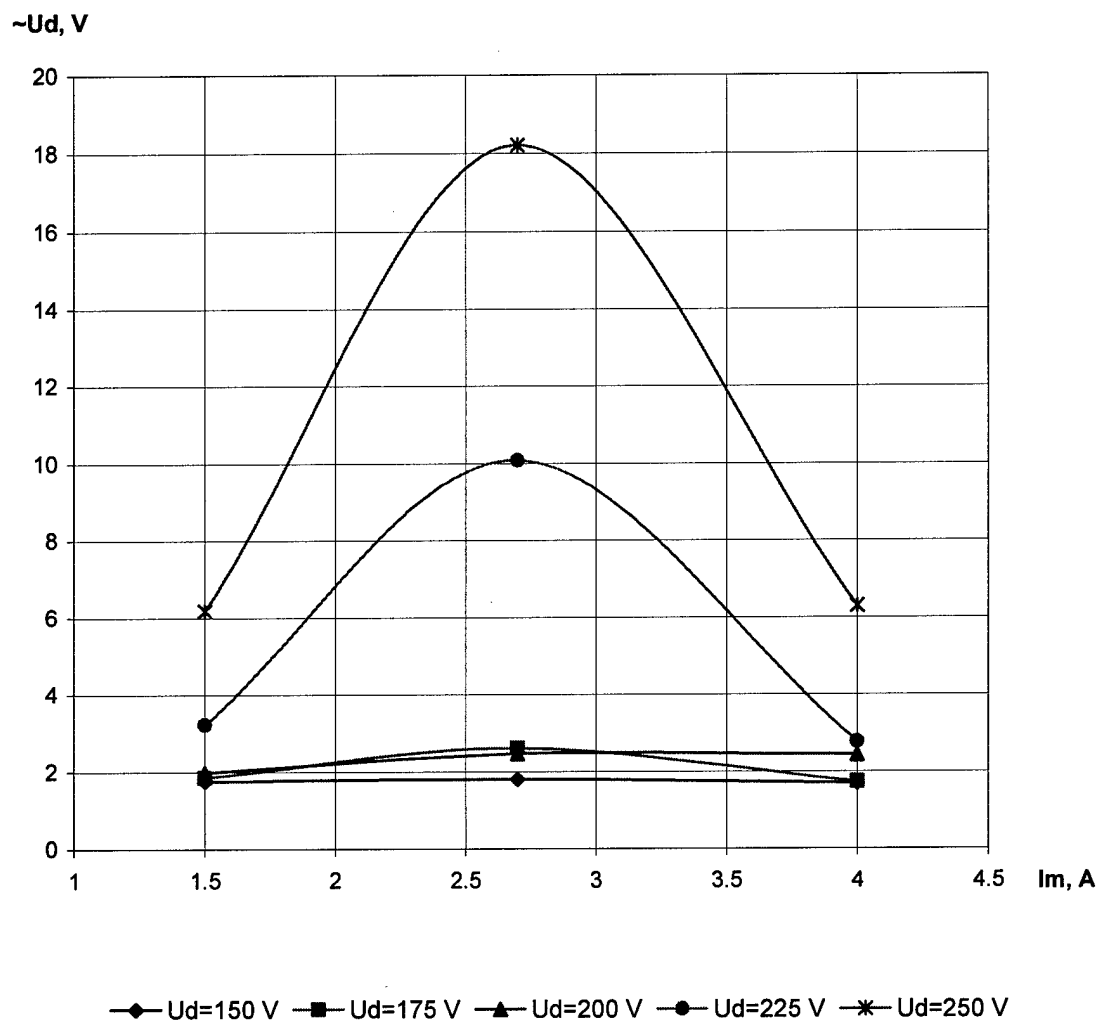
SPT-25 BGP#2, $m=0.6$ mg/s.

Fig.1.127. The discharge voltage oscillations RMS amplitude versus the magnetization current.

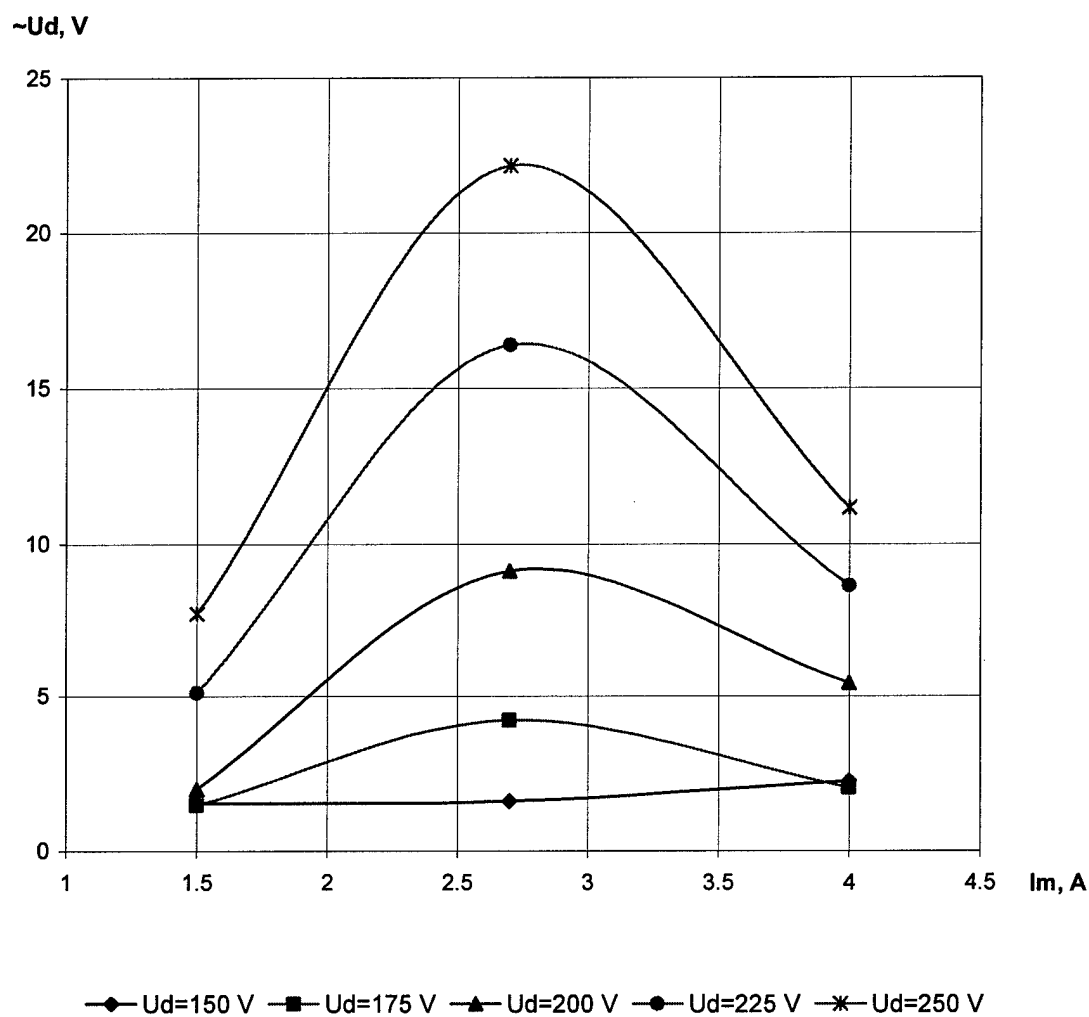
SPT-25 BN#2, $m=0.6$ mg/s.

Fig.1.128. The discharge voltage oscillations RMS amplitude versus the magnetization current.

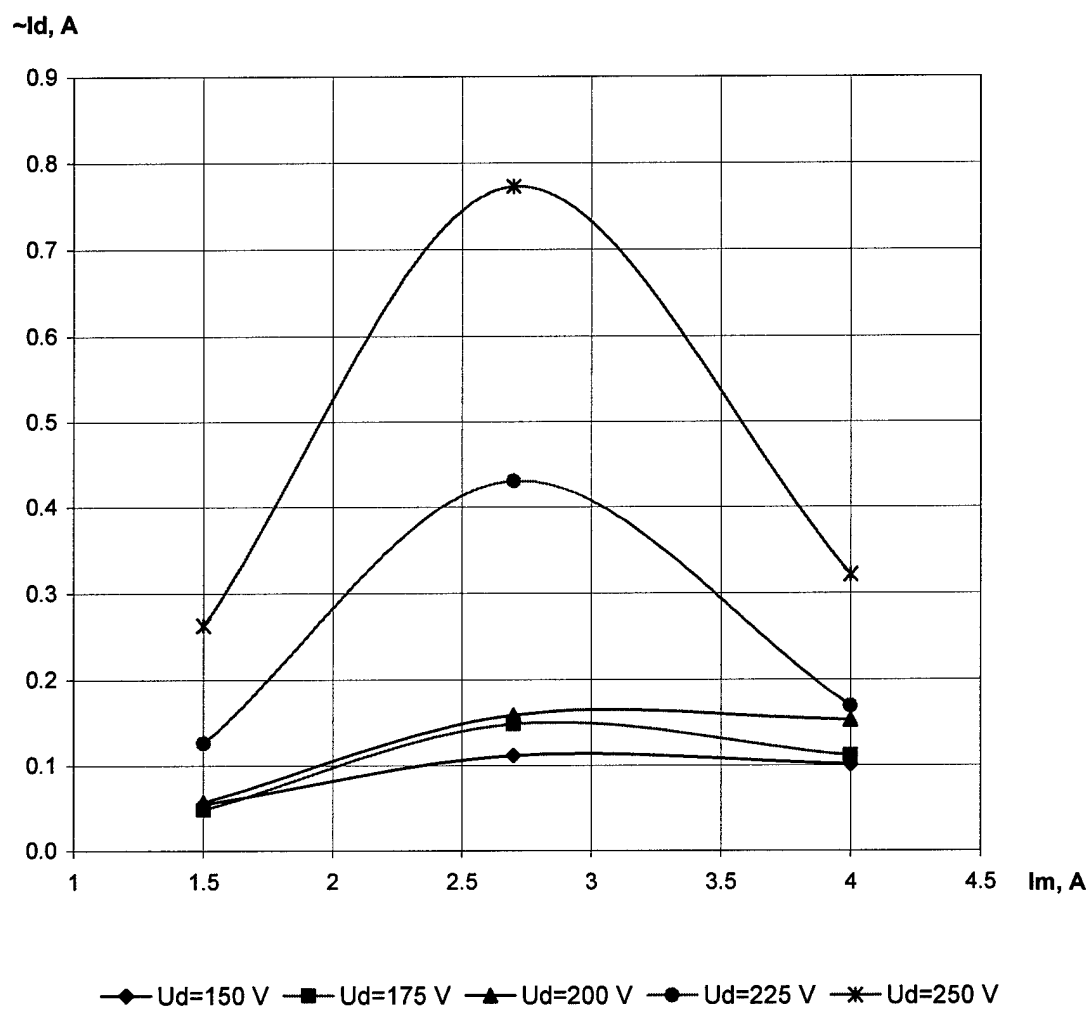
SPT-25 BGP#2, $m=0.6$ mg/s.

Fig.1.129. The discharge current oscillations RMS amplitude versus the magnetization current.

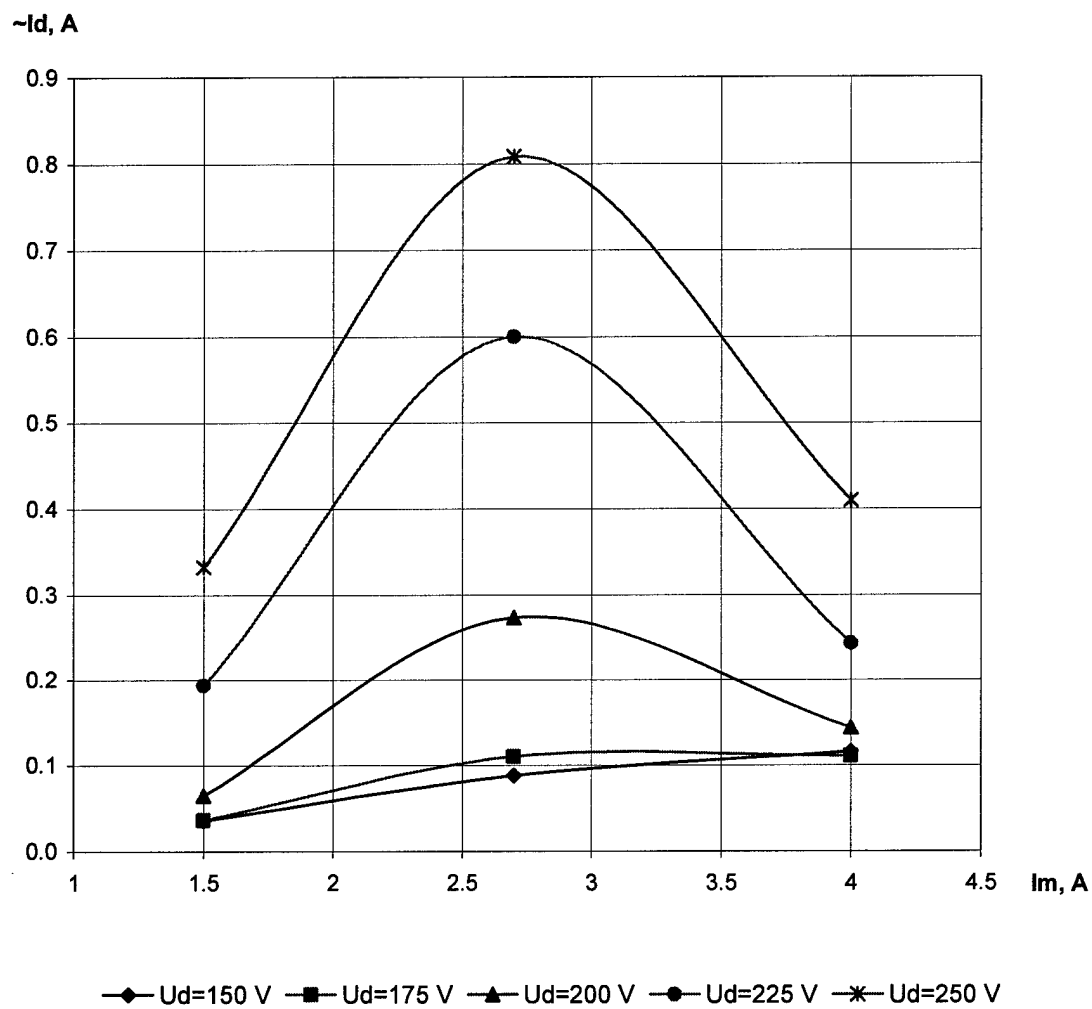
SPT-25 BN#2, $m=0.6$ mg/s.

Fig.1.130. The discharge current oscillations RMS amplitude versus the magnetization current.

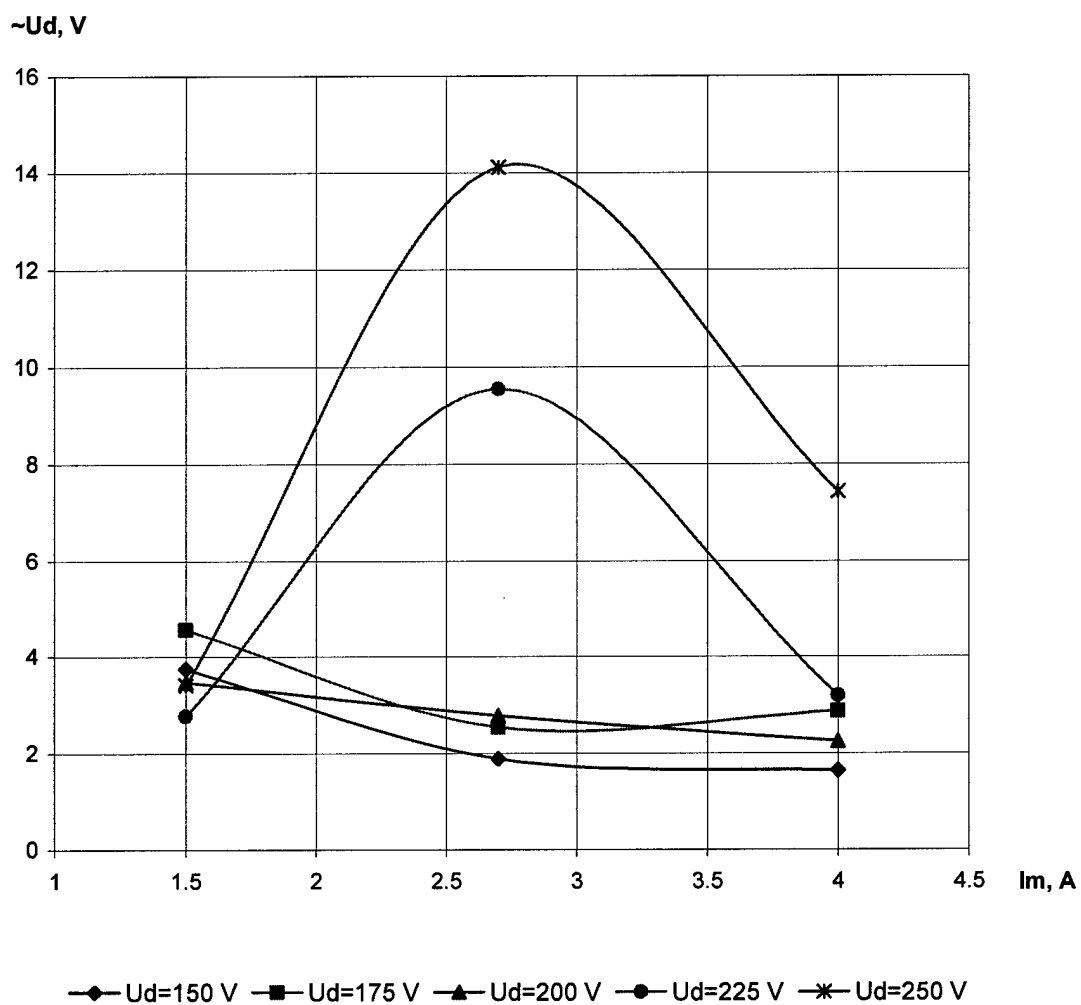
SPT-25 BGP#2, $m=0.7$ mg/s.

Fig.1.131. The discharge voltage oscillations RMS amplitude versus the magnetization current.

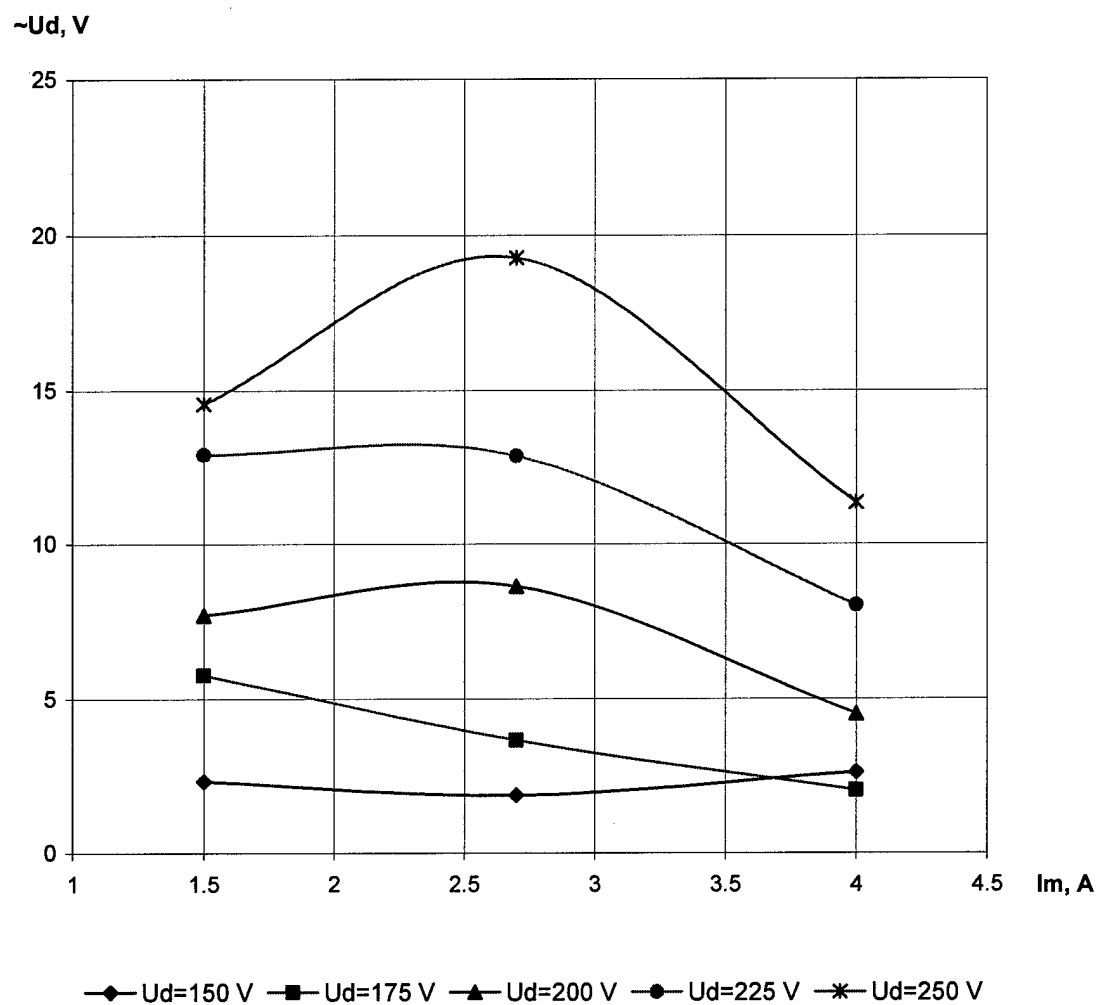
SPT-25 BN#2, $m=0.7$ mg/s.

Fig.1.132. The discharge voltage oscillations RMS amplitude versus the magnetization current.

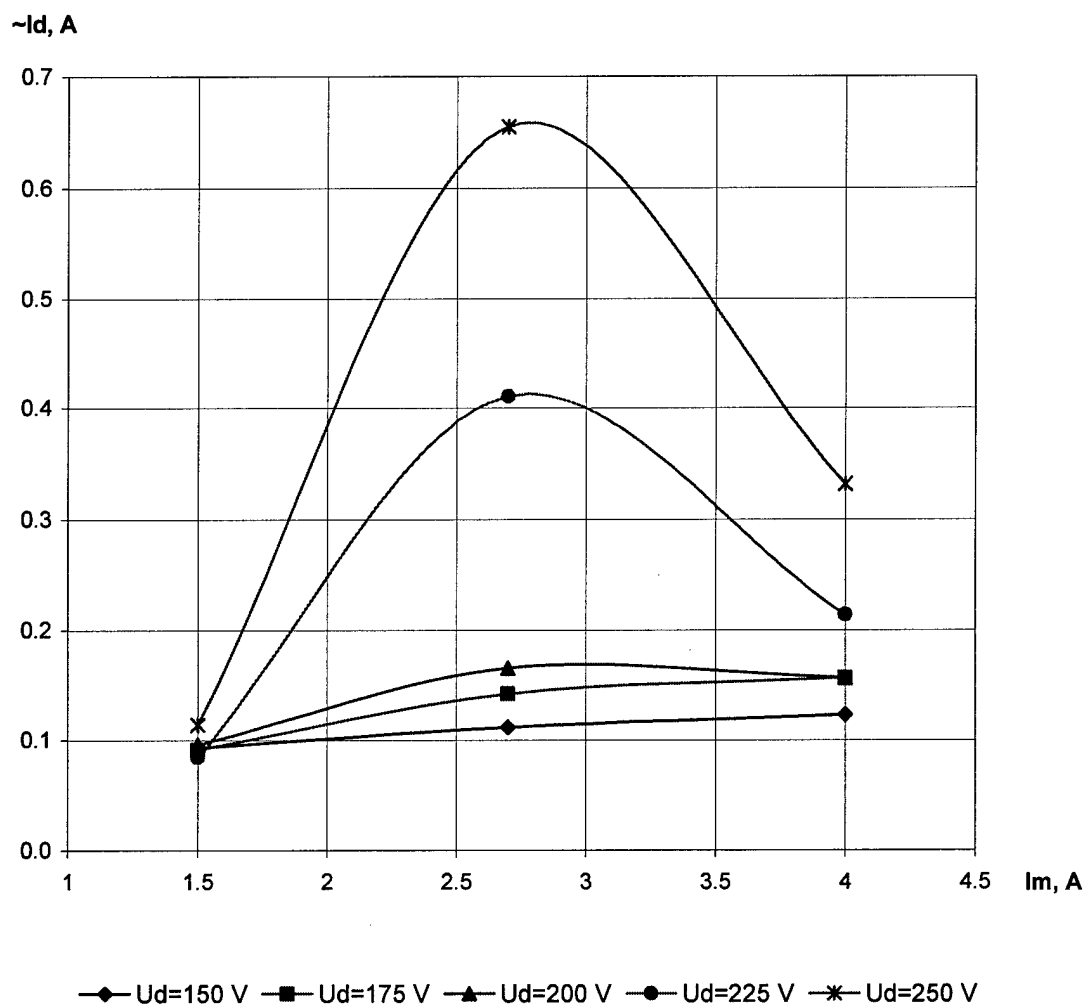
SPT-25 BGP#2, $m=0.7$ mg/s.

Fig.1.133. The discharge current oscillations RMS amplitude versus the magnetization current.

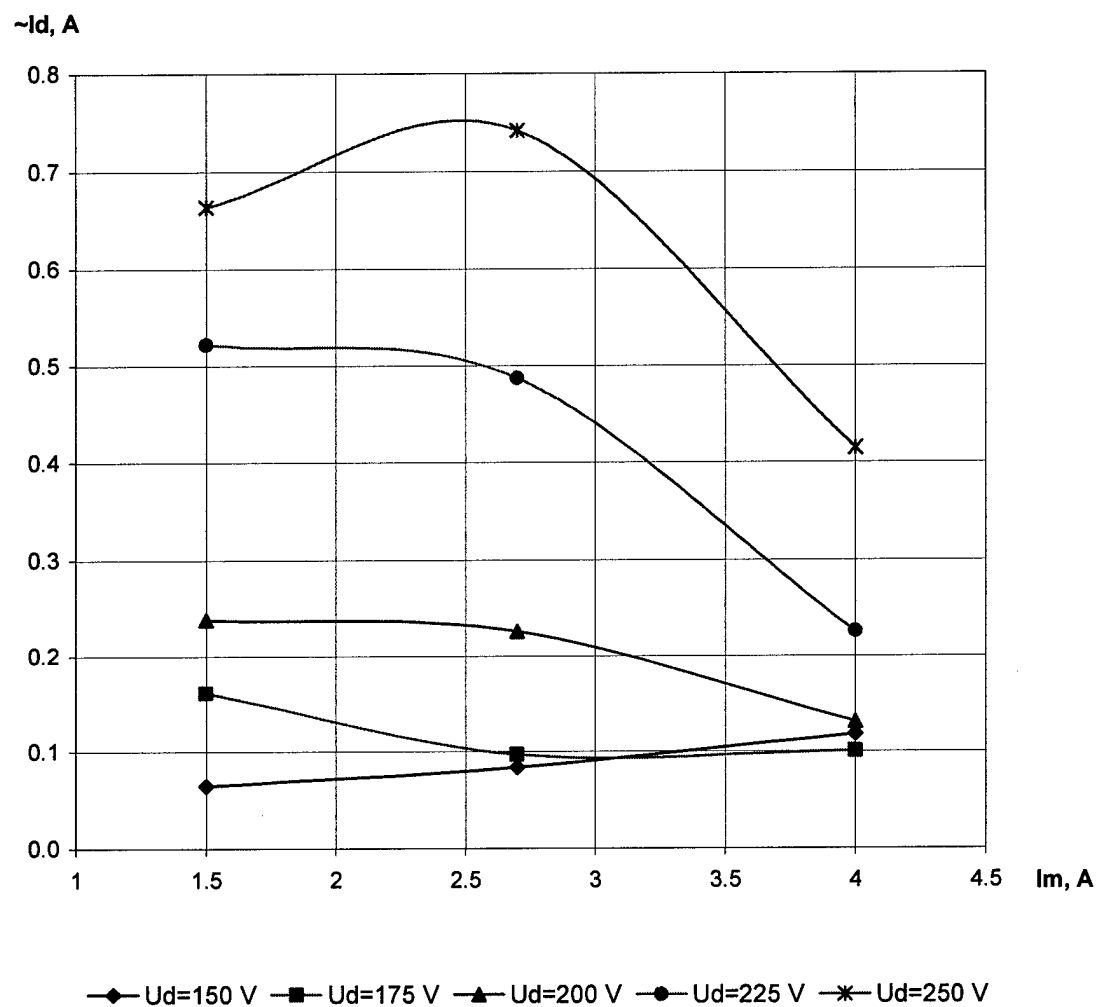
SPT-25 BN#2, $m=0.7$ mg/s.

Fig.1.134. The discharge current oscillations RMS amplitude versus the magnetization current.

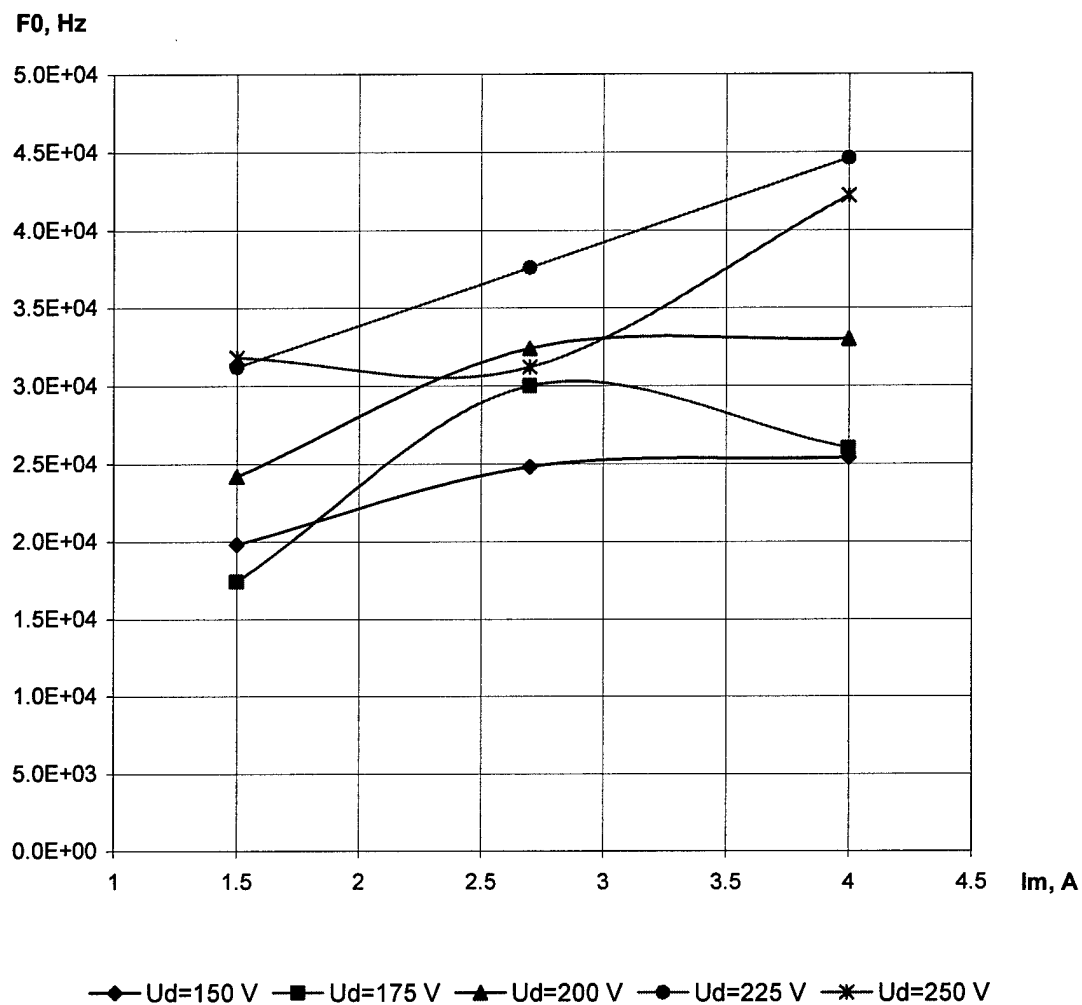
SPT-25 BGP#2, $m=0.6$ mg/s.

Fig.1.135. The dominating discharge voltage oscillation mode frequency versus the magnetization current.

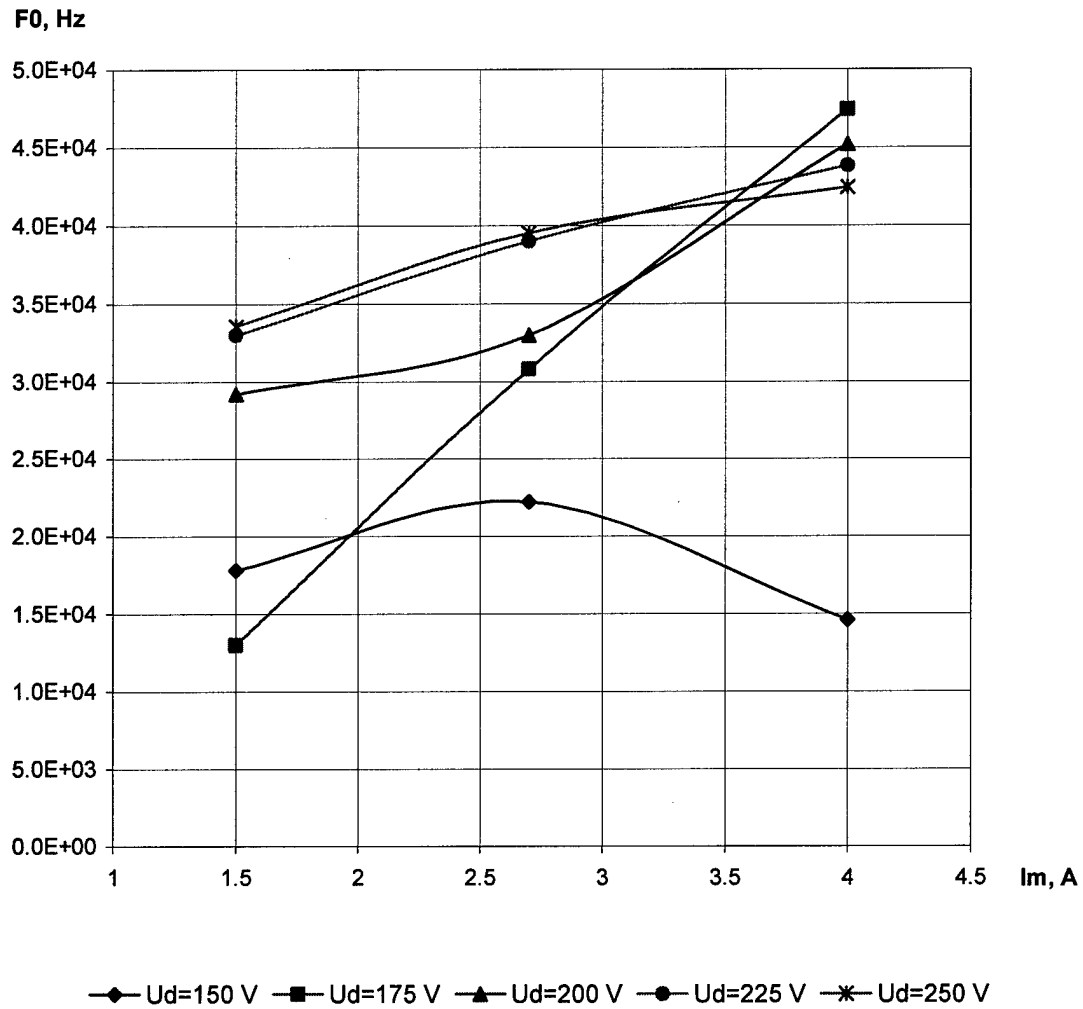
SPT-25 BN#2, $m=0.6$ mg/s.

Fig.1.136. The dominating discharge voltage oscillation mode frequency versus the magnetization current.

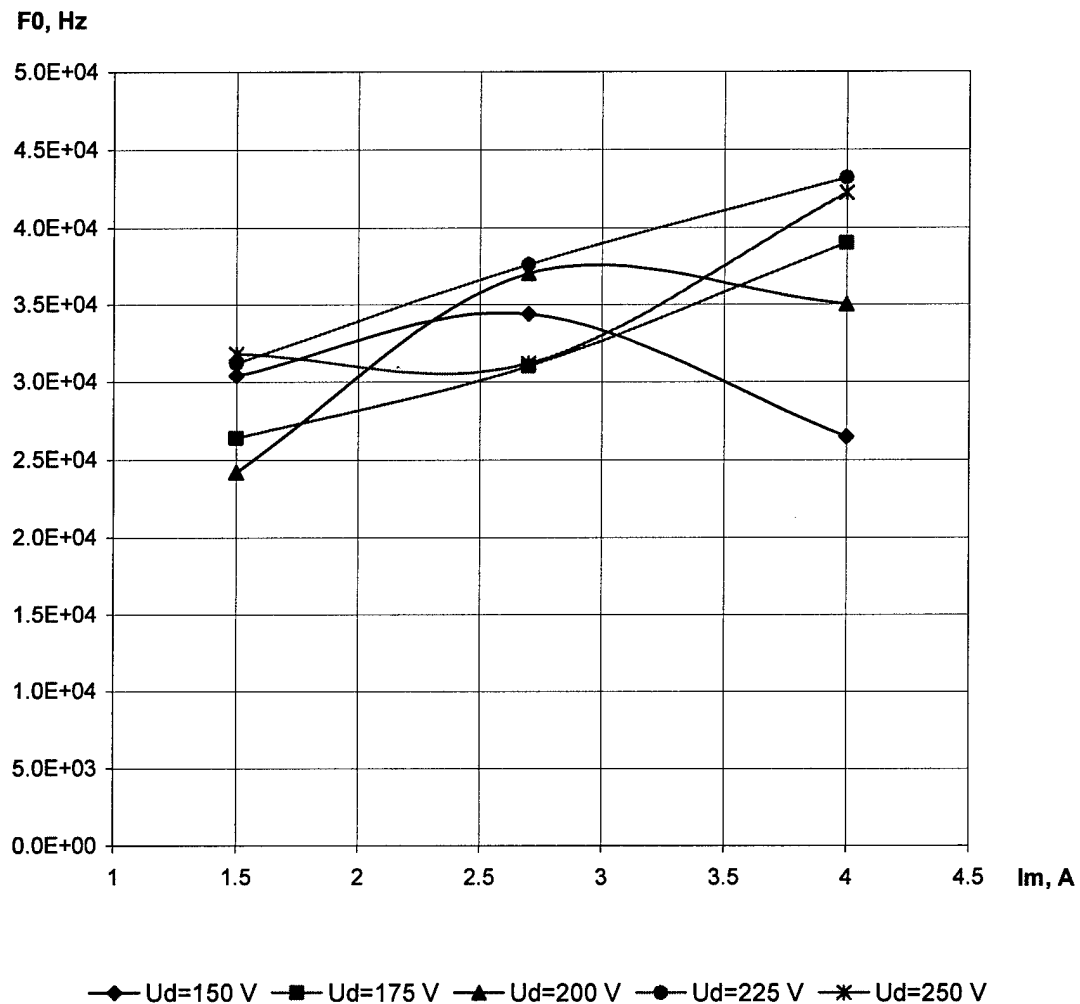
SPT-25 BGP#2, $m=0.6$ mg/s.

Fig.1.137. The dominating discharge current oscillation mode frequency versus the magnetization current.

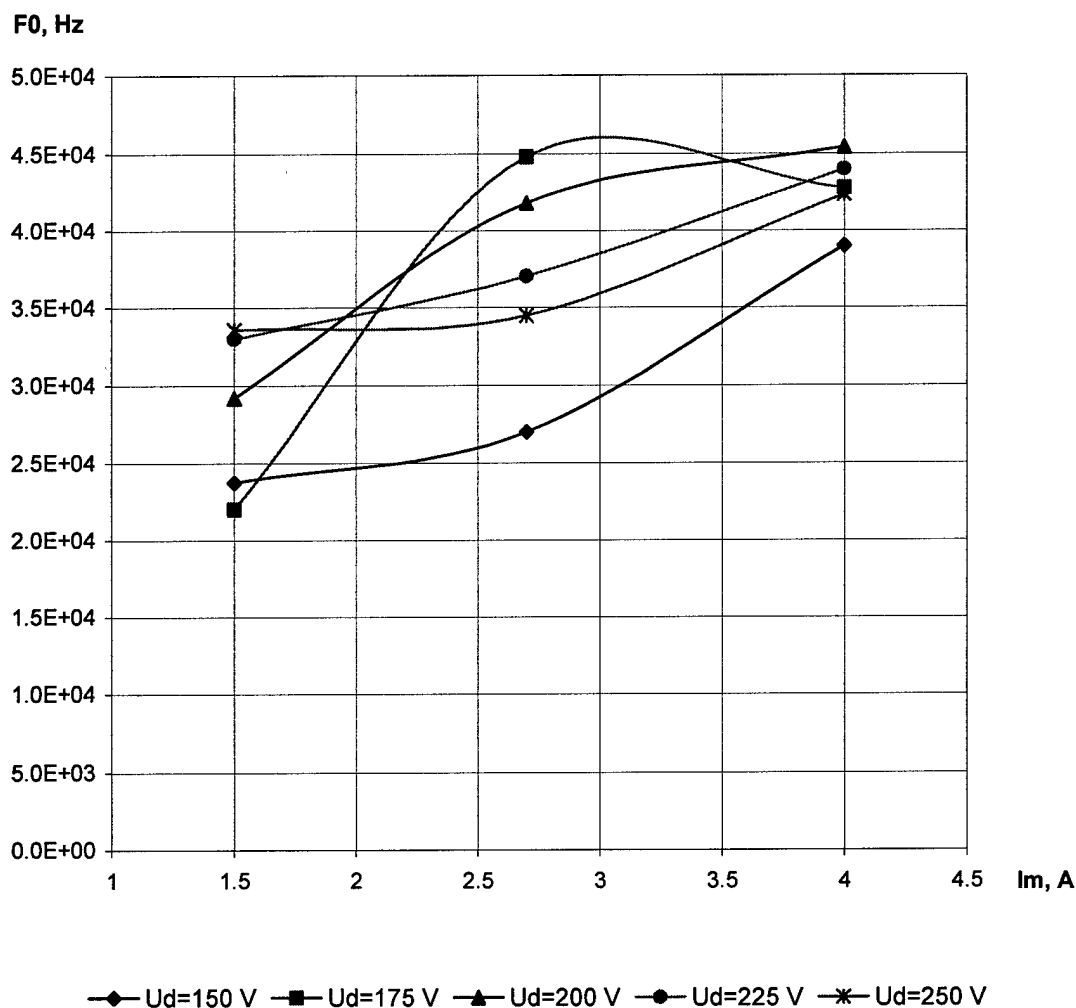
SPT-25 BN#2, $m=0.6$ mg/s.

Fig.1.138. The dominating discharge current oscillation mode frequency versus the magnetization current.

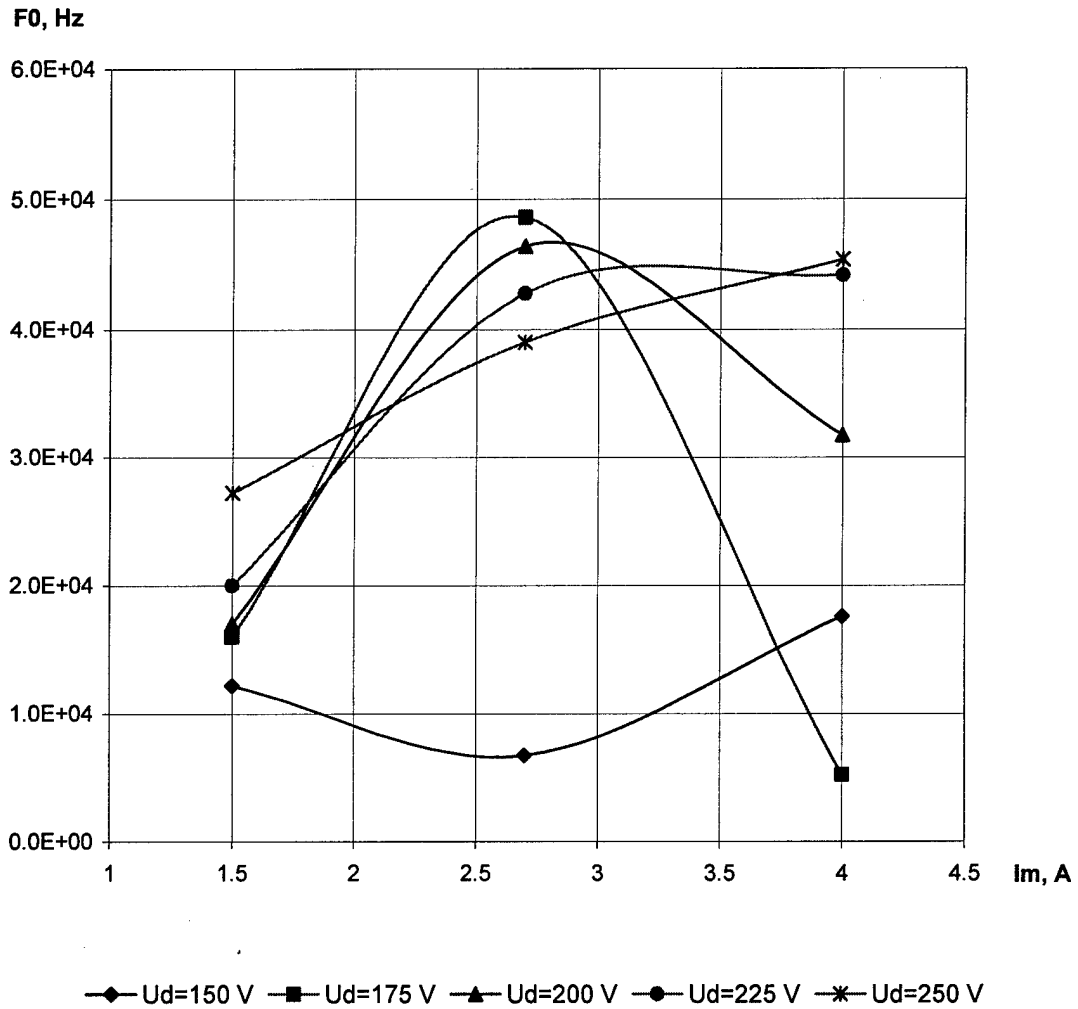
SPT-25 BGP#2, $m=0.7$ mg/s.

Fig.1.139. The dominating discharge voltage oscillation mode frequency versus the magnetization current.

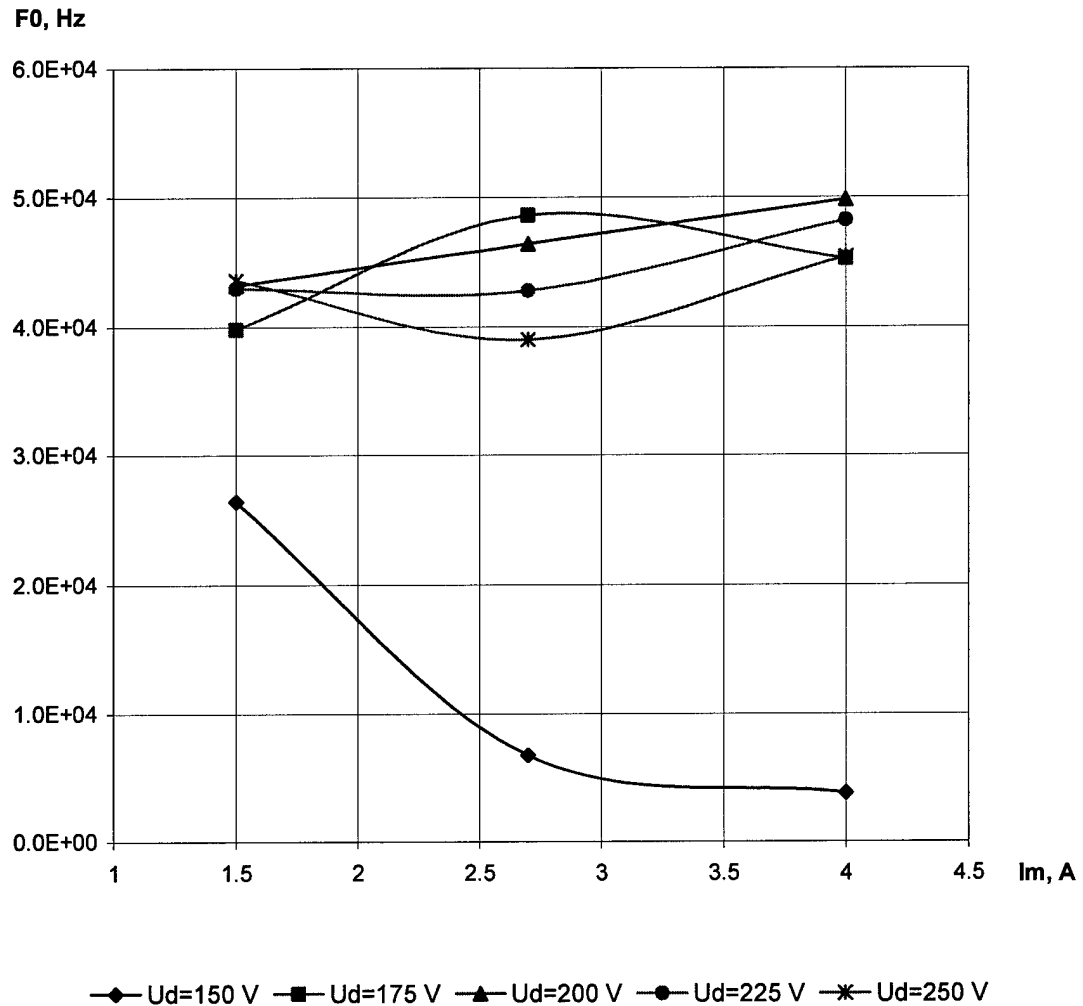
SPT-25 BN#2, $m=0.7$ mg/s.

Fig.1.140. The dominating discharge voltage oscillation mode frequency versus the magnetization current.

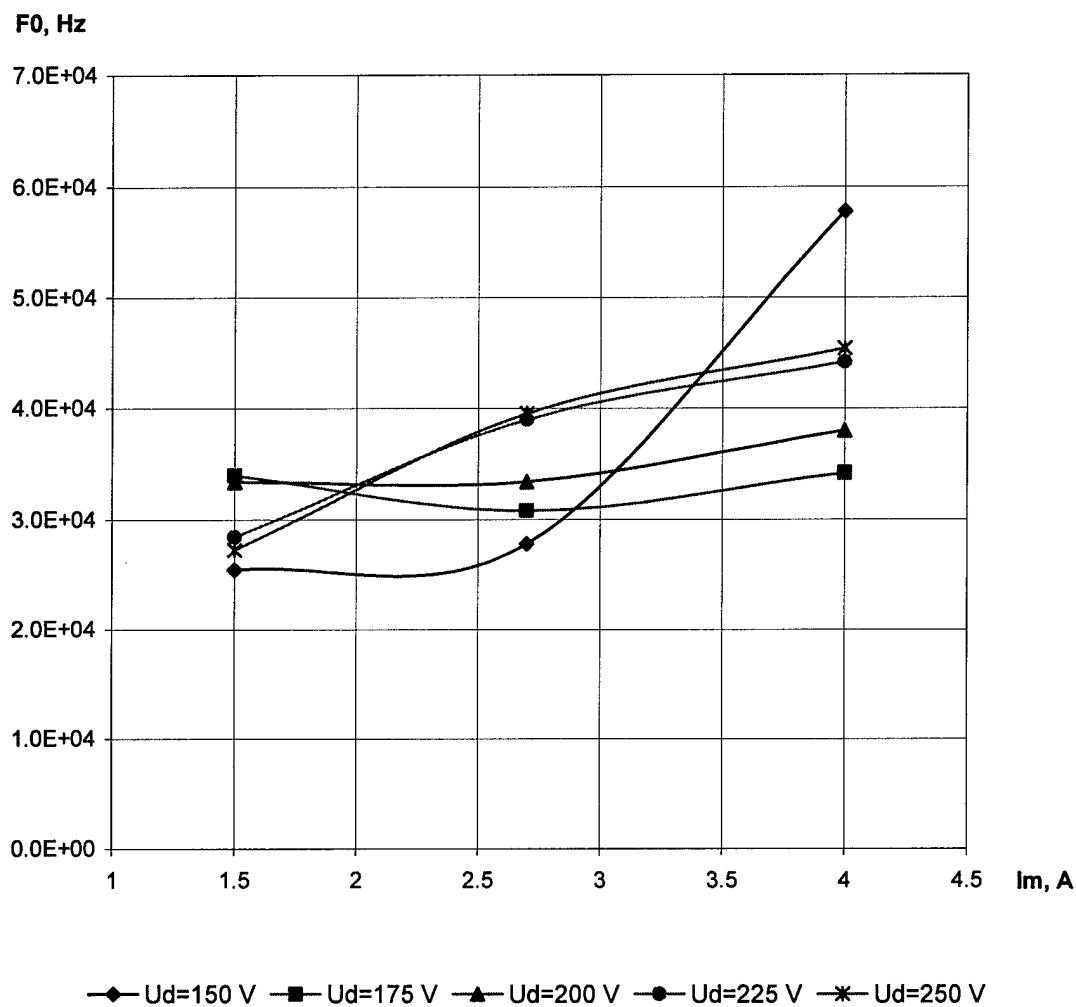
SPT-25 BGP#2, $m=0.7$ mg/s.

Fig.1.141. The dominating discharge current oscillation mode frequency versus the magnetization current.

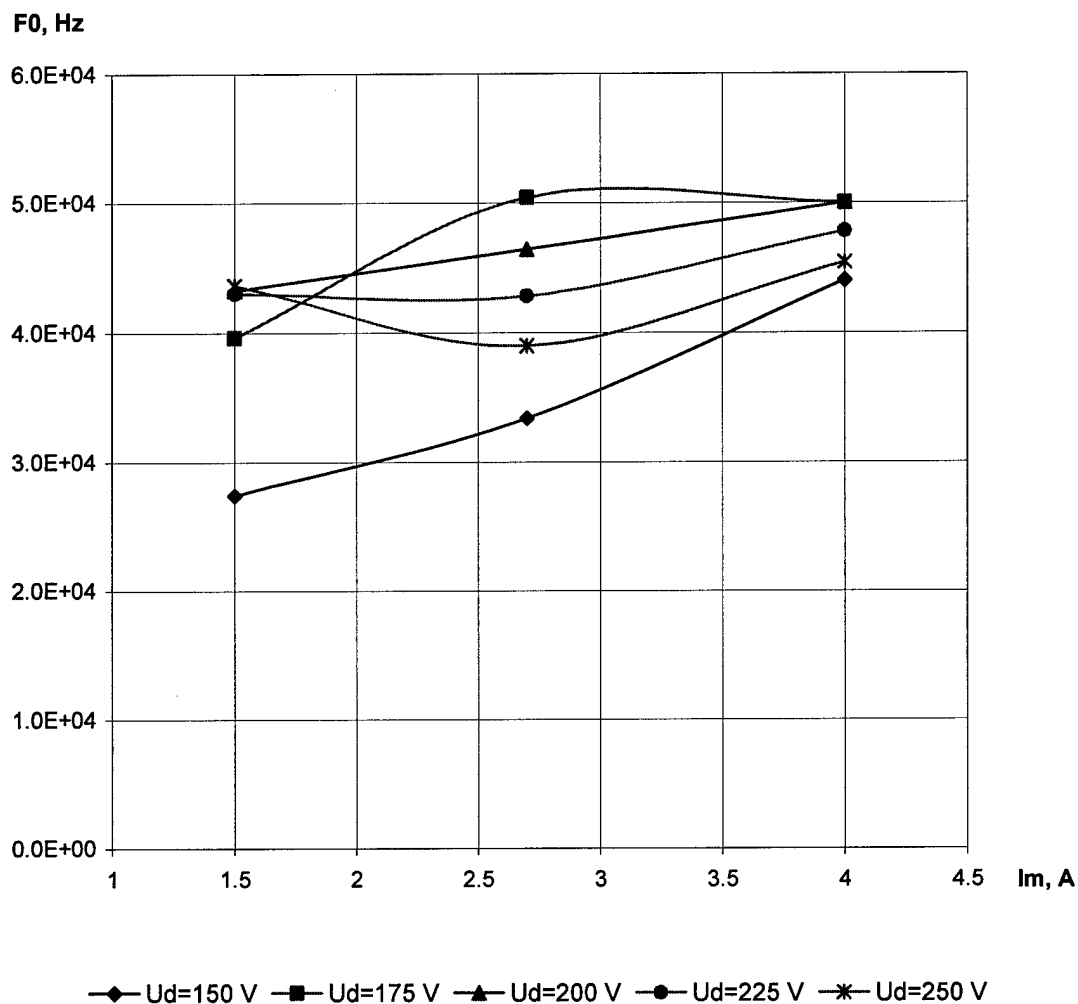
SPT-25 BN#2, $m=0.7$ mg/s.

Fig.1.142. The dominating discharge current oscillation mode frequency versus the magnetization current.

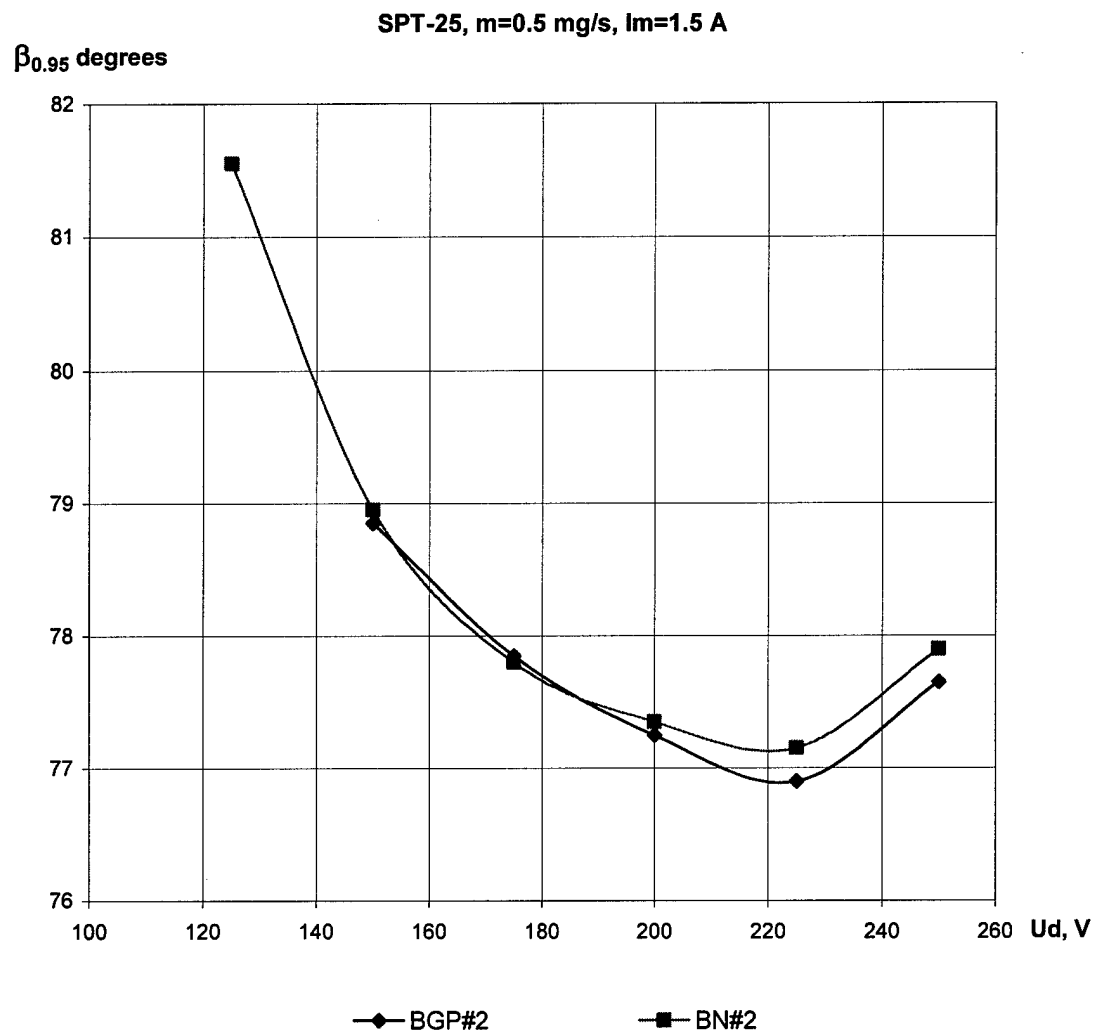


Fig.1.143. Plume half angle versus the discharge voltage.

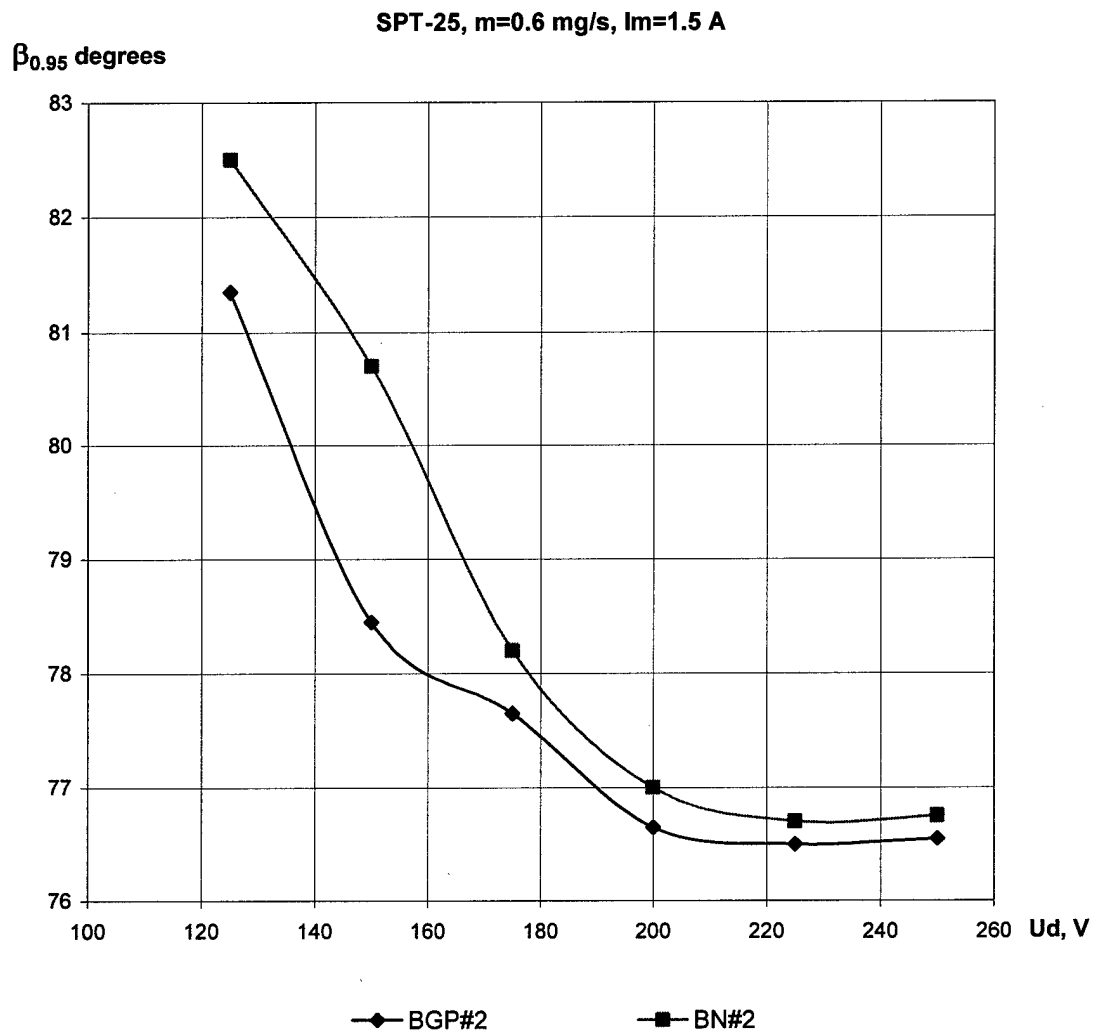


Fig.1.144. Plume half angle versus the discharge voltage.

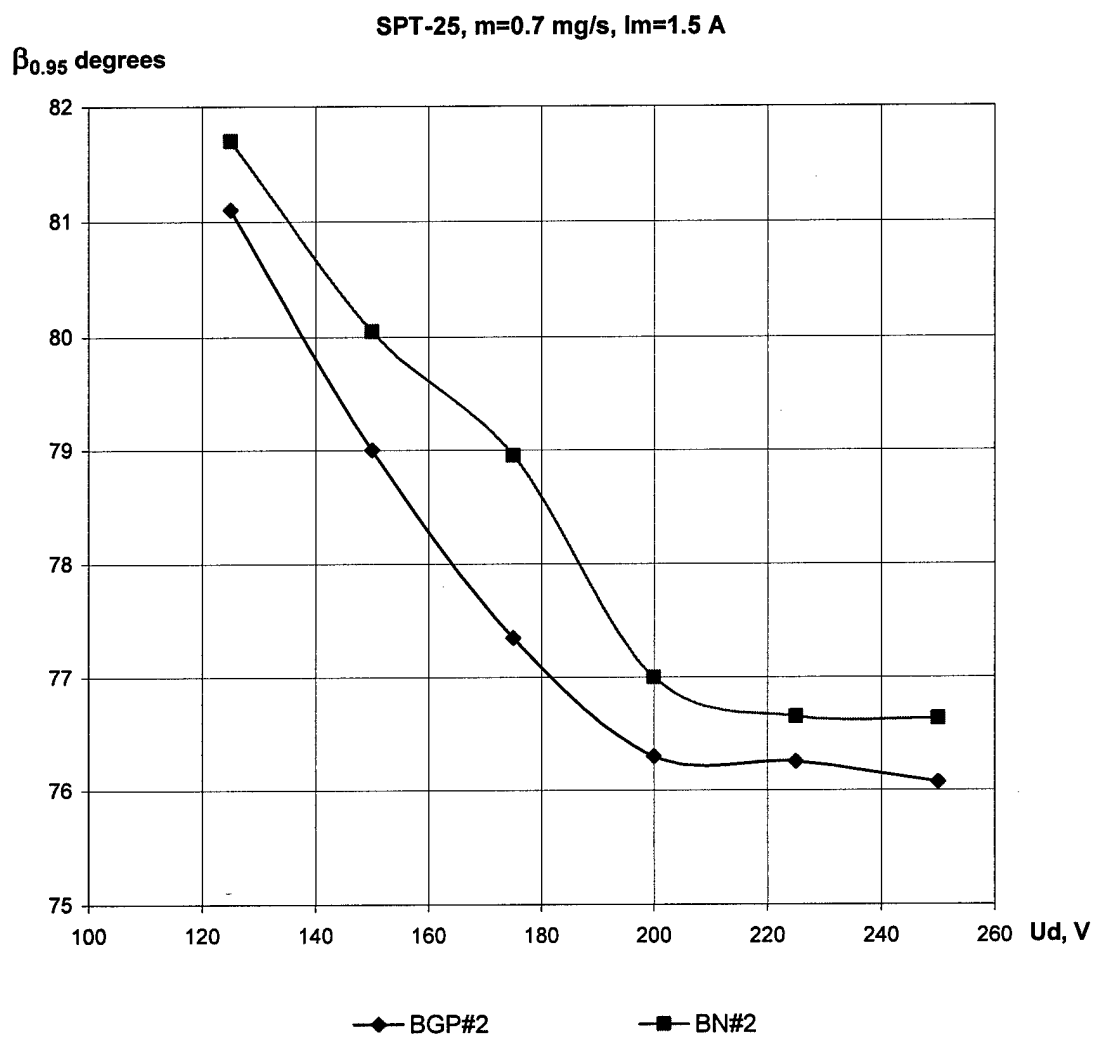


Fig.1.145. Plume half angle versus the discharge voltage.

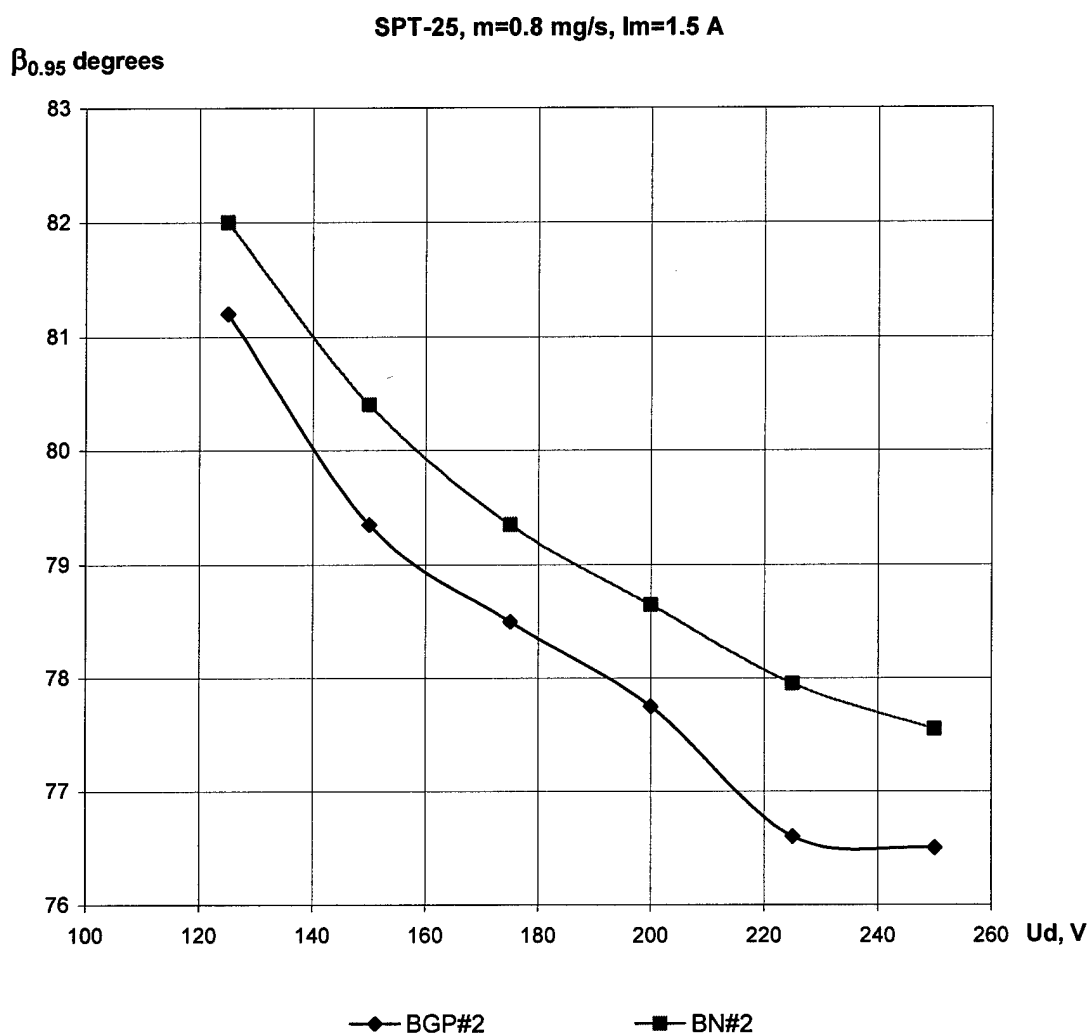


Fig.1.146. Plume half angle versus the discharge voltage.

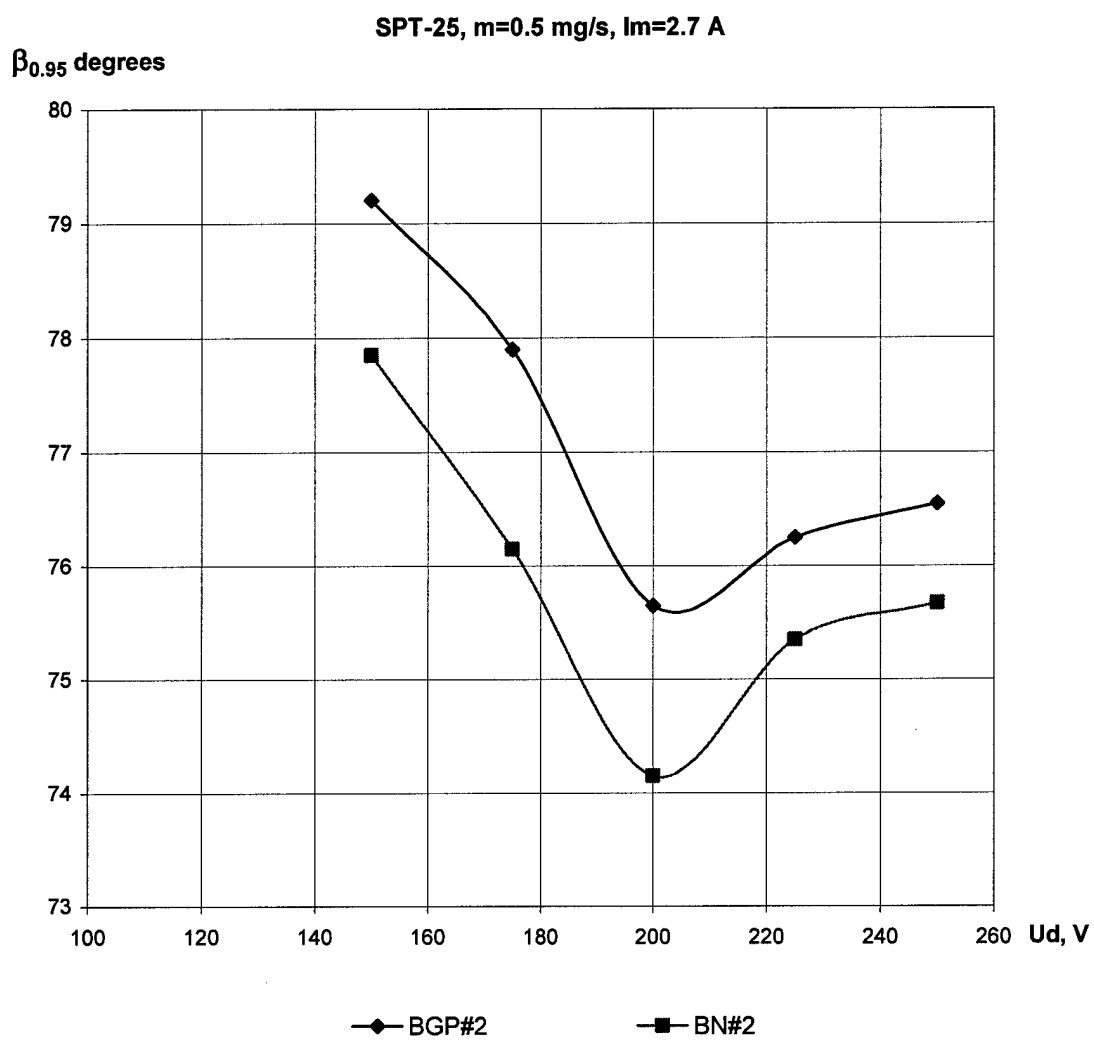


Fig.1.147. Plume half angle versus the discharge voltage.

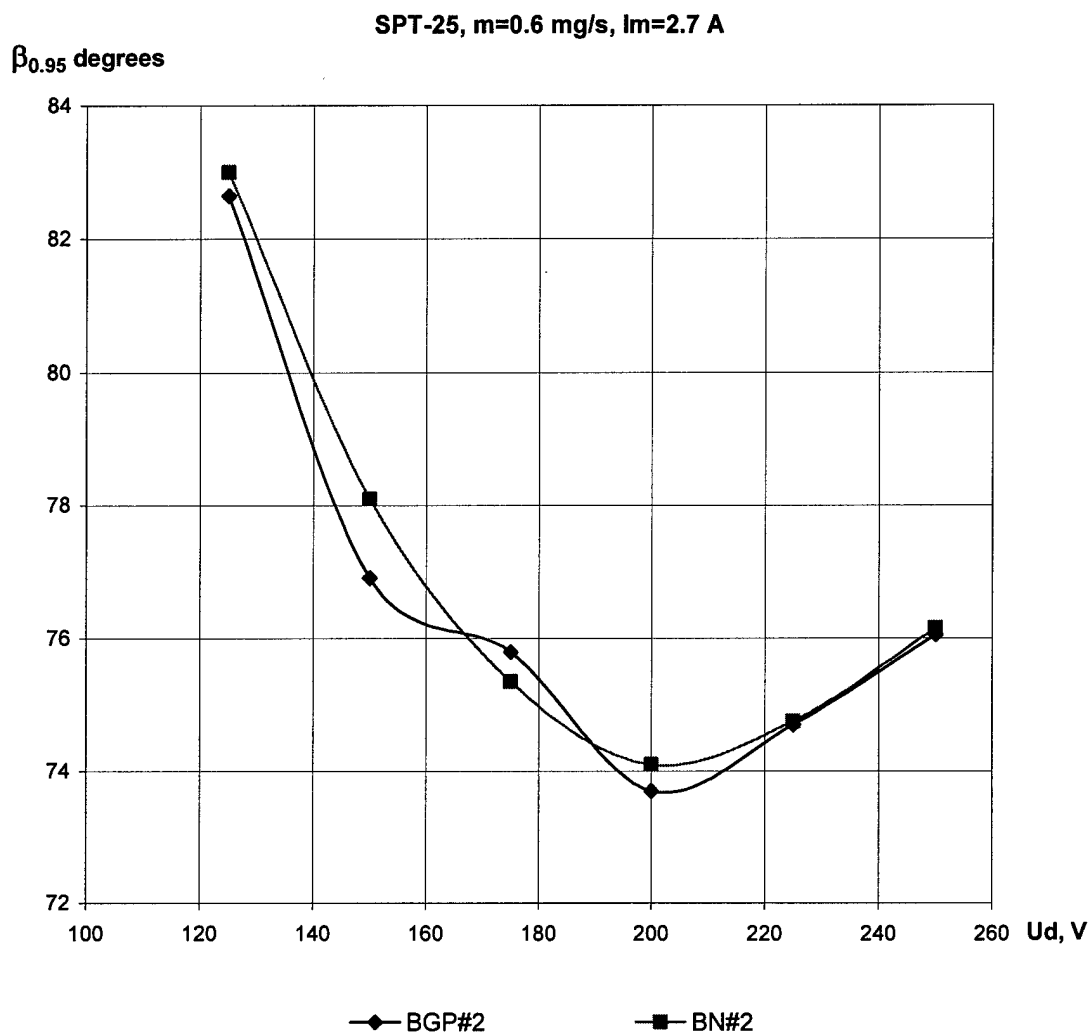


Fig.1.148. Plume half angle versus the discharge voltage.

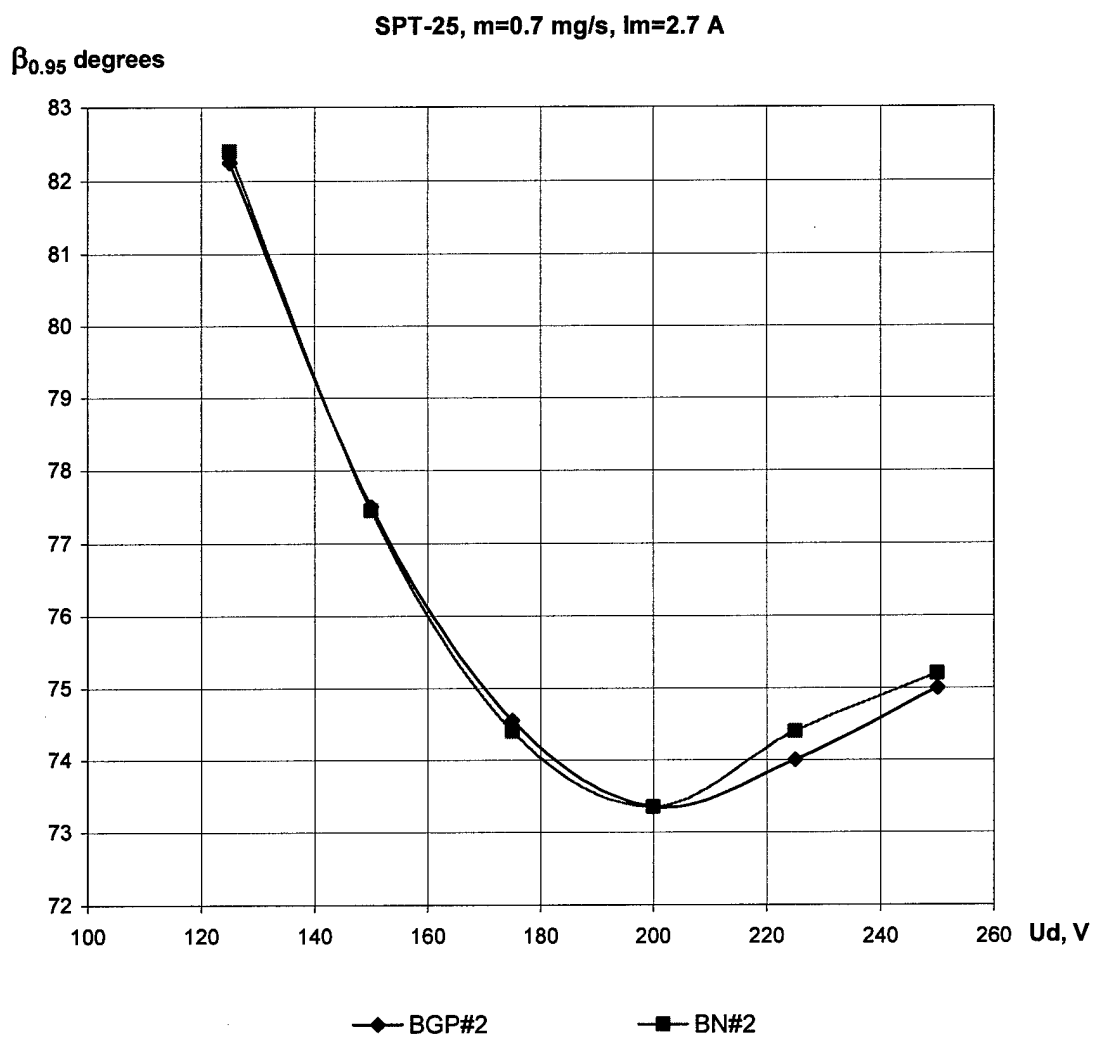


Fig.1.149. Plume half angle versus the discharge voltage.

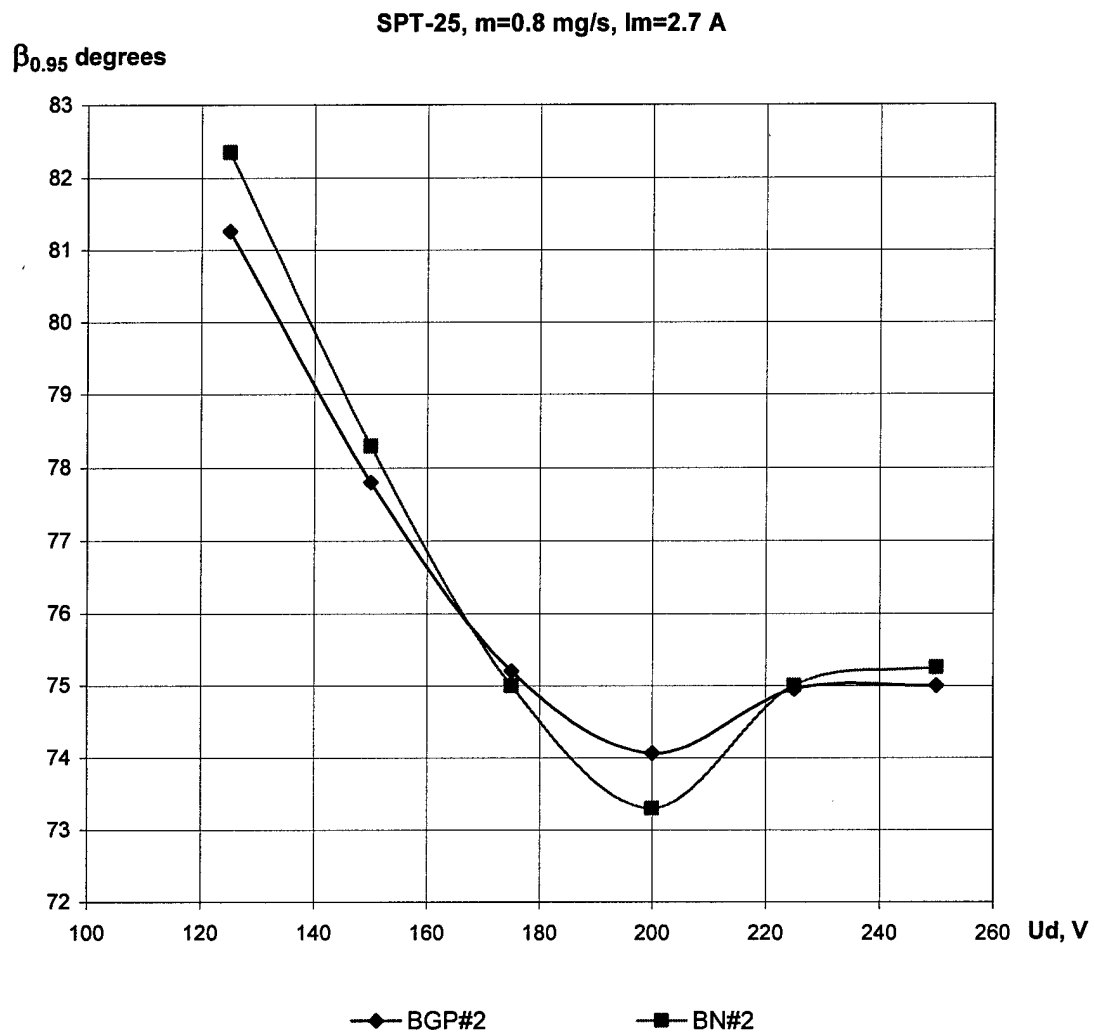


Fig.1.150. Plume half angle versus the discharge voltage.

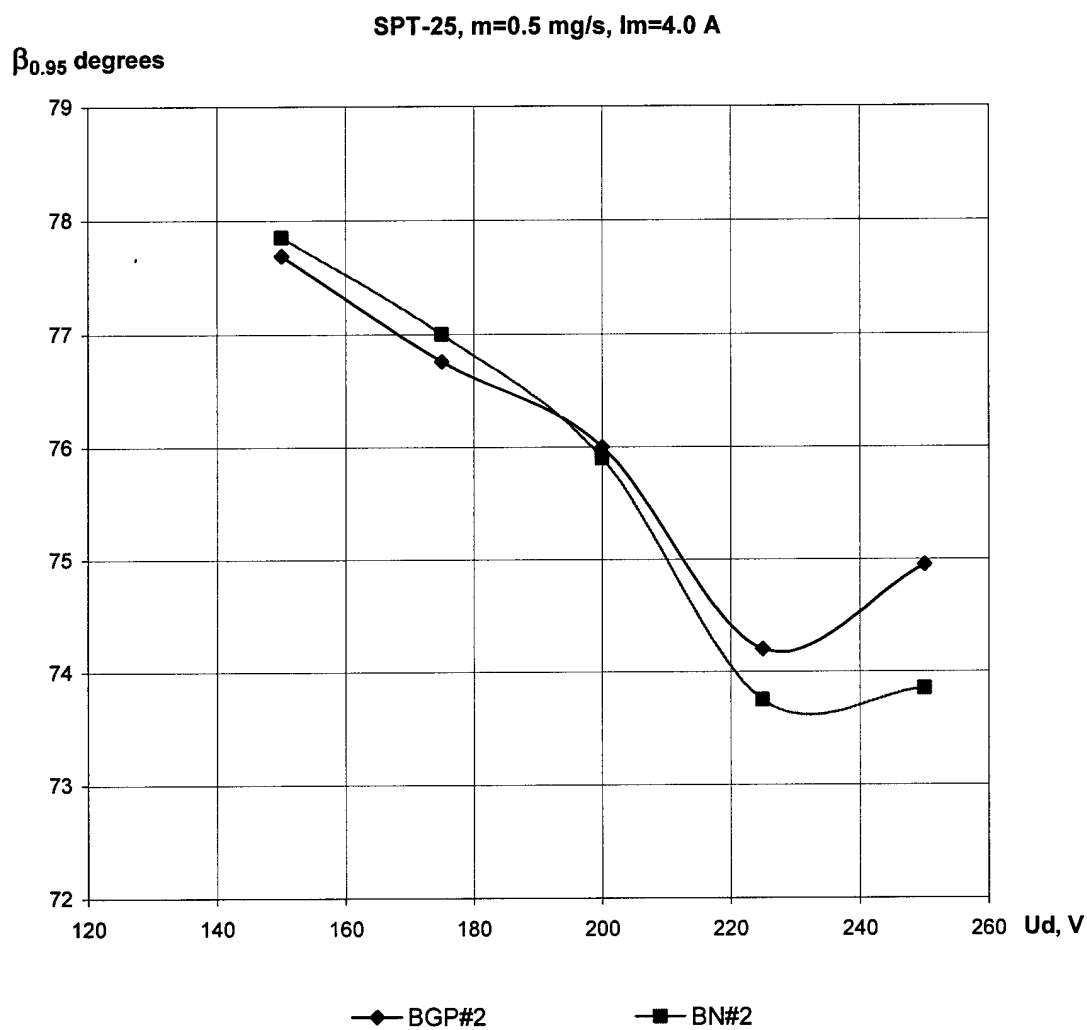


Fig.1.151. Plume half angle versus the discharge voltage.

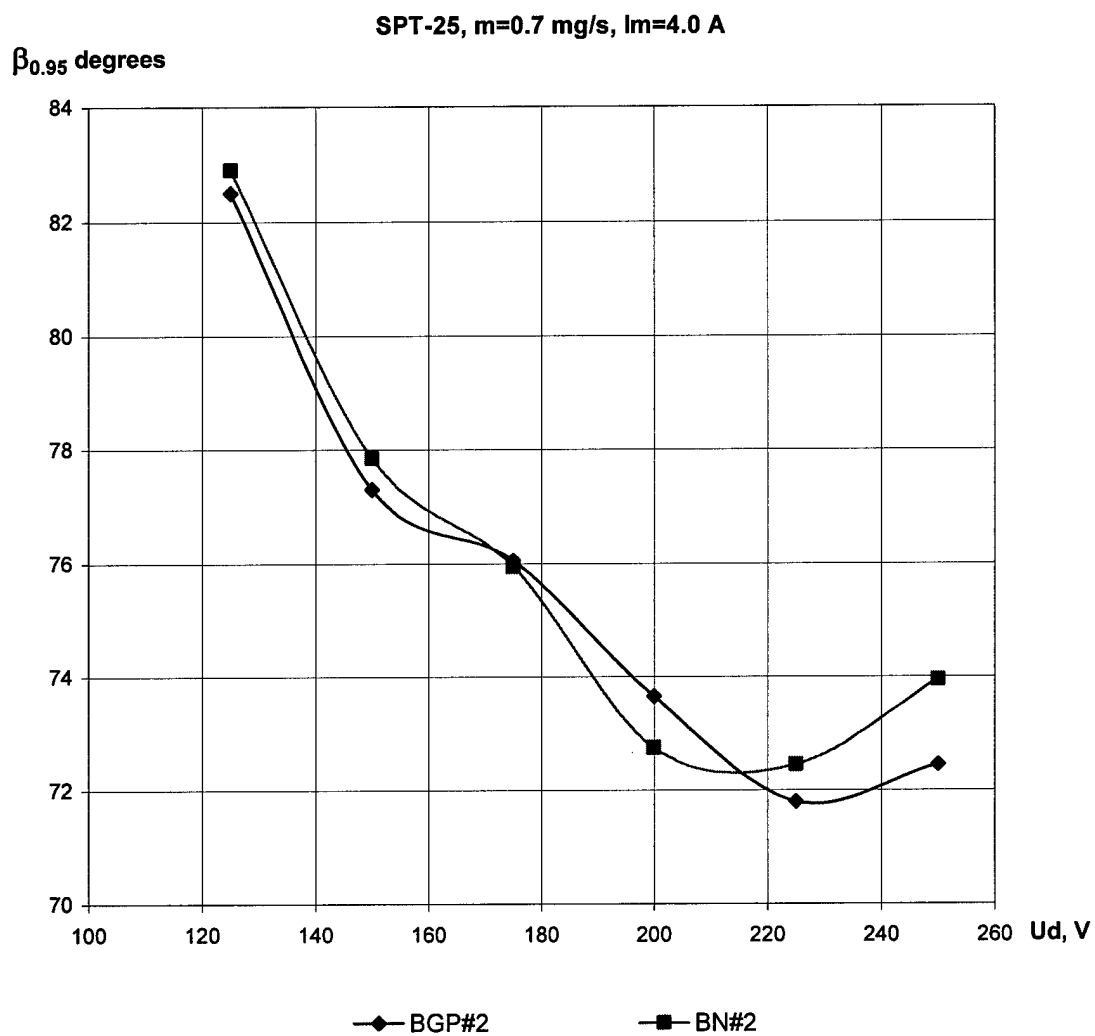


Fig.1.153. Plume half angle versus the discharge voltage.

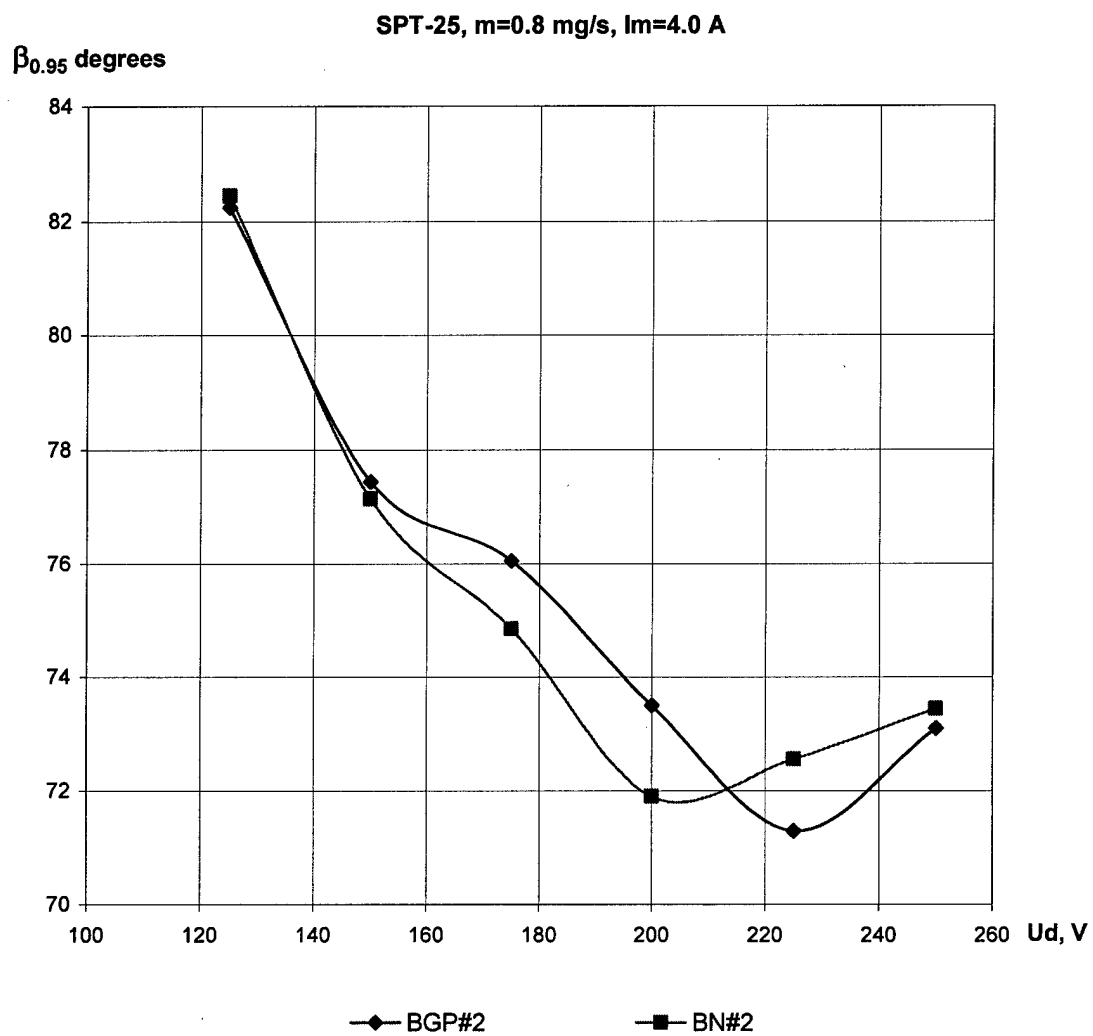


Fig.1.154. Plume half angle versus the discharge voltage.

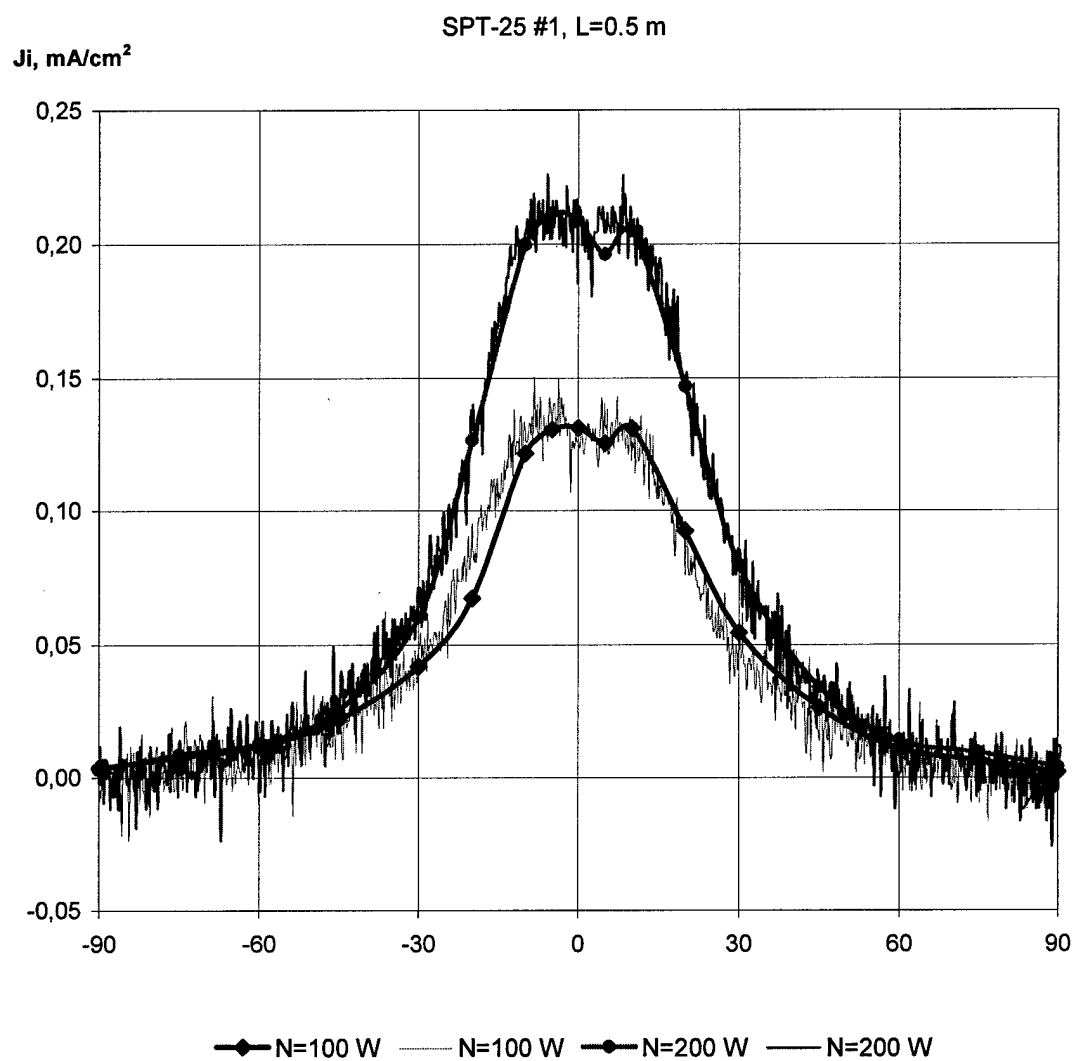


Fig.1.155. The accelerated ion current distributions in off-axis angle

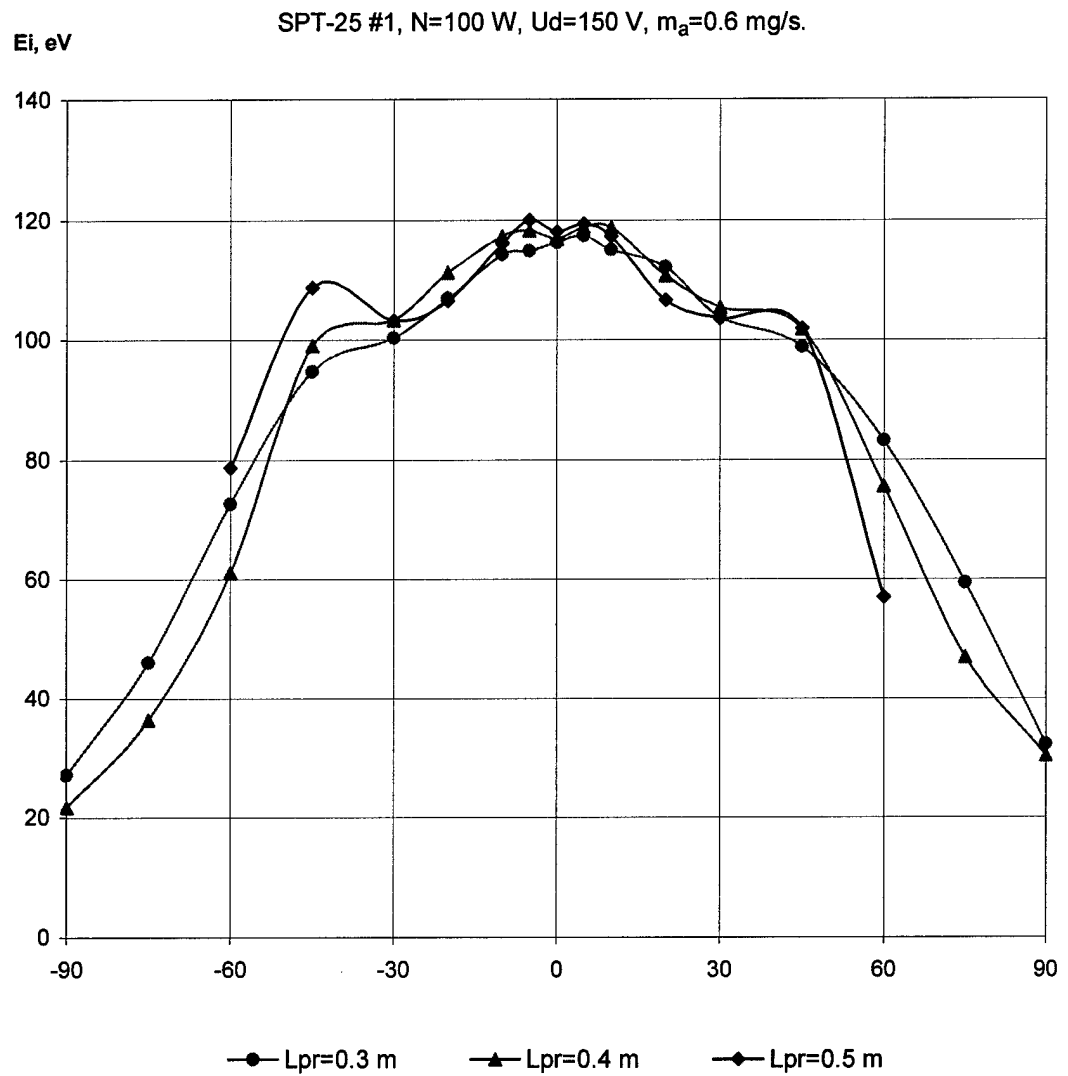


Fig.1.156. Mean energy of ions versus the off-axis angle

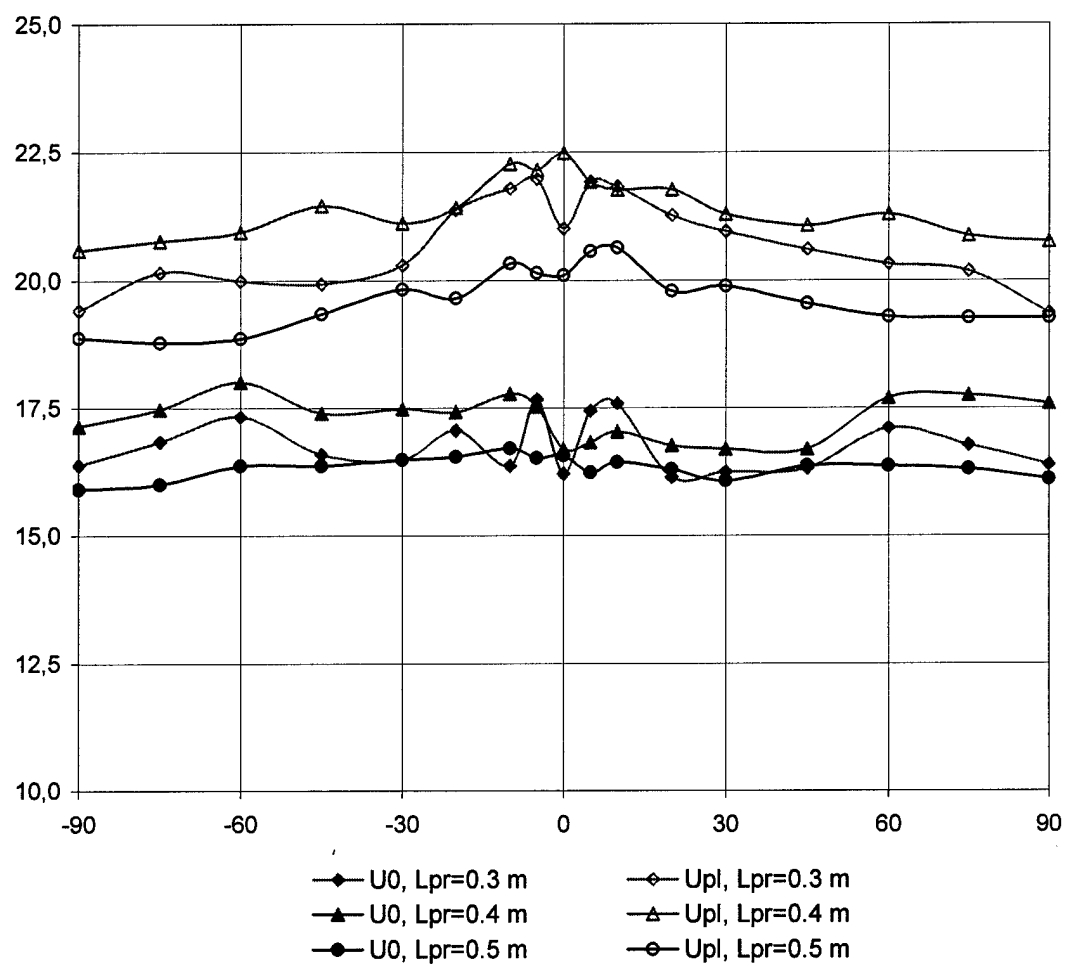
SPT-25 #1, $N=100$ W, $U_d=150$ V, $m_a=0.6$ mg/s. U_0, U_{pl}, V 

Fig.1.157. Probe floating potential U_0 and plasma potential U_{pl} values versus the off-axis angle

SPT-25 #1, N=100 W, $U_d=150$ V, $m_a=0.6$ mg/s.

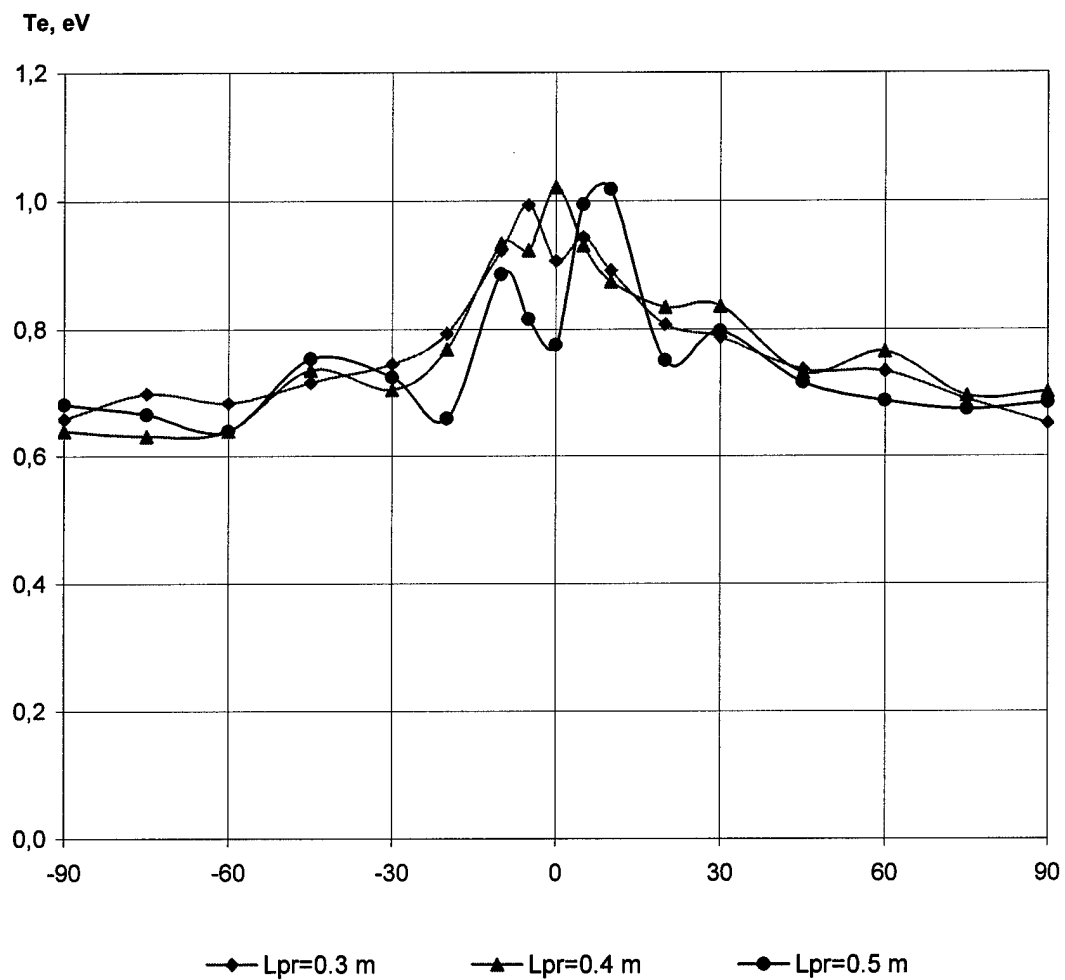


Fig.1.158. Electron temperature versus the off-axis angle

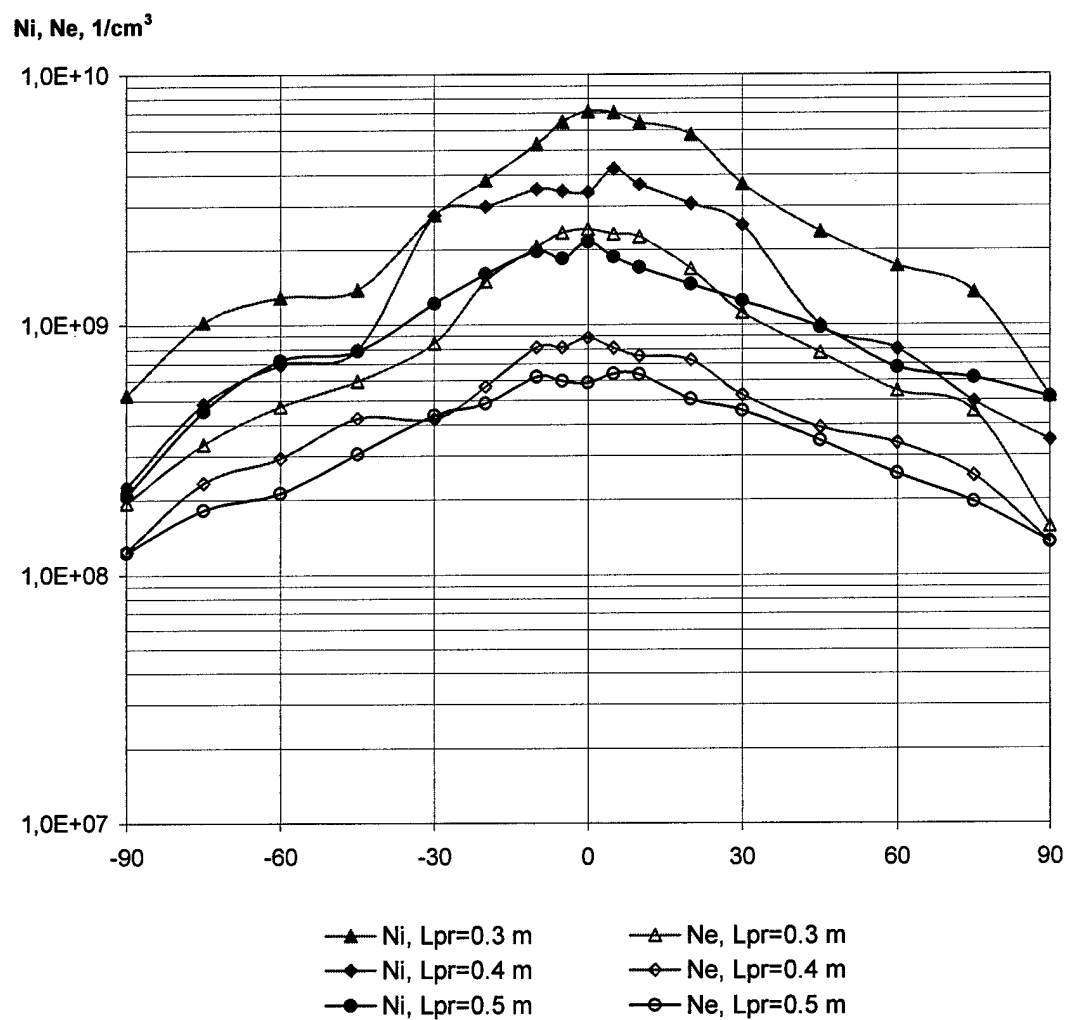
SPT-25 #1, $N=100$ W, $U_d=150$ V, $m_a=0.6$ mg/s.

Fig.1.159. Plasma density numbers derived from ion current value (Ni) and electron current value (Ne) versus the off-axis angle

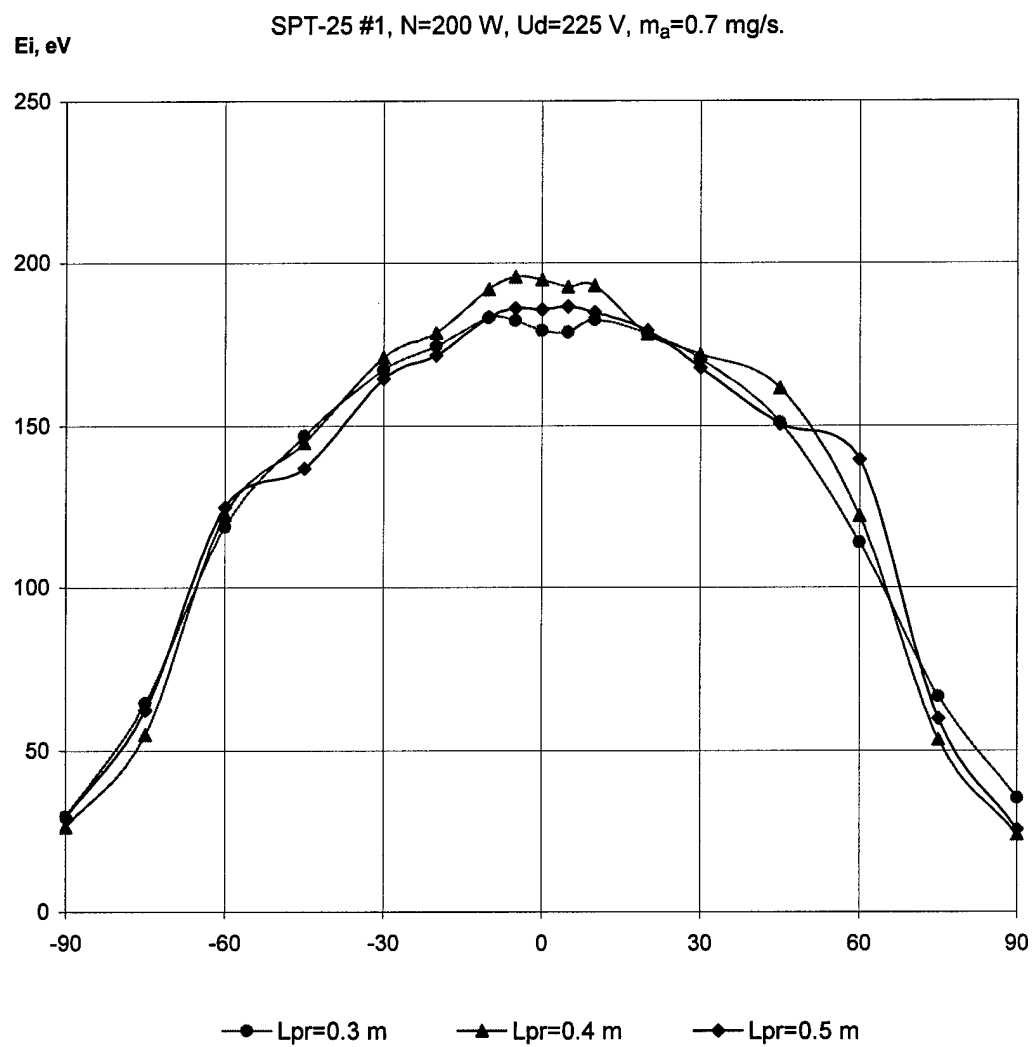


Fig.1.160. Mean energy of ions versus the off-axis angle

SPT-25 #1, $N=200$ W, $U_d=225$ V, $m_a=0.7$ mg/s.

U_0, U_{pl} , V

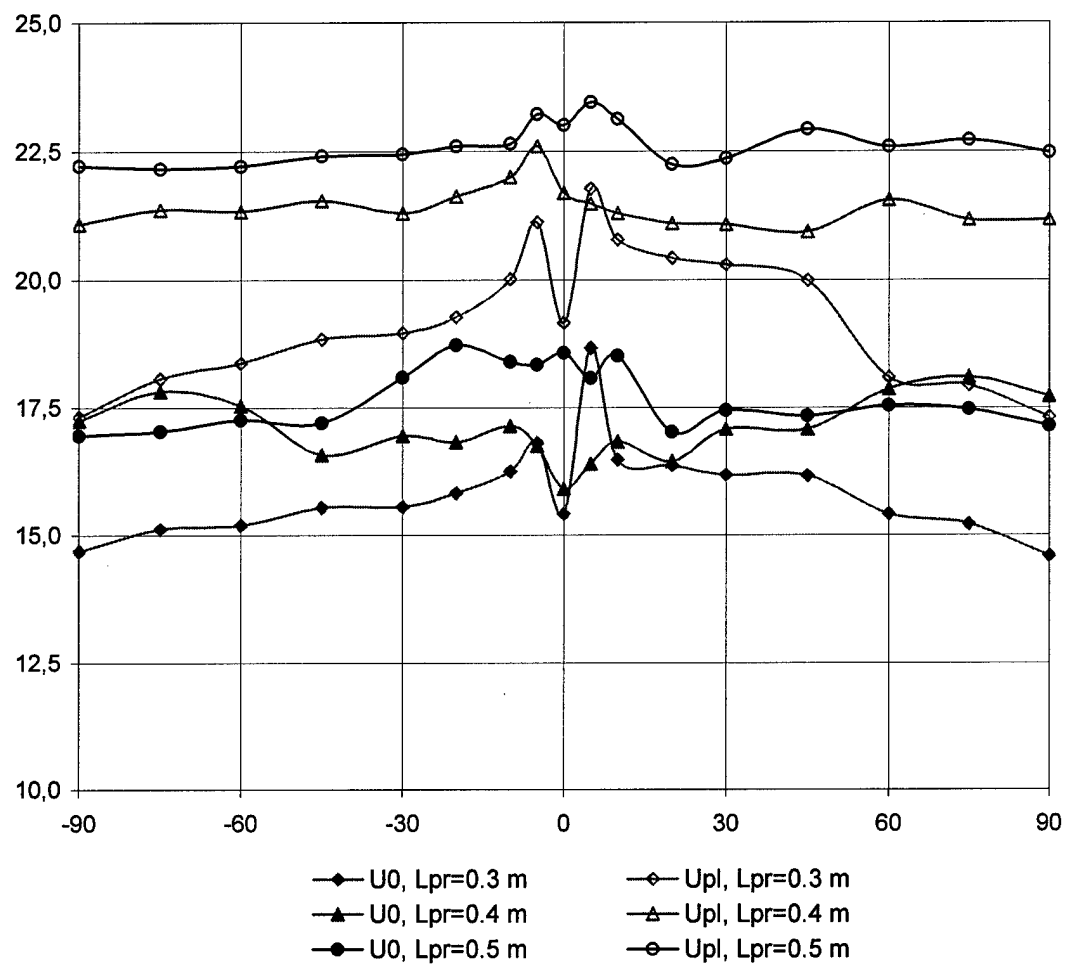


Fig.1.161. Probe floating potential U_0 and plasma potential U_{pl} values versus the off-axis angle

SPT-25 #1, $N=200$ W, $U_d=225$ V, $m_a=0.7$ mg/s.

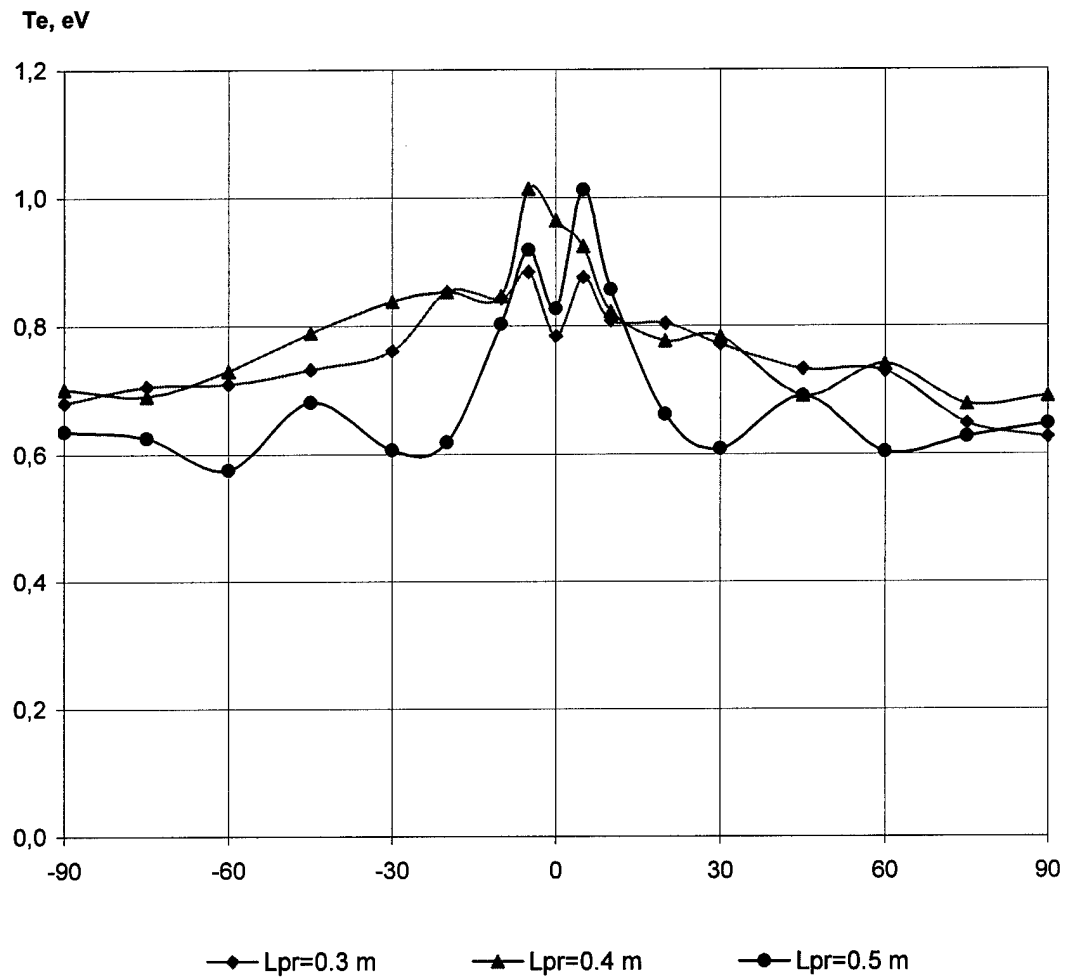


Fig.1.162. Electron temperature versus the off-axis angle

SPT-25 #1, N=200 W, $U_d=225$ V, $m_a=0.7$ mg/s.

Ni, Ne, $1/\text{cm}^3$

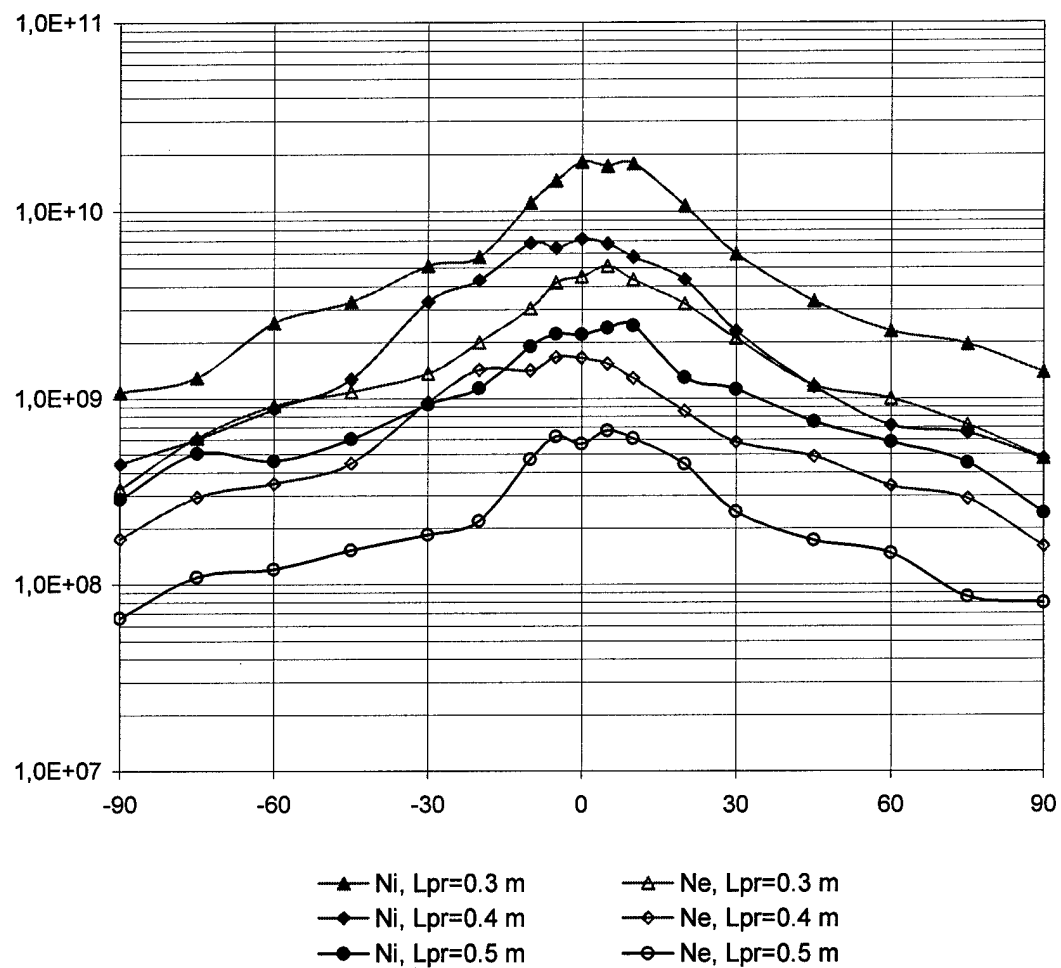


Fig.1.163. Plasma density versus the off-axis angle

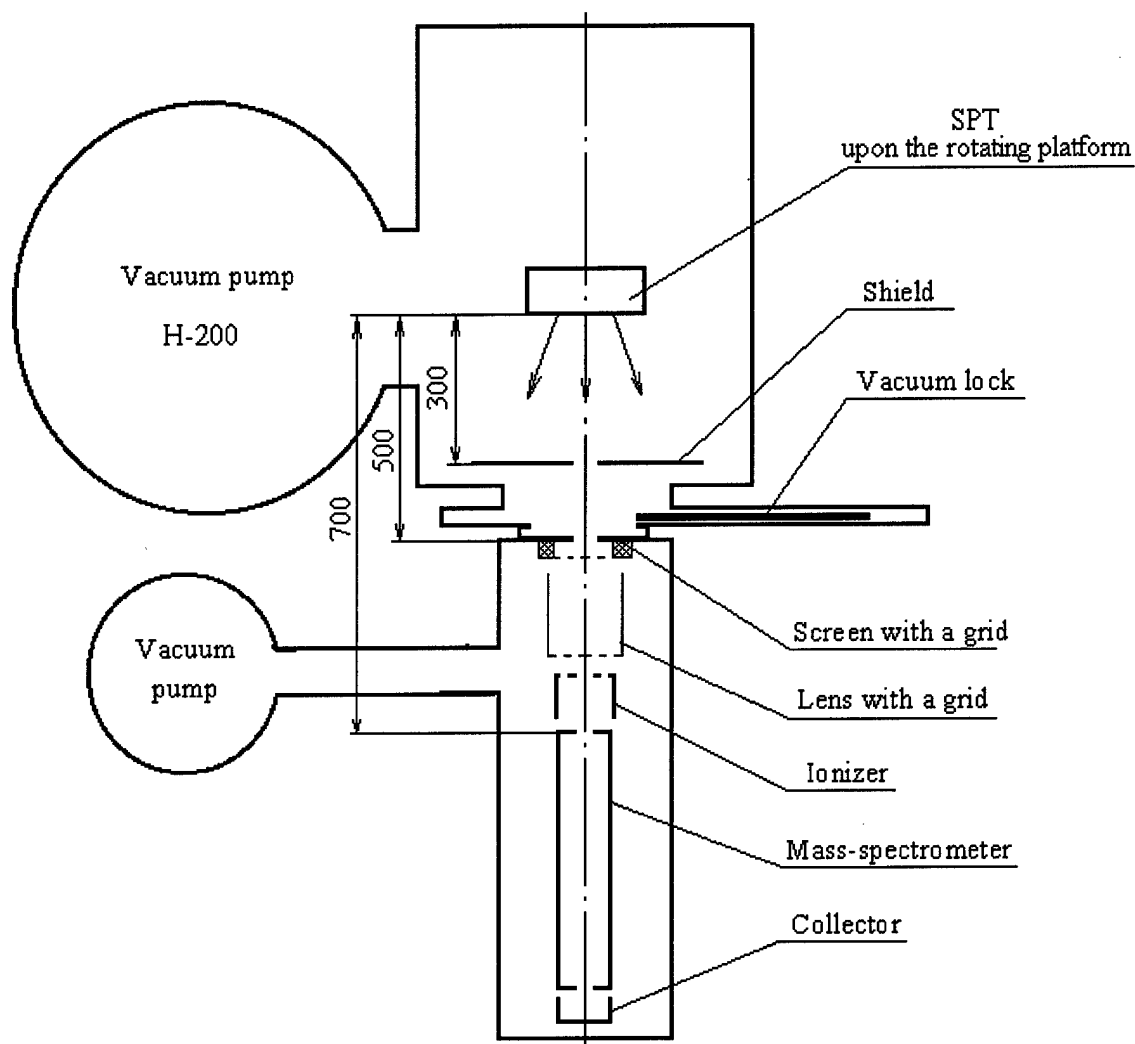


Fig.1.164. Circuit-diagram for measuring the mass (charge) composition of the SPT-25-plasma jet with a mass-spectrometer, MX 7304.

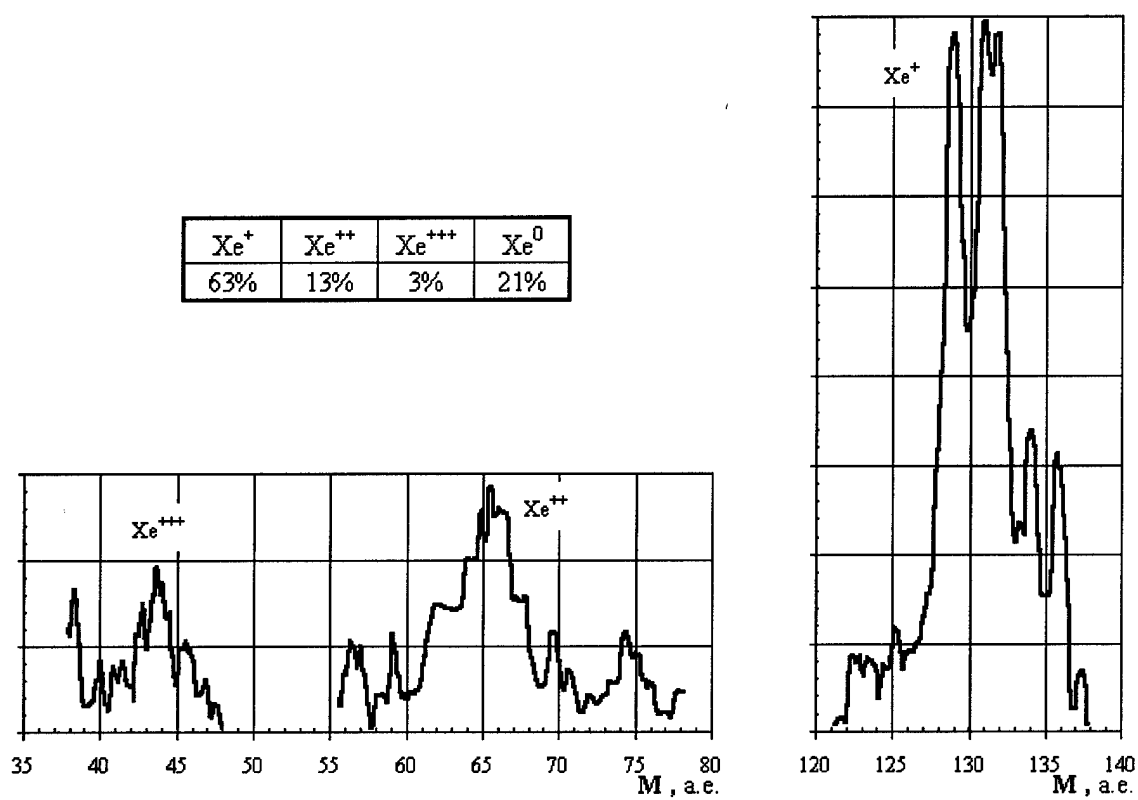


Fig.1.165. Mass-spectrogram of SPT-25-plasma jet
($N = 200W$, $U = 225V$, $P_{ch} = 4 \cdot 10^{-5}$ mm Hg).

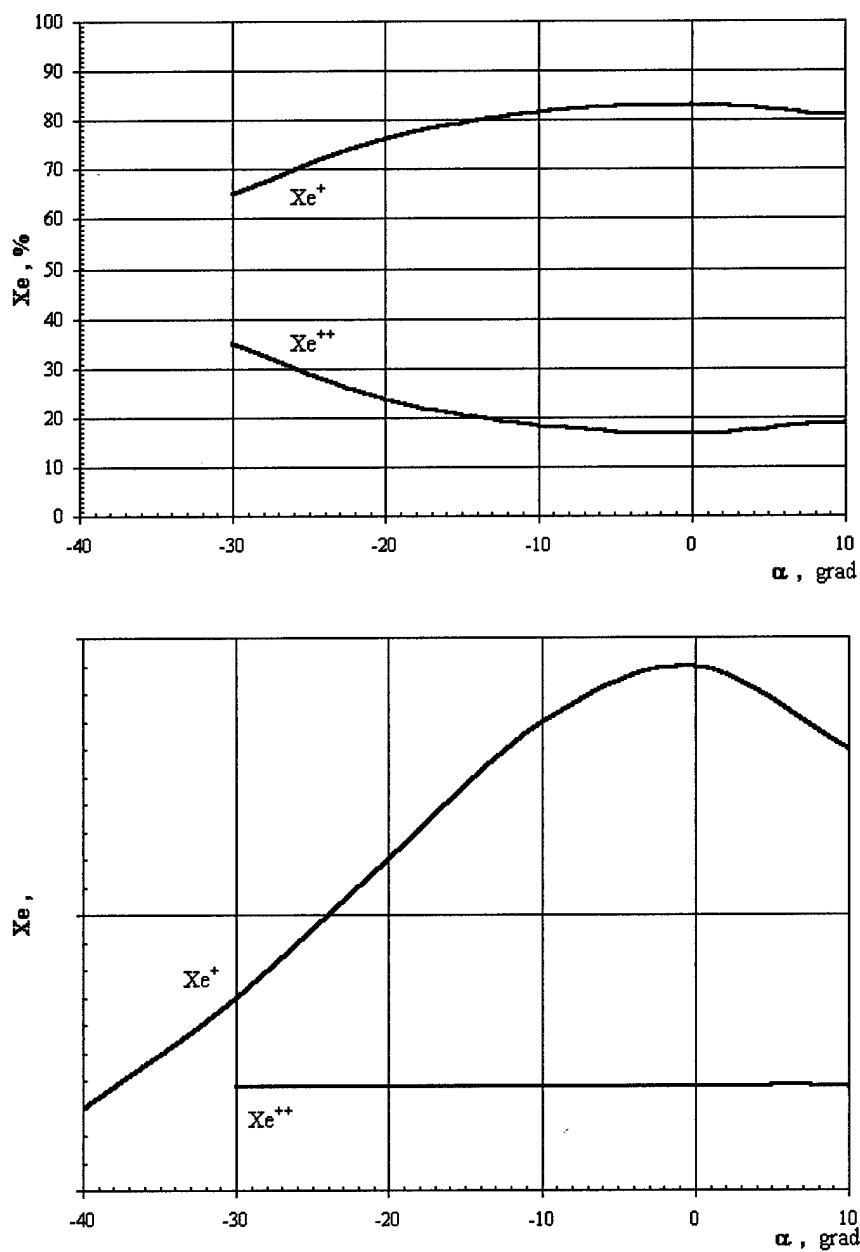


Fig.1.166. Distribution of ion components, Xe^+ and Xe^{++} , dependent on the angle in the SPT-25 jet.

III Task 2. Ablative Pulsed Plasma Thruster Study

III.1 Introduction

Ablative Pulsed Plasma Thrusters (APPT) were the first application of electric propulsion in space almost 40 years ago^[1]. The basic operation of the APPT consists of repeated discharge pulses across a solid propellant surface. Useful thrust is mainly produced by the electromagnetic acceleration of the ablated mass that has been ionized. The similar technique automatically provided the matching of a propellant feed with the APPT parameters and allows one to produce relatively effective plasma acceleration. The applications ranged from control propulsion for larger satellites to primary propulsion for small satellites. Currently, APPTs are considered as an attractive propulsion option for stationkeeping and drag makeup purposes of mass and power limited satellites.

However, the potential use of APPTs for formation-flying applications require longer-life components and lower system mass to meet mission requirements. Moreover, application of APPTs to orbit raising maneuvers of power-limited spacecraft require higher performance than has been previously demonstrated. External circuit resistance, mass loss at low speed, non-matched propellant flow rate multiply to provide a total thruster efficiency of less than 10%. By applying each of the inefficiencies in turn, it should be possible to improve the performance of the PPT substantially^[2].

In the 90's, the low thrust capabilities of APPT have been reopened, thanks to the tendency to decrease satellite mass. As the same time the experiments on improving of APPT performance have given noticeable results. Russian APPTs demonstrated efficiency on the level 20–30% for bank energy range 60–150 J^[3,4] for the last few years. APPT with such high thrust efficiency make possible solving of many control problems for small spacecrafts (SSC). This opens up new fields of their use as propulsion systems for SSC orbit control^[5].

Modeling^[6,7] shows that the APPTs can enhance their efficiency, when one manages to control the propellant flow rate, because the discharge parameters are strongly dependent on boundary conditions in the inlet of accelerating channel. Therefore the understanding of propellant ablation and ionization is very important for adequate numerical simulation of a discharge in APPT acceleration channel and thrusters development^[8]. Modeling of APPT using experimentally obtained dependencies of propellant flow rate presents useful approach for numerical modeling of APPT. However, it is necessary to have adequate understanding of propellant ablation and ionization at the inlet of APPT to control this for APPT discharge optimization^[9].

According Work Plan (Task 2), this section presents:

- Development of numerical APPT model,
- Study of heat flux transfer to propellant and ablation losses,
- Study of plasma parameters and discharge optimization,
- Development and tests of the APPT model.

We developed the 2D MHD model of plasma acceleration in coaxial APPT using experimental data. Main attention is devoted to conditions at the inlet of accelerating channel, which dramatically determine plasma dynamics in accelerating channel. Boundary conditions for propellant flow rate are based on the of energy flux propagated from a discharge to propellant. Propellant flow rate will be accounted from kinetics of thermal degradation of Teflon with use of measured energy flux onto propellant. Data obtained will be analyzed, approximated to be serving as boundary condition for APPT.

Experimental efforts were intended to the study of energy fluxes transferred from plasma onto propellant surface. Experiments were produced on APPT stand at Kurchatov Institute. The method of energy flux measurement and obtained results are presented. Energy flux measurements together with Teflon mass loss and current and voltage measurements have been carried out. Experiments to split particle flux and radiation flux are described and discussed.

Improvements in APPT performances have been done due to finding the optimum relations between the electric circuit parameters and the discharge channel dimensions, realizing the quasi-a-periodic discharge in the thruster and optimizing the current distribution in the discharge channel^[3,4].

For further APPT efficiency increasing as well as for retaining the achieved efficiency under APPT flight prototypes manufacturing it is necessary to understand more clearly the physical processes in thruster discharge channel. For this purpose the interferometric investigations inside APPT discharge channel, piezoprobe measurements of dynamic pressure distributions and ultra high-speed photography with visualization of plasma flow were undertaken. Besides, two APPT mock-ups operating at energy levels of 20 J and 40 J were developed and tested.

The objective of this work is to analyze the distinctive features of physical processes in APPT to study these through the use of different diagnostic methods, tests and numerical modeling. This makes possible to develop next generation APPT, with increased thrust characteristics.

III.2 Semi-Phenomenological Numerical Model of Plasma Acceleration in the APPT Thruster.

III.2.1 Problem statement

A rather complete model of a plasma flow in APPT should take account of the vapour molecule dissociation and neutral particle ionization; the model should represent the dynamics of molecules, atoms ions and electrons. However, even some attempts to represent the gas ionization only in a classical approach of the stationary flow encounter essential difficulties, since the gas ionization process in a thin layer is non-equilibrium one and the temperatures of ions and electrons can essentially differ from each other. Moreover, one should take account of the pulsed insulator evaporating kinetics. In this situation, it often turns out to be expedient to use a power approach to the description of an ionization process in plasma, using the idea of an electron cost, ε

$$\varepsilon = I + 3/2 T_e + R,$$

where I is the ionization potential, T_e is the electron temperature, R is radiation energy fraction per one act of ionization. The introduction of ε into consideration essentially simplifies the gas ionization process consideration in APPT^[7]. On the other hand, the attempts of strict and sequential ionization process consideration are often not confirmed by the experiments, since the development of ionization and radiation are mainly determined by the presence of impurities in the plasma. Rather small plasma temperature changes in acceleration channel are a specific feature of the electric discharge in APPT. This fact is related with a strong plasma radiation intensity growth with an increase in temperature. Weak temperature changes in the acceleration channel allow one to use an isothermal model of the acceleration.

Then, the plasma dynamics in APPT can be represented by the set of magnetic hydrodynamics equation, which has the following form in CGS - units:

$$\frac{\partial \rho}{\partial t} + \text{div} \rho \mathbf{v} = 0 \quad (1)$$

$$\frac{\partial \mathbf{v}}{\partial t} + (\mathbf{v} \nabla) \mathbf{v} = - \frac{\nabla P}{\rho} + \frac{1}{4\pi\rho} [\text{rot} \mathbf{H}, \mathbf{H}] \quad (2)$$

$$\frac{\partial \mathbf{H}}{\partial t} = \frac{c^2}{4\pi\sigma} \Delta \mathbf{H} + \text{rot}[\mathbf{v}, \mathbf{H}] + \frac{M_i c}{4\pi e} \text{rot} \frac{[\text{rot} \mathbf{H}, \mathbf{H}]}{\rho} \quad (3)$$

$$P = \frac{2\rho k T}{M_i} \quad (4)$$

$$T = T_i = T_e = \text{const} \quad (5)$$

The generally- adopted designations of the values are used in Equations. (1-5): ρ is the plasma density, \mathbf{v} is the velocity, P is the pressure, \mathbf{H} is the magnetic field, T is the temperature, σ is the conductivity, M_i is the ion mass, c is the velocity of light, e is the electron charge. In the equation of motion we neglect the viscosity forces; in the equation of magnetic field induction, the electron pressure gradient. The last term in the equation of induction (3) takes account of the Hall effect in plasma.

III.2.2 Two-dimensional non-steady model

Experiments have shown that the plasma flow in coaxial APPT are essentially two-dimensional ones; there are current loops in the accelerating channel, flow focusing towards the APPT-axis is observed etc. Therefore a two dimensional model is expedient to be used for an adequate representation of a plasma flow geometry and focusing in the instrument under consideration. APPT is schematically represented in Figure III.1.

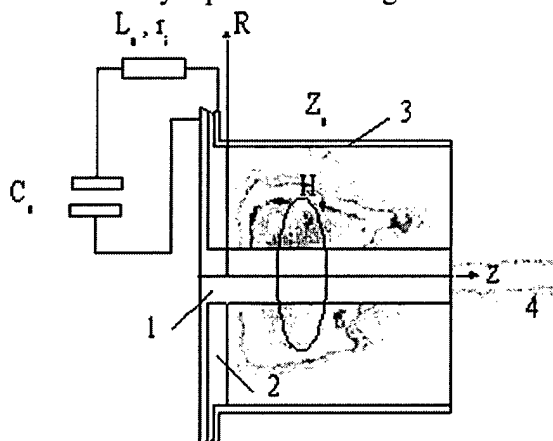


Figure III.1. APPT and the electric circuit loop; 1- internal electrode, 2 – propellant bar, 3 - external electrode, 4 -plasma.

III.2.3 Equations

Equations, representing the plasma acceleration within the framework of a two-dimensional model, can be obtained from Eqs. (1-5) and from the relationships for the initial and boundary conditions considered above.

In this case, as in one-dimensional model, in Ohm's law for the plasma, the electron pressure gradient, the thermal force, and the Hall term are dropped. Moreover, it assumed that

the degree of plasma ionization is $c = 1$, and $T = T_e = T_i$. The plasma conductivity is calculated from the relation $\sigma = 1.5 \cdot 10^{17} T_e^{3/2}$ (the Coulomb logarithm $= 6$). It is also assumed that the plasma temperature is constant at 3 eV. This last assumption distorts the real distribution of values in the acceleration channel, especially at the leading edge of the stream and at the dielectric surface.

III.2.4 Dimensionless equations

The choice of main units is:

$t_0 = 1/c\sqrt{L_0 C_0}$, - characteristic time of electric circuit;

$R_0 = R_1$ - radius of central electrode of accelerating channel;

V_0 is the initial voltage on the capacitor bank.

Other units are:

Velocity - $v_0 = R_0/t_0$, magnetic field is $H_0 = cV_0 t_0/R_0^2$, plasma density is $\rho_0 = H_0^2/4\pi v_0^2$, energy unit is $E_0 = C_0 V_0^2/2$, current is $cR_0 H_0/2$, resistance unit - $r_{g0} = 2V_0/c^2$.

Taking the assumption made above into account, we write a system of dimensionless equation with the same notation for the quantities used in the problem:

Then dimensionless equations can be written as:

$$\begin{aligned} \rho \left(\frac{\partial v_z}{\partial t} + v_x \frac{\partial v_z}{\partial z} + v_z \frac{\partial v_z}{\partial R} \right) &= -A_3 \frac{\partial \rho}{\partial z} - H \frac{\partial H}{\partial z}, \\ \rho \left(\frac{\partial v_R}{\partial t} + v_z \frac{\partial v_R}{\partial z} + v_R \frac{\partial v_R}{\partial R} \right) &= -A_3 \frac{\partial \rho}{\partial R} - \frac{H}{R} \frac{\partial}{\partial R} (RH), \\ \frac{\partial H}{\partial t} &= \frac{\partial}{\partial R} (v_R H) - \frac{\partial}{\partial z} (v_z H) - A_2 \left(\frac{1}{R} \frac{\partial}{\partial R} R \frac{\partial H}{\partial R} - \frac{H}{R^2} + \frac{\partial^2 H}{\partial z^2} \right) - \\ &\quad \xi \left[\frac{\partial}{\partial R} \left(\frac{H}{\rho R} \right) \frac{\partial}{\partial z} (RH) - \frac{\partial}{\partial z} \left(\frac{H}{\rho R} \right) \frac{\partial}{\partial R} (RH) \right], \\ \frac{\partial \rho}{\partial t} + \frac{1}{R} \frac{\partial}{\partial R} (R \rho v_R) + \frac{\partial}{\partial z} (\rho v_z) &= 0, \quad P = A_3 \rho. \end{aligned} \quad (6)$$

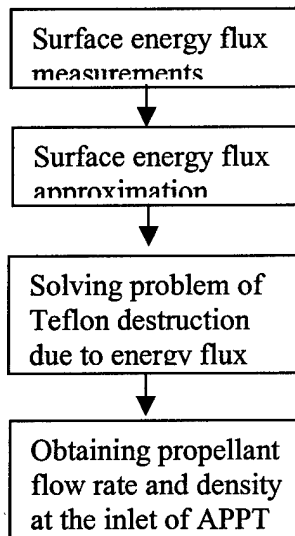
Here $A_2 = \frac{c^2}{4\pi\sigma R_0 v_0}$, $\xi = \frac{cM_i}{eR_0\sqrt{4\pi\rho_0}}$, Morozov parameter

$$A_3 = \frac{2kT}{M_i v_0^2}.$$

III.2.5 Boundary and initial conditions

III.2.5.1 Inlet plasma density

Propellant flow rate is determined by dissipation of energy transferred from electrical discharge and can be obtained from approach of Teflon ablation with accounting of kinetics (see Appendix 1).



In considered problem statement, boundary condition at the inlet is referred to the outer part of ionization layer where ionization degree is near 1. We neglect the processes in thin layer where plasma is ionized. Only account of energetic losses for ionization will take place. Propellant flow rate will be accounted according the procedure shown in Figure III.2.

Figure III.2. Inlet propellant flow rate obtaining procedure

Boundary condition for propellant (Teflon) flow rate is based on energy flux measurements and approximation. Data obtained will be used for solving a problem of Teflon destruction and ablation due to energy flux propagated from electrical discharge.

The version of the device for registration of energy flow falling on APPT propellant has been developed. The basis of the registration is the thermistor ($1.6 \times 3.2 \text{ mm}^2$, weight 9 mg), assembled in a bridge scheme. The estimations show, that the sensitivity of the sensor is sufficient for measurement of energy flows on propellant surface.

The boundary condition for magnetic field are determined by the equations of electric circuit of the APPT:

Electric circuit equation can be written as:

$$V - \ln(\lambda) \left[v_z H(1,0,t) + A_2 \frac{\partial}{\partial z} H(1,z,t) \Big|_{z=0} \right] - A_1 \frac{\partial}{\partial t} H(1,0,t) - H(1,0,t) r_g = 0$$

$$\frac{dV}{dt} = A_1 H(1,0,t) \quad (7-8)$$

$A_1 = L/2R_0$ - ratio of initial inductance to diameter of central electrode, $\lambda = R_2/R_1$.

At the initial stage of the discharge, the gap between the APPT-electrodes is filled with some amount of plasma due to an initiating device. As a rule, the relative amount of igniting plasma, at various discharge ignition techniques, is no more, the a few percent of a total plasma mass, taking part in the discharge. Therefore one can assume that the plasma occupies a cylindrical layer, l -thick, at $t=0$:

$$0 < z < z^*, \quad R_1 < R < R_2,$$

and it is characterized by the following parameters

$$v_z = v_0, \quad v_r = 0, \quad H = 0, \quad T = T_0, \quad \rho = \rho^*$$

ρ^* - is initial plasma density in thin cylindrical layer at $t=0$. Value of ρ^* provide initial plasma mass at the level of (1-10)% of total evaporated mass per discharge.

Some complicated processes occur at the plasma- metal interface. The heat release at electrodes under Ohm heating of their surface layer and under absorption of radiation from discharge, as well as a result of electron and ion plasma heat conduction can result in the electrode melting and evaporation. Nevertheless, these phenomena, in the microsecond range of the discharge duration even in high power APPT, weakly affect APPT parameters. Indeed, it has experimentally been shown that the losses at the electrodes do not exceed 10-15 % in the total energy balance. The boundary layer thickness in the plasma should be of the order of a few particle mean free paths and the consideration of this range within the framework of the MHD- model does not seem to be possible. Therefore it is expedient to formulate the boundary conditions to the problem to exclude the boundary layer consideration near electrodes. Within the framework of the MHD -model it can be done, assuming that

$$\frac{\partial v_z}{\partial R} = 0, \quad \frac{\partial \rho}{\partial R} = 0, \quad \frac{\partial}{\partial R}(RH) = 0, \quad V_R = 0, \quad (9)$$

At the electrode surfaces (when $R=R_1, R=R_2$) and

$$\frac{\partial v_R}{\partial z} = 0, \quad \frac{\partial \rho}{\partial z} = 0, \quad \frac{\partial H}{\partial z} = 0, \quad (10)$$

at the central electrode face (when $z = z_0, R < R_1$).

As for the velocity v_z at $z=z_0, R < R_1$, i.e. at the cathode cut, two versions of boundary conditions are possible:

$v_z = 0$, the cathode end is impenetrable for the plasma,

$$\frac{\partial v_z}{\partial z} = 0, \quad (11)$$

the cathode end is absolutely penetrable (divertor).

At the APPT-axis, when $R=0, z > z_0$, the boundary conditions, follow from the condition of symmetry for all the values

$$H=0, \quad v_R=0, \quad \frac{\partial v_z}{\partial R} = 0, \quad \frac{\partial \rho}{\partial R} = 0. \quad (12)$$

At the start of the acceleration channel ($z=0$), the following boundary conditions are used ($R_1=1$):

$$v_z = v_0, \quad v_R = 0, \quad \rho = \rho_0, \quad T = T_0, \quad H(R,0,t) = \frac{H(1,0,t)}{R}. \quad (13)$$

The magnetic field at the point (1,0) is determined from the circuit equation.

Since the plasma conductivity is a finite in our case, one should formulate the boundary condition for the magnetic field. At the output from the APPT- channel ($z=z_0$), the condition has been used.

$$\frac{\partial H}{\partial z} = 0$$

It is often used in the MHD- calculation. It corresponds to the neglecting of a radial current density component at the acceleration channel output.

III.2.6 Results of Simulation

The parameters of the APPT under modeling are shown in Table 1.

Table 1 Parameters of the APPT under modeling

Inner electrode radius, R_1	1 cm
Radius of outer electrode, R_2	5 cm
Length of inner electrode, z_0	5-10 cm
Length of outer electrode, z^*	17 cm
Initial voltage, V_0	1-3 kV
Bank capacitance, C_0	300 μ F
Inductance, L_0	10^{-7} H
Average mass of ion, M_i	16,6
Temperature, T	1.5 –3 eV
Input plasma density, ρ	$10^{-7} - 10^{-6}$ g/cm ³
Input plasma velocity, v_0	$2-5 \cdot 10^5$ cm/s

Below we discuss an example with dimensionless parameters to be: $A_1=50$, $A_2=3.6$, $A_3=1$. Radial distribution of ablated mass obtained in balance experiments is in inverse proportion to radius, $\sim 1/r$. Total ablated mass is proportional to power of discharge. For relatively high energy flux falling onto the propellant surface propellant flow rate is proportional to this flux. Approximation of inlet condition for propellant flow rate was deducted from mass loss measurements and modeling.

$$\dot{m} = \dot{m}_0 + \alpha R / R_1 \frac{\partial}{\partial z} H^2(R_0, t),$$

\dot{m}_0 is plasma generated by ignition device, α - is the coefficient providing a correlation between simulated and ablated mass loss, R_1 –is the radius of central electrode.

As it was already marked, the discharge in APPT is accepted conditionally to divide into following stages:

- formation of the discharge, which includes a temporary interval from the moment of initiation of the discharge up to plasma occurrence at the outlet of the accelerating channel;
- quasi- steady plasma flow, which in our case covers an interval $2t_0$. In this stage the distribution of parameters of plasma in the accelerating channel varies poorly;
- damping, when a current and power of the discharge are small in comparison with their maximum values.

To find the parameters of numerical model close to experimental model, firstly the current - voltage diagram of the model was found similar to experimental one. This is the initial point of modeling. Accordance of simulation - experimentation in integral parameters of discharge

(current, - voltage, energy transfer to APPT) is necessary for next modeling of plasma parameters.

The current-voltage diagram of APPT discharge under consideration is shown in Figure III.3.

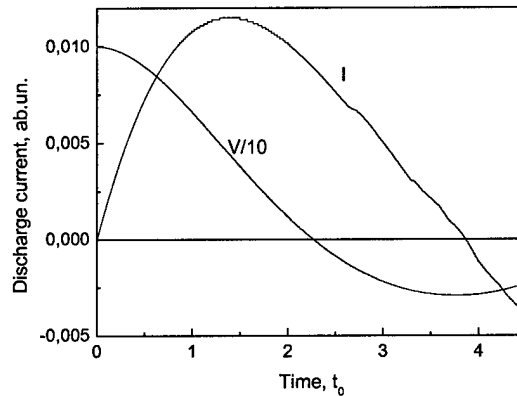


Figure III.3. Time dependencies of a current and bank voltage in APPT and bank voltage. $t_0 = 5 \mu s$.

The maximal current and forms of current and voltage have a good correlation with experiment. Figure III.4, Figure III.5 give the distribution of plasma density and magnetic field in the acceleration channel for moment of time equal 1 ($5 \mu s$).

These distributions are changed in time with duration as current and voltage. Other words at the time $t = (1 - 2) t_0$, quasi-steady plasma flow takes place. Experiments show that ionization layer thickness is on the level of not higher than 0.1 mm. So, in this time ionization process does not effect significantly on plasma dynamics near the inlet of the thruster.

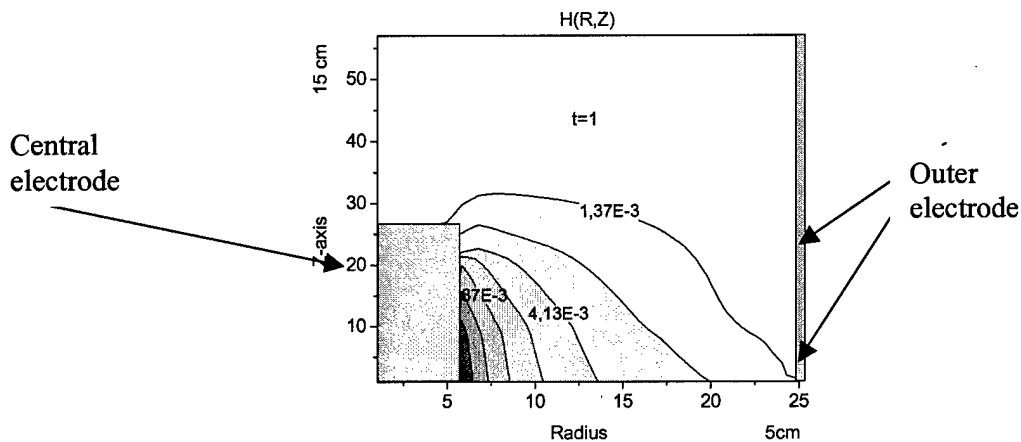


Figure III.4. Magnetic field distribution in APPT accelerating channel ($t = 5 \mu s$).

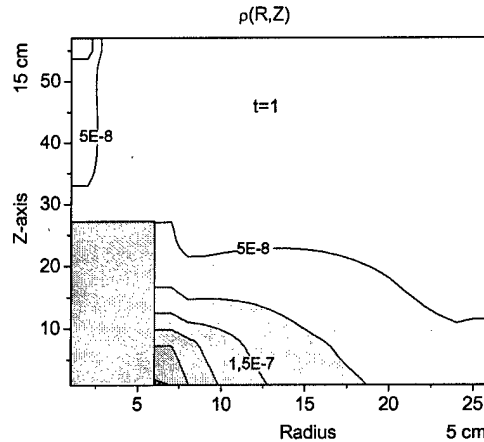


Figure III.5. Plasma density distribution in APPT accelerating channel ($t = 5 \mu s$).

Due to radial distribution of plasma density in the inlet to the acceleration channel outlet axial velocity of plasma have weak radial dependence. Other picture arises for radial velocity. Inner part of plasma flow is focused to the axis. Plasma located near outer electrode has negative value of radial velocity. Accordingly near outer electrode (anode) insignificant increase in plasma density arises. This does not change noticeably plasma dynamics in the thruster.

When the front of plasma flow reaches the end of the central electrode, the flow with characteristic tubular structure is formed in this area. The similar structure of a flow exists at the end of the central electrode and further the distribution of plasma parameters varies poorly. The tubular distribution of density received at the simulation, has a good correlation with interferometric results.

Part of plasma focused in the axis producing plasma focus (the area of increased plasma density).

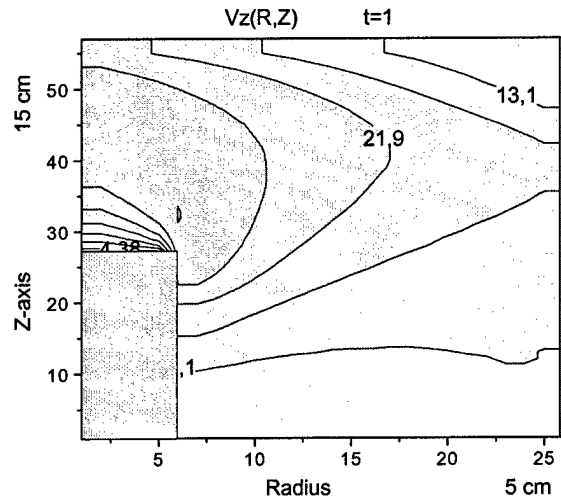


Figure III.6. Axial velocity distribution in APPT accelerating channel ($t=5 \mu s$).

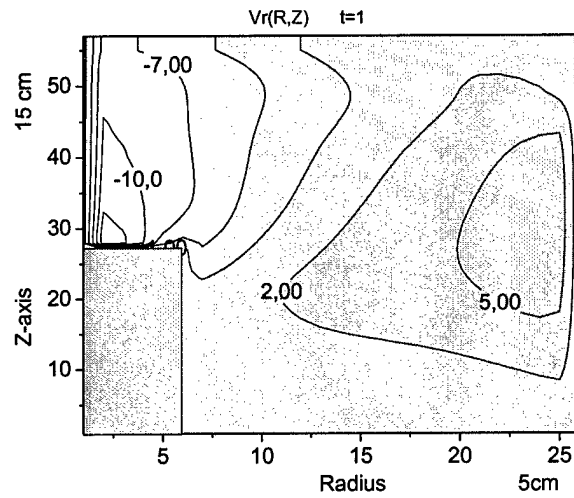


Figure III.7. Radial velocity distribution in APPT accelerating channel ($t=5 \mu s$).

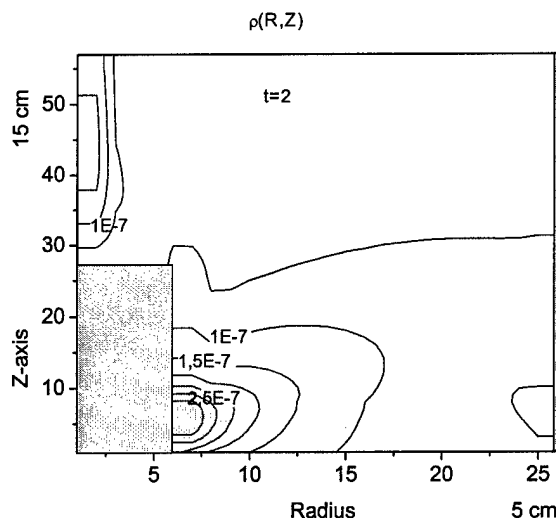


Figure III.8. Plasma density distribution in APPT accelerating channel ($t = 10 \mu s$).

Plasma density distribution near the zero of a current ($t = 10 \mu s$) shows that significant part of plasma having low velocity located in the inlet of the accelerating channel. Seems, this part of a plasma at the end of first half-period of a current create late time ablation mass flow visible in the interferogram.

There are not effectible current loops in volume of the accelerating channel that is due to rather weak dependence of plasma velocity, from radius and large size of average plasma velocity. Thus the skin-effect, causing occurrence of current loops, plays a smaller role.

As a whole demonstration of two-dimensional model of APPT shows that this adequately describes formation and acceleration of a plasma flow in coaxial accelerating channel. The simulated parameters of considered APPT have appeared close to, measured in experiments.

The model gives a correct qualitative picture of separate stages of discharge in APPT:

- plasma flow formation,
- appearance of tubular structure at the end of the central electrode,
- focusing of a flow etc.
- appearance of low accelerated mass near the zero of the bank voltage.

The features of propellant flow rate determine monotonous character of distribution of density and especially axial velocity of plasma, and magnetic field in accelerating channel.

The developed numerical model of APPT is a tool to improve thruster parameters.

III.3 Heat Flux Transfer to the Propellant and Ablation Losses.

III.3.1 Experimental Stand for the Propellant Study

The quasi-steady APPT is housed in a rectangular stainless steel tank of volume near $1.2 m^3$. Prior to thruster ignition, the tank is evacuated down to approximately 3×10^{-5} Torr by an oil diffusion pump and mechanical pump. The evacuation velocity is equal 5000 l/s under the pressure 10^{-4} Torr. The pulsed power supply was assembled of capacitors with the total capacitance up to 300 μF . Maximal initial voltage is up to 5 kV. The capacitor bank is connected with the feeder through the low inductive cable bridge composed of 48 high current coaxial cables. The estimated cable bridge inductance is 3×10^{-9} H. The inductance of vacuum feeder is 5×10^{-8} H. So, bank and feeder can simulate pulsed power source of APPT in wide

range of circuit inductance and capacitance. The thruster (Figure III.9) consists of a cylindrical copper anode and a tungsten cathode. The accelerating coaxial channel is near 9 cm long and 10 cm and 2 cm in diameter respectively. Outer electrode is anode. Teflon is the solid propellant. The main high current discharge in accelerating coaxial channel is triggering by low power breakdown plasma moving through the holes in the inner electrode to the outer electrode

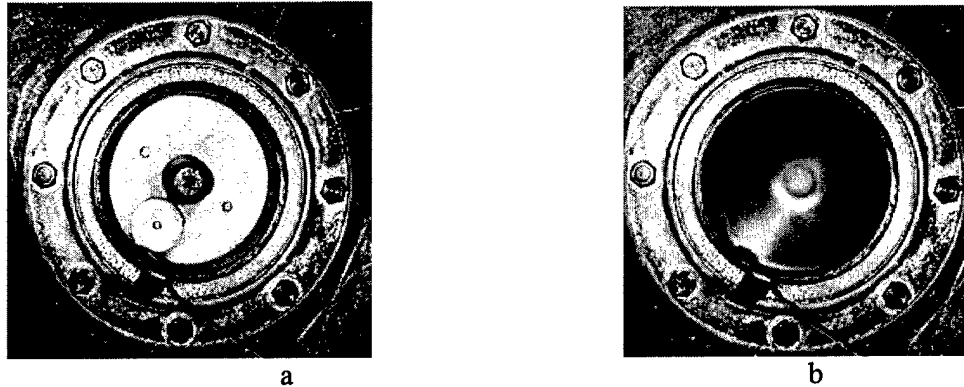


Figure III.9. Coaxial APPT. a- face view, b – photo of the discharge in the APPT.

III.3.1.1 Diagnostics

Electrical measurements include the discharge current, voltage and the magnetic field measurements. The discharge current was measured by the Rogowski coil connected to low inductance and low resistance shunt. The voltage across the capacitor bank and at other points was measured by capacitive voltage dividers. The high-speed photography of the discharge is produced with a high-speed photo camera. Maximal time resolution of the camera in streak mode is $2 \cdot 10^{-8}$ s.

Energy flux propagated to propellant surface was measured with the tool based on low dimensions (1 mm scale) thermistor. Sensor is located into hole of the propellant bar. It is glued to thin mica plate, serving as a support. A layout of involved elements is shown in Figure III.10. Energy flux through small hole in the propellant bar impacted with the sensor. So, sensor stored integral flux, which produced temperature increase and a change in the resistance. A comparison bridge circuit is used to measure resistance change due to temperature increase. Temperature increase occurs after near 1 s after shot. Heat transfer from the sensor to the outer space has typical time of 1 minute. Sensor is adjusted on azimuthal direction for maximal energy flux signal.



Figure III.10. Draft of the measuring tool located into Teflon insert (a) and propellant bar with Teflon insert (b).

Energy flux can be transferred from discharge to the propellant by particles and by radiation. To outline the energy flux content a number of filters were used. Data on filters are shown in

Table 1. Absorbance dependencies on radiation spectrum are shown in Figure III.11. Filters are placed on the surface of propellant bar closely to the hole.

Table 1. Used filters

Material	Thickness, μm
Teflon	4, 10, 20
Polyether	6
Nitrocellulose	0.1

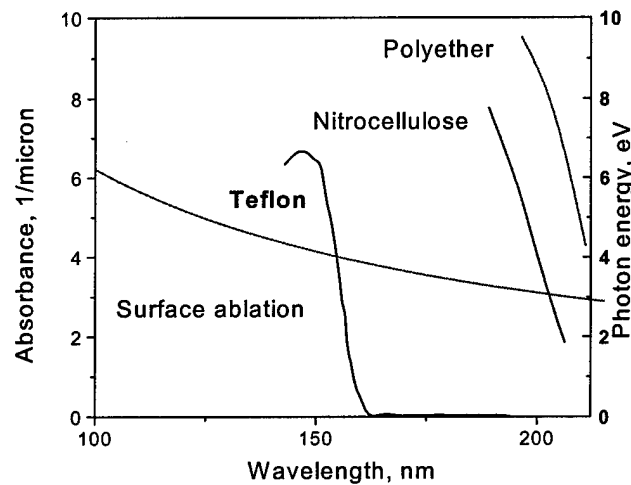


Figure III.11. Absorbance of used filters. Absorbance of Teflon and polyether is given from ^[10], absorbance of Nitrocellulose was accounted.

III.3.2 Results of Experiments

APPT discharge under consideration has not symmetric current distribution. (Figure III.9-b). Such a discharge is similar as in breach fed rail geometry thrusters. Results obtained for this discharge include current and voltage distributions, light intensity registration from fiber inserted near energy flux registration point. Teflon mass loss measurements were performed in full range of bank energies. Teflon mass loss per single pulse was obtained for not less than 300 pulses and each stored energy. Time dependency of the discharge parameters are shown in Figure III.12.

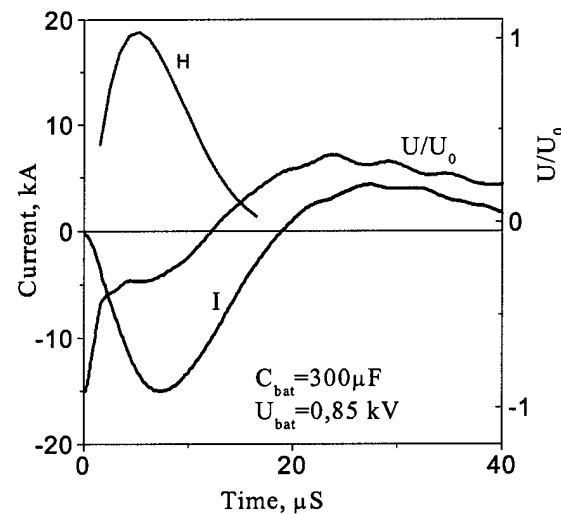


Figure III.12. Time dependencies of the discharge current I , voltage on the bank, U and radiation flux density, H (visible wave range, optical fiber signal, ab. units).

Calibration of energy flux measurements was produced by introducing to the sensor known quantity of heat. It is realized by means of electrical discharge through thin platinum foil glued on thermistor. Calibration signal was similar working one. Typical voltage – time dependency of the sensor for 180 J bank charge is shown in Figure III.13. Layout of sensors is given in Figure III.14.

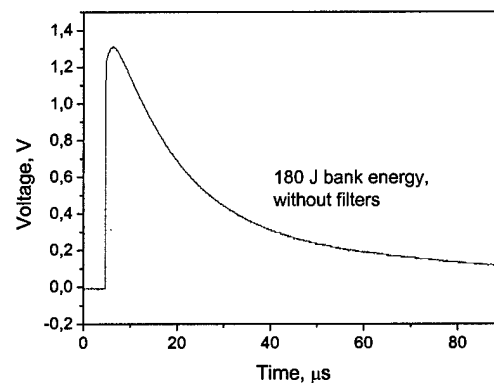


Figure III.13. Sensor voltage for 180 J discharge

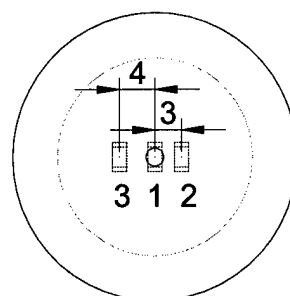


Figure III.14. Placement of sensors, face view

Radiation flux determined with polyether and nitrocellulose filter was not more than 1% of energy flux measured without filters. Installation of 6 μm , 10 μm , and 20 μm Teflon filters produced the signal at level 5% of total (particle + radiation). Teflon filters were not destroyed. Nitrocellulose filters were usually destroyed in the discharge after one shot.

Measured energy fluxes are shown in Figure III.15. Curve "1" show energy flux measurements from centered sensor position (Figure III.14, #1). In this case all particle and radiation flux should impact with sensor. Curves "2" and "3" obtained with radial displacement of the sensor. "2" - surface of the sensor located in 1 mm from side of hole. "3" - surface of the sensor located in 3 mm from side of hole. In position "3" sensor does not see area of plasma. So, as seen from Figure III.15, conductive energy transfer to the propellant exceed 10% of total transferred energy. There are no visible damages on the sensor surface during measurements.

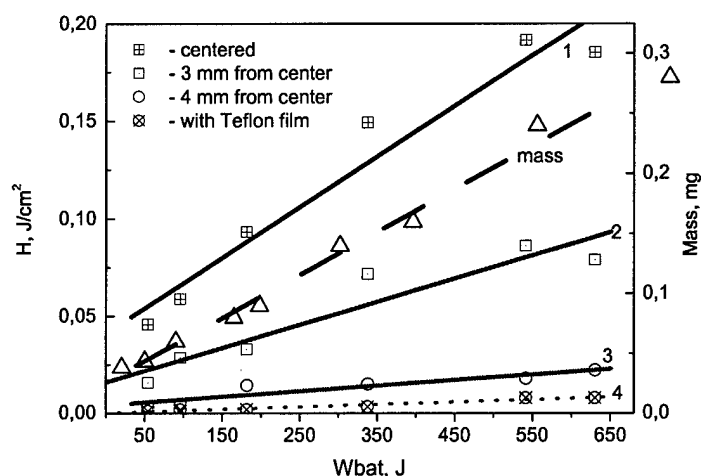


Figure III.15. Measured energy fluxes propagated onto propellant (1-4) and mass loss in dependence on the bank energy. 1- without filter (centered); 2- without filter, 2 mm displacement from hole, 3 - without filter, 3 mm displacement from hole; 4 - 6 μm Teflon film filter.

The electron density of plasma in the near propellant surface area was measured with Mach-Zehnder interferometer. The ruby laser - in a quasi-continuous generation mode with wavelength 0.69 μ - was used as an illuminator. The propellant plane was aligned in parallel

to the optical interferometer axis with the accuracy up to $3'$. The interference pattern shift was registered with a streak camera. Streak photo interferogram of near propellant area are given in Figure III.16. The time resolution was $5 \cdot 10^{-8}$ s. Electron density depended on the input voltage and measured at the level of 10^{16} cm^{-3} for 0.5 kV (inter-electrode gap voltage) with some deviation due to shot-to-shot changes in thruster firing.

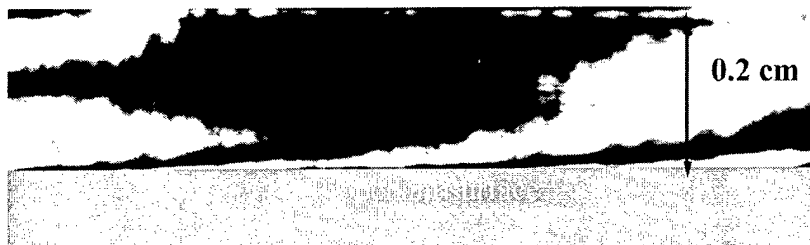


Figure III.16. Streak photo interferogram of near propellant area. Time of streak is $1.5 \mu\text{s}$. Estimated electron density is 10^{16} cm^{-3} . Voltage on electrodes is near 0.5 kV (4 cm inter-electrode gap).

It is seen from Figure III.16, that there are oscillations in electron density at a distance – near (0.2 – 0.3) mm from propellant surface. Estimated period of these oscillations (instabilities) is 70 ns.

Dependence of mass loss distribution in the inlet of the accelerating channel is necessary for semi-phenomenological modeling. Model needs the azimuthally symmetric conditions. To initiate azimuthally symmetric discharge a small quantity of Aluminum (significantly smaller than propellant loss) was evaporated and deposited onto propellant surface. Accordingly vacuum switch was used in the electric circuit. The discharge became azimuthally symmetric. An example of radial distribution of a mass loss in APPT obtained from balance measurements is shown in Figure III.17.

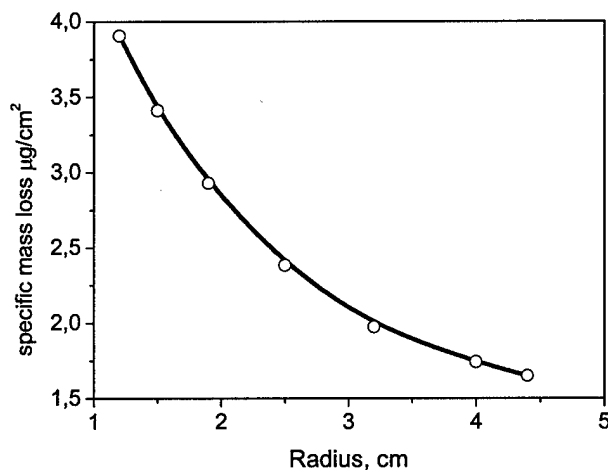


Figure III.17. Dependence of mass loss distribution in APPT in azimuthally-symmetric discharge. Bank energy is 180 J.

III.3.2.1 Measurements of Energy Dissipated in a Thermal Skin-Layer.

To measure energy dissipated in a thermal skin-layer the discharge was produced in the surface of thin Teflon film, which was closely pushed to the sensor as shown in Figure III.18.

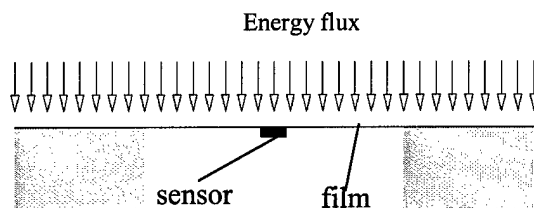


Figure III.18. Method of thermal energy measurement in the skin-layer

Measured energy bit dissipated in Teflon propellant per one discharge is shown in Figure III.19.

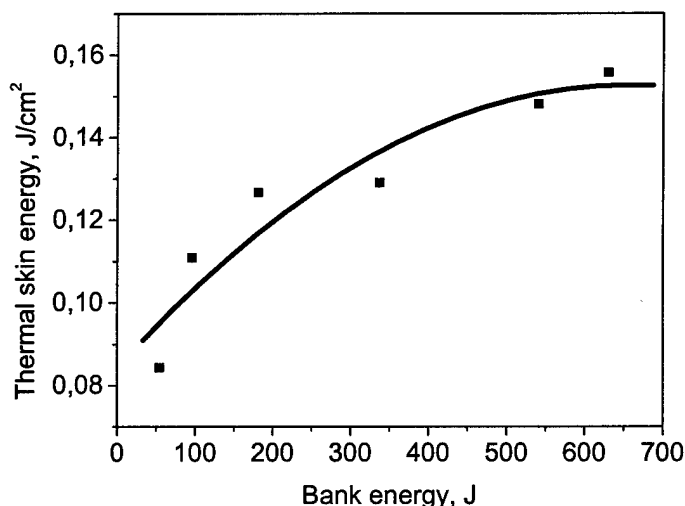


Figure III.19. Thermal energy bit dissipated in Teflon propellant at the discharge.

III.3.2.2 Measurements of Radiative Part in the Energy Flux .

Measurements of radiative flux with the use of available filters are limited of wavelength near 160 nm. It is shown above that radiative part of energy flux with wavelength more than 160 nm does not exceed 0.05 of total measured energy flux. Shorter radiation can be studied using mirrors. Tantalum mirrors adjusted to sensor were used to detect radiative part of energy flux. Reflectivity of Tantalum in near 100 nm for normal slope is near 20%. Adjustment and de-adjustment of reflecting mirror was produced for transparent source illumination located near propellant surface. With adjusted mirror sensor should detect optical signal. With de-adjusted mirror optical signal did not fall onto sensor (Figure III.20, a, b)

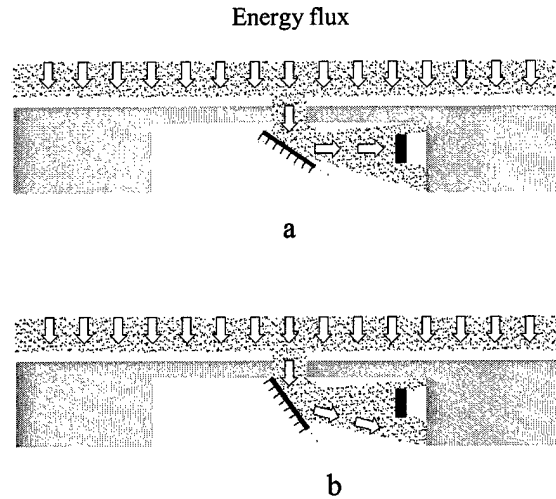


Figure III.20. Determining of energy flux structure; a- mirror adjusted to sensor for measuring of radiation, b-mirror does not register radiation (not adjusted).

Taking into account some uncertainties due to shot-to-shot variations in thruster firing, sensor did not detect appreciable energy flux transferred by radiation (Figure III.21). So, noticeable addition associated with radiative energy flux has not detected.

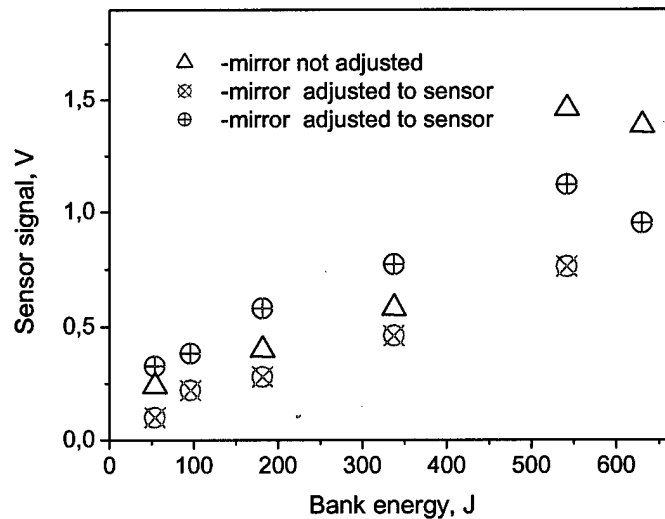


Figure III.21. Determining of energy flux structure, results of measuring. Signals of sensor for adjusted and de-adjusted mirrors.

III.3.3 Discussion of Results

In the APPT, the considerable energy fraction released on the propellant bar surface may be transferred by particles and ultraviolet radiation in the wavelength range 100 nm. The absorption depth of this radiation in polymers does not exceed 10^{-5} cm^[10], meanwhile the thickness of an propellant material heating due to the heat conduction is about 10^{-4} cm. Schematic of the energy transfer in APPT is shown in Figure III.22. At present, the relative role of conductive and radiation mechanisms for energy transfer to the propellant is not exactly determined. Now conductive mechanism is more expanded and developed^[9]. Probably the main mechanism of energy transfer to propellant depends on propellant and thruster operation mode.

In considered experiment we measure energy flux through a low dimensions hole in propellant bar. Most probably this hole destroys boundary layer near the propellant surface, because its thickness exceeds significantly the thickness of boundary layer. In this case we possibly measure energy flux falls on boundary layer. For this reason experiments with use of Teflon filters are more reliable.

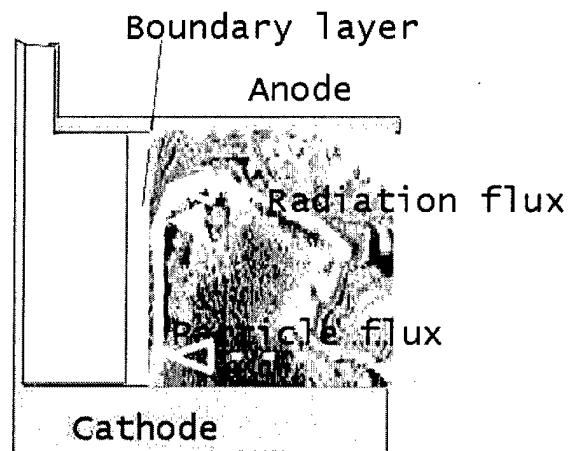


Figure III.22. Schematic of the energy transfer in APPT

The approximation of energy flux transferred onto the propellant is shown in Figure III.23. This flux could be used as a boundary condition for accounting. Accounts of Teflon degradation based on thermal degradation kinetics (Annex 1) have been done. The results of accounts are shown in the Table 2: H_{\max} - maximal power of energy flux, q - total energy flux per cm^2 , M_{abl} - ablated mass, Q_{skin} - energy of thermal skin layer, Q_{abl} - Teflon destruction energy and T_s - maximal temperature of the propellant surface.

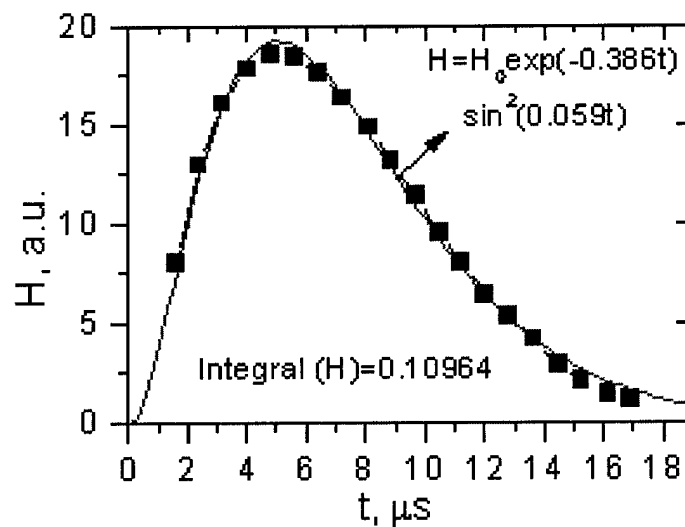


Figure III.23. Time dependence of energy flux onto propellant.

Table 2. Results of accountings

H_{\max} , kW/cm^2	$q = \int H dt$ J/cm^2	M_{abl} , $\mu\text{g/cm}^2$	Q_{skin} , J/cm^2	Q_{abl} , J/cm^2	T_s , $^{\circ}\text{K}$
12.2	0.11	0	0.126	0	705
24.3	0.218	0.75	0.224	$3 \cdot 10^{-3}$	1090
48.6	0.435	39	0.260	0.168	1170
73.2	0.653	83.3	0.262	0.375	1190
97.6	0.871	130	0.258	0.603	1210
122	1.09	184	0.252	0.862	1230

The results of accounting show that Teflon begins to destruct from surface temperature $> 1100^{\circ}\text{K}$. Further, temperature increases insignificantly with energy flux increasing. When the power of energy flux increases 8 times, the temperature increases on 100° . For $T_s = 1200^{\circ}\text{K}$ and for energy flux, equal shown in Figure III.23, thermal skin-layer contain 0.260 J. High mass loss case is demonstrated in Figure III.24, where H , M_{ABL} , T_s and ε are shown for $H_{\text{MAX}} = 73 \text{ kW/cm}^2$. Temperature distribution and Teflon destruction rate for $H_{\text{MAX}} = 73 \text{ kW/cm}^2$ ($t = 4 \mu\text{s}$) are shown in Figure III.25.

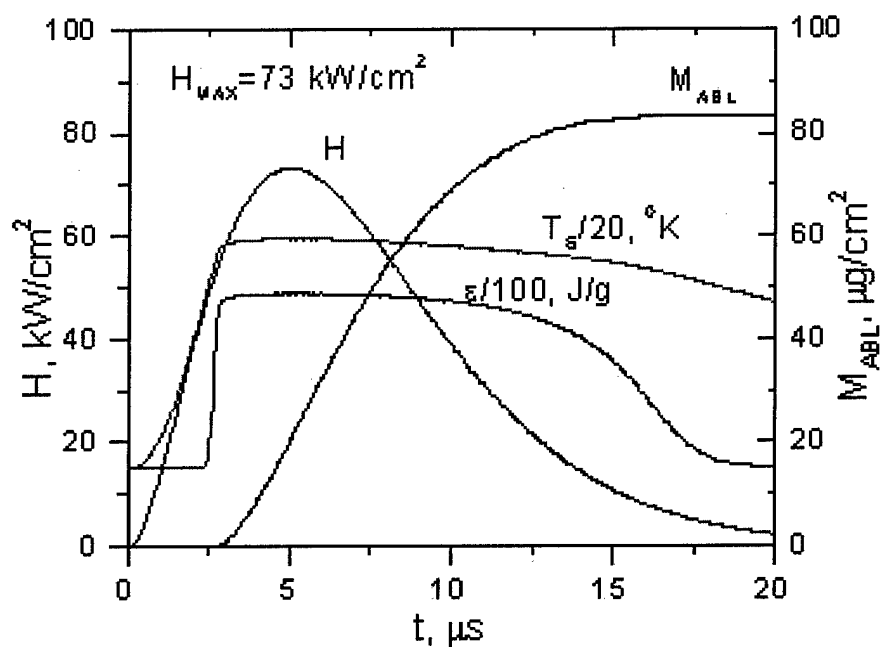


Figure III.24 Time dependencies of H , M_{ABL} , T_s and ϵ for $H_{MAX}=73$ kW/cm².

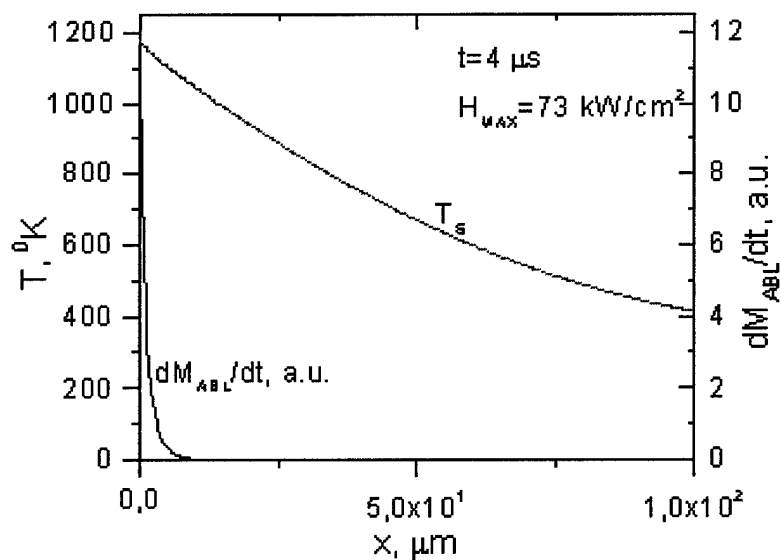


Figure III.25. Temperature distribution and Teflon destruction rate for $H_{MAX}=73$ kW/cm² ($t=4$ μs).

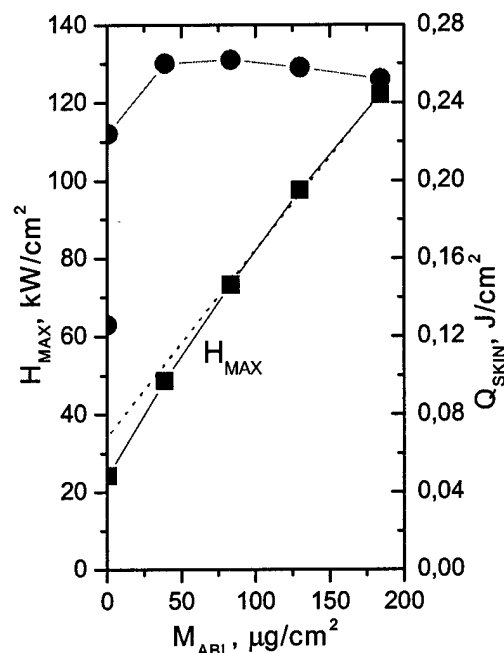


Figure III.26. Dependencies of H_{MAX} и Q_{SKIN} of ablated propellant mass.

Maximal value of energy flux power to the propellant H_{MAX} , necessary to evaporate mass M_{ABL} . In dependence of M_{ABL} is shown in Figure III.26 together with thermal energy in skin-layer. It follows from the last figure that Teflon degradation for measured energy fluxes falling onto the propellant can take place if temporal or spatial inhomogeneities in energy flux occur. In this case measured energy is average value and can be significantly lower than local values of energy flux.

Such model can explain the mass loss in a frame of thermal degradation kinetics if maximum energy flux to the propellant exceeds $25 \text{ kW}/\text{cm}^2$ (Integral flux more than $0.2 \text{ J}/\text{cm}^2$). So, in a frame of used thermal degradation model of Teflon, for measured energies shown in Figure III.15 and Figure III.19 degradation of Teflon is doubtful. However inhomogeneities in energy flux distribution can explain observed mass loss for relatively low energy fluxes. Figure III.16, where oscillations in electron density at a distance – near (0.2 – 0.3) mm from propellant surface are shown could confirm inhomogeneities in energy flux distribution.

III.4 Study of plasma parameters and discharge optimization

III.4.1 Study of the charged plasma component concentration in discharge channel

The electron density is the fundamental parameter of APPT plasma. The distinctive features of APPT physical processes, current distribution, acceleration mode of plasma blob and thrust performances such as impulse bit, plasma velocity (specific thrust), thrust efficiency etc are in many respects dependent on the value and the distribution of electron density as well as ion density.

A method of plasma laser interferometry was used for measuring the electron density inside the discharge channel of next generation APPT and in the plasma blob outside the discharge channel. The advantage of this method lies in the fact that plasma under study is not disturbed and that this method allows spatial and temporal distributions of electron density be measured in non-equilibrium plasma with acceptable accuracy.

Test data on the measured electron density in the discharge channel zone between the Teflon bars were obtained while fulfilling this work for the first time. Plasma flow is formed in this zone as a result of initial breakdown of the discharge gap, propellant ablation and ionization, and a current sheet is formed also that is later accelerated by electromagnetic forces. Thus, studies for the electron density distribution in the zone between the bars are very important for the understanding of operating processes in APPT.

III.4.2 Measurement procedure

Laboratory model of next generation APPT with the stored energy of about 100 J was used in the tests on measuring the electron density distribution and its variation in time. Main elements of the discharge channel unit of that model are shown in Figure III.27. Discharge channel comprises electrodes 1 and 2, two propellant (Teflon) bars 3 and the end insulator 4. A side location of Teflon bars was used in the APPT model. The anode is installed in the base 5 and cathode – in the cover 8. The APPT electrodes are manufactured of copper. The end insulator is made of alundum plates, which have been pasted together. They are mounted in yoke 6 made of glass-cloth laminate. The Teflon bars 3 are installed in yoke 6 closely to the end insulator 4. Distance between electrodes of 70 mm in length was 38 mm, while the longitudinal size of Teflon bars was 30 mm.

The APPT discharge initiation is carried out by three-electrode igniter 7 installed in cover 8. The igniter is powered from the discharge initiation unit. Capacitor bank consisted of four low-inductive capacitors.

APPT model was tested in the vacuum tank at the residual gas pressure of about 10^{-4} torr. The known procedures and measuring equipment described in ^[11] were used for measuring the APPT main parameters (current pulse, energy, thrust, specific thrust impulse, mean propellant flow rate per pulse, thrust efficiency, etc.).

Electron density N_e in the APPT plasma was measured by laser interferometer with photoelectric signal registration ^[12]. In preparation for experiments the interferometer was updated with the aim to improve the spatial and temporal resolution and to increase the measurement accuracy. The laser power of updated interferometer was 10 times greater in comparison with the laser used before ^[3]. The noise-immunity for electrical circuit was

improved and the damping system was refined for reducing the mechanical vibrations. The updated laser interferometer provides for measuring the electron density in the range from $3 \cdot 10^{14}$ to 10^{16} cm^{-3} with the spatial resolution of $\sim 2 \text{ mm}$ and temporal resolution of $\sim 1 \mu\text{s}$.

The optical scheme of interferometric measurements is presented in Figure III.28. The updated interferometer used during the experiments was one of the versions of classical three-mirror laser interferometer,^[13] Active resonator of the interferometer is the 15 mW single-mode helium-neon laser 1. Passive resonator, in which the investigated APPT plasma is placed, is formed by an output mirror of the laser and external spherical mirror 5. The mirror 5 of this resonator with the focal distance of 1 m has the reflection coefficient of 95 % for the wavelength $\lambda = 6328 \text{ \AA}$.

To generate periodic oscillations of optical length in the passive resonator, the external mirror is fixed to the piezoelectric ceramic cylinder providing periodic shift for the mirror with a frequency of 50 Hz when the modulating voltage of $\approx 10 \text{ V}$ is applied. The movable diaphragm 6 is used while choosing an interference order, which is necessary for measurements. The input and output of laser radiation through the vacuum chamber is carried out by using quartz windows of 5 cm in diameter.

The registration of optical signal is carried out by photomultiplier 8 and digital memory oscilloscope. The highest spectral sensitivity of photomultiplier corresponds to the wavelength of $\sim 600 \text{ nm}$ that is rather close to the laser wave length ($\lambda = 632.8 \text{ nm}$).

During the experiments the optical scheme was adjusted so that the amplitude of signal measured by the photomultiplier did not exceed 500 mV, that corresponded to linearity boundary of this device. The number of laser ray passes in the passive resonator is evaluated by the value of 10...12.

The photomultiplier was powered by a high-voltage stabilized power supply. The nominal value of voltage was equal to 1050 V. A resolution of the photomultiplier was estimated by the value of $\sim 1 \mu\text{s}$. This may be apparently considered as satisfactory because, on the one hand, this value essentially exceeds relaxation time of physical processes in resonators of the interferometer and, on the other hand, it is much less than the duration of discharge process in APPT ($\sim 15...20 \mu\text{s}$).

The noise-immunity of the electrical circuit was ensured by grounding the experimental instrumentation. Besides, all high-voltage and a part of low-voltage circuits were passed through ferrite rings, that allowed the reduction of noise down to an acceptable level.

Some precautionary measures against light interferences in the receiving part of photomultiplier accompanying the APPT operation were taken also. At the exit of the vacuum chamber the light screen with a hole of 10 mm for a ray passing, neutral light filters and movable diaphragm of 0.7 mm in diameter were installed. Besides, a photomultiplier was located at distance of $\sim 1 \text{ m}$ from APPT model, and it was also housed in a package, which was opaque to light and had an inlet opening of $\sim 2 \text{ mm}$ for laser radiation passing. All measurements were conducted at exterior black-out.

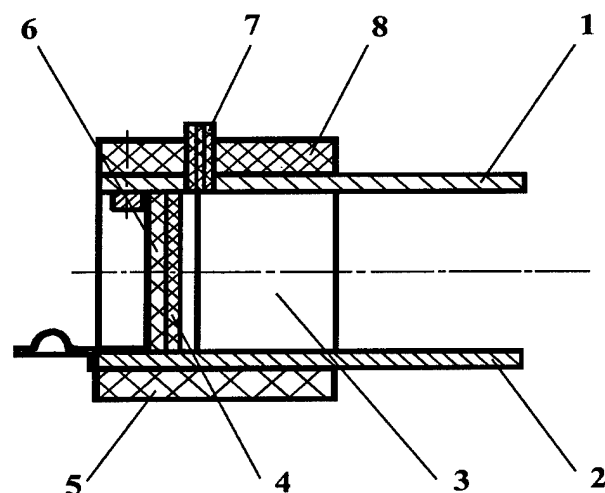


Figure III.27. Discharge channel unit schematic

1 – cathode, 2 – anode, 3 – teflon bars, 4 – back insulator,
5 – basis, 6 – yoke, 7 – igniter, 8 – cover.

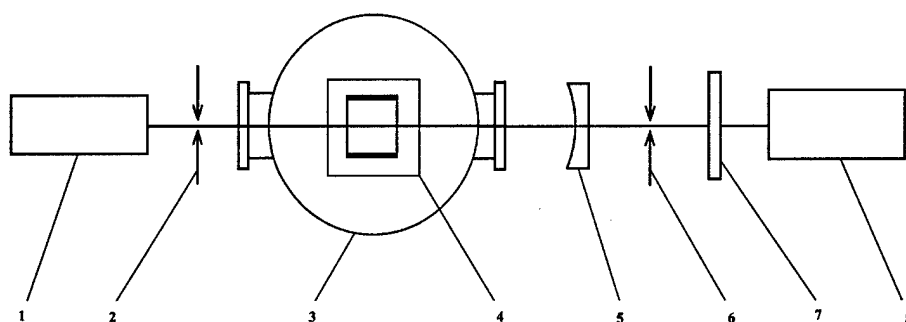


Figure III.28. Optical scheme for interferometric measurements.

1 – He-Ne laser, 2 – diaphragm, 3 – vacuum chamber, 4 – APPT model, 5 – mirror, 6 – diaphragm, 7 – filter, 8 – photomultiplier.

To reduce a level of optical system vibrations, all devices of the laser interferometer (helium-neon laser, mirrors, diaphragms, filters, photomultiplier) are located on a metal plate with the mass of more than 100 kg suspended by four rubber braids from the metal frame. This frame surrounding the vacuum chamber is mounted rigidly to a metal construction of 200 kg in mass placed on the floor of experimental stand by using the multi-layer damping spacers made of

elastic materials. After each cycle of measurements the plate with laser interferometer was arrested by a special device, that allowed the off-loading of rubber suspending braids. In general, the whole construction has ensured the reduction in level of optical system vibrations by the factor of 15...20.

Thus, during experiments protection was provided for the electric circuit of interferometer and measuring equipment against different noises. The amplitude of noises in the measuring circuit (mechanical, electromagnetic, thermal) comprised less than 10% of the main signal amplitude.

The synchronization of measurements was carried out by multi-channel pulse generator making it possible to adjust measurement process in time with an accuracy of 0.1 μ s. All incoming data was recorded by two digital memory oscilloscopes. The current pulse of APPT model and the interferogram of APPT operating process were recorded by one oscilloscope and the instrumental function of the interferometer was fixed by the other oscilloscope at time of APPT model switching. Experimentally, from 6 to 10 measurements of electron density N_e were carried out in each given spatial point and then measurement results were averaged.

Electron density measurement in plasma by application of laser interferometer is based on the registration of changing the phase of laser radiation passing through plasma under study [4]. This change of the phase $\Delta\phi$ is proportional to electron density N_e and plasma size d in the direction of laser ray

$$\Delta\phi = \frac{e^2}{mc^2} \lambda N_e d = \text{const} \cdot N_e d, \quad (1)$$

where λ is the wave length laser radiation, e and m are, correspondingly, charge and mass of electron, c is the light velocity. Thus, the information on the electron density value averaged in the direction of laser ray may be obtained by measuring the phase difference $\Delta\phi$ if the plasma size d is known.

A method of laser interferometry may be used effectively for plasma diagnostics when the following requirements are met [14, 15]:

1. Laser radiation should not be absorbed in plasma.
2. Radiation entering plasma should keep its initial direction, and laser ray deflection at the electron density gradients should be negligibly low.
3. Modulation of radiation intensity as it leaves plasma should be mainly substantiated by the interference effect, and the effect of the polarization plane rotation for the laser radiation (Faraday effect) upon its intensity at a presence of magnetic fields in plasma should not be considerable.

It was revealed as a result of analytical assessments and experimental check for the Ne gradient presence in plasma by a shade method that for the plasma with parameters equal to the APPT under study [11] the above requirements are met. Besides, assessment by formulae presented in [14] showed that under the conditions of these tests the plasma refraction is defined by electrons, and the contribution of atoms may be neglected. Thus, application of laser interferometry for measuring the electron density was quite correct in that work.

At the presence of APPT plasma in the passive resonator its optical length varies and according to this the fundamental frequency of radiation leaving the resonator varies. This frequency shift $\Delta\nu$ is defined by the formula [16]

$$\Delta\nu = (\Delta n \cdot d) \frac{c}{\lambda L_r}, \quad (2)$$

where $\Delta n \cdot d$ is the change in optical length caused by plasma,

Δn is the change of refraction index in the resonator,

d is the size of plasma along the laser ray direction,

L_r is the resonator length,

λ is the wave length of laser radiation.

As the three-mirror interferometer operates as an amplitude-frequency discriminator with linear performance, the frequency shift caused by plasma will cause proportional change in laser power ΔE at the exit of the interferometer

$$\Delta E = E_{\max} \frac{\Delta \nu}{\delta}, \quad (3)$$

where E_{\max} is the maximum laser power,

δ is the interval of frequency variation.

The electron density in plasma is determined on the basis of interferometer signals recorded at the presence of plasma in the passive resonator. Periodic displacement of external mirror in the passive resonator provides the registration of interferometer instrumental function used as a calibration signal. The typical instrumental function obtained during one of the experiments is presented in Figure III.29.

Measurement of the photomultiplier signal amplitude, which is proportional to ΔE , and measurement of instrumental function parameters (amplitude G_{\max} , front duration t_{in} and period T_{in}) makes possible to define Q value as a product of electron density N_e by the plasma size d in the direction of laser ray ($Q = N_e \cdot d$) characterizing the radiation phase change at the plasma appearance in resonator. Equation for Q obtained on the basis of known relations for the plasma refraction factor and laser power change ^[13] has the following form:

$$Q(x, y, t) = N_e \cdot d = 1.8 \cdot 10^{17} \frac{\Delta E(x, y, t)}{E_{\max}} \cdot \frac{\Delta t_{in}}{T_{in}} \approx 1.8 \cdot 10^{17} \frac{\Delta F(x, y, t)}{G_{\max}} \cdot \frac{\Delta t_{in}}{T_{in}}, \text{ cm}^{-3}, \quad (4)$$

where: E_{\max} – maximum power of the laser;

ΔF – the value of signal under study received by photomultiplier;

G_{\max} – signal amplitude for the instrumental function;

Δt_{in} – duration of the instrumental function front (Figure III.29);

T_{in} – instrumental function period (Figure III.29);

x – longitudinal coordinate for the point under study in the direction of APPT axis;

y – transversal coordinate for the point under study in the direction between the electrodes;

t – time.

Electron density N_e was measured in the discharge channel in the zone between the Teflon bars and in the interelectrode gap after the bar cut, as well as outside the discharge channel after the electrode cut.

A diagram for the location of lines along which plasma was examined by the laser ray while measuring N_e is shown in Figure III.30. The ray of helium-neon laser crosses the APPT plasma under study in parallel to the electrode plane, i.e. along the line being parallel to z axis. Points shown in Figure III.30 are the points in which lines of plasma examination intersect the plane being perpendicular to the electrodes and including the geometric axis of APPT channel. N_e was measured on the discharge channel axis (line I – I), near the cathode (line II – II), and near the anode (line III – III), as well as on the line IV – IV being perpendicular to the direction of plasma blob motion outside the APPT at a distance of 5 cm from the electrode cut.

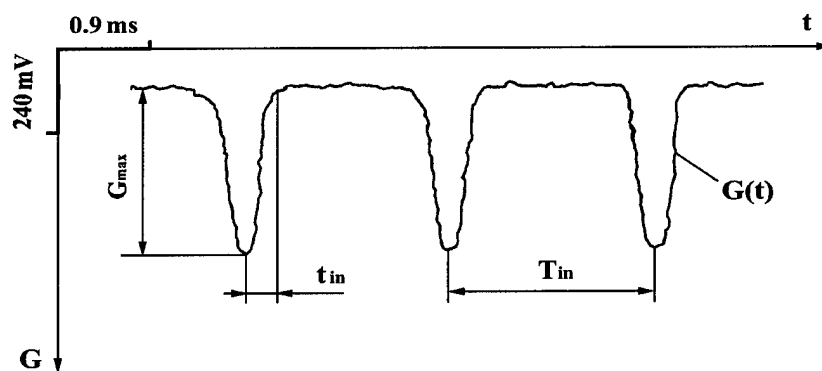


Figure III.29. Interferometer instrumental function diagram

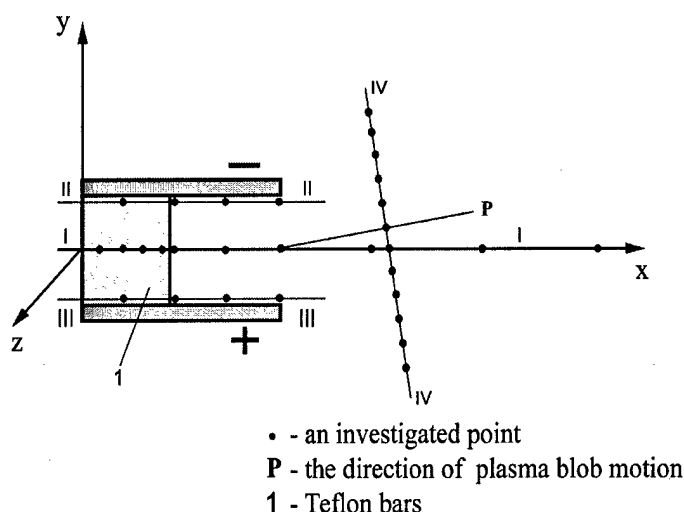


Figure III.30. Arrangement of points for interferometric measurements in APPT

One hole of about 4 mm in diameter was made in each Teflon bar in accordance with the location of line of plasma examination for the laser ray to pass through them. These holes were consequently closed by Teflon caps after measurements were finished in each of the examination directions. According to the data of comparative tests, a presence of one pair of holes in the propellant bars does not influence practically the APPT characteristics (integral parameters of the model varied by $\sim 1 \dots 2\%$).

With the known plasma blob extension d along z axis, an electron density averaged along the laser ray direction may be defined by (4) for the studied points of APPT.

Within the volume between Teflon bars, the blob size d along z axis is a fixed value defined by the discharge channel width. For the other points under study (Figure III.30), d was defined similarly to the procedure presented in ^[11], i.e. by measuring the blob boundaries using the traces left by plasma blob on the dielectric screen during the APPT model operation in the frequency mode. This screen was mounted perpendicularly to the direction of blob

motion at different distances from the electrode cut. The variation of plasma blob extension $d(x,0)$ along x axis in the plane being parallel to electrodes and including the channel axis while plasma blob moves after the electrode cut is presented in Figure III.31.

In addition to the above method and for the verification of test results with screens, plasma size d was also determined by interferometric measurements. The plasma extension d was assessed by the interferometer signal decay and thus by the reduction of $Q(z)$ parameter when plasma was examined in the direction parallel to the plane of electrodes (y axis).

During that test, the APPT model was turned by 90° relative to the longitudinal axis x for the laser ray to be directed in parallel to y axis (Figure III.30). Distribution of the parameter $Q = N_e \cdot d$ characterizing the variation of phase for the laser radiation was defined by interferometer along z axis. Measurements were made with 5 mm step in the cross-section of discharge channel located in the middle of the electrode part after the Teflon bar cut, and in the cross-section of the channel at the electrode cut. The obtained $Q(z)$ distributions allow the extension of plasma blob $d(z)$ be assessed by defining the blob boundaries on the basis of Q value drop down to the given level with the growth of distance from the APPT channel axis.

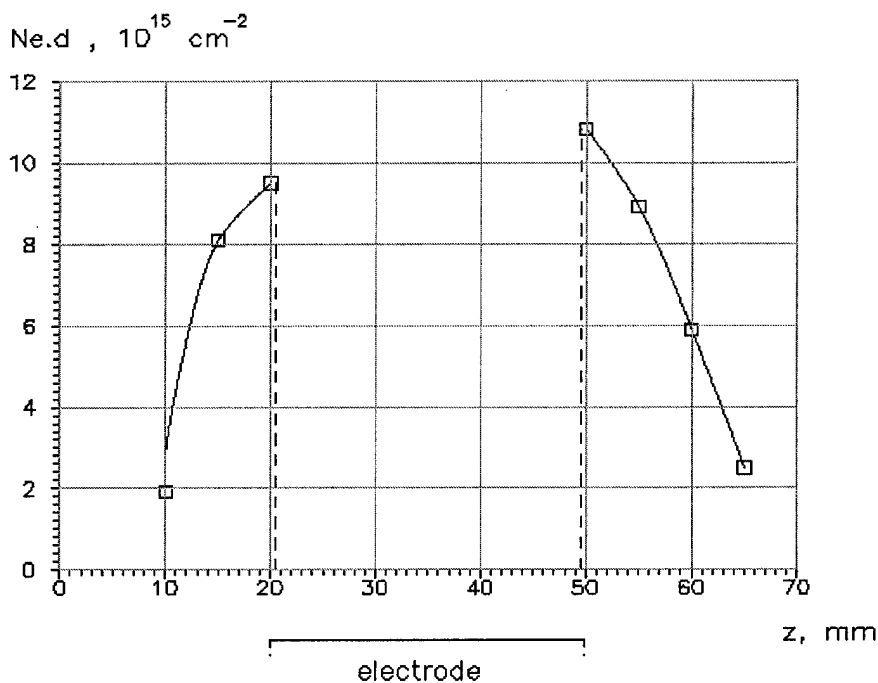


Figure III.32 illustrates the variation of value $Q = N_e \cdot d$ in the areas adjacent to the electrodes, in the channel cross-section located in the middle of the electrode part after the Teflon bar cut. Points, in which Q value dropped five times comparing to the maximum value, were considered as the boundaries of plasma blob along the examination line while the test data was processed. Blob size d determined by measuring the distributions $Q(z)$ differed from d size determined as a result of tests with screens by no more than 20%. Such agreement of test results is quite satisfactory.

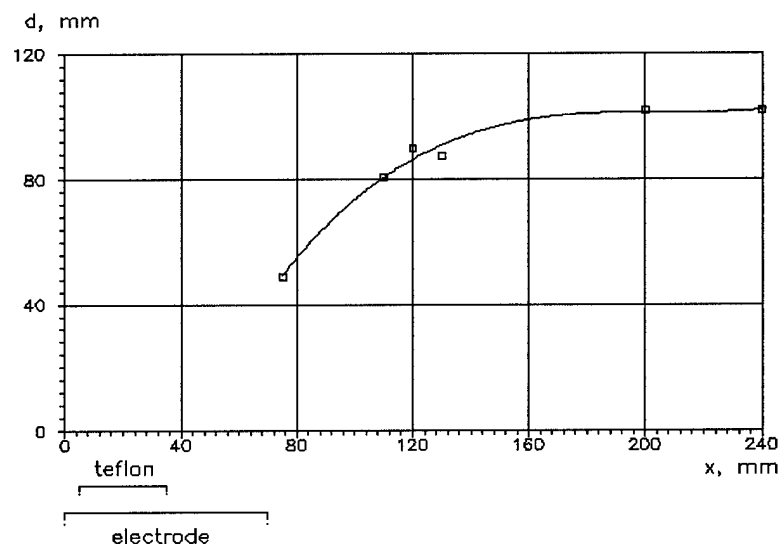
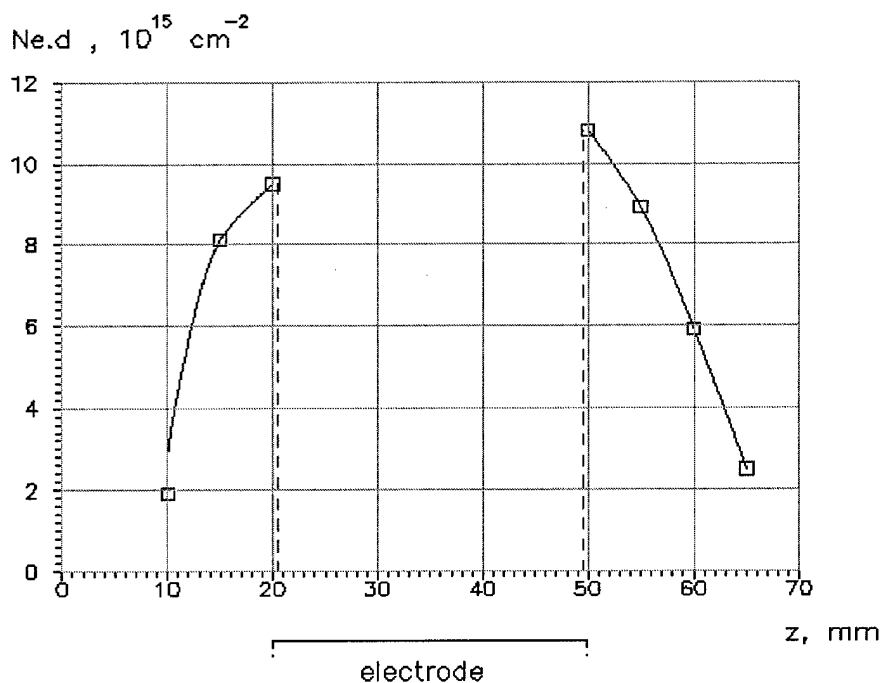


Figure III.31. Variation of plasma blob size along the APPT axis

Figure III.32 Variation of $Q=N_e d$ parameter in areas adjacent to electrodes

III.4.3 Test results and their discussion

Integral characteristics of next generation APPT model were studied within the stored energy range of 70...100 J at the first stage of tests. Main parameters of this model, averaged

over the results of five measurements, are presented in Table 3. Parameters of the APPT model under study are substantially better than parameters of the typical APPT's. For comparison it should be pointed out that in typical APPT at energy $W = 100$ J the thrust efficiency η_t amounted to 0.12, impulse bit $P_{bit} = 2.2$ mN·s and specific impulse $I_{sp} = 11$ km/s [2].

Table 3 Characteristics of the next generation APPT model

Discharge energy, J	70	100
Thrust impulse bit, mN·s	1.82	2.7
Teflon consumption per pulse, mg	0.12	0.15
Thrust efficiency	0.20	0.24
Specific impulse, km/s	15.4	18

The discharge current oscillogram for the APPT model under study at the energy of 100 J is presented in Figure III.33. It is seen that the discharge in the channel of next generation APPT is close to aperiodic. Current amplitude was 27.9 kA during the first half-period of the discharge and 5.4 kA during the second half-period (at the opposite current direction). The duration of the discharge first half-period was 8.9 μ s that was close to the duration of the process of plasma blob formation. This provided optimum conditions for the electromagnetic acceleration of plasma ^[1]. Electron density N_e in the discharge channel between the Teflon bars was measured for the first time while studying the parameters of next generation APPT by the method of laser interferometry. N_e measurements in the points located in the interelectrode gap after the bar cut and outside the discharge channel (Figure III.30), which had been presented earlier in ^[1], were made again in order to obtain data on the N_e variation along the entire length of discharge channel during one run of measurements. It follows from the analysis of data of interferometric measurements obtained inside the discharge channel that the duration of interferometric signal corresponds to the duration of half-period for the discharge current. This may probably witness of the fact that ablation processes inside the channel proceed during the time interval of 7-8 μ s from the discharge start mainly. Interferometric measurements of the electron density N_e showed that the current sheet being formed inside the discharge channel has a longitudinal size (along x axis) of 5-7 cm, and that there is a plasma area in the central part of the current sheet, in which the electron density is as high as the maximum value.

Time-dependent distributions of maximum electron density $N_e(x, 0, t)$ along the next generation APPT axis while plasma moves in the zone between Teflon bars, in the interelectrode gap after the bar cut and outside the discharge channel is shown in Figure III.34. Time moments since the discharge start, which correspond to the appearance of plasma layer with maximum values of electron density in the APPT points under study, are presented near the measured values of N_e also.

The trend of N_e variation during the plasma motion through the space between bars corresponds to the variation of discharge current $J(t)$ for the next generation APPT, in which the duration of the discharge first half-period ($\tau_1 = 8.9$ μ s) exceeds substantially the duration of the first half-period for the typical APPT's with the oscillatory discharge ($\tau_1 \sim 3$ μ s). For the APPT under study maximum current value J_{max} is achieved at $t=3.4$ μ s, when plasma blob is in the channel zone between the Teflon bars and maximum values for N_e are reached in the same zone also. After that, when plasma comes close to the exit plane of bars ($t \geq 4$ μ s), the discharge current drops and electron density decreases.

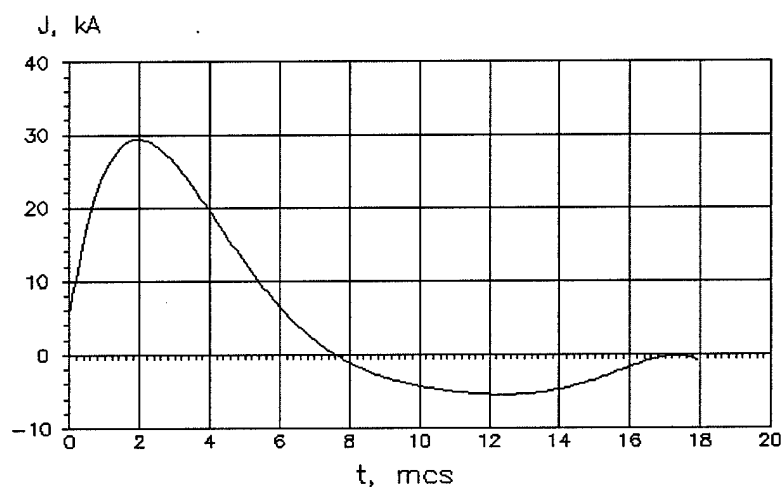


Figure III.33 Time dependence of discharge current for APPT model

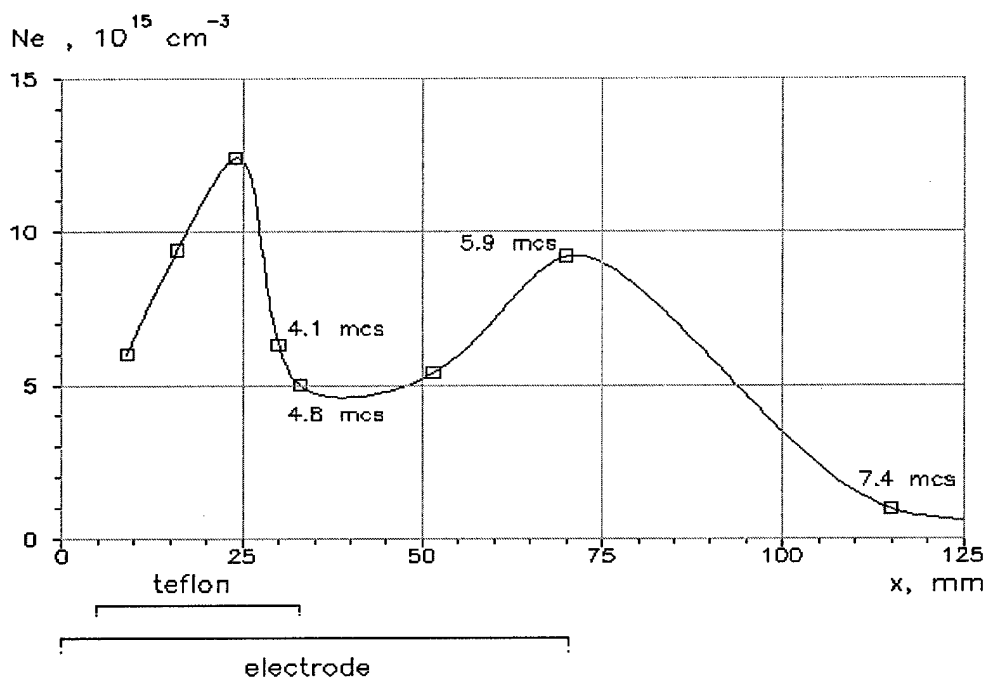


Figure III.34. Time-dependent distribution of maximum electron density along channel axis of the next generation APPT

With subsequent plasma motion through the interelectrode gap after the bar exit plane, electron density grows during the essential part of the first half-period ($t > 4.8 \mu\text{s}$). This is evidently connected with the discharge distribution along the whole electrode length and formation of outflowing ("carry-out") currents at the discharge channel outlet. As a result, current density j and, correspondingly, electron density N_e grow near the electrode cut; this agrees with the data of j measuring by magnetic probes presented in ^[17, 11]. Electron density

outside the channel after the electrode cut drops (Figure III.34), and this is explained by the blob expansion after it has left APPT.

Comparison for the electron density time-dependent distributions in APPT of next generation and typical APPT is illustrated by Figure III.35. It is seen that in the APPT of next generation and typical APPT the distributions of N_e differ from each other. In the APPT of next generation when plasma is moving from the cut of Teflon bars to the cut of electrodes the electron density is increasing. This is connected with discharge expanding at the end of the first half-period and with increasing of current density close to cut of electrodes.

In the case of typical APPT with oscillatory discharge and low level of performance, the current is localized near the bar cut during nearly the entire first half-period of discharge and is not carried out into the interelectrode gap within the discharge channel part from the bar cut to the electrode cut. At this part of the typical APPT discharge channel, electron density and current density drop during the plasma blob motion towards the APPT outlet.

Thus, test data on N_e measuring witness of the current redistribution in the channel of next generation APPT. With this, considerable part of current is not localized in the area of bar cut, but is carried out into the interelectrode gap after the bar cut providing rather efficient acceleration of propellant by electromagnetic forces. Such discharge dynamics exactly and such distribution of electron density and current density promotes the APPT efficiency growth.

Experiments showed that current sheet propagates inside the channel at an average velocity of about 6-8 km/s. Taking into account that the velocity registered at the electrode cut is over 20 km/s [11], it is evidently possible to consider the process of plasma blob acceleration as rather efficient.

According to the data obtained by interferometric method in the area after the Teflon bar cut, average velocity of plasma layer with maximum value of N_e near the anode (~ 30 km/s) is higher substantially than that near the cathode (~ 20 km/s). Thus, inclination of lines connecting the points with maximum values of N_e near the anode and cathode is observed in the discharge channel, and, correspondingly, the inclination of electric current j lines relative to the electrodes. This distinction in the distribution of N_e and j is evidently connected with the Hall effect exhibition.

Figure III.36 shows the N_e variation along the channel length during the plasma movement near the cathode (curve 1) and near the anode (curve 2). Distributions of $N_e(x, t)$ are not monotonous: in the middle part of the zone between Teflon bars and at the electrode cut the electron density is higher near the anode than near the cathode, and at the discharge channel part ranging from the bar cut to the electrode cut the values of electron density in the near-cathode region exceed the N_e values near the anode.

The indicated differences in the N_e distributions in the near-cathode and near-anode areas are evidently connected with influence of competing transversal forces – electromagnetic and gasdynamic – upon plasma in the discharge channel. Transversal electromagnetic force appears as a result of Hall effect and interaction of longitudinal Hall current and transversal magnetic field formed by the APPT operating current.

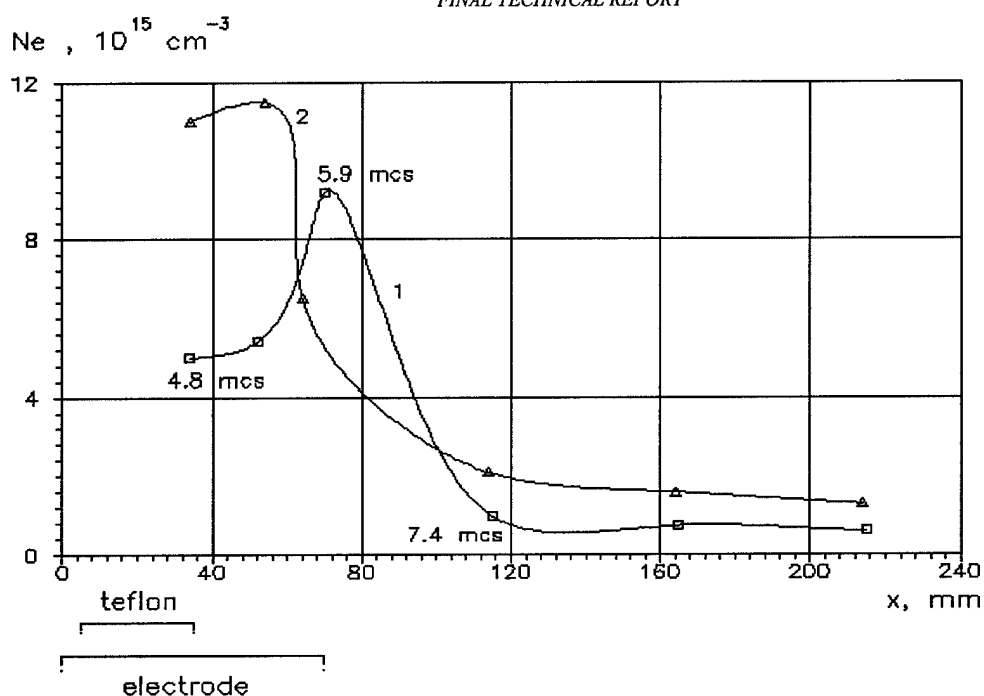


Figure III.35. Comparison for electron density time-dependent distribution along channel axis in the next generation APPT and the typical APPT1 – the next generation APPT; 2 – the typical APPT

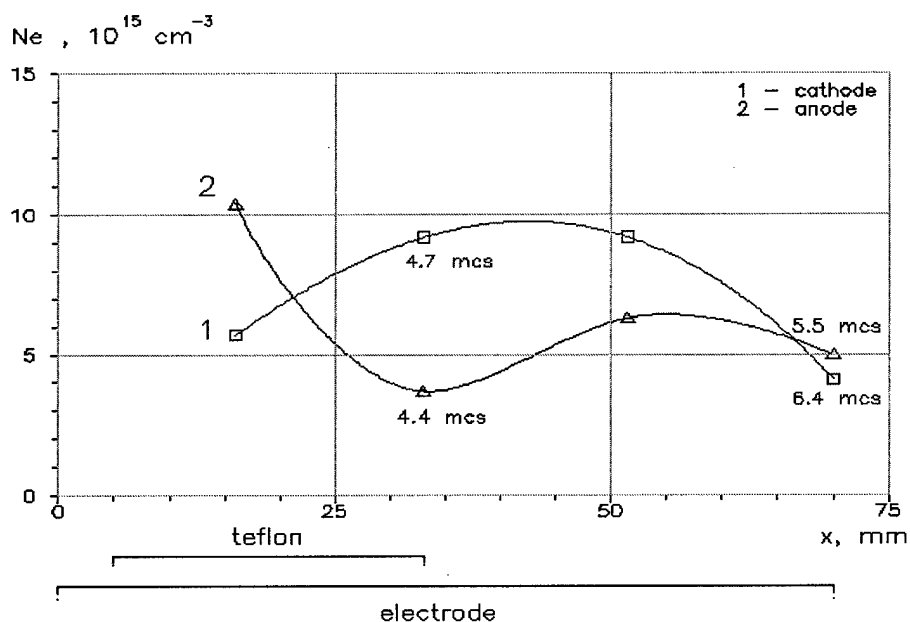


Figure III.36. Time-dependent distributions of maximum electron density

Transversal electromagnetic force presses plasma flow to the cathode and is counterbalanced by the transversal gradient of pressure. As a result, gasdynamic pressure grows near the cathode, and plasma blob may be forced out from the cathode and deflected to anode during

its motion under the influence of gasdynamic force. Thus, dynamics of transversal force influence upon plasma in the discharge channel is evidently exhibited by the periodic deflection of flow to cathode and anode. It should be noted that the difference in N_e values in the next generation APPT channel close to cathode and anode near-cathode and near-anode areas in the zone between bars is observed in the case of time intervals of about $1 \mu s$ from the discharge start, and Hall effect starts to influence substantially the dynamics of discharge evolution at the very early stages of this process already.

Plasma blob deflection at the APPT outlet from the channel axis to the cathode to the angle of $\sim 6^\circ$ under the influence of transversal electromagnetic force is connected with the Hall effect exhibition also. Such blob deflection was discovered while measuring the flow boundaries using screens [11] and recorded while fulfilling this work also.

Figure III.37 shows the N_e distribution transverse the plasma blob at a distance of 5 cm from the APPT electrode cut (lines IV-IV, Figure III.30). N_e distribution is non-symmetric relative to the direction of plasma blob motion (under the angle of $\sim 6^\circ$ to the APPT axis), while in the blob part being close to the cathode the N_e values are higher than near the anode.

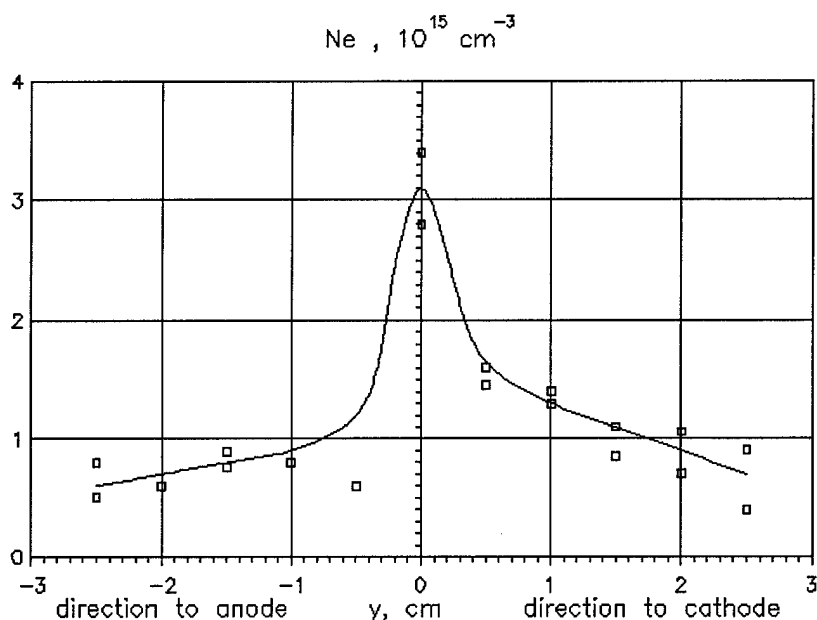


Figure III.37. Distribution of maximum electron density across plasma blob at the distance of 5 cm from APPT electrodes

III.4.4 Piezoprobe Measurements of Impact Pressure in APPT Plasma Flow

The main purpose of the piezoprobe measurements is to determine the "spread" of mass according to velocity and angle influencing the operation efficiency of APPT as a thruster and effecting the fields with variable effectiveness of plasma acceleration.

The laboratory model of the next generation thruster has been investigated. Teflon used as a propellant. The energy stored in the capacitor bank was $W = 100 \text{ J}$, the thrust impulse $P_{\text{int}} = 2.3 \text{ mN}\cdot\text{s}$, the pulse mass flow rate $m_{\text{pulse}} = 0.12 \text{ mg/pulse}$, the thrust efficiency $\eta_t = 0.22$ and the specific impulse $I_{\text{sp}} = 19 \text{ km/s}$. The photo of thruster is presented in Figure III.38. The scheme of thruster discharge channel is presented in Figure III.39.

Piezoprobe of impact pressure (piezoprobe) is a thin plate of piezoceramics glued between two rods made of quartz glass. The length of the rods (100 mm) has been chosen on the basis of the fact that the propagation time of forward and reflected acoustic waves in quartz was considerably more in comparison with the characteristic time of the plasma flow being for the given thruster type $t \sim 20 \mu\text{s}$. Such a ratio makes possible to avoid the noise effect on a recorded signal the source of which is a thruster itself and its systems. Besides, a piezoprobe was placed into a copper tube to provide an additional noise shielding; and a coaxial cable connecting a probe with a pressure-seal feed-through of a vacuum chamber was arranged into a flexible screen, a kind of a copper braiding. The diameter of a piezoprobe end part is 4 mm to sense plasma impact pressure. The piezoprobe's time resolution is $0.1 \mu\text{s}$, the space resolution is 5 mm and the sensitivity is $3 \cdot 10^5 \text{ Pa/V}$. The scheme of piezoprobe is presented in Figure III.40

During the experiment the probe was moving with the use of a remote controlled coordinating device. A digital two-beam storage oscilloscope was used to record the discharge current curve and a signal from a piezoprobe. One of the oscillograms is presented in

Figure III.41.

The signal recorded by a piezoprobe, in case of supersonic plasma flow, is proportional to the total gas-dynamic pressure $(p + \rho V^2/2)$, where p - static pressure; ρ and V - flow density and velocity respectively.

The total signal integral in any plane, perpendicular to a flow longitudinal axis X , $P = \iint (p + \rho V^2/2) dydz$ is proportional to the flow impulse in this plane at the given moment.

The integral $\int P dt$ according to the whole period of the discharge time is proportional to the total thrust impulse P_{int} created by the thruster.

The measurements were performed in three cross-sections, corresponding to the Teflon bars cut section (1), electrodes' cut section (2) and distance 14 cm from the electrodes' cut section (3). The positions of these cross-sections are presented in Figure III.42. The piezoprobe was moving along the axis Y and Z with a spacing of 1 cm.

The result of measurements in three cross-sections are presented in three-dimension diagrams in Figure III.43- Figure III.64. It is seen that in all cross-sections the maximum flow impulse is shifted to the thruster anode.

The piezoprobe's signal integration was obtained in two cross-sections' plane corresponding to the electrode's cut ($X=0$) and the distance 14 cm from the electrode's cut ($X=14 \text{ cm}$). The relevant curves $P(0)$ and $P(14 \text{ cm})$ are given in Figure III.65. There, for the time fixing there is a discharge current J oscillogram. It is obvious that the curve $P(0)$ is of a two-humped character. The second maximum of the curve corresponding to a flow accelerated within the second discharge current half period is significantly lower by 3-4 times than the first maximum which appropriates to the first half period. In the curve $P(14 \text{ cm})$ there is no second maximum. It can be explained by an essential larger flow divergence according to the angle in the second half period, that is seen in high-speed discharge photograms. The curve $P(14 \text{ cm})$ is also much smoother than the curve $P(0)$, that is explained by the flow inhomogeneity according to the particles' velocities.

It is possible to determine the maximal V_{max} , minimal V_{min} and middle V_{mid} particles' velocities:

$$V_{\text{max}} = 14 \text{ cm} / 2 \mu\text{s} = 7 \cdot 10^4 \text{ m/s};$$

$$V_{\text{min}} = 14 \text{ cm} / 8 \mu\text{s} = 1.75 \cdot 10^4 \text{ m/s};$$

$$V_{\text{mid}} = 14 \text{ cm} / 4 \mu\text{s} = 3,5 \cdot 10^4 \text{ m/s.}$$

The average angle of flow divergence (only in the first half period) can be estimated by the relation of integral impulses $\int P dt$ in cross-sections ($X=0$) and ($X=14 \text{ cm}$). The appropriate evaluations give angle $2\varphi \sim 28^\circ$.

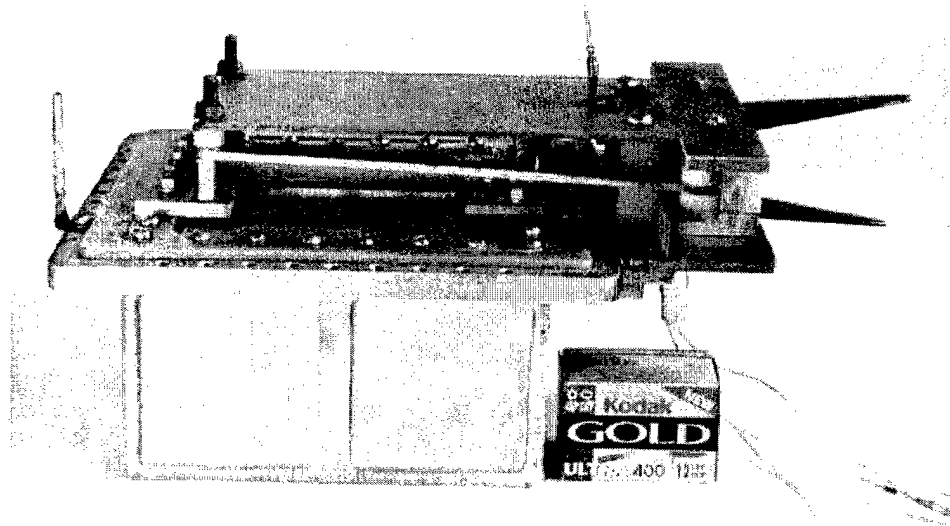


Figure III.38. APPT laboratory thruster

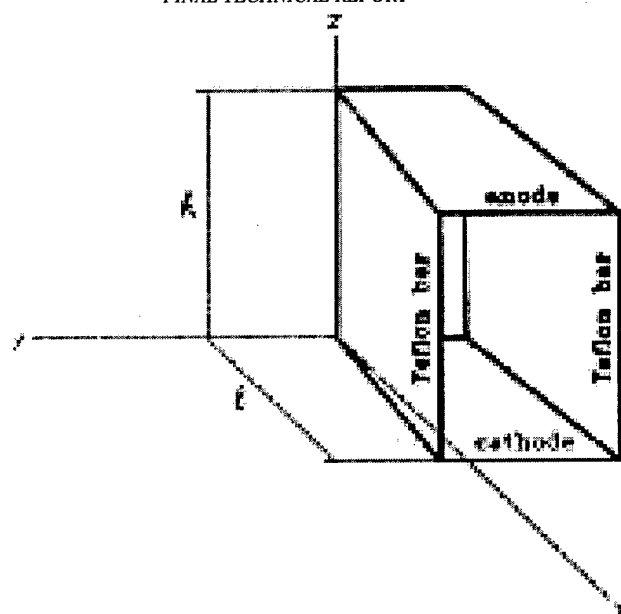


Figure III.39. APPT discharge channel

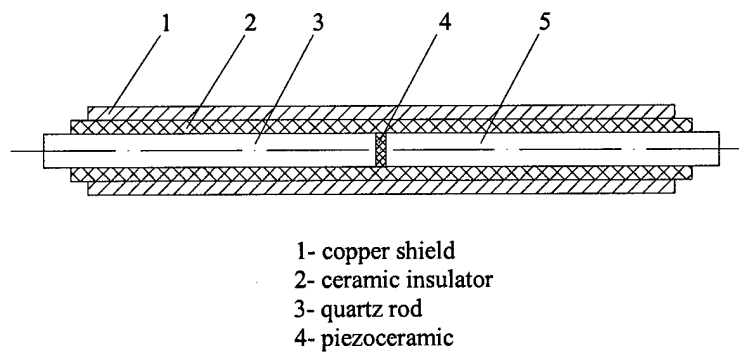


Figure III.40. Piezoprobe

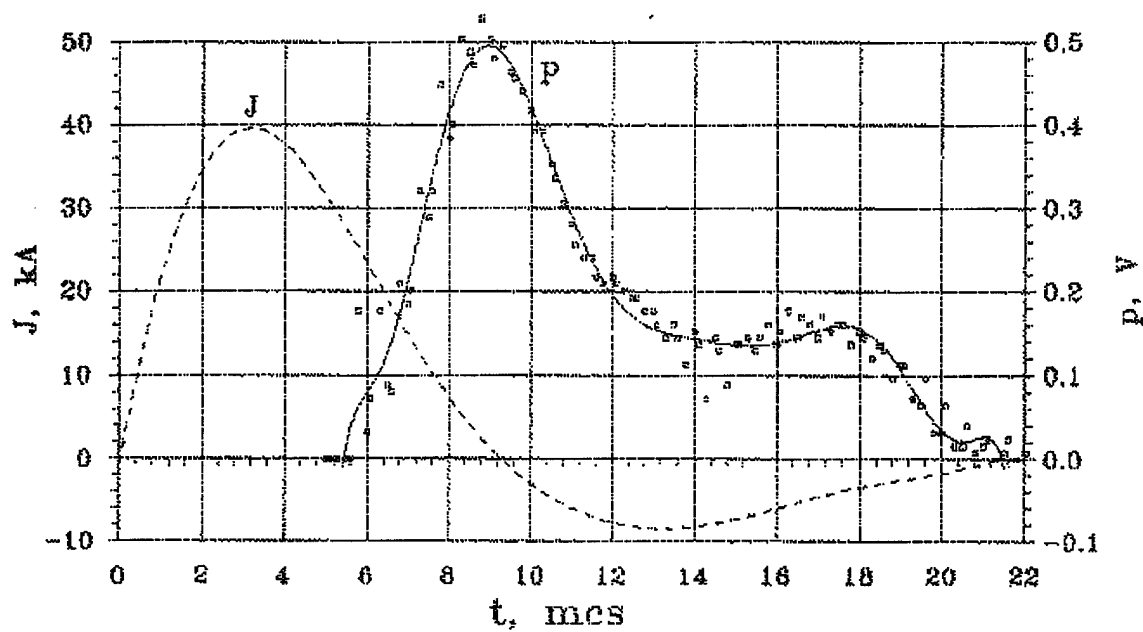


Figure III.41. APPT discharge current J and piezoprobe's signal P curves

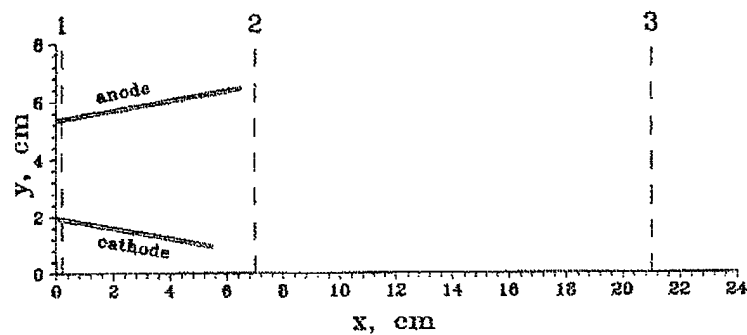


Figure III.42. Piezoprobe measurement's cross-sections

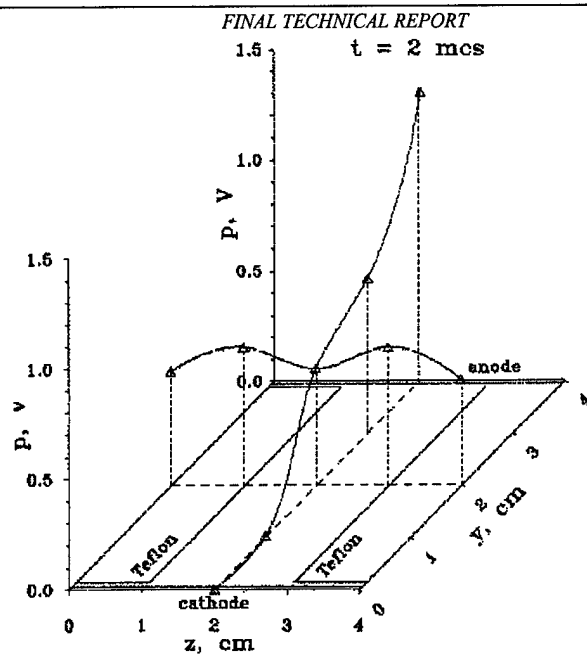


Figure III.43. Distribution of impact pressure in Teflon bars cut section (cross-section 1)

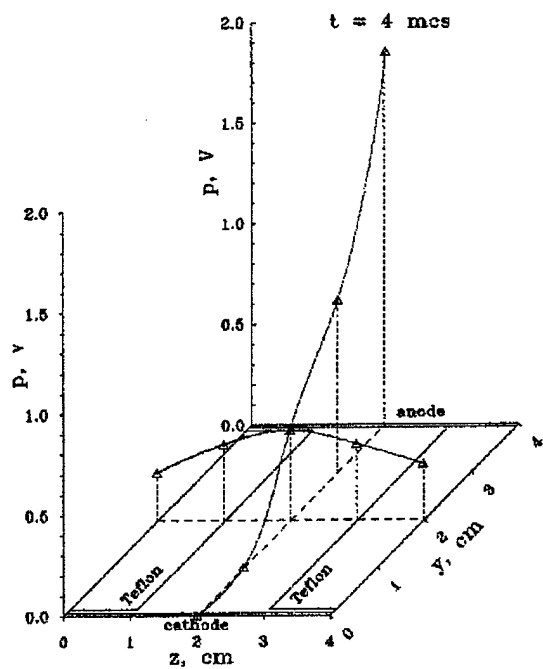


Figure III.44. Distribution of impact pressure in Teflon bars cut section (cross-section 1)

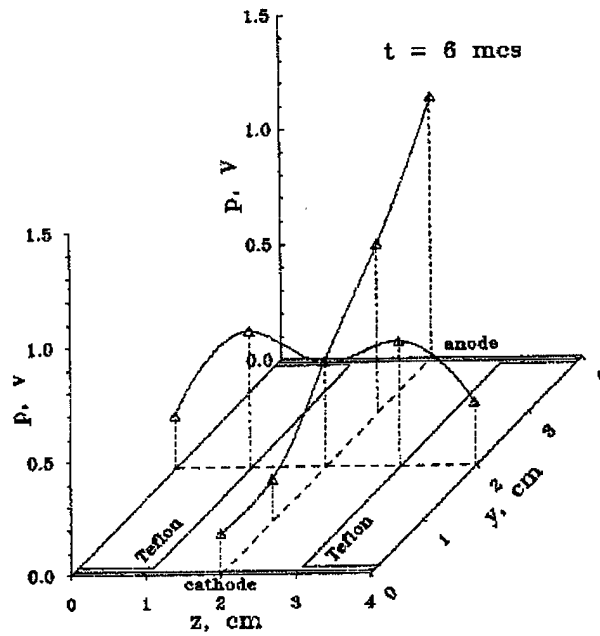


Figure III.45. Distribution of impact pressure in Teflon cut section (cross-section 1)

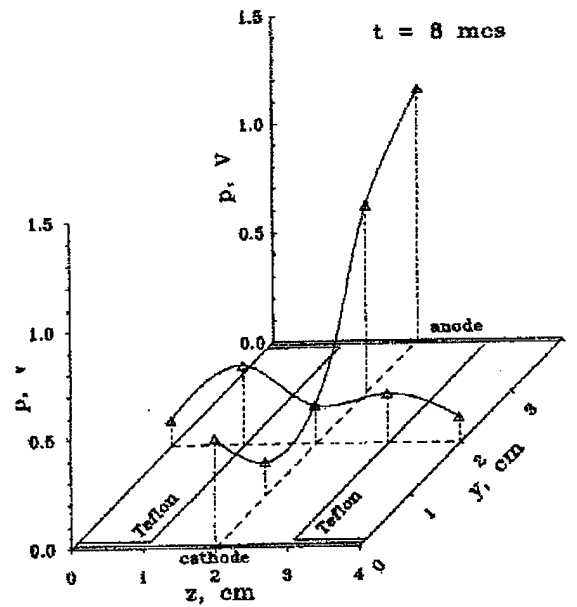


Figure III.46. distribution of impact pressure in Teflon bars cut section (cross-section 1)

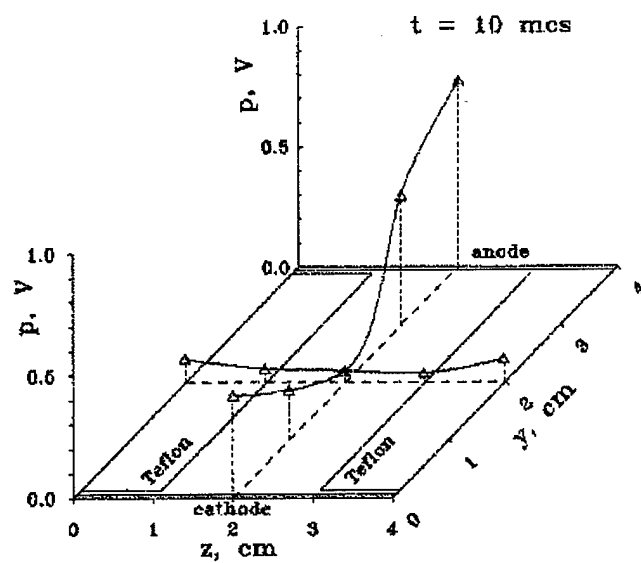


Figure III.47. Distribution of impact pressure in Teflon cut section (cross-section 1)

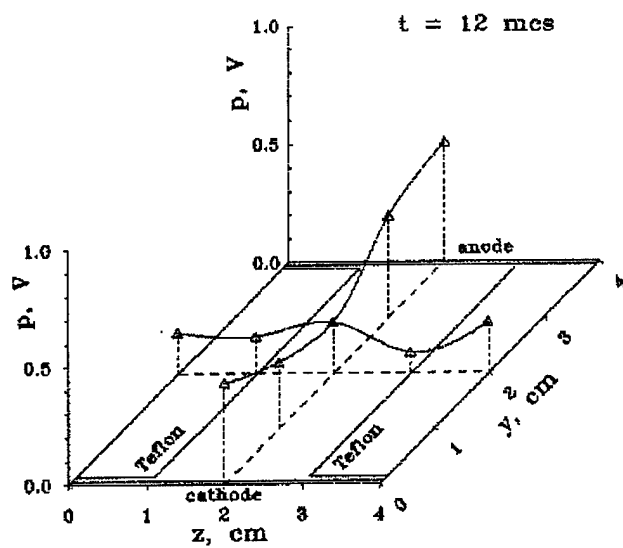


Figure III.48. Distribution of impact pressure in Teflon cut section (cross-section 1)

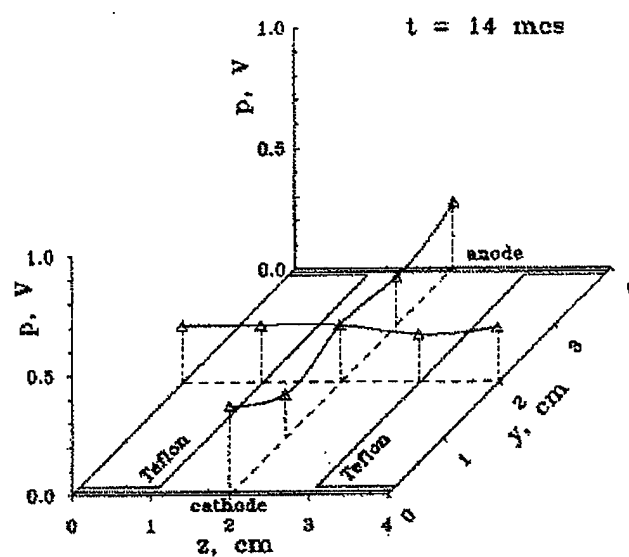


Figure III.49. Distribution of impact pressure in Teflon cut section (cross-section 1)

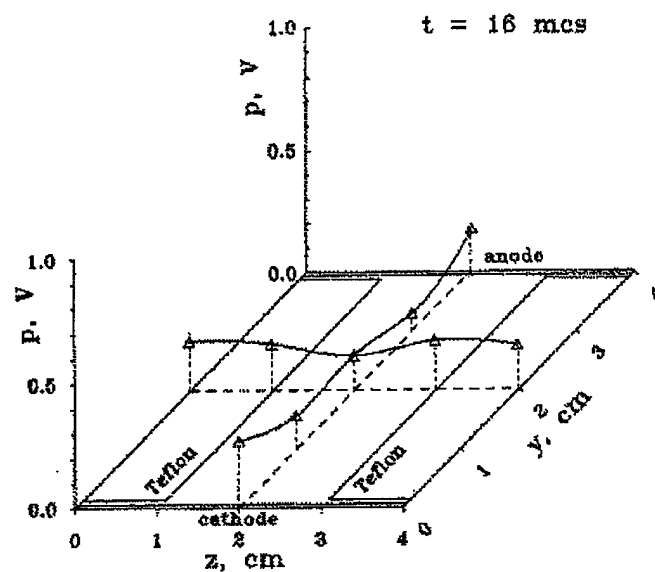


Figure III.50. Distribution of impact pressure in Teflon cut section (cross-section 1)

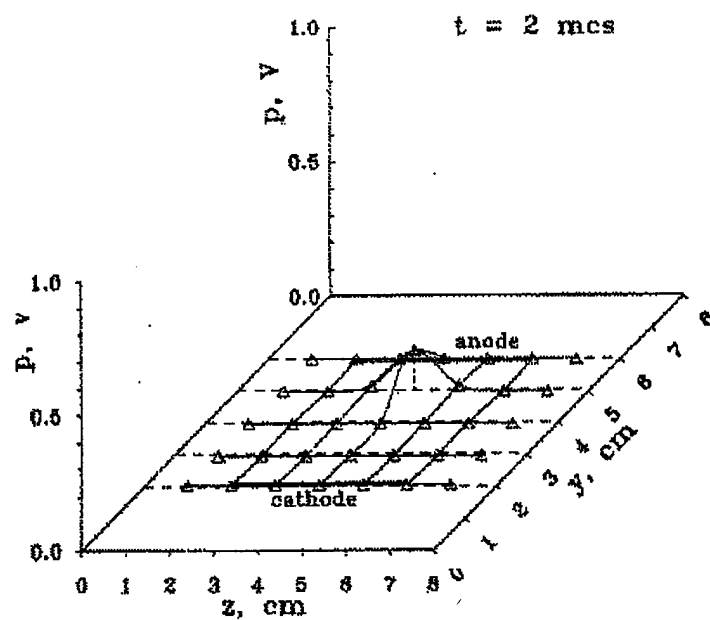


Figure III.51. Distribution of impact pressure in electrodes' cut section (cross-section 2)

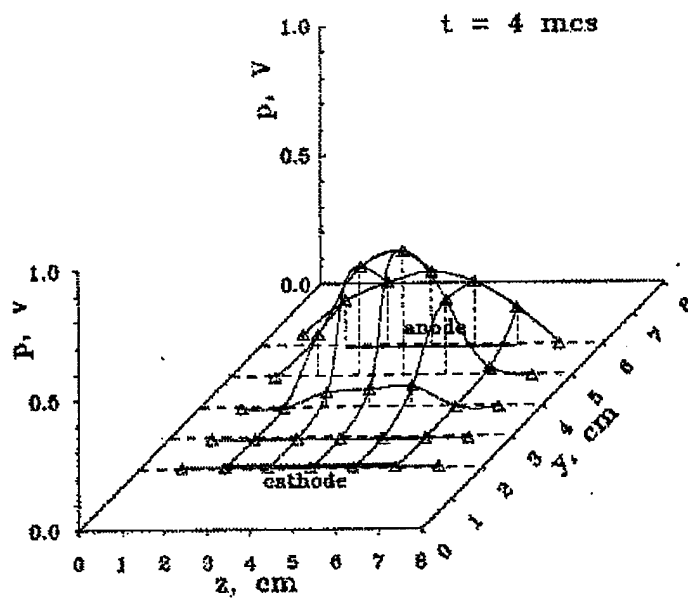


Figure III.52. Distribution of impact pressure in electrodes' cut section (cross-section 2)

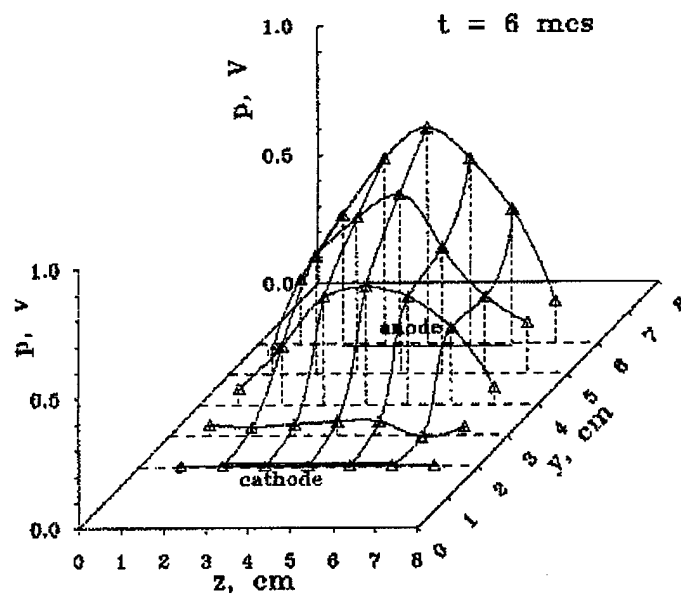


Figure III.53. Distribution of impact pressure in electrodes' cut section (cross-section 2)

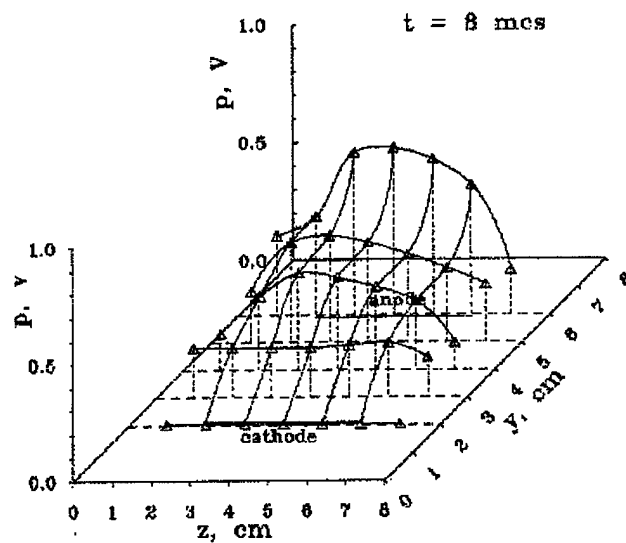


Figure III.54. Distribution of impact pressure in electrodes' cut section (cross-section 2)

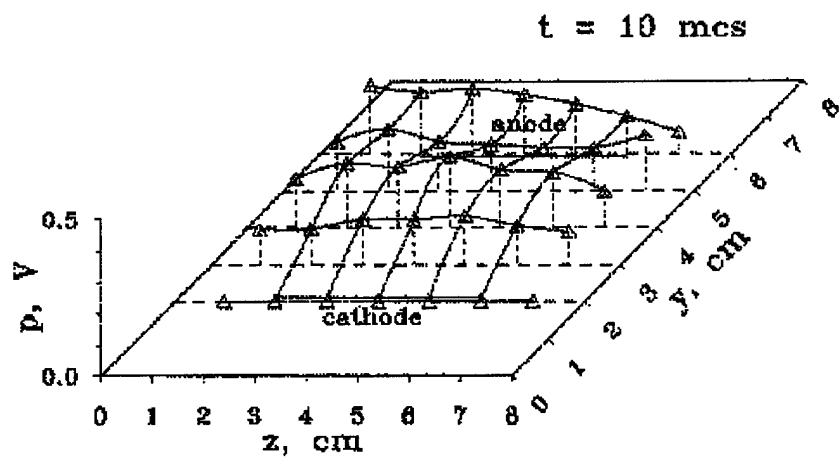


Figure III.55. Distribution of impact pressure in electrodes' cut section (cross-section 2)

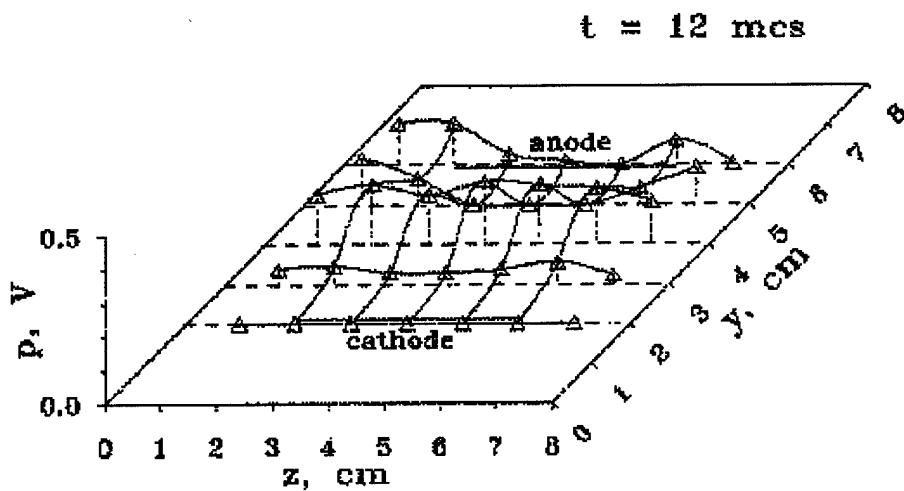


Figure III.56. Distribution of impact pressure in electrodes' cut section (cross-section 2)

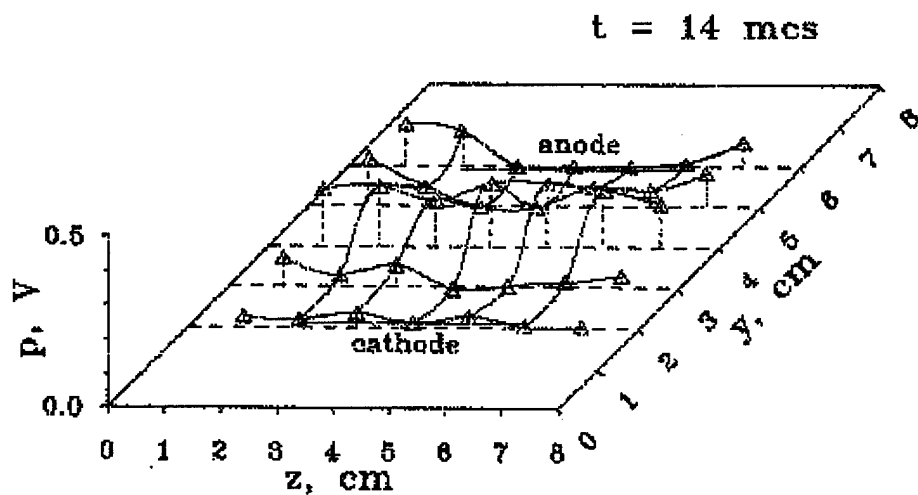


Figure III.57. Distribution of impact pressure in electrodes' cut section (cross-section 2)

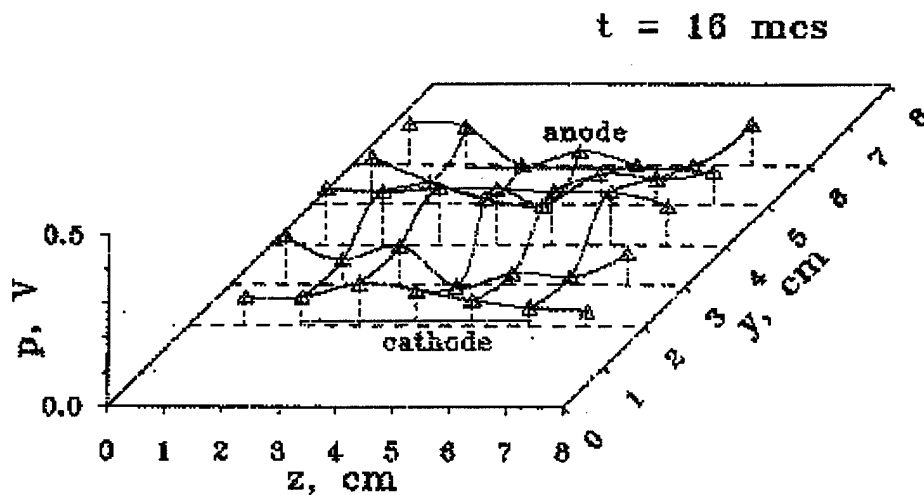


Figure III.58. Distribution of impact pressure in electrodes' cut section (cross-section 2)

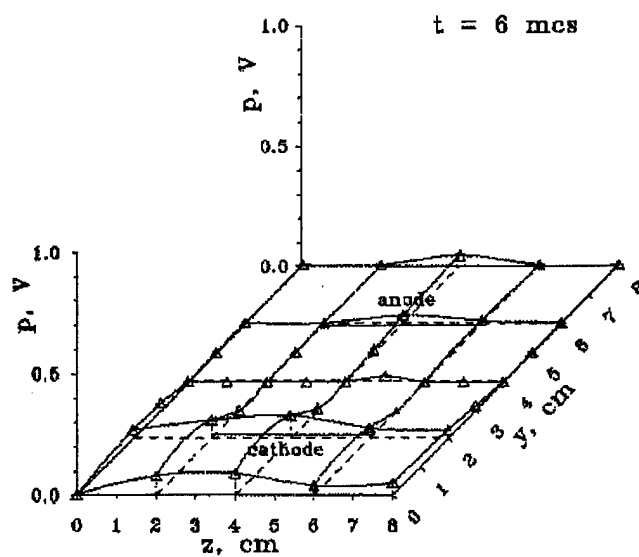


Figure III.59. Distribution of impact pressure at a distance 14 cm from the electrodes' cut section (cross-section 3)

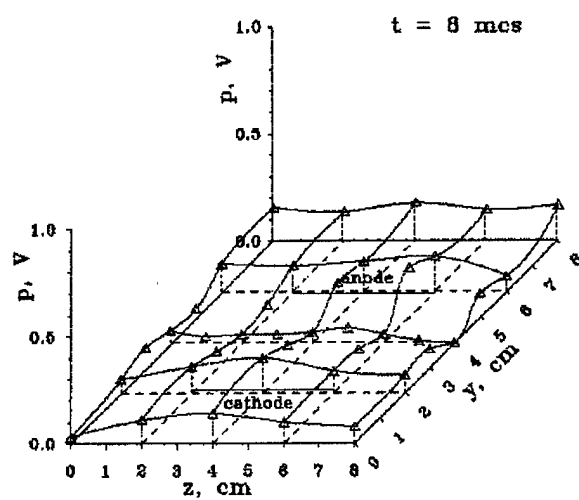


Figure III.60. Distribution of impact pressure at a distance 14 cm from the electrodes' cut section (cross-section 3)

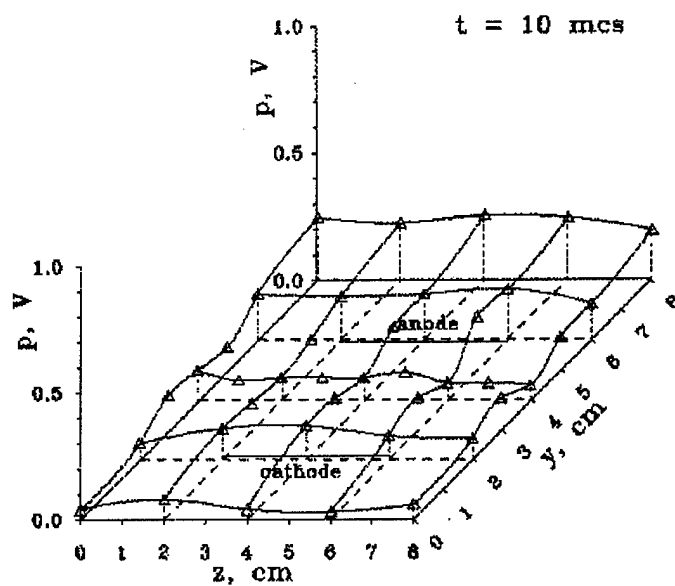


Figure III.61. Distribution of impact pressure at a distance 14 cm from the electrodes' cut section (cross-section 3)

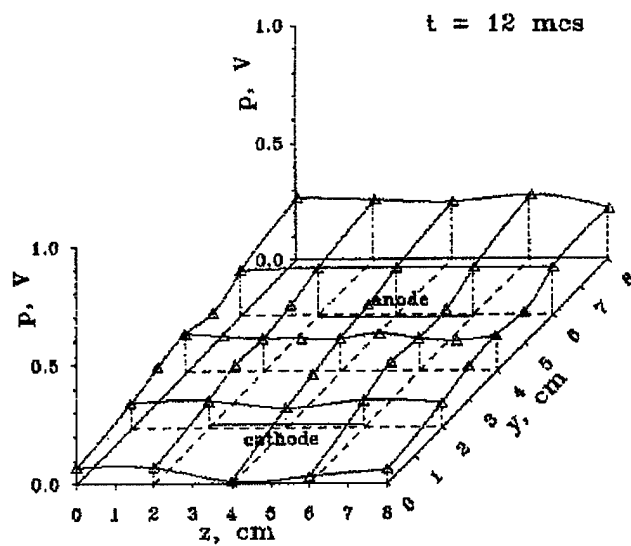


Figure III.62. Distribution of impact pressure at a distance 14 cm from the electrodes' cut section (cross-section 3)

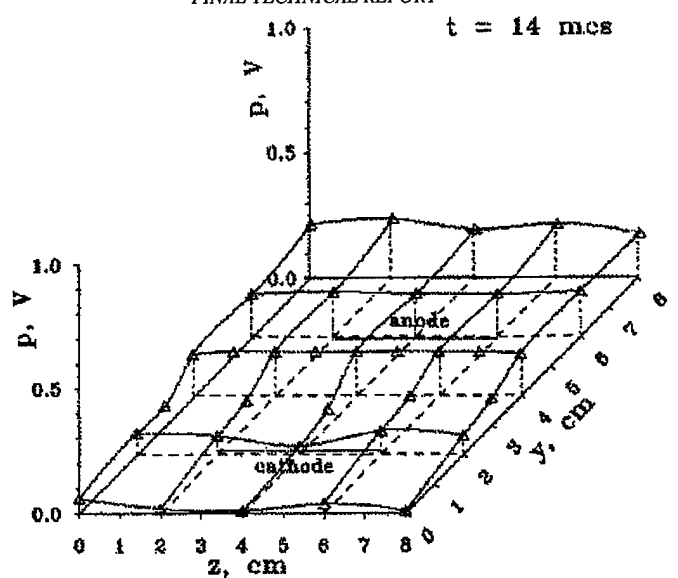


Figure III.63. Distribution of impact pressure at a distance 14 cm from the electrodes' cut section (cross-section 3)

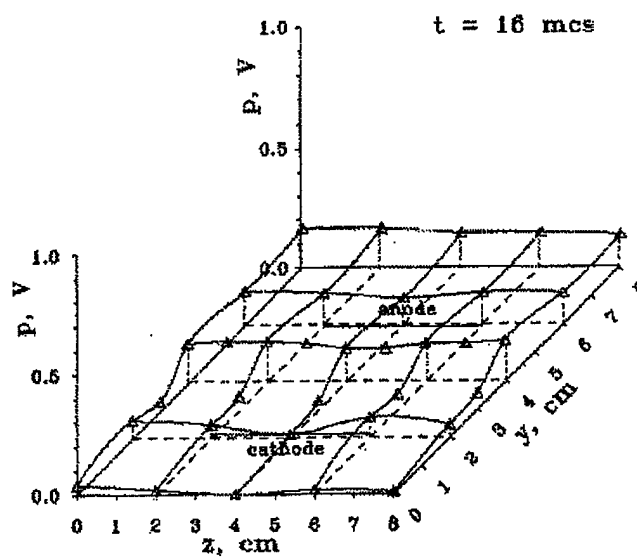


Figure III.64. Distribution of impact pressure at a distance 14 cm from the electrodes' cut section (cross-section 3)

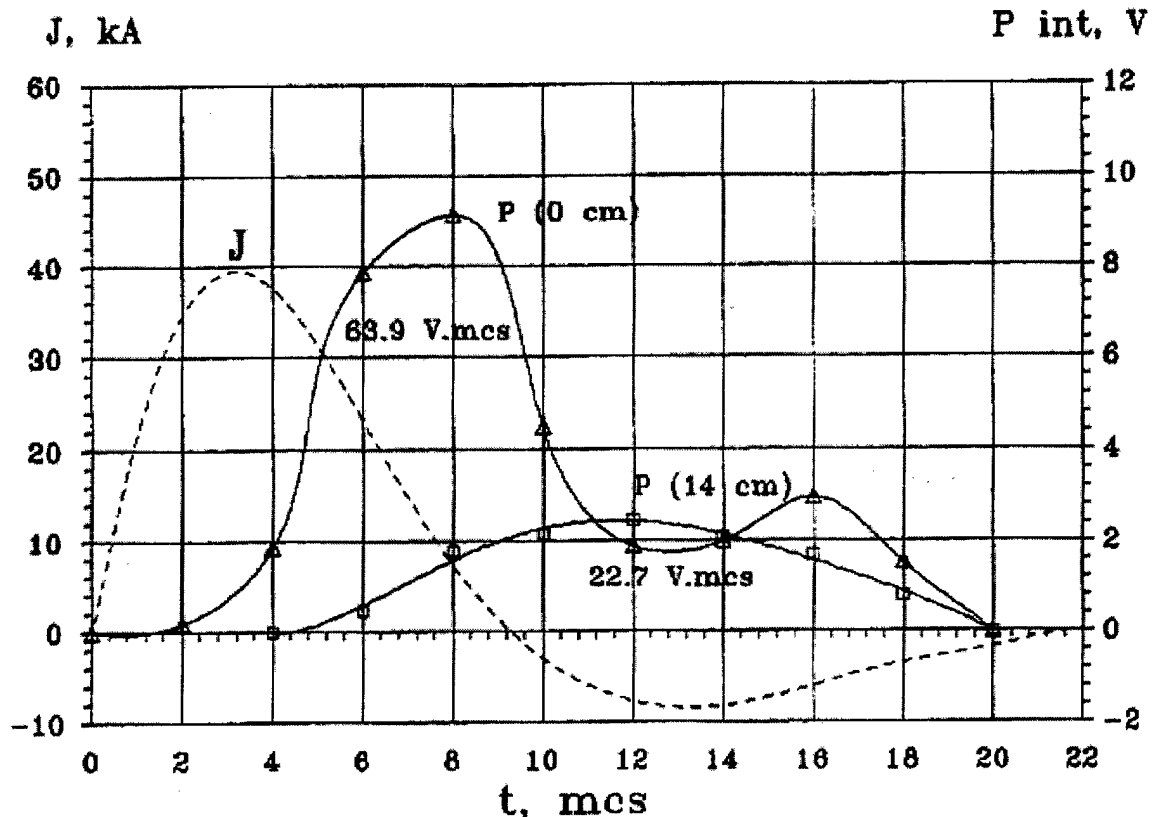


Figure III.65. Integral piezoprobe's signal P in cross-sections 2 (0 cm) and 3 (14 cm)

III.4.5 Ultra high speed photography with visualization of plasma flow

Ultra high-speed photography of discharge and experimental determination of Mach numbers in plasma flow were tried out using the measurement procedure for the APPT of next generation. The appearance of thruster laboratory model is presented in Figure III.38. For increasing the discharge glowing the energy stored in the capacitor bank was increased from $W = 100 \text{ J}$ to $W = 150 \text{ J}$. In this case the APPT thrust impulse was $P_{\text{int}} = 4.5 \text{ mN}\cdot\text{s}$, the pulse mass flow rate $m_{\text{pulse}} = 0.22 \text{ mg/pulse}$, the thrust efficiency $\eta_t = 0.30$ and the specific impulse was $I_{\text{sp}} = 19 \text{ km/s}$. The oscillogram of discharge current is presented in Figure III.66. High-speed photographic record of plasma flow was performed with the help of ultra high-speed photographic camera. The camera has a long-focus objective, rotating mirror and an electromagnetic or electrodynamic shutter. The maximum speed of mirror rotation is 60,000 rev/min. The temporal resolution is $\sim 2 \mu\text{s}$; the spatial resolution is $\sim 1.5 \text{ mm}$; the time spacing between frames is $\sim 2 \mu\text{s}$.

To make the direction and velocity of plasma flow visible a sharpened wedge of quartz glass was put into a flow. The wedge thickness was 1 mm, the width - 20 mm, the angle of point sharpening $\sim 30^\circ$. The wedge was moving in the flow according to two axis (X and Y) with the help of a remote controlled coordinate device. In this case the shocks typical for a supersonic flow were generated at the wedge sharp point and were easily observed in photograms. The

vector direction of the flow speed and Mach number $M=1/\sin(\alpha/2)$, where α is an angle between oblique shocks, can be determined by the shock slope to a longitudinal axis X.

The photographic flow record was carried out according to two mutually perpendicular optical axis Y and Z, perpendicular to longitudinal thruster axis X. The wedge was positioned by the coordinate device in four cross-sections, corresponding to the Teflon bars cut section (1), middle of electrodes' length (2), electrodes' cut section (3) and distance 7 cm from the electrodes' cut section (4). The positions of these cross-sections are presented in Figure III.67.

A characteristic pictures of oblique shocks is presented in photographs in Figure III.68, which was taken by a mirror photographic camera in the integral discharge glowing.

Ultra high-speed photograms of thruster discharge and shocks in plasma flow are presented in Figure III.69 - Figure III.78. The bright glowing spot visible in photograms below the discharge channel is a beam of the laser used for high-speed camera optical tuning.

In photograms in Figure III.69 - Figure III.76 the optical axis of the objective was directed along the axis Y. It is seen the discharge expansion from the Teflon bars cut section (cross-section 1) to the electrodes' cut section (cross-section 3). The discharge glowing is beginning near anode in $t \sim 1 \mu s$ and finishing in $t \sim 15 \mu s$. The maximum of glowing is registering in $t \sim 5 \mu s$, that is about $2 \mu s$ later than the maximum of discharge current. The oblique shocks near the wedge sharpening are visible from $t \sim 3 \mu s$ to $t \sim 13 \mu s$.

In photograms in Figure III.77 - Figure III.78 the optical axis of the objective was directed along the axis Z. In photograms in Figure III.77 it is seen that a flow has two characteristic glowing areas:

- 1) the main flow core, directed along the longitudinal axis with low divergence,
- 2) a peripheral flow directed along the end surfaces of the Teflon bars with a large divergence angle.

The flow core is inclined to the longitudinal axis at the angle of $\beta \sim 5^\circ$ in the cathode direction. In the first discharge half period the flow core is the main source of glowing. In the second half-period the core is split up and the peripheral flow becomes the main source of glowing.

The pictures of oblique shocks obtained in photogram in different flow points and different moments of time are given in Figure III.79 - Figure III.90. It is seen that the Mach number near anode is essential less ($M = 1.5 - 1.8$) than the Mach number in another parts of the plasma flow. In the flow core the Mach number $M = 2.5 \pm 0.2$ practically constant within the first discharge half period is a distinctive feature of the plasma flow created by APPT.

The calculated estimations testify that this number M corresponds to the ratio of flow velocity V to the Alfven velocity: $M_a = V/c_a$, rather than the ratio of flow velocity V to the thermal sonic velocity: $M_t = V/c_t$ (it was calculated that in APPT plasma flow $M_t > 10$). It means that in the first half period plasma has a rather high degree of ionization, as a result of it, Alfven magnetosonic waves are considered to be the basic mechanism to transfer the disturbances instead of thermal sound.

We can estimate the angle of flow divergence in planes XY and XZ by a bisectrix inclination angle of oblique shocks to the thruster longitudinal axis X. The corresponding measurements in photograms showed that in the first discharge half period this angle did not exceed $2\varphi \sim 20^\circ$. In the second half period plasma glowing is not enough to make photographic record of shocks.

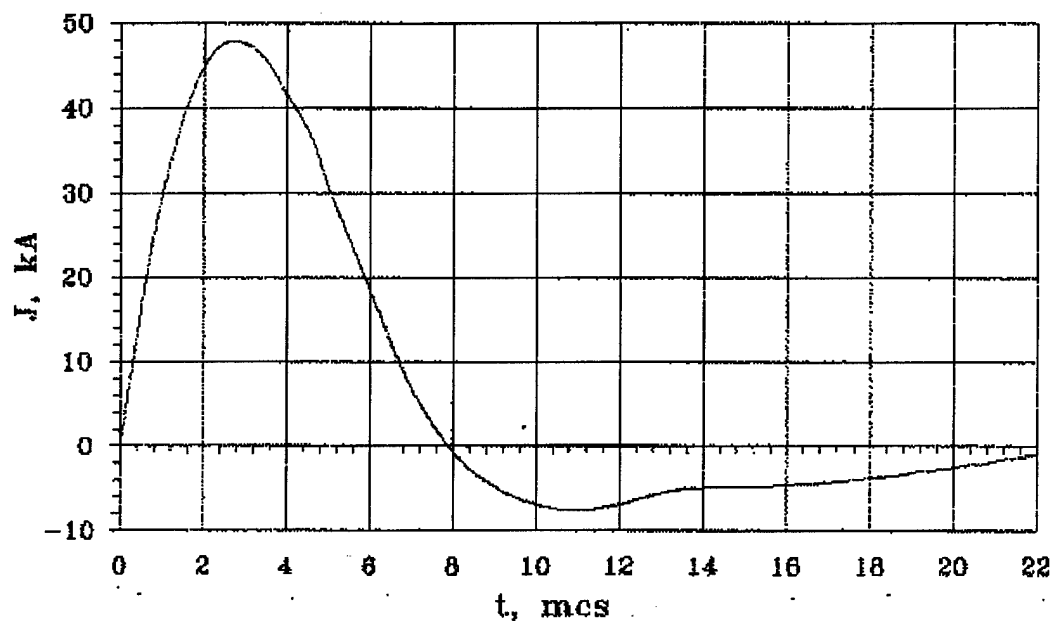


Figure III.66. Discharge current oscillogram

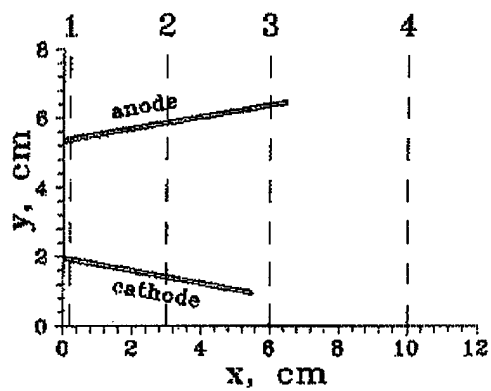
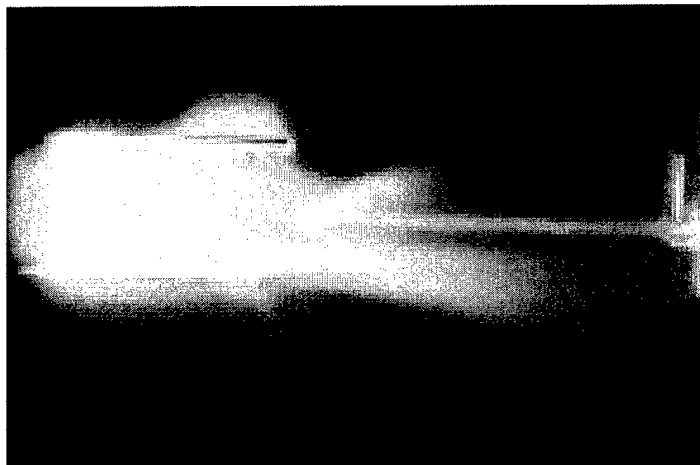


Figure III.67. High-speed photography cross-sections



a



b

Figure III.68. APPT discharge and oblique shocks integral photo (a - cross-section 3, b - cross-section 4)

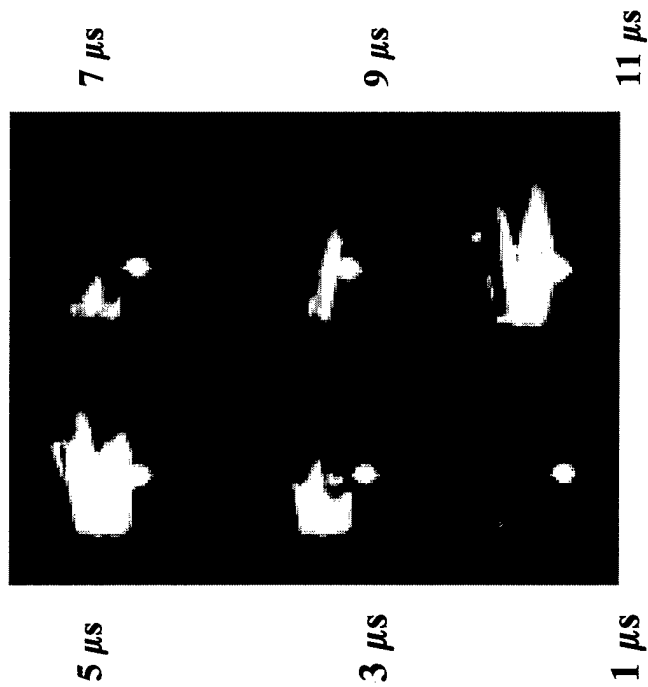


Figure III.69. Photogram of APPT discharge and shocks (optical axis Y, cross-section 1)

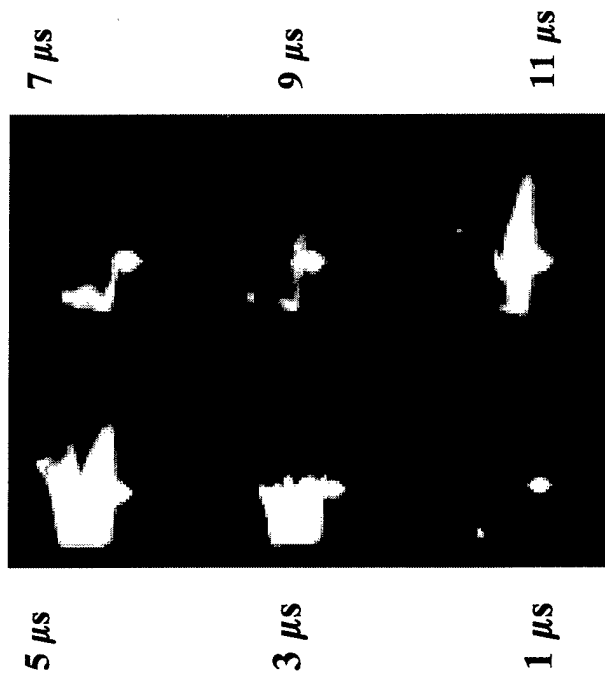


Figure III.70. Photogram of APPT discharge and shocks (optical axis Y, cross-section 2)

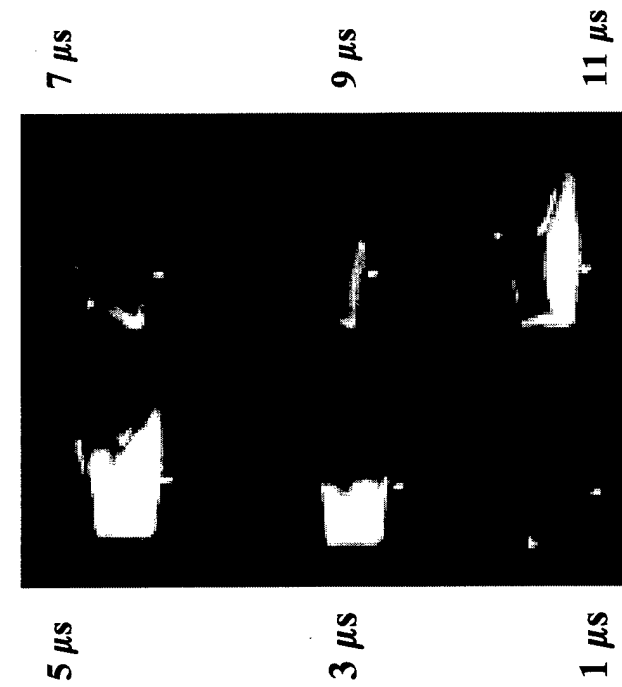


Figure III.71. Photogram of APPT discharge and shocks (optical axis
Y, cross-section 3

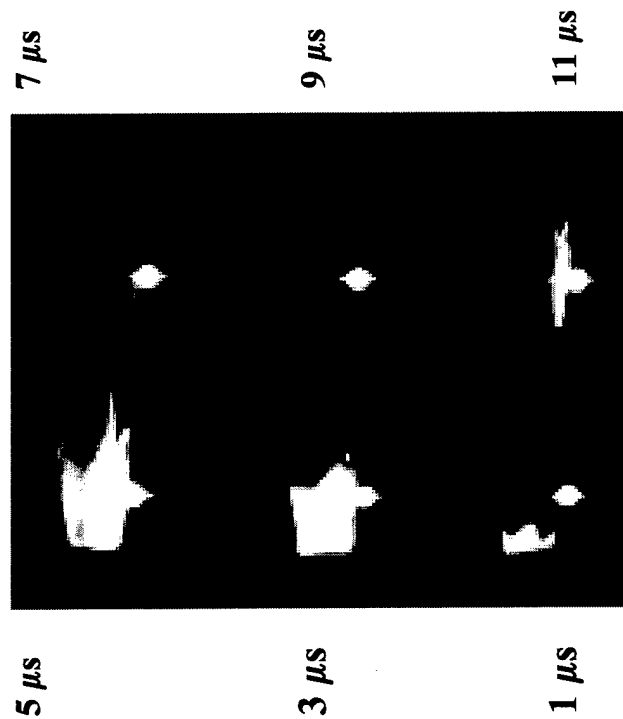


Figure III.72. Photogram of APPT discharge and shocks (optical axis
Y, cross-section 3, near-cathode)

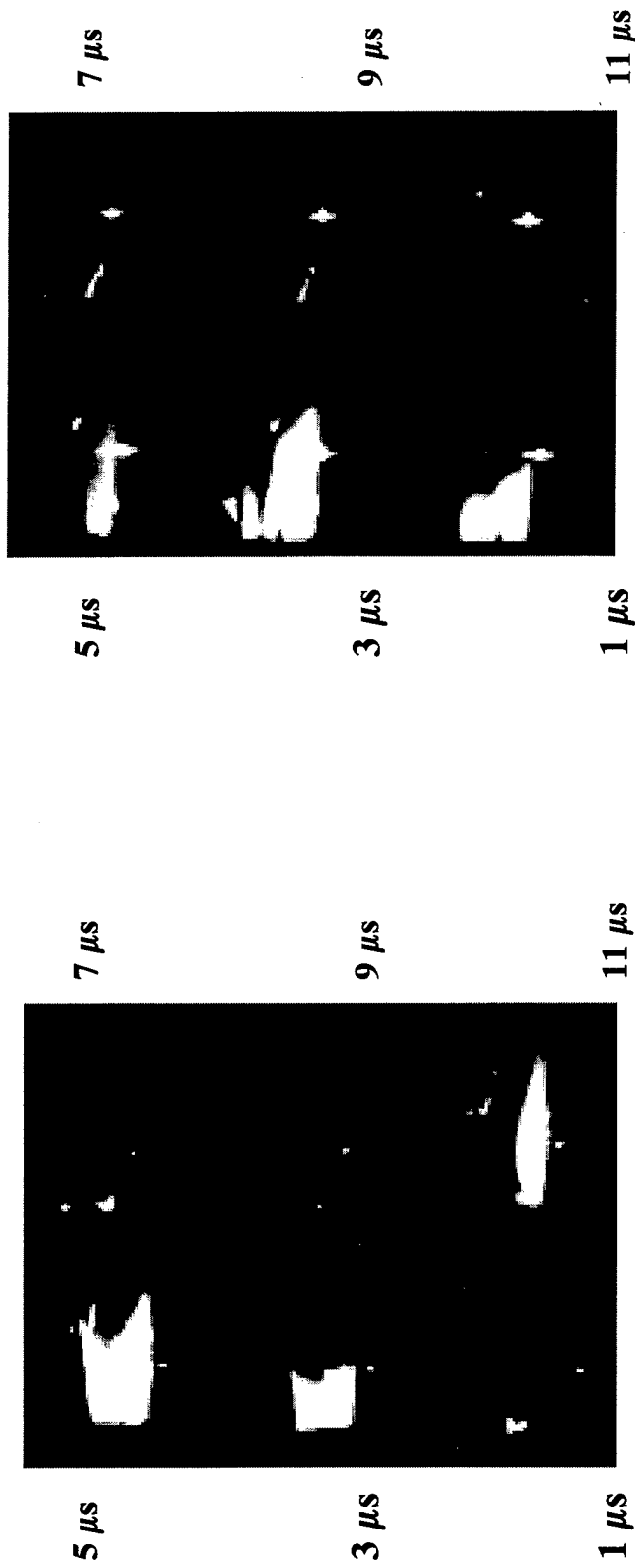


Figure III.73. Photogram of APPT discharge and shocks (optical axis Y, cross-section 3, near-anode)

Figure III.74. Photogram of APPT discharge and shocks (optical axis Y, cross-section 3, near-anode)

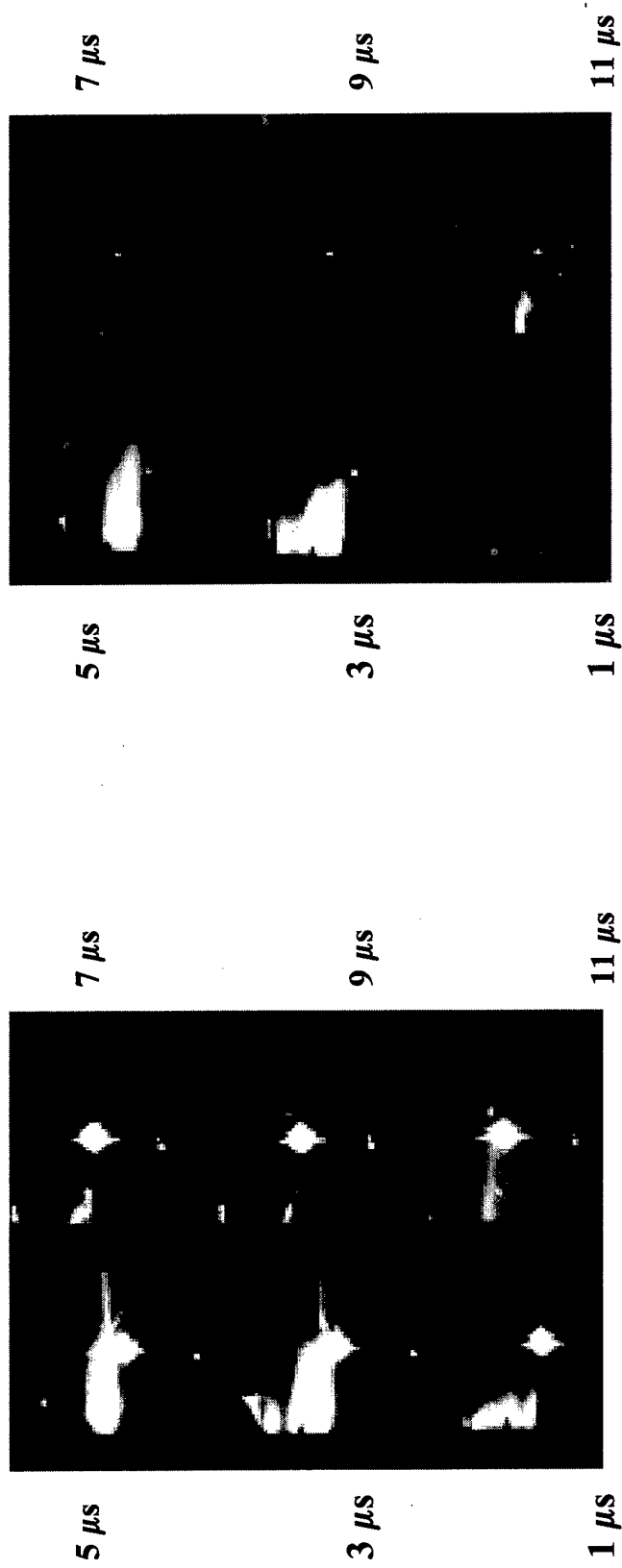


Figure III. 75. Photogram of APPT discharge and shocks (optical axis Y, cross-section 4, near-cathode)

Figure III. 76. Photogram of APPT discharge and shocks (optical axis Y, cross-section 4, near-anode)

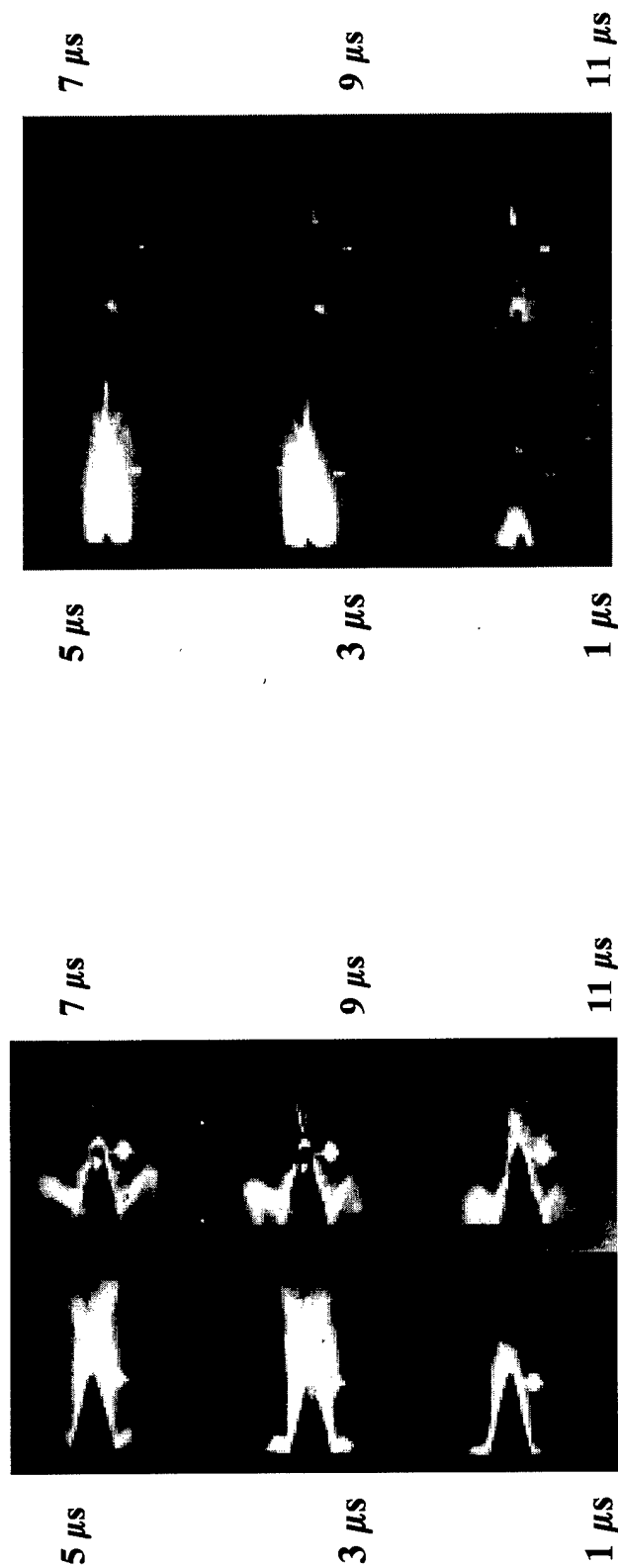


Figure III.77. Photogram of APPT discharge and shocks (optical axis Z, cross-section 3)

Figure III.78. Photogram of APPT discharge and shocks (optical axis Z, cross-section 4)

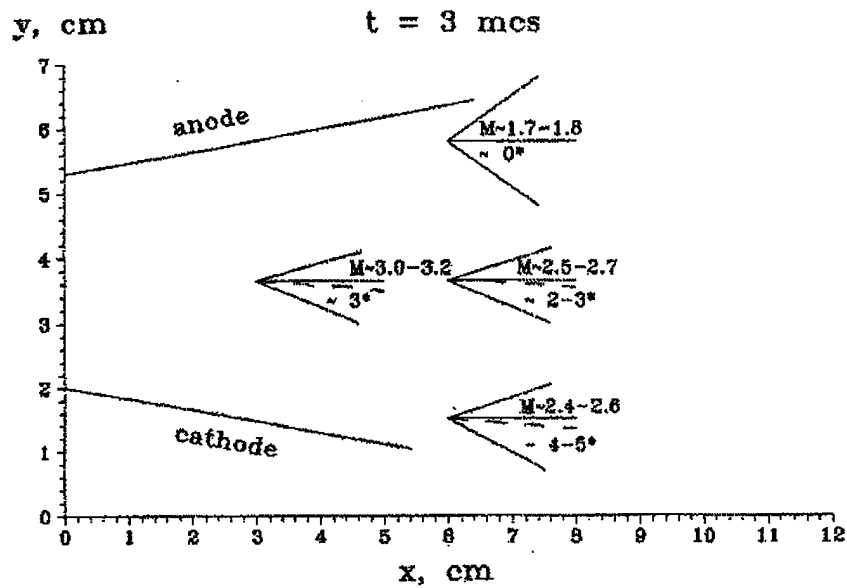


Figure III.79. Diagram of oblique shocks in APPT's plasma flow (axis Y)

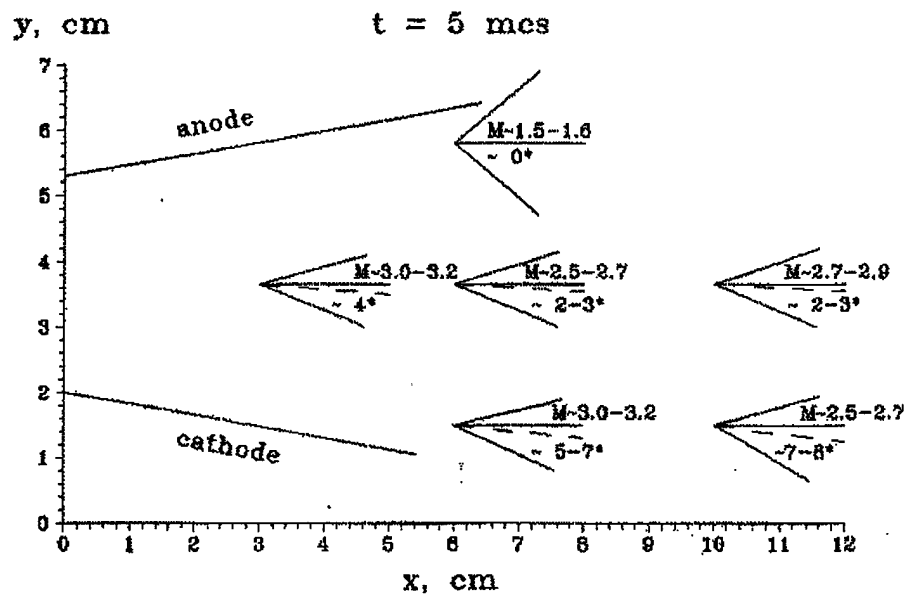


Figure III.80. Diagram of oblique shocks in APPT's plasma flow (axis Y)

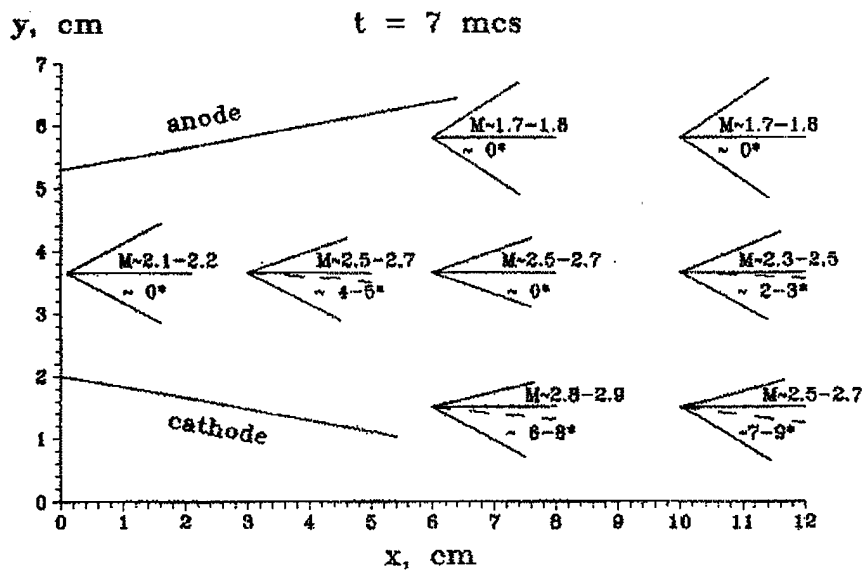


Figure III.81. Diagram of oblique shocks in APPT's plasma flow (axis Y)

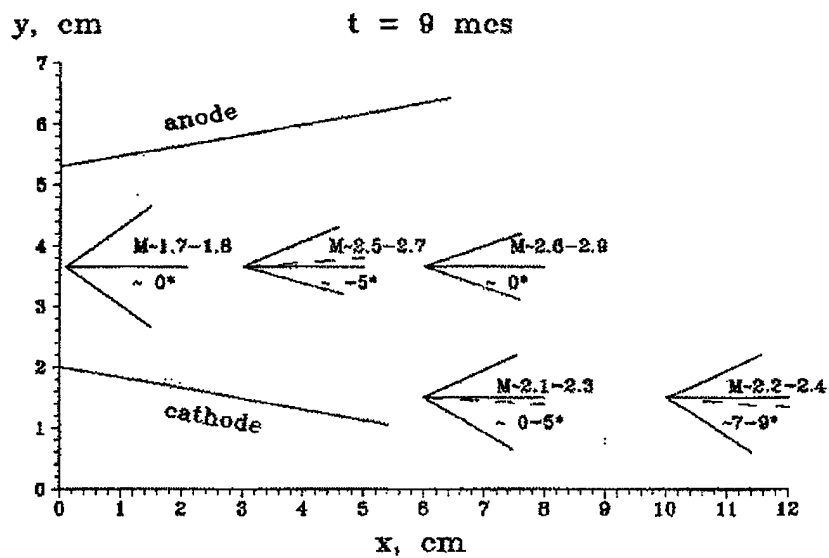


Figure III.82. Diagram of oblique shocks in APPT's plasma flow (axis Y)

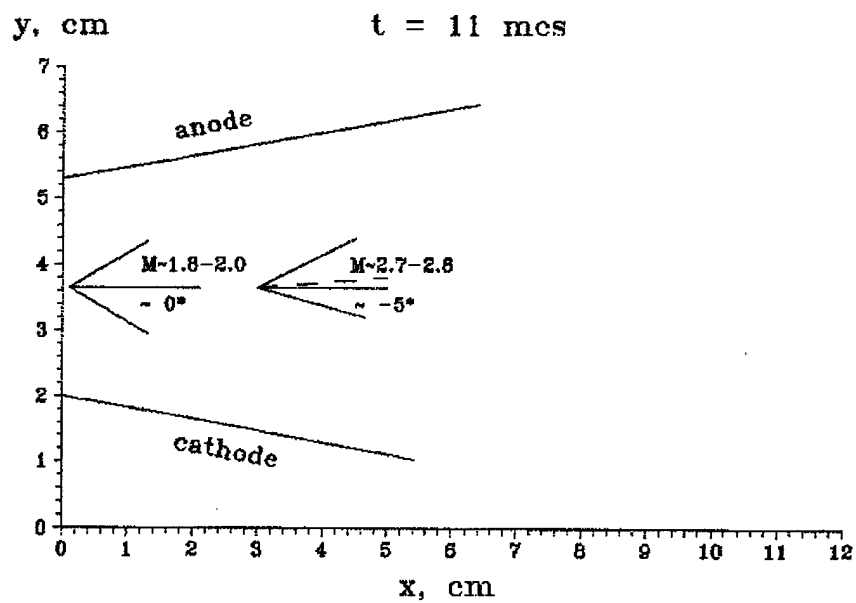


Figure III.83. Diagram of oblique shocks in APPT's plasma flow (axis Y)

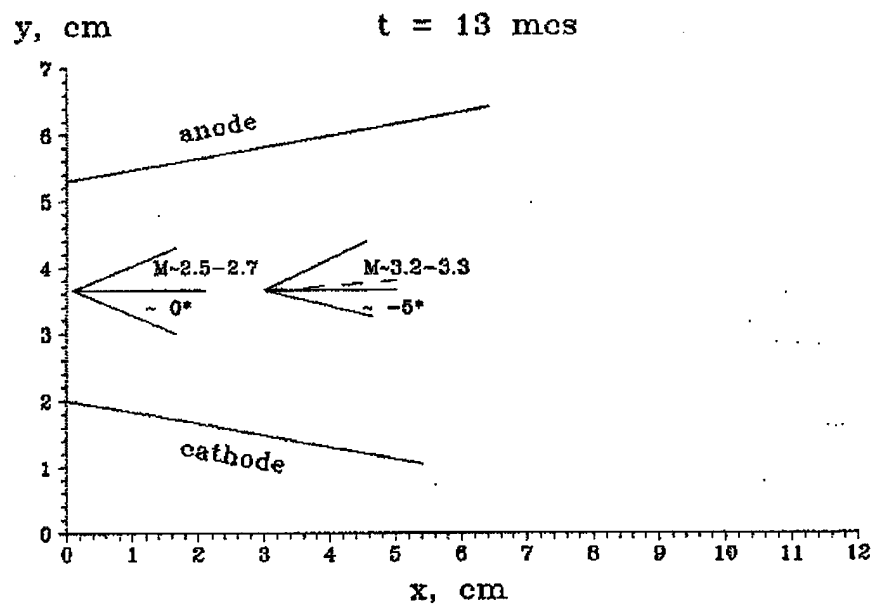


Figure III.84. Diagram of oblique shocks in APPT's plasma flow (axis Y)

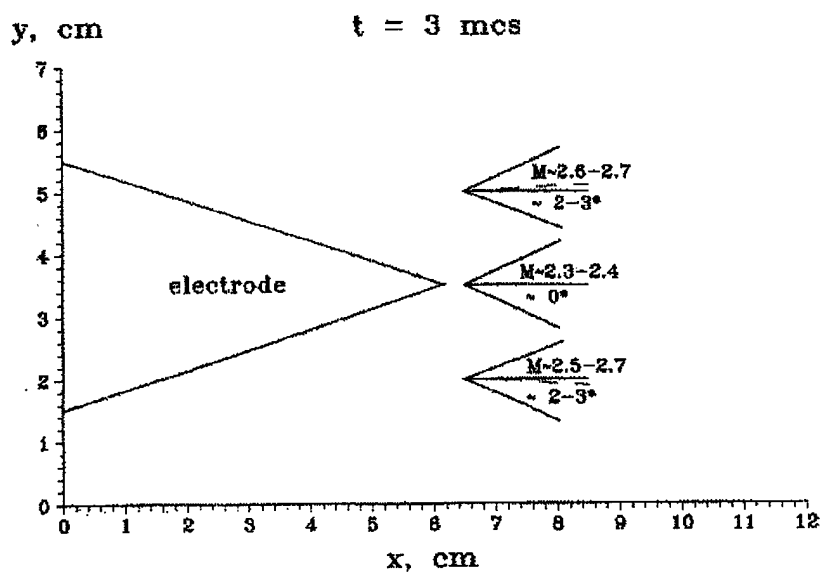


Figure III.85. Diagram of oblique shocks in APPT's plasma flow (axis Z)

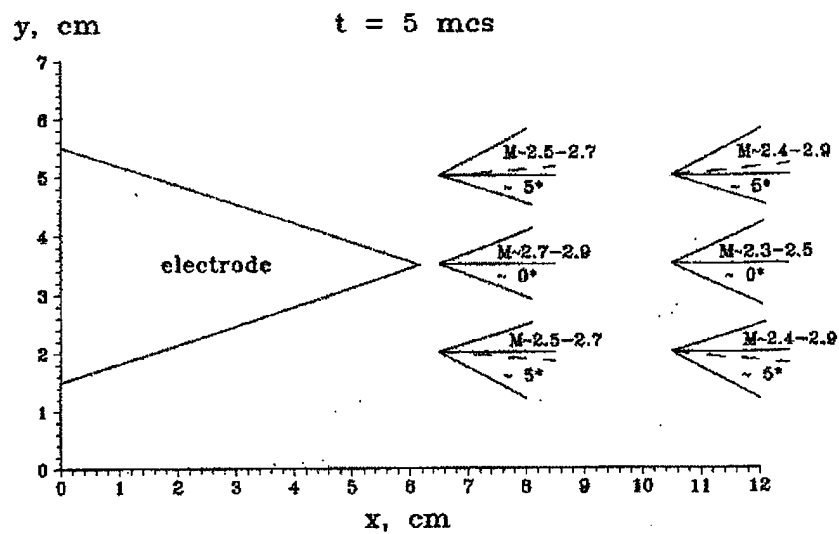


Figure III.86. Diagram of oblique shocks in APPT's plasma flow (axis Z)

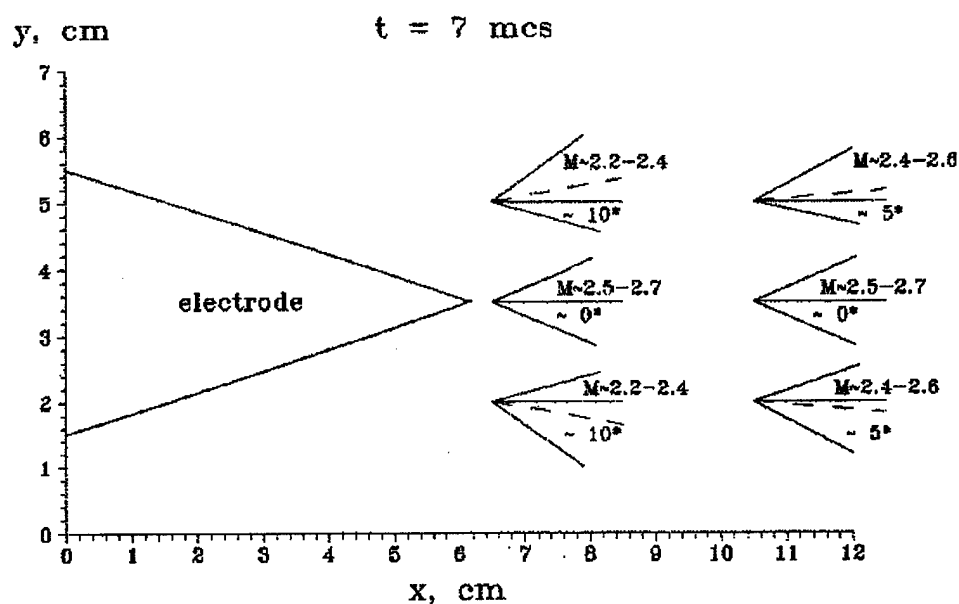


Figure III.87. Diagram of oblique shocks in APPT's plasma flow (axis Z)

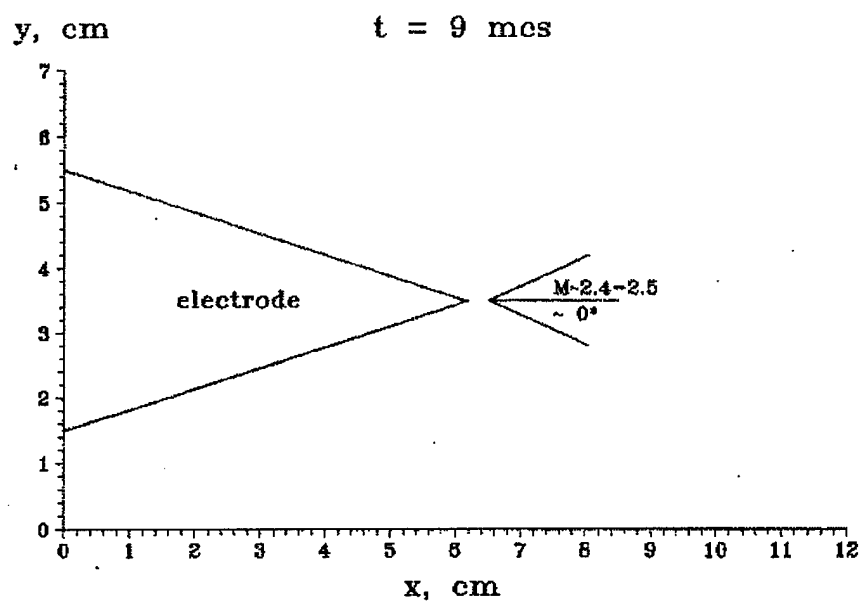


Figure III.88. Diagram of oblique shocks in APPT's plasma flow (axis Z)

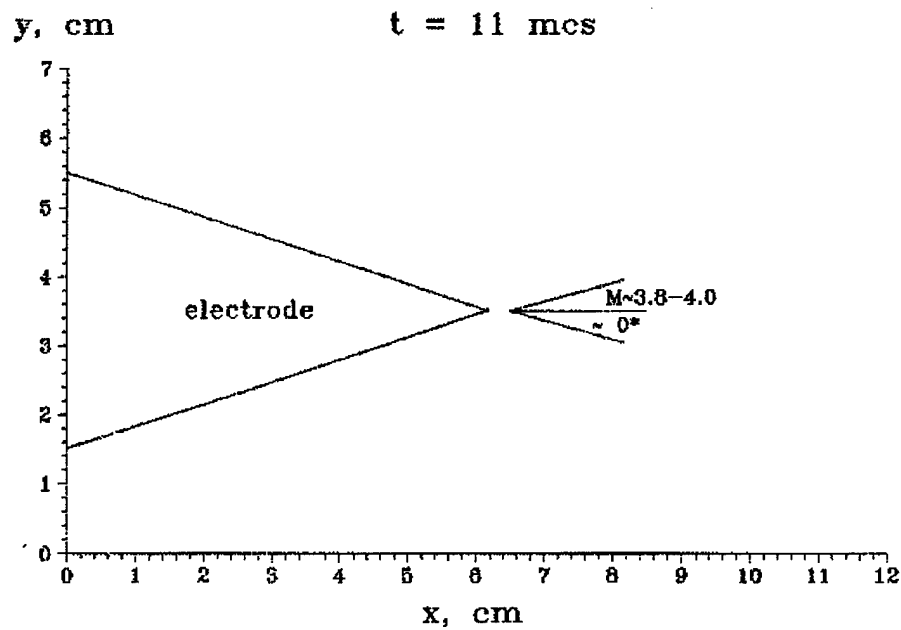


Figure III.89. Diagram of oblique shocks in APPT's plasma flow (axis Z)

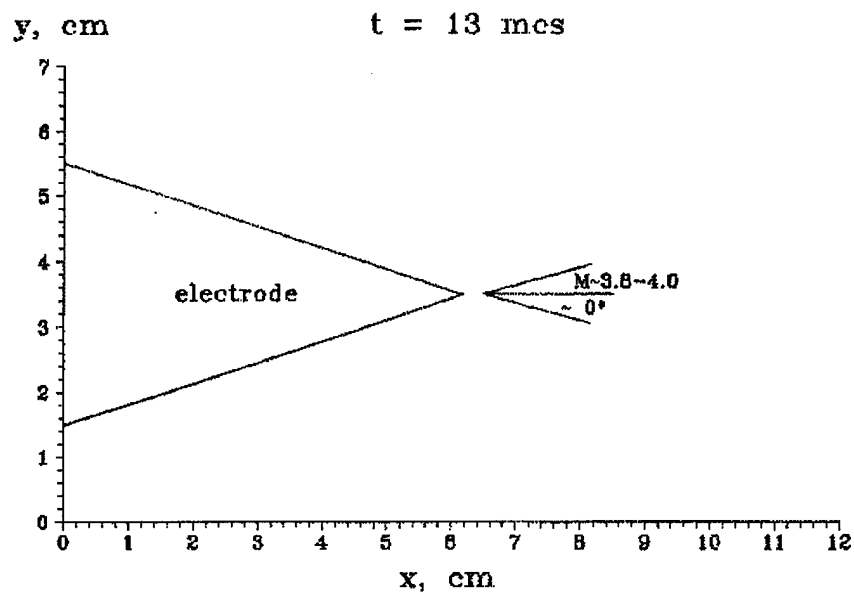


Figure III.90. Diagram of oblique shocks in APPT's plasma flow (axis Z)

III.5 Development and tests of the APPT model

For a number of years after the effect of rail APPT thrust efficiency substantial growth under certain conditions had been revealed, main attention was focused on the study and experimental refinement for the models of highly efficient thruster operating within the power consumption range of (60–150) J. Such approach seemed to be justified, because to our mind within this power range exactly the APPT is the most universal thruster capable to solve problems of attitude control for a small satellite of 50–500 kg in mass most effectively. A number of reports devoted to this subject were made at international conferences and several articles concerning this issue were published. Some results of investigations and refinements for the models with the stored energy of 100 J and 150 J with higher efficiency than that of traditional thrusters are presented in the above parts of the present report also.

An opinion was already expressed at the initial stage of highly efficient APPT study, that without the introduction of additional matching devices (it is extremely undesirable from the point of view of securing the thruster competitiveness), the external electric circuit of real APPT have a limited abilities for its optimization. In particular, estimations showed that when the energy stored in the accumulator is decreased down to (20–30) J, potentialities for improving the thruster performance by matching the elements of its circuit might appear to be exhausted.

In view of the current vast interest to APPT with the stored energy of up to 20 J, that is capable to provide efficient orbital and attitude control for micro- and nano-satellites, we made an attempt for experimental determination of the minimum stored energy, at which the thruster efficiency could be increased by optimizing the elements of its circuit. For this, APPT laboratory models with the nominal energy of 40 J and 30 J were developed, which allowed the energy variation within 25% of the nominal value by changing the discharge voltage. Besides, at the disconnection of one of three capacitors, the 30 J model could be transformed easily into the 20 J model. Thus, the range of stored energy from 50 J down to 15 J could be covered during the test. External appearance of the models is presented in Figure III.91 and Figure III.92, correspondingly. The model with the stored energy of 40 J (Figure III.91) is placed on a thrust-metering device designed specially for measuring low thrust. Energy storage of both models comprises several capacitors, while the discharge channel, formed by two plane electrodes and propellant bars fed from the side directions, is located at a minimum distance from the storage.

Results of experimental refinement for APPT models are presented in the Table 4.

Performance data for the APPT models with the standard power supply circuit is from ^[18] mainly. It is obvious from data presented in Table 4, that within the energy range from 50 J down to 20 J at least the APPT with improved power supply circuit has considerably better characteristics than the thruster with the standard circuit. At that, within the above energy range the relation of values, for the thruster efficiency for example, which is close to two, is kept practically always. At the energy value of below 20 J only, some convergence of efficiency values may take place.

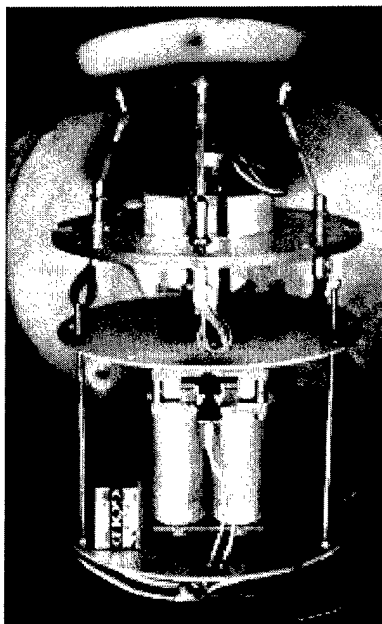


Figure III.91. APPT 40 J appearance



Figure III.92. APPT 20 J appearance

We did not manage to find traditional analogue (prototype) for the improved 15 J thruster and to compare their characteristics, but test results obtained give good reason to believe that advances of highly efficient thruster will be kept down to energy level of 15 J at least.

Table 4

Storage energy	Thrusters with improved circuit			Thrusters with standard circuit		
	Impulse bit	Propellant consumption	Thrust efficiency	Impulse bit	Propellant consumption	Thrust efficiency
J	mNs	kg	%	mNs	kg	%
50	1.25	$0.8 \cdot 10^{-7}$	0.2	0.85	$0.65 \cdot 10^{-7}$	0.11
40	1.0	$0.7 \cdot 10^{-7}$	0.18	0.74	$0.62 \cdot 10^{-7}$	0.1
30	0.7	$0.6 \cdot 10^{-7}$	0.13	0.46	$0.4 \cdot 10^{-7}$	0.08
20	0.47	$0.6 \cdot 10^{-7}$	0.11	0.3	$0.35 \cdot 10^{-7}$	0.06
15	0.35	$0.4 \cdot 10^{-7}$	0.09	no data		

It follows from above presented that investigations of highly efficient APPT within the range of relatively low energies are of preliminary nature and should be continued for obtaining the array of test points sufficient for making more definite conclusions. In particular, in the nearest future it is planned to continue experimental comparison for the traditional and improved thruster models within the range of relatively low energies. APPT models with the stored energy of 15 J and 10 J of both designs will be produced and tested for this.

III.6 Conclusion

Two-dimensional semi-phenomenological numerical model of APPT have been developed. Boundary condition for propellant flow rate is accepted from experiments and calculations on the base of propellant thermal degradation. Developed model adequately describes formation and acceleration of a plasma flow in coaxial accelerating channel. The simulated integrated parameters of considered APPT have appeared close to, measured in experiments. The model gives a correct qualitative picture of separate stages of discharge in APPT: plasma flow formation, appearance of tubular structure at the end of the central electrode, focusing of a flow etc. The features of propellant flow rate determine monotonous character of a distribution of an electron density and especially an axial velocity of a plasma, and magnetic field in accelerating channel. The developed numerical model of APPT can serve as a tool to improve thruster parameters through experimentation – calculation process.

Energy flux onto propellant, Teflon mass loss, current and voltage, near-propellant bar electron density have been measured in APPT stand. Energy fraction released from the discharge region upon the propellant surface in the APPT is near 10^{-2} of the energy stored in the power supply source. Main part of measured flux is transferred by particles. For bank energy 20- 100 J, measured energy in a thermal skin layer is less than accounted from model of Teflon thermal degradation. There is no observed delay between the current beginning and plasma appearance near propellant. So, at the beginning of the discharge, propellant flow rate is provided due to non-thermal or high power energy flux mechanisms. Near propellant the electron density depends on the input voltage and measured at the level of 10^{16} cm^{-3} for 0.5 kV (inter-electrode gap voltage) with some deviation due to shot-to-shot changes in thruster firing. Thickness of boundary layer is order of 0.1 mm

Electron density measurements in the APPT discharge channel in the area between propellant (Teflon) bars and in the interelectrode gap, as well as outside the discharge channel, were made by the method of laser interferometry. A diagnostic system developed on the basis of three-mirror laser interferometer was used during tests. Due to the optimization of the electric circuit parameters, the studied APPT has high specific characteristics. In particular, current efficiency and specific impulse at the stored energy of 100 J comprise 24% and 18 km/s, correspondingly.

Studies for the spatial and temporal distributions of the electron density in the discharge channel make possible to reveal main features of physical processes of the next generation APPT's possessing the improved thruster characteristics. Dynamics and structure of plasma flow in high-efficiency APPT with stored energy of 150 J were studied.

The data confirming the established concept in respect to the dominant role of electromagnetic mechanism under plasma acceleration in high-efficiency APPT were obtained by using the ultra-high speed photo camera. These measurements have shown that plasma flow in such thruster have the insignificant divergence near the electrode cut. The insignificant part of propellant flies apart at the more angle relevant the thermal velocity under the discharge decay only. This propellant part can constitute some threat to optical surfaces of spacecrafts.

Piezoprobe measurements of plasma flow impulse distributions have shown that the impulse maximum is displayed to the thruster anode. This must be taken into account in the design of propulsion systems based on APPT. The divergence angle of plasma flow, which was obtained at piezoprobe measurement processing, was somewhat higher (about 30°) in comparison with measurement carried out by ultra-high speed photo camera. However, in this case the good focusing of flow was observed.

Two APPT models having the level of bank energies 20 J and 40 J, are developed and tested. The improved APPT characteristics are obtained with completion of an optimization between parameters of an electric circuit and the sizes of an accelerating channel of the thruster, when the discharge is close to aperiodic. Laboratory refinement of these models have shown that engineering approach making possible to increase the APPT operation efficiency may be used over the energy range, which is limited on the underside by energy values close to 20 J.

Based on interest which is aroused by APPT with stored energy of ~20 J and less it would be useful to conduct extended studies for the purpose of raising the thruster operation efficiency over this energy region.

Two presentations have been done under Project in International Electric Propulsion conference, IEPC-2003, Toulouse, France: ^[19] ^[20].

III.7 Annex 1. Propellant Flow Rate Modeling

III.7.1 Introduction

Almost all APPT's to date have used solid Teflon (Polytetrafluoroethylene, or PTFE) as a solid propellant, because it does not exhibit carbon buildup on itself or the surrounding structure and because its high temperature degradation. In connection with this, the dynamics of the insulator ablation is of a definite interest for comprehending the plasma acceleration mechanism in similar instruments and for finding an optimal mode of their operation.

In the APPT, the considerable energy fraction released from the propellant surface may be transferred not only by particles but ultraviolet radiation in the wavelength range near 1000 Å. The depth of this radiation absorption in polymers does not exceed 10^{-5} cm; meanwhile the thickness of an propellant material heating due to the heat conduction is about 10^{-4} cm. At present the relative role of conductive and irradiative mechanisms for energy transfer to the propellant is not exactly determined. Now conductive mechanism is more expanded and developed. Probably the main mechanism of energy transfer to propellant depends on thruster operation mode. In any case, if one assumes that the energy flux released upon the propellant surface from the discharge zone and that the evaporated substance is instantaneously removed, the problem of propellant ablation in the APPT will be reduced to the solution of a nonlinear heat conduction equation with a moving interface. In this connection, studying the propellant ablation in these instruments, one is forced to consider the kinetic of thermal degradation that considerably complicates the problem. On the other hand, the thickness of an evaporating layer in the propellant is very small, and therefore one can limit himself by a study of 1D-heat conduction equation.

Below we take into account thermal PTFE-degradation kinetics to solve problem of propellant ablation in the APPT. The approach of the PTFE- degradation kinetics developed by Madorski is expounded. The statement and the results of solving the problem are given, taking account of polymer degradation obeying the kinetic equation of the first order. Also it is proposed to use two branches of degradation reaction more to represent the thermal polymer degradation at the energy flux densities to the propellant $> 10^4$ W/cm³.

III.7.2 Kinetics of Teflon Thermal Degradation

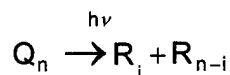
Let us briefly speak about modern ideas concerning the thermal degradation of polymers. Since the propellants made of Teflon have been more often studied in the APPT, all the quantitative data are referred to this polymer.

According to ^[21,22], the following mechanism of degradation is applicable to all the polymers which undergo the thermal degradation up to a monomer, dimer and to the other oligomeric molecules produced as a result of rupture in the main chain:

Reaction	Reaction rate	Energy
Initiation (formation of radicals) $Q_n \rightarrow R_i + R_{n-i}$	$2 k_1 n Q_n$	ϵ_1
Growth of a chain (product formation) $R_n \rightarrow R_{n-1} + M$	$k_2 R$	ϵ_2
Rupture of the chain (recombination) $R_i + R_j \rightarrow Q_{i+j}$	$2 k_4 R^2$	ϵ_4

Here, Q_n is the concentration of polymer molecules including n - links of C_2F_4 ; R_i is the concentration of radicals having i - monomeric links; M is the concentration of monomers.

If, along with heating, the polymer is irradiated, there will be one opportunity more to initiate the reaction



The rate of this reaction is equal $2\phi I n Q_n$, where I is the radiating power released under absorption in a polymer, ϕ is the radiation-chemical yield of radicals.

As for the radiation-chemical yield of irradiation, ϕ , the mechanism of electron excitation and of the subsequent dissociation results in that the radiation-chemical yield for the γ -radiation and for ultraviolet one turn out to be the same by the order of magnitude. Taking account of the fact that a considerable fraction of the energy released upon the propellant is transferred by radiation, one can expect that the contribution of radiation into the reaction of initiation will be essential, at the initial stages of a discharge in particular, when the propellant temperature is not great and radiation initiation of the depolymerization reaction can considerably exceed the thermal one.

Thus, taking account of the radiation initiation, the equation of radical formation can be written in the form

$$\frac{dR}{dt} = 2(k_1 + \phi I) \sum_n n Q_n - 2k_4 R^2 \quad (2.1)$$

On the other hand, according the chain growth reaction, the rate of monomer formation is equal

$$\frac{dM}{dt} = k_2 R \quad (2.2)$$

Let us assume that the molar fractions of radicals and monomers in the sample are small, i.e.

$$\sum_i i R_i \ll \sum_n n Q_n \quad \text{and} \quad M \ll \sum_n n Q_n, \quad (C \approx 0).$$

Making transition to dimensionless variables - relative concentration of radicals $R \rightarrow R/(n_0(1-C))$ and conversion, $C=M/n_0$, one obtains a set of equations representing the thermal Teflon-degradation from (2.1) and from (2.2):

$$\left\{ \begin{array}{l} \frac{dR}{dt} = 2(k_1 + \phi I) - 2k_4 R^2 n_0 (1-C), \\ \frac{1}{1-C} \frac{dC}{dt} = k_2 R \end{array} \right. \quad (2.3)$$

And, finally, if one assumes that the radiation initiation can be neglected in comparison with the thermal one, the following equation of the polymer degradation will take place for the equilibrium case:

$$\frac{1}{(1-C)^{1.5}} \frac{dC}{dt} = k_2 \left(\frac{k_1}{k_4 n_0} \right)^{0.5},$$

$$R = \left(\frac{k_1}{k_4 n_0} \right)^{0.5}. \quad (2.4)$$

The equation (2.4) coincides with the conversion equation produced in [22] and the quantity k_2 ($k_1 / k_4 n_0$) is a constant of the reaction $k^u = 4.14 \cdot 10^{18} \exp(-3.5/T_{ev})$.

Some thermo-physical parameters and kinetic constants for the Teflon are given Table 1.

Table.1. Teflon thermo-physical parameters

Density at a normal temperature, ρ	2.2 - 2.3 g/cm ³
Heat capacity at normal temperature, c_p	1.06 J/grad C
Heat conductivity at normal temperature, η	$2.5 \cdot 10^{-3}$ J/(cm s)
Energy of bonds:	
C-C	2.78 eV
C=C	4.8 eV
C-F	5.0 eV
Constants:	
thermal initiation, k_1	$-2.110^{28} \exp(-\frac{5.15}{T_{ev}}) s^{-1}$
chain growth, k_2	$710^{11} \exp(-\frac{1.57}{T_{ev}}) s^{-1}$
chain rupture, k_4	$510^{-8} \exp(-\frac{1.3}{T_{ev}}) s^{-1}$
radiation-chemical yield (order of magnitude) ϕ	$10^{-2} eV^{-1}$

III.7.3 Equation of Energy Transfer in the Propellant

The equation of energy transfer in the propellant, in the immobile coordinate systems, has the form:

$$\frac{\partial \varepsilon}{\partial t} = \frac{\partial}{\partial x} \eta \frac{\partial T}{\partial x} \quad (3.1)$$

Here ε is the intrinsic energy in 1 cm³ of the substance. Taking account of the polymer degradation mechanism given in Section 2, the intrinsic energy of the substance can be written in the form

$$\varepsilon = \rho (c_p T + \frac{\varepsilon_1}{2} R n_0 + \varepsilon_2 C n_0), \quad (3.2)$$

or

$$\varepsilon = \rho (c_p T + \frac{\varepsilon_1^*}{2} R + \varepsilon_2^* C), \quad (3.2a)$$

where $\varepsilon_1^* = 4900$ J/g and $\varepsilon_2^* = 1517$ J/g.

Substituting (3.2a) into (3.1), one obtains

$$\frac{\partial}{\partial t} \rho (c_p T + \frac{\varepsilon_1^*}{2} R + \varepsilon_2^* C) = \frac{\partial}{\partial x} \eta \frac{\partial T}{\partial x}. \quad (3.3)$$

Adding the relationships (2.3), (2.4) in the equation (3.3) and taking account of the fact that $C \approx 0$, one obtains the set of the equations which can be used for representation of the pulsed propellant depolymerization (evaporation) in the APPT

$$\begin{cases} \frac{\partial}{\partial t} \rho (c_p T + \frac{\varepsilon_1^*}{2} R + \varepsilon_2^* C) = \frac{\partial}{\partial x} \eta \frac{\partial T}{\partial x} \\ \frac{\partial R}{\partial t} = 2k_1 - 2k_4 R^2 n_o, \quad \frac{\partial C}{\partial t} = k_2 R. \end{cases} \quad (3.4)$$

Before formulating the boundary conditions for (3.4), let us make some assumptions on a polymer degradation model in our case. First, let us assume that the density, heat conductivity and heat capacity of the polymer remain to be constant. Thus the polymer degradation problem is reduced to the problem similar to the evaporation of a fluid from the surface. Since the heated layer thickness, δ , is small and the thickness of the layer, where an intense polymer degradation occurs, is $\sim \delta/10$, one can assume that the diffusion of a monomer from the propellant goes on at the infinite rate. At high depths of heating the monomer yield can be controlled by diffusion process^[21]. Second, let us assume that the maximal propellant surface temperature does not exceed 1300°K, i.e. a relative amount of radicals in the layer is small.

The relative concentration of radicals in the heated layer will attain its equilibrium value for the time, $\tau \sim 1/k_1$, which is about $2 \cdot 10^{-8}$ s for $T=1200^\circ$ K that is considerably lower than the characteristic plasma acceleration time in the instruments under consideration. Therefore the number of radicals in 1 cm³ of the substance is determined by the second relationship in (2.4), and the contribution introduced by radicals into the intrinsic energy, ε , is considerably smaller than $c_p T$. Indeed, for $T = 1200^\circ$ K, $c_p T = 960$ J/g and $\varepsilon_1^* \frac{R}{2} = 105 - 125$ J/g

Taking the above expressed assumption, the set (3.4) can be written in the form

$$\begin{cases} \frac{\partial T}{\partial t} = \chi^2 \frac{\partial^2 T}{\partial x^2} - \frac{\varepsilon_2^*}{c_p} \frac{\partial C}{\partial t} \\ \frac{\partial C}{\partial t} = k_2 \left(\frac{k_1}{k_4 n_o} \right)^{0.5} = 4.44 \cdot 10^{18} \exp \left(-\frac{3.5}{T_{ev}} \right), \quad \chi^2 = \frac{\eta}{\rho c_p}. \end{cases} \quad (3.5)$$

Eqs. (3.5) are solved in the range $s(t) \leq x \leq J$, where $s(t)$ is the phase interface. The boundary and initial conditions for (3.5) have the form

$$\begin{aligned} \text{at } x = s(t) \quad & -\eta \frac{\partial T}{\partial x} = H(t), \\ T(t, \infty) &= T_o, \\ T(0, x) &= T_o. \end{aligned} \quad (3.6)$$

The interface rate, $\frac{\partial s}{\partial t}$, can be found from the relationship

$$\frac{\partial s}{\partial t} = \int_s^{\infty} \frac{\partial C}{\partial t} dx = \int_s^{\infty} k_2 \left(\frac{k_1}{k_4 n_o} \right)^{0.5} dx. \quad (3.7)$$

Eqs. (3.5, together with (3.6) and (3.7), were solved numerically. The equations were made dimensionless.. The following parameters $DT = 900^\circ$, $t_o = hc_p r DT^2 / H_o^2$ were chosen to be scaling law quantities. Having remained the previous designations of the quantities, one obtains a dimensionless heat conduction equation

$$\frac{\partial T}{\partial t} = \frac{\partial^2 T}{\partial x^2} - \frac{1-A}{A} \frac{\partial C}{\partial t}, \quad (3.8)$$

where $A = \frac{c_p \Delta T}{c_p \Delta T + \varepsilon_2^*}$. Initial and boundary conditions, in this case, acquire the form

$$\frac{\partial T}{\partial x} = -1, \quad T(0, x) = \alpha, \quad T(t, \infty) = \alpha, \quad (3.9)$$

where $\alpha = \Delta T - 1 / T_o$. The monomer yield rate was determined from the relationship

$$\frac{\partial C}{\partial t} = B \exp\left(-\frac{\beta}{T}\right), \quad (3.10)$$

where $B = 4.14 \cdot 10^{18} t_o$, $\beta = 45.1$. The heat conduction equation was solved numerically.

III.7.4 High Temperature Branches of Degradation

As noted above, at the energy flux densities upon the propellant surface greater than $5.10^3 \text{ J/cm}^2 \text{ s}$, the stationary propellant surface temperatures exceed 1250 K. A relative amount of radicals in the substance becomes equal to ~ 1 that contradicts to the assumption about the smallness of R , made in Section 2. Unfortunately, there are no experimental data on the Teflon -degradation rate at the temperatures $> 800 \text{ K}$.

At the transition to higher energy flux densities upon the propellant surface and, as a result, to higher polymer degradation temperatures one should take into account of the fact that the formation of difluoro-methylene radicals $(CF_2)^*$ and excited molecules $(C_2F_4)^*$, at such temperatures, can occur with greater probability than the formation of monomers at the ends of a polymer chain. In this case, the chain reaction diagram should include two reactions more:

Reaction	Reaction rate
Formation of a difluoro-methylene radical $R_i \rightarrow R_{i-1/2} + R_{1/2}$	$k_1 R / 2$
Formation of the excited molecule of monomer $R_i \rightarrow R_{i-1} + M^*$	$k_1 R$

If one assumes that the thermal disrapture of bonds of the ends of a chain occurs with the same probability as that at its other pieces, one will be able to use the initiation constant, k_1 , for the estimations.

The Teflon - degradation rate, taking account of all the above - considered possible reactions considerably exceeds the monomer formation rate on radicals at the temperatures $> 1100 \text{ K}$.

At the same time, the diagram under consideration does not contradict the known experimental results ^[22], since the contribution of these two chain reaction branches is negligible in the temperature range up to 800 K.

Let us assume that, in this case under consideration, a relative amount of radicals in a substance is small. Then, the heat conduction equation will acquire the form

$$\frac{\partial T}{\partial t} = \chi^2 \frac{\partial^2 T}{\partial x^2} - 1/c_r [3/2 k_1 \varepsilon_1^* + k_2 \varepsilon_2^*] (k_1/k_4 n_0)^{0.5} \quad (4.1)$$

(values of the constants k_1, k_2, k_4 are given in Section 2). The boundary and initial conditions of problem, as well as an expression for the interface velocity, remain to be previous.

It is easy to obtain that the temperature, T_{st} , weakly depends on H_0 . When the energy flux is changed from 10^3 to 10^6 J/cm² s, the temperature varied by 150° only. If one takes account of the fact the degradation mechanisms introduced in this Section have the reaction energy ε_1 , the average Teflon -degradation energy, ε , will be determined by the following expression

$$\varepsilon = \frac{1.5 \varepsilon_1^* k_1 + \varepsilon_2^* k_2}{1.5 k_1 + k_2} \quad (4.2)$$

It is in agreement with an experimental dependence on the power supply source energy of a total substance mass evaporating from the propellant surface. Indeed, if one assumed that the propellant surface area - from where evaporation takes place - remained to be constant, then, with increase in the energy flux, the ratio m/W_0 will be reduced from 1.5 to 0.5 µg/J. The energy flux density, in this case, is increased from $5 \cdot 10^4$ to $5 \cdot 10^5$ J/cm² s.

III.8 References for Task 2

- ¹ R. L. Burton, P. J. Turchi. "Pulsed Plasma Thruster." *Journal of Propulsion and Power*. Vol. 14, no. 5, September-October 1998. p.716-735.
- ² P.J. Turchi, "Direction for Improving PPT Performance", 25th International Electric Propulsion Conference, IEPC97-038, pp 251-258, Cleveland, USA, Aug., 1997.
- ³ N. Antropov, G. Diakonov, M. Orlov, G. Popov, V. Tyutin, V. Yakovlev, Yu. Alexeev, M. Kazeev, F. Darnon "High Efficiency Ablative Pulsed Plasma Thruster Characteristics", 3rd International Conference on Space Propulsion, paper #206, Cannes, France, 2000.
- ⁴ G. Popov, N. Antropov et al "Experimental Study of Plasma Parameters in High-Efficiency Pulsed Plasma Thrusters", 27th International Electric Propulsion Conference, IEPC paper 01-163, Pasadena, USA, 2001
- ⁵ N. Antropov, G. Popov, V. Yakovlev, F. Darnon, M. Kazeev, V. Akimov, I. Ogloblina, Yu. Nagel "Application of Pulsed Plasma Thrusters for Small Satellites", Proceedings of the 3rd International Conference on Spacecraft Propulsion, Cannes, France, 2000.
- ⁶ P.G. Mikellides, P.J. Turchi, R.J. Leiweke, C.S. Schmahl, L.G. Mikellides, "Theoretical Studies of a Pulsed Plasma Microthruster", IEPC-97-037, pp.245-250.
- ⁷ M.N. Kazeev, V.F. Kozlov, G.A. Popov, "Two-Dimensional Numerical Simulation of Coaxial APPT", 27th International Electric Propulsion Conference, IEPC paper 01-159, Pasadena, CA 2001.
- ⁸ M. Keidar, I. D. Boyd, F.S. Gulczinski, E.L. Antonsen and G.G. Spanjers, "Analyses of Teflon Surface Charring and Near Field Plume of a Micro-Pulsed Plasma Thruster", 27th International Electric Propulsion Conference, IEPC paper 01-166, Pasadena, CA 2001.
- ⁹ E.J. Steppard and M. Martines - Sanchez, "Ionization Rate Models and Inlet Ignition in Self-Field APPT Thrusters". Proceeding 23th International Electric Propulsion Conference, 1993, IEPS-93-071.
- ¹⁰ R.H. French, R.C. Wheland, D.J. Jones, J.N. Hilfiker, R.A. Synowicki, F.C. Zumsteg, J. Feldman, A.E. Feiring, "Fluoropolymers for 157nm Lithography: Optical Properties from VUV Absorbance and Ellipsometry Measurements", *Optical Microlithography XIII*, SPIE Vol. 4000, edited by C. J. Proglar, 1491-1502 (2000).
- ¹¹ G. Popov, N. Antropov, G. Diakonov, M. Orlov, V. Tyutin, V. Yakovlev "Experimental Study of Plasma Parameters in High-Efficiency Pulsed Plasma Thrusters", Proceedings of the 27th International Electric Propulsion Conference, IEPC-01-163, Pasadena, USA, 2001.
- ¹² "Methods of Plasma Investigation", edited by W. Lochte-Holtgreven, Moscow: Mir, 1971, 552 p., - in Russian.
- ¹³ L.N. Pyatnitskiy, "Laser Diagnostics of Plasma", Moscow: Atomisdat, 1976, 424 p. - in Russian.
- ¹⁴ A.N. Zaidel, G.V. Ostrovskaya, "Laser Methods of Plasma Investigation", Leningrad: Nauka, 1977, 219 p. - in Russian.
- ¹⁵ L.A. Dushin, O.S. Pavlichenko, "Plasma Investigation with Use of Lasers", Moscow: Atomisdat, 1988, 144 p. - in Russian.
- ¹⁶ "Plasma Diagnostics", edited by R.H. Huddleston and S.L. Leonard, Moscow: Mir, 1967, 515 p. - in Russian.
- ¹⁷ N. Antropov, G. Diakonov, M. Orlov, G. Popov, V. Tyutin, V. Yakovlev, Yu. Alexeev, M. Kazeev, F. Darnon "High Efficiency Ablative Pulsed Plasma Thruster Characteristics", Proceedings of the 3rd International Conference on Spacecraft Propulsion, Cannes, France, 2000.

¹⁸ Lynn A. Arrington, Thomas W. Haag "Multi-Axis Thrust Measurements of the EO-1 Pulsed Plasma Thruster", AIAA 99-2290, Los-Angeles USA, 2001.

¹⁹ Y.A. Alexeev, M.N. Kazeev, V.F. Kozlov, Propellant Energy Flux Measurements in Pulsed Plasma Thruster 28th International Electric Propulsion Conference, Toulouse, France, 2003. IEPC-paper #39.

²⁰ N. Antropov, G. Diakonov, M. Orlov, G. Popov, V. Tyutin, V. Yakovlev, Development and Refinement of Highly Efficient 150 J APPT. 28th International Electric Propulsion Conference, IEPC-paper #61, Toulouse, France, 2003.

²¹ Fluoropolymers ed. by Leo A. Wall, New York-London-Sydney-Toronto, 1972

²² S.L. Madorsky, Thermal Degradation of Organic Polymers, Interscience Publishers, John Wiley R, Sons, N.Y., 1964

IV. List of presentations at conferences and meetings with abstracts

1. Y.A. Alexeev, M.N. Kazeev, V.F. Kozlov, Propellant Energy Flux Measurements in Pulsed Plasma Thruster 28th International Electric Propulsion Conference, IEPC-paper #39, Toulouse, France, 2003.

The Ablative Pulsed Plasma Thruster (APPT) performance is essentially dependent on propellant behavior. Understanding of physics of energy transfer from electrical discharge to propellant is necessary for adequate modeling of APPT and its design and optimization. In the APPT, the considerable energy fraction absorbed by the propellant surface may be transferred not only by particles but ultraviolet radiation from discharge. In this paper the density of the energy flux absorbed by propellant surface in the APPT was measured with a small size temperature probes. APPT model works at 60–300 J bank energy with average mass flow rate of order $10^{23} \text{ cm}^{-2} \text{ s}^{-1}$. Heat flux and mass flow rate measurements were analysed on the base of propellant ablation model, accounting kinetics of polymer thermal degradation. Degradation energy and of mass flow rate values are estimated. Relative shares of conductive and irradiative energy fluxes delivered to propellant from APPT discharge, and the effect of propellant behaviour on thruster efficiency are discussed.

2. N. Antropov, G. Diakonov, M. Orlov, G. Popov, V. Tyutin, V. Yakovlev, Development and Refinement of Highly Efficient 150 J APPT. 28th International Electric Propulsion Conference, IEPC-paper #61, Toulouse, France, 2003

Operation conditions for a majority of small spacecrafts (SSC) with the mass ranging from 50 kg up to 500 kg require regular correction for their orbits that makes it necessary to use small-scale propulsion systems. (PS) capable to operate efficiently under the conditions of limited power consumption (up to 20-200 W). Because of relative simplicity and cheapness of SSC, simplicity and cheapness of PS should play not the last part in this choice. From this point of view, ablative pulsed plasma thruster (APPT) having many engineering and operational advantages is the most perspective option for SSC. However, low thrust efficiency of the widely known "traditional" APPT limits its real capabilities in the control. Design, technologic and operational simplicity of the "traditional" thruster were kept in the APPT developed during the few previous years. Along with this, new thruster is characterized by a highly efficient operating process offering thrust efficiency of up to 20-40% within the stored energy range of 50-200 J. This paper presents the development and refinement results for the APPT with the stored energy of 150 J (APPT-150) that may be used rather efficiently for a control within the power consumption range of 20-200 W.

3. V.Kim, V.Kozlov, A.Skrylnikov, A.Vesselovzorov, J.Fife, S.Locke, "Investigation of operation and characteristics of small SPT with discharge chamber walls made of different ceramics- paper AIAA-2003-5002, 39th JPC, 20-23 July 2003, Alabama, USA.

There was made characterization of the SPT-25 model with discharge chamber walls made of different materials such as the Russian BN-SiO₂ (BGP) type ceramics, AlN-BN and BN types ceramics produced in France and in USA, respectively. The SPT-25 model has external accelerating channel diameter 25mm and acceptable performance level under discharge powers (100-200)W. To characterize its operation with discharge chamber walls made of different ceramics there were determined the voltage-current characteristics of the mentioned model under different magnetic fields inside the accelerating channel and different mass flow

rates through the accelerating channel. There were determined also the thrust values and other output parameters such as the thrust efficiency and specific impulse, the accelerated ion flow divergence by measurement of the accelerated ion current distributions in off-axis angle by RPA probe, some plume plasma parameters measured by cylindrical electrostatic probe and discharge voltage and current oscillation characteristics.